

Contents

Acknowledgements	3
1 Introduction	4
2 Nonlinear Elastic Wave Propagation in heterogeneous materials	8
2.1 Classical Nonlinear Elasticity	9
2.1.1 Basic theory	9
2.1.2 Classical nonlinear effects in elastic wave propagation	12
2.2 Nonclassical Nonlinear Elasticity	16
2.2.1 Experimental phenomenology	17
2.2.2 Phenomenological models and numerical simulation codes	26
3 Nonclassical Nonlinear elastic behaviour of damaged concrete	45
3.1 Structure of concrete and its elastic behaviour	46
3.2 Fast and slow dynamics experiments with undamaged and damaged concrete samples	48
3.3 Setups of the numerical simulated resonance experiments	50
3.4 Comparison between numerical simulations results and experimental data	53
3.4.1 Fast dynamics experiments and simulations	53
3.4.2 Slow dynamics experiments and simulations	54
3.4.3 Comments on the experimental and simulation results	58
4 Time Reversal Elastic Wave Propagation for the localization and characterization of nonlinear scatterers in damaged materials	64
4.1 The Physics of Time Reversal Elastic Wave Propagation	64
4.1.1 Theoretical and historical considerations	64
4.1.2 Theory of the Time Reversal Cavity (TRC)	66
4.1.3 Time Reversal Elastic Wave Propagation Experiments	74
4.1.4 TR elastic wave propagation in attenuative and nonlinear media	91
4.1.5 Imaging techniques by TR elastic wave propagation	94
4.2 Computational Nonlinear TR imaging of scatterers in 2D	97
4.3 Computational TR imaging of scatterers in 3D	114
4.3.1 Test of the computational TR imaging method with 3D numerical simulations	115
4.3.2 3D numerical simulations of real-world TR imaging experiments	116
5 Conclusions and future developments	125
5.1 Summary of achieved results	125
5.2 Supplementary work to be done	126
5.3 Ongoing and future developments	126

5.3.1	Selective localization and characterization of defects in solid NCNL elastic materials	126
5.3.2	Spatial and temporal characterization of Earthquake sources and physical mechanisms	126
Appendix I. LISA-Spring 1D model and computational code		129
Appendix II. LISA-Spring 2D model and computational code		133
Appendix III. LISA-Spring 3D model and computational code		135
Bibliography		136

Acknowledgements

It is always hard to acknowledge all the people who have supported, inspired, helped and guided you in such a complicated and long experience as a Ph.D.: for space and time reasons, someone is always not cited. What I would like to do is to express my lifelong gratitude to all people who have accompanied and sustained me along such path. I would like to acknowledge the helpful guide of my scientific mentor, Prof. Pier Paolo Delsanto, who has taught me much about Science and Human Beings in general. I would like to re-call the daily support and inspiring collaboration with Dr. Marco Scalerandi. I am thankful towards Dr. Antonio Gliozzi, Matteo Nobili (who has shared with me every moment of the Ph.D. as a Ph.D. student in the same Group), Dr. Federico Bosia: all of them have been helpful, inspiring and wilful colleagues and headmasters. I am grateful towards my parents and a bunch of my friends because they have supported me in difficult or critical moments and have been very comprehensive and always helpful in listening to me: it is not necessary to cite all of them, I think they are aware of the important role they have played during many occasions of my Ph.D. with suggestions, phone calls of support, letters, e-mails, etc... . I would like to acknowledge the patience and willingness of Gianpaolo Perego (and of his team) of Aethia - Power Computing Solutions S.r.l. and Fabrizio Conicella of Bioindustry Park of Canavese, because through them the collaboration with the Bioindustry Park of Canavese and the Research Group of Prof. Delsanto has been possible, giving me the unequal opportunity of taking advantage of facilities for High Performance Scientific Computing, especially Parallel Computing, and of learning about it, sometimes with the day-per-day support on technical issues and problems. I think my collaboration with them has been a great opportunity from the scientific and human point of view and I wish the knowledge and practice I have obtained will be a good return asset for their invested efforts in such a collaboration. I would like to remember the support of Simona Balestracci and Corrado Debortoli, of CNR-CNISM, Torino-Polytechnic Research Unit. I am grateful to Dr. Paul A. Johnson and his team at the EES-11 (Geophysics) Division of the Los Alamos National Laboratory (Los Alamos, New Mexico, USA) for the collaboration started towards the end of the final year of the Ph.D. and for having involved me in their Project about Time Reversal Elastic Wave Propagation Physics, but also for their support and friendship.

Finally, I would like to thank all the Italian tax-payer fellows because my Ph.D. has been funded by public financial resources for scientific Research: despite many disadvantages, difficult conditions of work, many different types of problems affecting the “Scientific Research System” in Italy, I have had the occasion, with the Ph.D. experience, to extend my knowledge and professional background, through the annual funds for mobility erogated by the Polytechnic of Torino to each Ph.D. student I have had the possibility to attend summer schools and courses about High Performance Computing that has let me to obtain the necessary basic knowledge for oriented self-study and practice that have already given me professional opportunities and personal great satisfaction. It is common knowledge (maybe, it should be more common) the difficulties and structural problems of Scientific Research funding and policy in Italy, however I would like to remember and underline that many people working at Universities and public Research Institutions are working very well and hard, with great professionalism and passion, for making such a “System” work properly and, for what concerns the experience of my Ph.D., for letting new generations learn and acquire good skills in Scientific Research.

I wish for the future to use and put such knowledge and acquired skills at the service of my Country or generally of Human Beings and to be useful to them in order to payback what I received from all of them.

Chapter 1

Introduction

The part of Ph.D. work done in the last three years and reported in this Ph.D. thesis is concerned with a main, central, leading issue: exploit some peculiar characteristic nonlinear effects in elastic wave propagation through heterogeneous solid damaged materials in order to characterize the damage level and localize the sources of damage within the specimens. In a certain sense, the common objective of the Research work performed during the three years of Ph.D. at the Dept. of Physics of Polytechnic of Torino (and in a small part, during the end, at the Los Alamos National Laboratory, EES-11 (Geophysics), Nonlinear Elasticity Group) within the Group of Prof. P.P. Delsanto has been taking advantage of typical signatures of nonlinear elastic behaviors of damaged solid specimens as revealing and information-rich phenomena for studying the damage itself for nondestructive evaluation purposes.

The work has been performed within the branch of Research called Nonclassical Nonlinear (NCNL) Elasticity (or also Mesoscopic Nonlinear Elasticity), emerged from the interaction of different Research fields (Geophysics, Physics of rocks, Materials Sciences, Continuum Mechanics, Ultrasonics, Nondestructive Evaluation Techniques, Seismology) and concerned about a specific type of nonlinear elastic behavior which is shared among different types of solid materials, having in common some structural similarities (solid materials made essentially by two phases, a set of hard elastic grains interfaced and cemented among them by a soft poro-viscoelastic binding medium, usually very heterogeneous from the structural point of view, filling in the interfaces among the many grains). The first part of Chapter 2 of this Thesis is dedicated to an (incomplete) introduction to NCNL Elasticity, firstly studied in the case of consolidated and unconsolidated Earth materials of granular type and then investigated in reference to other types of solid materials, especially some types that do not exhibit such nonlinear elastic responses to perturbations applied to them except in the case their structure have been altered by some kind of damage, acquiring structural features similar to the ones of polycrystalline grainy Earth's materials.

I would like to make in advance, at this point, before the reader proceeds, a warning: these Earth's materials, whose such anomalous nonlinear elastic behavior has been investigated first, have been frequently labelled as granular materials and in effect they are granular materials but not in the sense the label "granular" materials is mainly used today in Physics and Materials Science. Indeed, in the last few years, great attention has been acquired by the field of Research of granular media [1, 2], being them specimens made of an ensemble of solid grains with dimensions of the order of mm collected together within certain spatial restricted domains, as in the case of sandpiles, granular solids in ducts or in layered domains, etc.... These materials differ from the ones initially studied in reference to NCNL Elasticity for the degrees of freedom of the grains: in granular media, there is no a binding medium with cementitious properties, so they are usually called also granular fluids [1, 2], however rocks and solid composite damaged materials with NCNL elastic behavior have solid grains with lower degrees of freedom, embedded in the

binding medium which have cementitious properties, so they can almost undergo poro-viscoelastic (local) deformations and not compressive translational movements. Although, recently the elastic properties of granular media have been investigated and some evidences of similar features have been found [3], granular fluids and grainy NCNL elastic materials are different kinds of composite materials.

Up to now, as reported in Chapter 2, the micro-mechanical mechanisms at the basis of such nonlinear anomalous elastic effects have not yet been understood, although recent investigations have started to confirm what has been proposed since the beginning of the studies in this Research field, i.e. the leading role of the multi-phase binding medium (i.e. solids and fluids filling in the interstices among the grains) in generating the typical signatures of NCNL Elasticity.

Due to such a lack of a physical theoretical background for the explanation and mathematical description of such elastic behavior, physical-mathematical models based on phenomenological knowledge have been used for such objectives. Chapter 2 introduces the reader to the LISA-Spring models for elastic wave propagation in solid materials with a high level of physical heterogeneity and with such typical two-phase structure with soft interstices interfacing hard grains among them. These models have been formulated in the first versions by Dr. M. Scalerandi and Prof. P.P. Delsanto, Dept. of Physics, Polytechnic of Torino, and have been shown to be successful in reproducing some experimental data about all the types of NCNL elastic effects, measured both in quasi-static and in dynamic (i.e. with traveling or stationary waves) probing experiments.

These models make use of the Preisach-Mayergoyz formalism for the mathematical description of systems with hysteretic nonlinear equations of state, as in the case of the stress-strain quasi-static constitutive relation of NCNL elastic materials. They have been the primary tools for my Ph.D. work, dedicated to their extension and to their applications in simulating elastic (mainly ultrasonic and acoustic) wave propagation in such materials. The second part of Chapter 2 and the three Appendixes are dedicated to the formulation of such models and to their respective implementations in computational codes, including 3D parallel computing codes, to which I have dedicated most of the final year of my Ph.D. work, being High Performance Scientific Computing one of the fields of specialization of my Ph.D. training.

Chapter 3 is dedicated to a specific, original, study about the NCNL elastic behavior of concrete and to the role of damage in increasing qualitatively and quantitatively its signatures. The study has been performed in collaboration with Dr. M. Bentahar and Prof. R. El Guerjouma, both formerly at the GEMPPM, *Groupe d'Etude en Metallurgie Physique and Physique des Matériaux*, UMR CNRS 5510 and INSA, *Institute Nationaux des Sciences Appliquées*, de Lyon, at the time this work was done, and with Dr. M. Scalerandi, Dept. of Physics, Polytechnic of Torino. It is one of the first and most complete investigation about the NCNL elastic properties of concrete and about the connection between NCNL Elasticity and damage. It consists both in experimental measurements and numerical simulations made by special versions of the LISA-Spring models as support tools for the analysis of the experimental data. It was motivated by two main purposes: the validation of the LISA-Spring 1D model in reproducing experimental data about most of the typical measurable effects characterizing NCNL Elasticity considering a unique type of material; the investigation of the role of damage in changing the structure of concrete resulting in an increase and enhancement of its NCNL elastic response. Studying such connections between damage in solid grainy and composite materials and their exhibition of NCNL elastic effects is of great importance from an applicative point of view, because they show some physical behavior to be probed and interrogated on solid specimens in order to get information about the level and (maybe) type of damage they have undergone.

Two European Research projects have been dedicated to such applicative issues and I have been involved in both of them: the European Science Foundation (ESF)-funded NATEMIS (Nonlinear Acoustic TEchniques for MIcro-Scale damage diagnostics) project, which ended in

August 2005; the European Union (EU)-funded AERONEWS (Nonlinear Elastic Wave Spectroscopy for health monitoring of aircraft components) project within the framework of the FP6 (ongoing).

While the performed investigation about the relationship between damage and NCNL elastic behavior of concrete could be useful in the exploitation of the experimental techniques able to measure the NCNL signatures in order to characterize the level of damage in a specimen of such materials (using the simulations as tools for assessing the connections between the measured parameters and the ones characterizing the damage and the specimen), Chapter 4 is dedicated to another original work of my Ph.D.: the development of a Computational Imaging approach exploiting the properties of Time Reversal Acoustics (TRA).

TRA is a field of Research in Acoustics and, generally, Elastodynamics, dedicated to the peculiar wave propagation features associated with the covariance of the Elastodynamics wave equations, for non-attenuative media, in respect of the transformation $t \rightarrow -t$, i.e. a time reversal (TR). Brought into Acoustics and Elastodynamics from Optics (Optical Phase Conjugation), it has been developed mainly by the Research group of Prof. M. Fink, Université de Paris VII. Fink *et al.* have developed experimental techniques for realizing the time-reversed version of a forward elastic wave propagation in a specimen. Due to the TR invariance in lossless media, from a theoretical point of view, elastic waves can travel along the same elastic ray-paths they have followed in an experiment throughout a medium but with reversed directions. It means that if a region within a specimen behaves as a primary or secondary source (i.e. scatterer) of waves during a propagation experiment, in the time-reversed version of the same experiment they act as focusing regions, where elastic energy is focused by incoming wavefronts. So, a technique for focusing elastic energy has been realized.

The initial part of Chapter 4 is dedicated to an overview of the theoretical basis of Time Reversal Acoustics and of the first experimental setups developed by Fink *et al.* for the experimental realization of TR elastic wave propagation experiments. Such setups are called Time Reversal Mirrors (TRMs). A review of the main properties of TR Wave Physics is presented to the reader, focused on the most important results obtained in the last fifteen years for the realization of techniques for retro-focusing elastic energy on such scatterers as linear inhomogeneities and nonlinear defects.

Then, it is introduced a new proposed technique for the localization of defects within solid specimens using the properties of TRA experiments and numerical simulations. The technique, developed by me, Dr. M. Scalerandi and Dr. A.S. Gliozzi, is labelled as a Computational TR Imaging one because it exploits numerical simulations, made by the LISA-Spring models, for realizing the second part of a typical TRA experiment, i.e. the TR backward propagation. The second part of Chapter 4 introduces such technique and the signal processing method proposed for the selective imaging of scatterers within solid specimens due to defects that generate NCNL elastic responses, the most interesting ones from a nondestructive evaluation point of view.

The results of virtual experiments applying such an Imaging technique are presented, performed both in 2D and in 3D. "Virtual experiments" in this case means that the forward propagation part of a TRA experiment has been simulated using the LISA-Spring models. After the validation of the proposed Computational Imaging technique, some issues are addressed regarding the application of the technique to the localization of NCNL scatterers within solid specimen, including the role of virtual 3D TRA experiments for studying some TR Wave Physics interference phenomena that can influence the selective retro-focusing of elastic waves, so of the formation of images revealing the position of the actual nonlinear scatterers (i.e. of defect regions like distributions of micro-cracks or extended macro-cracks, the most interesting from a nondestructive evaluation point of view).

The implementation of a 3D parallel LISA-Spring computational code has been one central objective in the development of such Computational Imaging technique, so that it constitutes

the basic tool for ongoing and future work (presented in Chapter 5) addressed to the application of the method as a nondestructive imaging technique for solid damaged specimens as well as for the basic investigation of TR elastic wave propagation Physics in NCNL elastic solids.

Chapter 5 reports also some ongoing work at the EES-11 (Geophysics) Division, Los Alamos National Laboratory (Los Alamos, New Mexico, USA), within the framework of a project funded by the US Department of Energy, dedicated to further investigations of TR Wave Physics in composite damaged solid materials but also to the application of parts of the results therein obtained to the development and exploitation of Computational TR Imaging techniques for 3D localization and characterization of Earthquake sources (TR Seismic Imaging).

Chapter 2

Nonlinear Elastic Wave Propagation in heterogeneous materials

Nonlinear elastic behavior in fluids and solid materials have been investigated experimentally and theoretically since the nineteenth century. Nonlinear Elasticity is today an extended field of Research both from an experimentally and mathematically point of view. However, different types of nonlinear elastic behaviors have been found out in the last decades. Indeed, since the 1950s, new quasi-static and dynamic elastic phenomena have been discovered regarding solid materials. These phenomena have been classified and thoroughly investigated under both basic and applied Research objectives. It has been introduced a specific terminology for labeling this new ensemble of nonlinear elastic phenomena, in order to putting them apart from another ensemble of nonlinear elastic phenomena investigated and characterized since the nineteenth century.

Section 2.1 reports a brief (incomplete) overview of the typical nonlinear elastic behavior of fluids and solids that has been studied since the development of a coherent Theory of Elasticity. The field of study of this nonlinear elastic phenomenology has been labelled as **Classical Nonlinear (CNL) Elasticity** not only for chronological reasons but also because it consists in the general formulation of the Theory of Elasticity directly derived from the classical theory of Continuum Mechanics. The traditional Theory of Linear Elasticity derives too from it, under approximations of infinitesimal deformations of media or material specimens. This classical theory has managed to explain and predict many quasi-static and dynamic elastic phenomena for viscoelastic fluids and monocrystalline solids.

The new nonlinear elastic phenomenology cited above and described in Section 2.2 regards first of all only solid materials and with typical structural features shared by different kinds of such materials. It has been proposed to collect this variety of solid materials into a single class due to their common exhibition of these alternative nonlinear elastic behavior and to their sharing of a common “blueprint” from a structural point of view: more or less, their structure, at a macroscopic scale, can be described roughly as composed by two phases, a set of hard viscoelastic “grains” embedded in a soft viscoelastic binding medium which fills up the interfaces between the different grains. The field of study of the nonlinear elastic behavior of such solid materials has been labelled as **Nonclassical Nonlinear (NCNL) Elasticity**, in order to be distinguished by the CNL one.

The two nonlinear elastic phenomenologies differ both in intensity and origin of the nonlinear elastic response. The NCNL elastic phenomenology has acquired even more importance for applications purposes in the last two decades because it has been shown to be exhibited by a vast class of composite materials having undergone some kinds of perturbations in real-world uses: as an example, monocrystalline solid specimens do not exhibit such NCNL response if their lattice structure is unperturbed, “pure”, but they do exhibit it after loading inducing dislocations

within their lattice [4]. Indeed, in the last decade, many experimental investigations have shown that damaged composite materials of interest for technological applications do exhibit such nonlinear elastic behavior and the “intensity” of such behavior is greater if the damage is more widespread or stronger. So, the NCNL elastic phenomenology has got a significant interest within the field of Nondestructive Evaluation and Imaging of solid composite materials just because its identification in solid specimens can be connected with the presence of defects and different types of damage.

2.1 Classical Nonlinear Elasticity

Classical Nonlinear Elasticity is the field of study of elastic deformations (and their propagation) with small but finite amplitudes. Elastic wave propagation in fluid or solid specimens in such conditions is described by nonlinear wave equations following from the general governing equations of Continuum Mechanics for moderate-amplitude displacements when the nonlinear terms are small compared with the linear one (which does not mean that their effect on the process is small). Nonlinear elastic wave propagation in fluids was studied successfully during the nineteenth century, particularly regarding the formation of shock waves in liquids and gases, giving rise to soliton-like propagation. Only in the twentieth century, nonlinear acoustics were studied both experimentally and theoretically in crystalline solids (the first analytic treatment predicting the harmonic generation in sound propagation in solids was proposed in the 1930s by Fubini and Fay, while the first solution to non-planar finite-amplitude sound wave equation in solids dated back to 1948 by Eckart).

2.1.1 Basic theory

The fundamental elastic wave equation for a perfectly elastic body (specimen) can be derived through the second law of Newton for a continuum and the constitutive stress-strain relation characterizing that body:

$$\rho \cdot \frac{\partial^2 u_i}{\partial t^2} = \frac{\partial \sigma_{ij}}{\partial x_j} \quad (2.1)$$

$$\sigma_{ij}(\vec{r}, t) = f(\epsilon_{lm}(\vec{r}, t)) \quad (2.2)$$

where $u_i(\vec{r}, t)$ is the i -th component of the displacement vector field ($i = 1, 2, 3$), $\sigma_{ij}(\vec{r}, t)$ is the stress tensor field (a rank = 2 tensor field) and $\epsilon_{lm}(\vec{r}, t)$ is the strain tensor field (again a rank = 2 tensor field), $\rho(\vec{r}, t)$ is the volumetric mass density scalar field, usually assumed constant in a specimen although a high level of heterogeneity, \vec{r} is the position vector in R^3 indicating a position within the medium of interest and t is the time variable. Eq. 2.1 is the second law of Newton written for a continuum medium while Eq. 2.2 defines a functional relationship between the stress and the strain tensor fields. In Eq. 2.1 the Einstein’s convention for repeated indexes used in Tensor Calculus is assumed (it means that a sum over the three possible values of the index $j = 1, 2, 3$ is intended and not directly explicitated). From now on such convention will be used throughout the Sections otherwise stated.

Substituting Eq. 2.2 in the right hand side of Eq. 2.1 leads to the elastic wave equation¹.

The stress-strain relation of Eq. 2.2 can be derived from thermodynamical considerations for a perfectly elastic body undergoing reversible deformations, i.e. mechanical deformations

¹Actually, from a mathematical point of view, it should be better to speak of a set of coupled wave equations because there is one wave equations for each scalar field $u_i(\vec{r}, t)$, $\forall i = 1, 2, 3$ and each of them is coupled to the other two.

corresponding to isentropic thermodynamic transformations so that at each time every region of the body is in a state of thermodynamic equilibrium. The infinitesimal work corresponding to an infinitesimal deformation can be expressed as $dW = -\sigma_{ij}(\vec{r}, t) \cdot d\epsilon_{ij}(\vec{r}, t)$. Using the first principle of thermodynamics and the isentropic relation deriving from the second one in adiabatic regimes ($dQ = T \cdot dS$), the subsequent infinitesimal relations can be derived for the basic thermodynamic potentials (actually volumetric densities of such energies):

$$dU - T \cdot dS = \sigma_{ij} \cdot d\epsilon_{ij} \quad (2.3)$$

$$dF = dU - T \cdot dS = \sigma_{ij} \cdot d\epsilon_{ij} - S \cdot dT \quad (2.4)$$

$$dG = dF - \sigma_{ij} \cdot d\epsilon_{ij} - \epsilon_{ij} \cdot d\sigma_{ij} = -S \cdot dT - \epsilon_{ij} \cdot d\sigma_{ij} \quad (2.5)$$

where U is the volumetric density of internal energy, F is the volumetric density of Helmholtz's free energy and G is the volumetric density of Gibb's free energy.

Three corresponding relations between stress-strain can then be derived in three different conditions using the preceding infinitesimal relations:

$$\sigma_{ij}(\vec{r}, t) = \left(\frac{\partial U}{\partial \epsilon_{ij}} \right)_S (\vec{r}, t), \quad (2.6)$$

$$\sigma_{ij}(\vec{r}, t) = \left(\frac{\partial F}{\partial \epsilon_{ij}} \right)_T (\vec{r}, t), \quad (2.7)$$

$$\epsilon_{ij}(\vec{r}, t) = - \left(\frac{\partial G}{\partial \sigma_{ij}} \right)_T (\vec{r}, t), \quad (2.8)$$

where the suffix labels T and S mean that these variables are considered as constants.

Eq. 2.7 is the most used because at the basis of the classical Theory of Elasticity there is an assumption about the relation between the volumetric density of Helmholtz's free energy and the components of the strain tensor field: F is assumed to be a function of the several ϵ_{ij} which can be represented under the form of a power series expansion in ϵ_{ij} :

$$F(\vec{r}, t) = F_0 + \frac{1}{2} \cdot C_{ijkl} \cdot \epsilon_{ij} \cdot \epsilon_{kl} + \frac{1}{3} \cdot C_{ijklmn} \cdot \epsilon_{ij} \cdot \epsilon_{kl} \cdot \epsilon_{mn} + \dots \quad (2.9)$$

where F_0 is the volumetric density of free energy in absence of deformations within the medium, $(F - F_0)$ is also called the volumetric density of elastic free energy of the medium, and the coefficients of the power series expansion are called as the elastic constants of the medium, being collected as components of tensor fields too ($C_{ijkl}(\vec{r})$ are called elastic constants of second order, $C_{ijklm}(\vec{r})$ of the third order and so on, being tensor fields in the case of an heterogeneous medium or tensors in the case of an homogeneous one).

Using Eq.s 2.7 and 2.9, the form of the stress-strain constitutive relation for the medium can be derived and introduced in Eq. 2.1, along with the most general definition of the strain tensor field

$$\epsilon_{ij}(\vec{r}, t) = \frac{1}{2} \cdot \left(\frac{\partial u_i}{\partial x_j} + \frac{\partial u_j}{\partial x_i} + \frac{\partial u_i}{\partial x_k} \cdot \frac{\partial u_j}{\partial x_k} \right), \quad (2.10)$$

so the form of the elastic wave equations can be derived, actually a set of coupled partial differential equations with the unknowns being the components of the displacement vector field, $u_i(\vec{r}, t)$ for $i = 1, 2, 3$, as previously noticed.

It should be reminded that, up to now, the choice of using Eq. 2.7 for the derivation of the stress-strain constitutive relation of the medium implies considering only isothermal deformations propagating through the medium itself.

The traditional linear Elastodynamics equations are obtained under the approximating hypothesis of infinitesimal amplitude displacements, so that in the definition of the strain tensor field the cross terms could be neglected and in the power series expansion of the Helmholtz's free energy only the quadratic terms in ϵ_{ij} could be retained, so that the stress-strain relation results to be a generalization of the Hooke's law,

$$\sigma_{ij}(\vec{r}, t) = C_{ijkl}(\vec{r}) \cdot \epsilon_{kl}(\vec{r}, t). \quad (2.11)$$

Under this approximation (linear regime), the Elastodynamics wave equations reduce to a set of coupled linear hyperbolic partial differential equations, with a second order time partial derivative operator and first order/second order pure/mixed partial derivative operators in respect to the coordinate spatial variables x_i for $i = 1, 2, 3$ of the Cartesian frame of reference. If the medium considered is homogeneous, the elastic constants of second order are constants so these equations are with constant coefficients.

From an experimental point of view, quasi-static (but also dynamic) investigations are usually conducted using material specimens tailored with a specific geometry, e.g. with a cylindrical or parallelepiped shape and with relative orientations of the crystallographic axes to the symmetry axes of the shape and dimensions such that the number of parameters of the problems can be reduced. Many solid (crystalline) materials could also be considered elastically isotropic under certain conditions, as an approximation which reduces the total number of elastic constants to only two independent ones.

Under these restrictive conditions and in the special case of uniaxial loads (a stress tensor with only one component along the main symmetry axis of a specimen with the shape of a bar and with a small cross section-to-length ratio), the stress-strain constitutive relation reduces to a simpler form more usual and similar to the Hooke's law:

$$\sigma(x, t) = E \cdot \epsilon(x, t) = E \cdot \frac{\partial u}{\partial x}(x, t) \quad (2.12)$$

where E is called the Young's modulus of the thin bar-shaped specimen, there is only one component of the displacement vector field, the one along the axis of the bar and due to the thin bar approximation the dependence on space relies only on the coordinate along the x axis assumed to be the one of the bar.

In these conditions which are very restrictive but usually matched experimentally, quasi-static experiment can be performed for checking the linear elastic behavior of the material. Usually a longitudinal stress is applied to one end of the bar-shaped specimen and its strain is measured relating to the whole specimen (and not to a specific point). Most linear elastic materials exhibit actually a linear relationship between σ and ϵ up to a certain value of the uniaxial load stress, above which the strain does not increase with the increase of the stress. Above that stress threshold, the material exhibits a plastic behavior, up to its failure at higher stress values.

When the displacement amplitudes cannot be considered infinitesimal, i.e. when they are small but finite, in Eq. 2.9 the terms of order greater than the second one in the components of the strain tensor must be considered and that leads automatically to a set of coupled nonlinear second order partial differential equations as the Elastodynamics wave equations. The greater the amplitudes of the displacement fields more terms must be retained in Eq. 2.9, so the stress-strain constitutive relation no longer expresses a linear relation between the components of the stress tensor field and the components of the strain tensor field.

As a first consequence of the presence of elastic constants of order greater than the second one in the stress-strain constitutive relation, the nonlinearity of the Elastodynamics wave equations

implies that the principle of superposition no longer holds for elastic wave propagation described by such equations, so the huge amount of wave phenomena like interference, diffraction, etc. ... are no longer valid in the forms described by linear wave Physics. Different types of nonlinear effects arise in such conditions, some of which have been successfully predicted and/or described by the theory reported above, considering for each case a different degree of expansion of F in terms of powers of ϵ_{ij} , i.e. different classical nonlinear elastic phenomena can be described with the use of different orders of elastic constants.

In Section 2.1.2 a brief review of the most important of such nonlinear elastic responses are presented, along with a reference to their theoretical descriptions and interpretations.

It should be reminded at this point that the theory of Elasticity introduced so far is valid for fluids and monocrystalline solids, which are the simplest materials studied in classical Elasticity.

2.1.2 Classical nonlinear effects in elastic wave propagation

A first example of classical nonlinear elastic effect in fluids or crystalline solids is called **non-linear wave mixing** (or **nonlinear wave modulation**). It consists in a kind of nonlinear interaction between (in the simplest case) two simple harmonic plane waves having two very different frequencies, ν_1 and ν_2 with $\nu_1 \ll \nu_2$, and two very different amplitudes, A_1 and A_2 respectively with $A_1 \gg A_2$, being at least A_1 a finite amplitude. When the two harmonic wavefronts get to interact² together in the same medium region, the resultant perturbation consists not in the superposition of two harmonic waves with different frequencies ν_1 and ν_2 but in two new harmonic quasi-planar waves with frequencies $(\nu_2 \pm \nu_1)$. A Fourier analysis of the resultant signal in a point of the medium just in the nearby of the interaction region shows evidence of a rich spectral content: beyond the two frequencies ν_1 and ν_2 of the two input waves (which do not disappear completely after the interaction), two other frequencies are present, called sidebands, $\nu_2 + \nu_1$ and $\nu_2 - \nu_1$, just around the main input frequency ν_2 .

This nonlinear wave propagation effect was firstly studied, from an applicative point of view, in the late 1950s-early 1960s by Westervelt in the USA and Zverev and Kalachev in Russia. The main objectives of their investigations were to create a *parametric array*, an experimental setup able to obtain directed radiation of a low frequency signal from the nonlinear interference of two narrow, finite-amplitude, overlapping high-frequency acoustic beams closed in frequency to each other. The classical nonlinear interaction between two harmonic plane waves in a viscous fluid, for example, creates a difference-frequency wave generated throughout the volume of interaction. Such a system can be used as a kind of virtual “antenna” that radiates a directed, low-frequency signal without sidelobes. Parametric arrays have found some applications in sonar marine imaging and communications.

A special kind of nonlinear wave mixing occurs with a single harmonic finite amplitude wave: in this case the input undergoes nonlinear interactions with itself and the result is an output propagating through the medium which, from a spectral point of view, contains not only the frequency of the input wave but also its integer multiples. This nonlinear elastic effect is known under the name of **harmonics generation**. Experiments about harmonics generation in crystals were first conducted during the 1950s by Zarembo and Krasil’nikov in Russia and by Breazeale in the USA.

From a theoretical point of view, sidebands or harmonics generation can be predicted by an approximated solution of the Elastodynamics wave equations via perturbative methods still in the case of a nonlinear medium with third order elastic constants, i.e. having a stress-strain relation containing second order powers of the several ϵ_{ij} [5].

²I prefer to use here the term “interaction” instead of “interference” just because in the case here analyzed the wave interference is nonlinear and anomalous in respect of the linear case, so I prefer to use the term “interference” referring to the traditional interaction of waves in a linear medium.

Figure 2.1 reports synthetically the results of an interesting experiment of nonlinear wave mixing with two simple harmonic waves throughout a plexiglass specimen, which shows to behave as a perfectly linear elastic body only when it is intact, while it shows evidence of harmonics and sidebands generation throughout it after having undergone a quasi-static load producing damage (so changing its structure) within it. In this second “state”, its classical nonlinear behavior seems to be stronger with an increasing amplitude of one of the two input waves. This emergence of nonlinear wave mixing with an increase of the input amplitude is a typical nonlinear elastic effect, common to all types of nonlinear elastic behaviors.

Another typical classical nonlinear elastic effect has been revealed by resonance experiments in specimens tailored as bars with a small cross section-to-length ratio, such that the main type of waves able to propagate throughout them and to reach stationary conditions are longitudinal waves along the symmetry axis of the (cylindrical or parallelepiped-like) bar. These experiments are defined as **Nonlinear Resonant Ultrasound Spectroscopy** (NRUS) [7, 8, 6, 9] experiments and are aimed at monitoring the change of one (SIngle MOde) [10] or many (MUlti MOde) [11] resonance frequencies associated to one or more *eigenmodes* of vibration of the bar when the amplitude of the excitation wave is increased. The resonance frequency of a vibration *eigenmode* of a bar (or of a solid specimen shaped in any way) is strictly dependent both upon the geometry and the elastic properties of the specimen itself. A perturbation of the resonance frequency by a change in the excitation amplitude means that the elastic response of the specimen (with unchanged geometry) changes with the excitation amplitude, which is a typical feature of the classical nonlinear elastic behavior in crystalline solids, for example, as the increase in vibration amplitude does excite the anharmonicity of the crystal lattice due to imperfections in the lattice itself like voids or inclusions (micro-inhomogeneities at the atomic scale).

In the case of a thin/long bar, the **MUMONRUS** [10] technique has been usually implemented, injecting a simple harmonic longitudinal wave into the bar from one of its end sides, measuring the particle velocity or acceleration at the other end side using contact (piezo-ceramic transducers for particle acceleration or displacement measurement) or non-contact (laser vibrometer for particle velocity measurements) methods after a sufficient time for the excitation of the chosen vibration *eigenmode* (formation of stationary waves), then changing the frequency of the harmonic input wave and repeating the same measurement. At each frequency the mean-in-time value of the recovered output signal (particle displacement, velocity or acceleration) is plotted. The frequency is swept on a interval across the theoretically known resonance frequency of the excited vibration *eigenmode*, so the resonance curve of the mode can be plotted, as reported in Fig. 3.4 of Section 3.4.1, first row and first column, for a non-crystalline material like concrete or Fig. 2.2. This set of measurements is then repeated increasing the amplitude of the input wave. Many resonance curves for the same *eigenmode* are then obtained, revealing a sligth (downward) shift of the resonance frequency with the increase of the excitation amplitude, see again Fig. 3.4 of Section 3.4.1 or Fig. 2.2. The absolute value of the relative shift of the resonance frequency has been found to be directly proportional to the square of the local strain amplitude, measured in the same point where the particle velocity or acceleration measurement is made.

Other important nonlinear elastic effects have been investigated thoroughly in the last century, among which the role of pre-stress in inducing a classical nonlinear elastic behavior also in the presence of small/infinitesimal amplitude input waves and the formation of shock waves as a consequence of a cumulative steepening in the wavefront up to a critical length of propagation, beyond which the soliton-like mode of propagation appears. In the latter case, a whole field of study has been developed under the name of shock/soliton wave propagation, particularly regarding soliton elastic waves in fluids. These other nonlinear elastic behaviors are not reviewed in this Ph.D. thesis for space and time issues and because they are not directly linked with the nonclassical nonlinear elastic behavior.

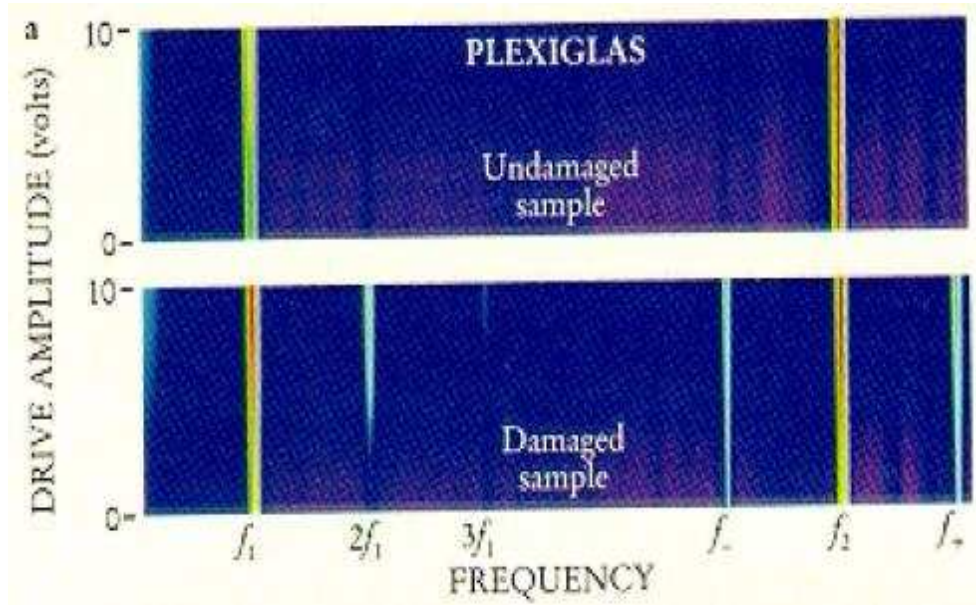


Figure 2.1: Results from a nonlinear wave modulation experiment into a slightly damaged plexiglass specimen. An intermediate-amplitude excitation simple harmonic wave with frequency ν_1 has been injected within a plexiglass specimen, used as a pump “wave”. At the same time, a high level-amplitude simple harmonic wave at frequency $\nu_2 \geq \nu_1$ has been injected into the specimen too (probe wave). The two inputs have been sustained for a long time window during which the amplitude of the pump wave has been gradually increased. The spectral content of the output signal, measured at a point of the specimen far from the zone of nonlinear interaction between the pump and the probe wave, has been plotted in correspondence of each value of the pump wave amplitude by the above color map. The first color map shows the spectrum contents of that signal in the case of a perfect intact plexiglass specimen, which behaves as a linear isotropic homogeneous elastic medium: the two input frequencies can be selectively resolved in the output signal (f_1 and f_2 in the color map plot), just as an evidence of the validity of the superposition principle, independently from the amplitude of the pump wave. So, the medium seems to be elastically linear and independent from the excitation amplitude. The second color map shows a change of behavior by the same specimen after a quasi-static damage which changes its structure: evidence of harmonics ($2 \cdot \nu_1$, $3 \cdot \nu_1$) and sidebands (ν_+ and ν_- around ν_2) generation becomes stronger as the pump amplitude increases, due to a correspondent increase in the nonlinear behavior of the medium. These results are taken from Ref. [6].

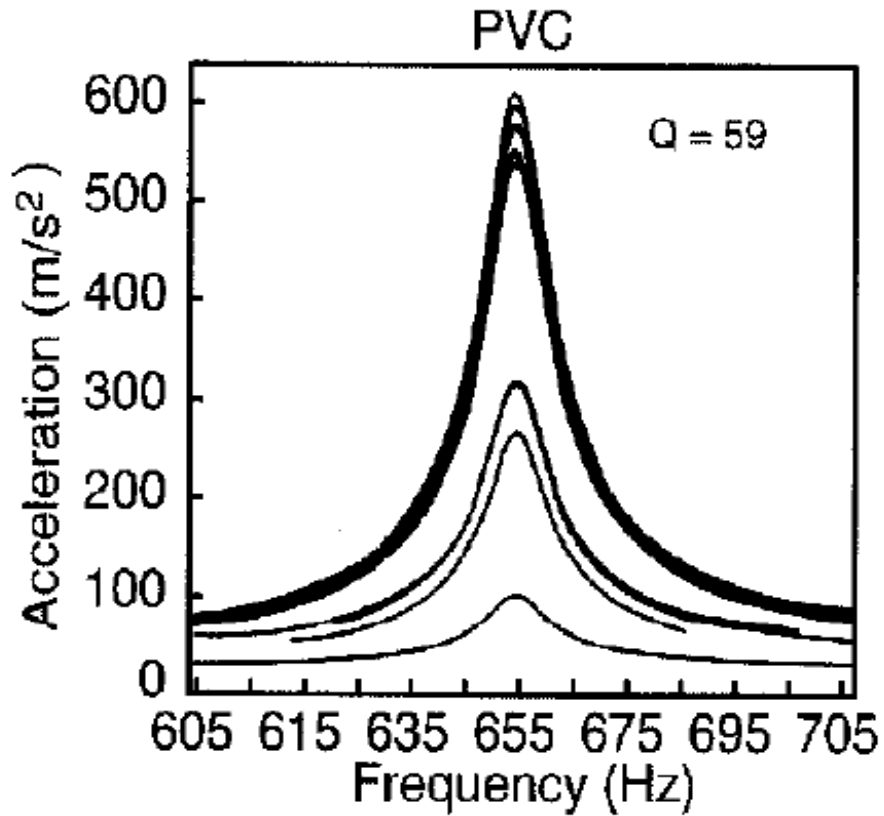


Figure 2.2: Nonlinear Resonant Acoustic Spectroscopy results in a specimen of polyvinylchloride (PVC) tailored as a thin long bar. This material has a Q factor with value 49, i.e. a high level of attenuation similar to the one of polycrystalline or granular rocks. However, the resonance frequency of its principal Young's *eigenmode* of vibration slightly changes with an increase or decrease of the amplitude of the excitation input wave, so its elastic response is the typical one for a classical nonlinear material. Figure taken from Ref. [12]

2.2 Nonclassical Nonlinear Elasticity

First evidences of anomalous nonlinear elastic behaviors not comprehensible within the framework of the classical Theory of Nonlinear Elasticity came since the 1950s regarding different types of materials whose elastic behaviors were investigated by different experimental techniques and approaches.

For example, during the 1950s, Granato and Lucke reported the first experimental data about anomalously strong hysteretic nonlinear elastic response of metals [13]. Their work became one of the first seminal study about the role of dislocations in crystalline materials in changing their overall mechanical properties.

During the 1940s, the Birch's group at the Harvard University performed quasi-static measurements on Earth's materials samples in order to study their stress-strain constitutive relations. Using mechanical presses, they interrogated the elastic behavior of such materials at strong low frequency (near DC) forcing. These quasi-static tests were of interest for studying the nature of Earth's interior materials in terms of pressure and temperature responses and for predicting mineral assemblages and mineral phases in the Earth's lower crust and mantle.

During the 1970s, Stacy's group at the University of Queensland performed the first ever reported investigations about mechanical hysteresis in rocks at low strain levels ($|\epsilon \simeq 10^{-7} \div 10^{-6}|$), still with quasi-static tests.

However, the first experimental studies about nonlinear dynamic elastic behavior (i.e. regarding wave propagation in the form of traveling waves or standing waves) connected with hysteretic quasi-static stress-strain relations were performed only during the 1980s, both in Russia (Bakulin and Protosenya's group, the group at the Radiophysical Institute and the Institute of Applied Physics in Nizhny Novgorod) and in USA (Los Alamos National Laboratory, Institute of Geophysics and Planetary Physics).

Section 2.2.1 presents a brief review of the main nonlinear elastic effects measured in laboratory experiments with quasi-static and dynamic experiments of different types. Such phenomenology of nonlinear elastic behavior has been investigated, first of all, extensively regarding Earth's materials like granular rocks, sandstones (granular consolidated Earth materials), regarding river sands and limestones (granular unconsolidated Earth materials) and then other types of solid materials which, as previously cited in the introduction to this chapter, have some structural features in common with such Earth materials, particularly the possibility of describing their structure, at a macroscopic scale, as essentially made of two phases, the first being an ensemble of viscoelastic hard grains, the second a viscoelastic soft binding medium, which can vary among the different materials.

Another common feature among such Earth materials and other types of solids, like polycrystalline solids or composite materials with localized macro damage or distributions of micro cracks, is the scale of the grains, usually of the order of tens to hundred of μm . For such reason, it has been proposed a label alternative to Nonclassical Nonlinear Elasticity, i.e. **Nonlinear Mesoscopic Elasticity**, just because the nonlinear elastic responses described briefly below and exhibited by all these types of solid materials is associated to the presence of such grains at an intermediate scale between the atomic/molecular and the macroscopic ones, being these grains interconnected and interacting together through the binding phase of the medium.

It has been proposed to identify a "universal class" of materials on the basis of such similar nonlinear elastic properties and similarities in their structure [6, 14]. However, in the last five years, new investigations [15] have suggested the impossibility of such a proposal in the sense that the concept of a "universal class" can not be used in this context as it has been developed in the field of Statistical Mechanics, particularly in the study of phase transitions [9]. Although recent experimental measurements have shown definitely the exhibition of typical NCNL elastic effects by a wide range of materials [16] other than Earth's materials, ranging from gray iron,

alumina ceramic, quartzite, marble, sintered metal, and perovskite ceramic to cracked Pyrex and other damaged composite materials like damaged concrete (see Chapter 3), it could only be underlined that the similar structural features of such materials lead to similar nonlinear elastic behaviors. As explained in Section 2.2.2, this fact is well established and accepted within the community of Researchers working in the field of NCNL Elasticity of solids because the source of such anomalous elastic nonlinearity has been identified with the two phases structure (as previously said) and with the soft viscoelastic binding medium, which plays a fundamental role in generating such elastic responses (see Section 2.2.2).

2.2.1 Experimental phenomenology

Quasi-static experiments

As previously reported, one of the first set of signatures of the NCNL elastic behavior, i.e. of common elastic responses to such types of solid materials, can be revealed by interrogating the stress-strain response of the overall specimen under study by a quasi-static experiment, where quasi-static means that a load (stress) is applied to the specimen, usually tailored as a bar, with a protocol of time variation over a long time interval and low rate of variations, while the total strain of the sample, i.e. its relative deformation along one axis, is measured. From a System Theory point of view, the stress applied (on both end sides of the bar) is the input signal, while the measured strain is the output signal. The values of such couple of signals are reported time-by-time on a plot stress vs strain or viceversa, a kind of 2D phase space for the system, also called input-output response plot or simply constitutive relation of the specimen.

Figure 2.3 shows an example of such an experiment-derived plot (inset (c)), the experimental apparatus for its derivation (inset (a)) and the stress (input) signal, also called load protocol. The first feature to be underlined is that the stress gradually increases up to a maximum value then decreases again towards zero. The consequent result is an hysteretic loop in the strain-stress plane, indicating that the specimen undergoes some kind of irreversible deformation. However, the fact that the strain gets back to zero value when the stress decreases toward it means the absence of plasticity, so of a permanent deformation in the specimen: the specimen recovers its initial dimension along the longitudinal axis of the bar, its behavior is viscoelastic and not elastoplastic, but the strain holds memory of the maximum value of loading stress reached and that is at the basis of hysteresis. Each branch of the hysteretic loop (one for the increasing phase of the load protocol, the other for the decreasing one) are curved, meaning a nonlinear relationship between stress and strain, so a first signature of a nonlinear elastic behavior.

The loading protocol includes, during the two main phases of increase and decrease, intermediate sets made by similar two phases in the reverse order: after having reached a certain value, the stress is slightly and slowly decreased then increased again up to the same point. These sub-protocols within the main ones are at the basis of the small loops that branches out of the main one. The fact that the state of the system (a point in the strain-stress plane) recovers the same starting value of the inner loop at its end is a typical signature of nonlinear hysteretic behavior known with the label of **end-point memory** or **discrete memory** (see Section 2.2.2). The end-point memory effect means that although an intermediate stress cycle is conducted during the main protocol, the quasi-static cycle, the main hysteretic loop is maintained as if the strain variable keeps memory of the previous maximum value reached.

Fast dynamics

Under the label **fast dynamics** goes a peculiar nonlinear elastic effect consisting in a lowering of the elastic constants of a solid specimen while a wave is propagating through it. The best type of experiment for showing evidence of such effect is a NRUS one, described in Section 2.1.2.

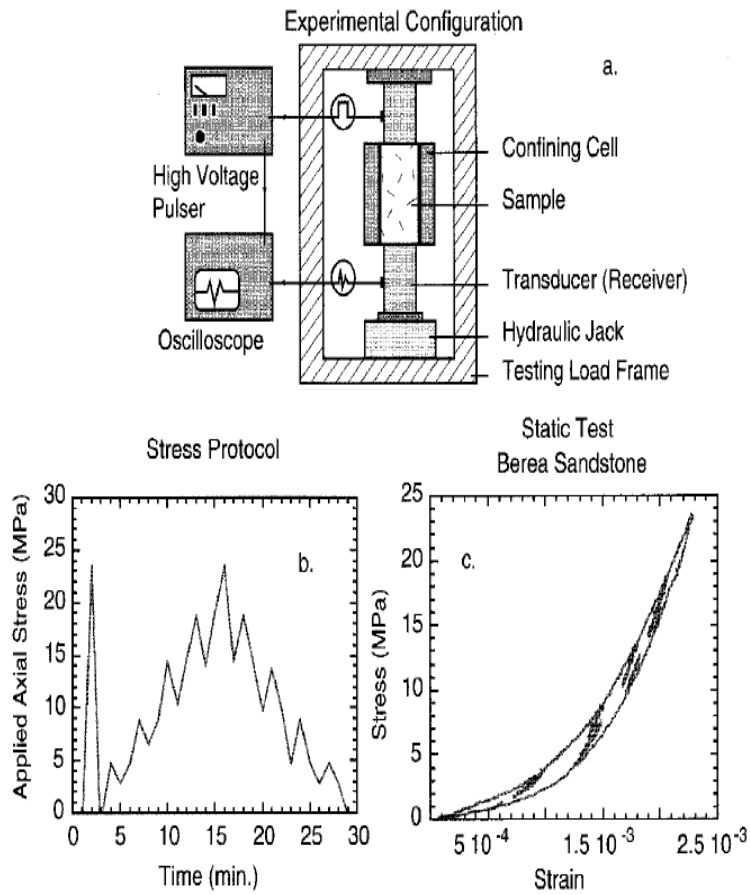


Figure 2.3: Example of experimental apparatus (inset (a)) and loading cycle protocol for a quasi-static measurement of the stress-strain constitutive relation of a solid specimen. The strain-stress plot (inset (c)) of a Berea sandstone measured with the loading protocol showed in the inset (b): the rock exhibits a nonlinear hysteretic strain-stress equation of state with the additional feature of end-point memory, i.e. memory of the maximum value reached by the strain during the main loop cycle when an intermediate small amplitude sub-cycle is performed. Figure from Ref. [12]

NRUS experiments have been usually performed with specimens tailored as long thin bars. For many materials exhibiting NCNL elastic behavior the approximation of longitudinal (Young's) vibration *eigenmodes* as the ones excitable has been valid such that the most of the NRUS experiment has been setup in order to excite the first Young's eigenmode, which has a resonance frequency ν_{1Y} given by the simple formula

$$\nu_{1Y} = \frac{1}{2 \cdot L} \cdot \sqrt{\frac{E}{\rho}}, \quad (2.13)$$

where L is the length of the bar along the symmetry/longitudinal axis, E is the Young's modulus and ρ the mass volumetric density. During a typical NRUS experiment in a NCNL elastic material, the downward shift of the resonance frequency ν_{1Y} , which corresponds to a decrease of the Young's modulus E as reported by Eq. 2.13, has been shown to be quantitative stronger than in the case of a solid material exhibiting a CNL elastic behavior, in particular it has been shown that the relative change in the resonance frequency is directly proportional to the strain measured in the same point the particle displacement, velocity or acceleration signal is measured as the output signal, while CNL materials shows a proportionality to the square of the strain signal³.

Figure 2.4 shows a typical experimental setup for the realization of a NRUS experiment with a thin long bar specimen (inset (a)) and the resulting resonance curves for a NCNL material (inset (b)). If compared with Fig. 2.2, it could be seen that a NCNL material exhibits a stronger downward shift of the resonance frequency. Fig. 3.4 in Chapter 3 shows another typical NCNL signature: the resonance curves are distorted with the increase of the excitation amplitude, so the Q factor (i.e. the attenuation of the specimen) changes at each driving amplitude. Other significant examples of such distortion, which implies a change in the attenuation of the materials with the amplitude of the perturbing wave, can be found in [12] regarding granite and river sand, in [6] for a sandstone and in [16] for a wide variety of solid composite or damaged materials. The change of the attenuation with the amplitude level of the exciting waves has been a well known phenomenon regarding metals since the work of Granato and Lucke and it has been attributed to the hysteresis induced by dislocations in their stress-strain equation of state [13], as recently shown by Campos-Pozuelo *et al.* in the case of fatigued metals [4] (fatigue induced by repeated loading cycles in quasi-static experiments is a source of dislocations networks within the lattice of the metal specimen). Figure 2.5 shows the dependence between the relative frequency shift and the strain amplitude obtained from NRUS experiments on different types of materials other than Earth's ones.

Another important nonlinear effect in the same NRUS fast dynamics experiments that have been observed in many materials sharing NCNL behaviors is the qualitative change of the resonance curve, at a fixed driving amplitude, with the sign of the first derivative of the frequency signal, that is a different curve is obtained sweeping the frequency upward (increasing its value) or downward (decreasing its value) coming across the resonance frequency value.

³Being the strain defined as an observable always lower than 1, a direct proportionality to it means a stronger dependence on it than in the case of a direct proportionality to its square

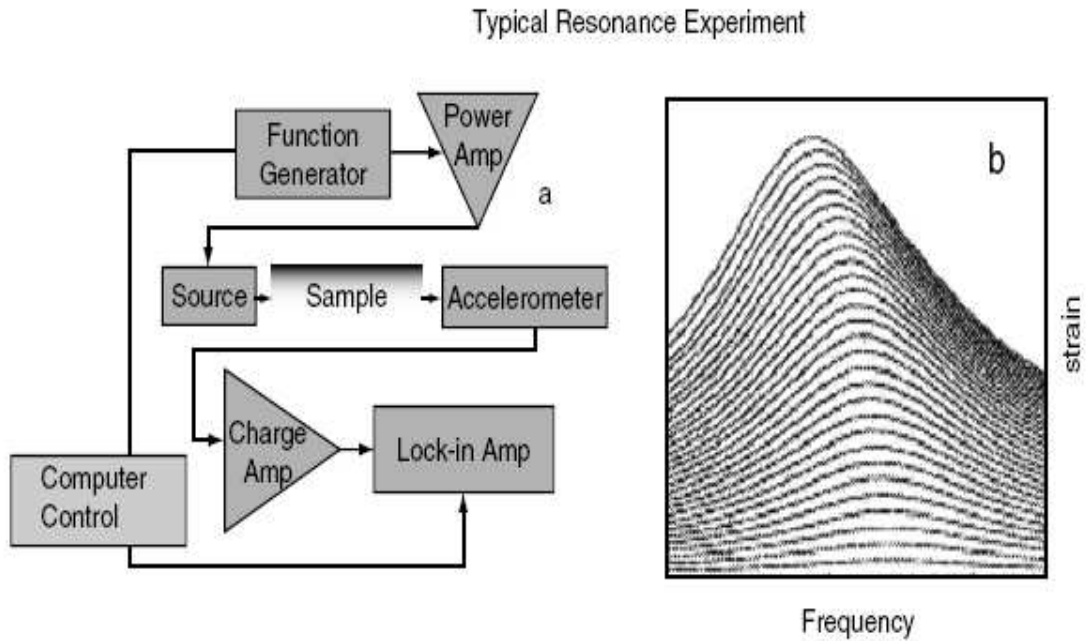


Figure 2.4: Typical NRUS experimental apparatus (a) and resonance curves obtained from a NCNL solid material (b). The source drives at a sequence of frequencies stepping from below to above the resonance frequency of a vibration *eigenmode*, usually the first Young's *eigenmode* in long thin bar specimens. The lock-in amplifier is used to recover the integral mean of a signal in a recording time window, used as an estimation of the amplitude of that signal in such time window. Usually that signal is the local longitudinal strain calculated from the direct measurement of the particle acceleration. In the case of a non-contact measurement, the signal is the particle velocity measured with a laser interferometer. The drive level is increased and the procedure is repeated over a certain number of drive levels. Figure taken from Ref. [9].

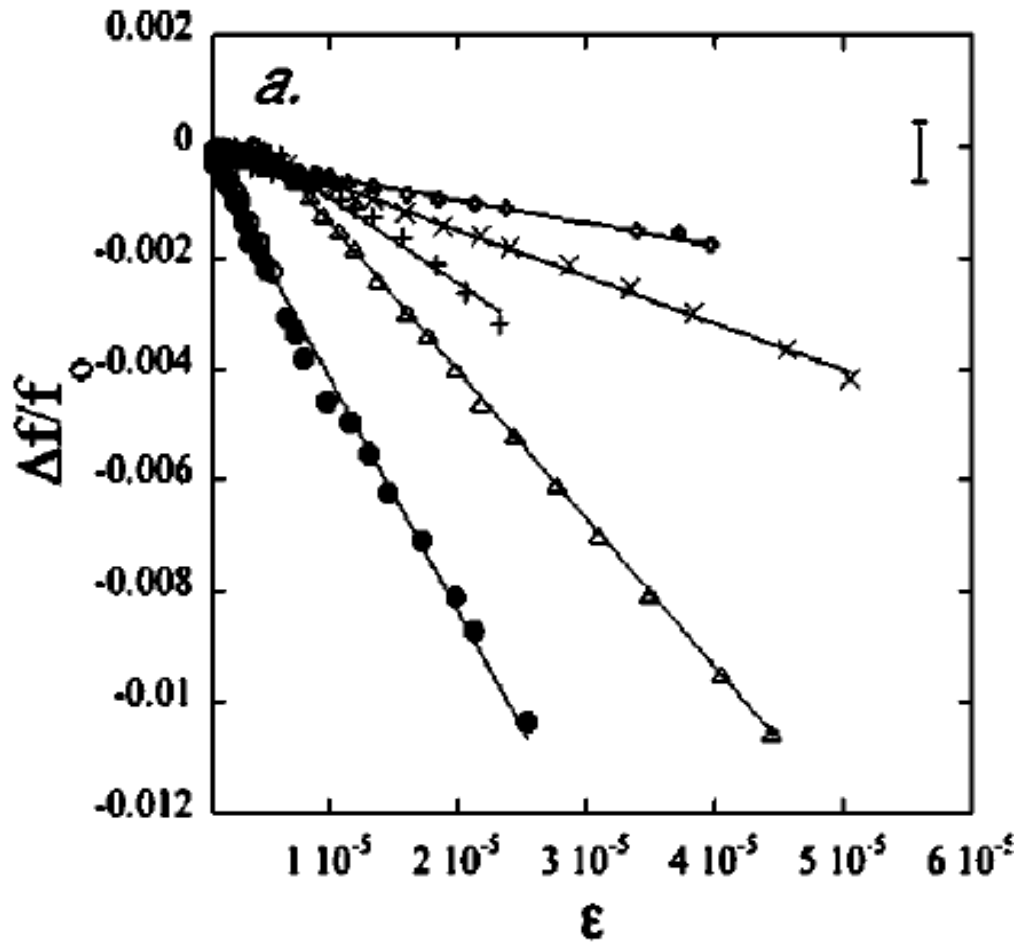


Figure 2.5: Relative resonance frequency shift vs the local longitudinal strain amplitude measured for a variety of solid materials other than Earth's ones during typical fast dynamics measurements. All the specimens exhibit a direct proportionality between the two variables, the typical NCNL signature in NRUS measurements, with different slopes which are characteristic of each material. Figure taken from Ref. [16].

Slow dynamics

A NRUS measurement technique has been devised for revealing another typical NCNL elastic effect called **slow dynamics** and consisting in a logarithmic-in-time recovery of the resonance frequency of the bar-tailored specimen after a short-in-time application of a high amplitude perturbation.

A typical slow dynamics experiment is realized with the same apparatus of a fast dynamics one, except for the fact that the resonance frequency of the excited vibration *eigenmode* is measured in correspondence to a low level (infinitesimal) amplitude of the exciting wave, except during a narrow time window when a high amplitude exciting wave is injected into the specimen. Such sudden increase of level of amplitude of excitation generates a softening of the material, the resonance frequency undergoes a strong decrease. After the sudden high level perturbation, the resonance frequency is monitored with the same initial infinitesimal amplitude excitation over a long time window: the resonance frequency recovers its original value very slowly as shown in Figure 2.6 or in Figure 3.10. The recovery time is a parameter typical of the material and of its level of elastic nonlinearity, so it has been proposed as a quantitative observable for characterizing the NCNL behavior or its sources (see Section 2.2.1 for the correlation between damage in composite materials and NCNL elastic signatures). It ranges between tens of minutes to hours.

The existence of such a recovery phenomenon means that these types of materials, from a macroscopic point of view, do not undergo irreversible deformations during the propagation of elastic waves throughout them. However, their hysteretic behavior in the quasi-static regime implies that some form of microscopic change happens during the loading.

Nonlinear Elastic Wave Spectroscopy (NEWS)

Nonlinear wave mixing, including harmonics generation, presented in Section 2.1.2 as a typical CNL elastic effect, is exhibited by NCNL materials too but with a stronger intensity and richer phenomenology. Figure 2.7 shows the results of an experiment similar to the one whose results are reported in Fig. 2.1 but with a Earth's material, a sandstone, known for its NCNL elastic behavior. The two-waves nonlinear wave mixing experiment with this specimen this time shows an output signal with a more complicated spectral content including not only the second harmonic of the lower input frequency but also the third one and the fifth one. Beyond this, both the harmonics and the sidebands generation exhibit a stronger dependence on the driving amplitude. Other experimental results of the same type have shown also the generation of second order sidebands i.e. harmonic waves, generated by the nonlinear interaction of the two input ones, having frequencies $\nu_1 \pm 2 \cdot \nu_2$ [12].

Another important feature that can distinguish between a specimen with CNL and NCNL elastic behavior is the dependence of the harmonic amplitude upon the amplitude of the strain signal (taken only the fundamental frequency, because this signal has an amplitude proportional to the excitation amplitude). In the case of a CNL elastic response, the output generated third harmonic has an amplitude proportional to the cubic power of the fundamental strain amplitude, while in the case of a NCNL response the relation is of the type of a quadratic power. Regarding the fifth harmonic amplitude, for a CNL it has been shown a fifth order power dependence, while for a NCNL still a quadratic power. It should also be noted that in many nonlinear wave mixing experiments with a NCNL specimen, some harmonics have not been observed (see Section 2.2.2 for some theoretical predictions).

Similar types of effects regarding the dependence upon the fundamental strain amplitude have been observed also in two-waves nonlinear wave mixing experiments: in NCNL materials, the second order sidebands at frequencies $\nu_1 \pm 2 \cdot \nu_1$ have amplitudes proportional to $\alpha \cdot A_1 \cdot A_2$, where A_1 and A_2 are the amplitudes of the two input waves at frequencies ν_1 and ν_2 respectively,

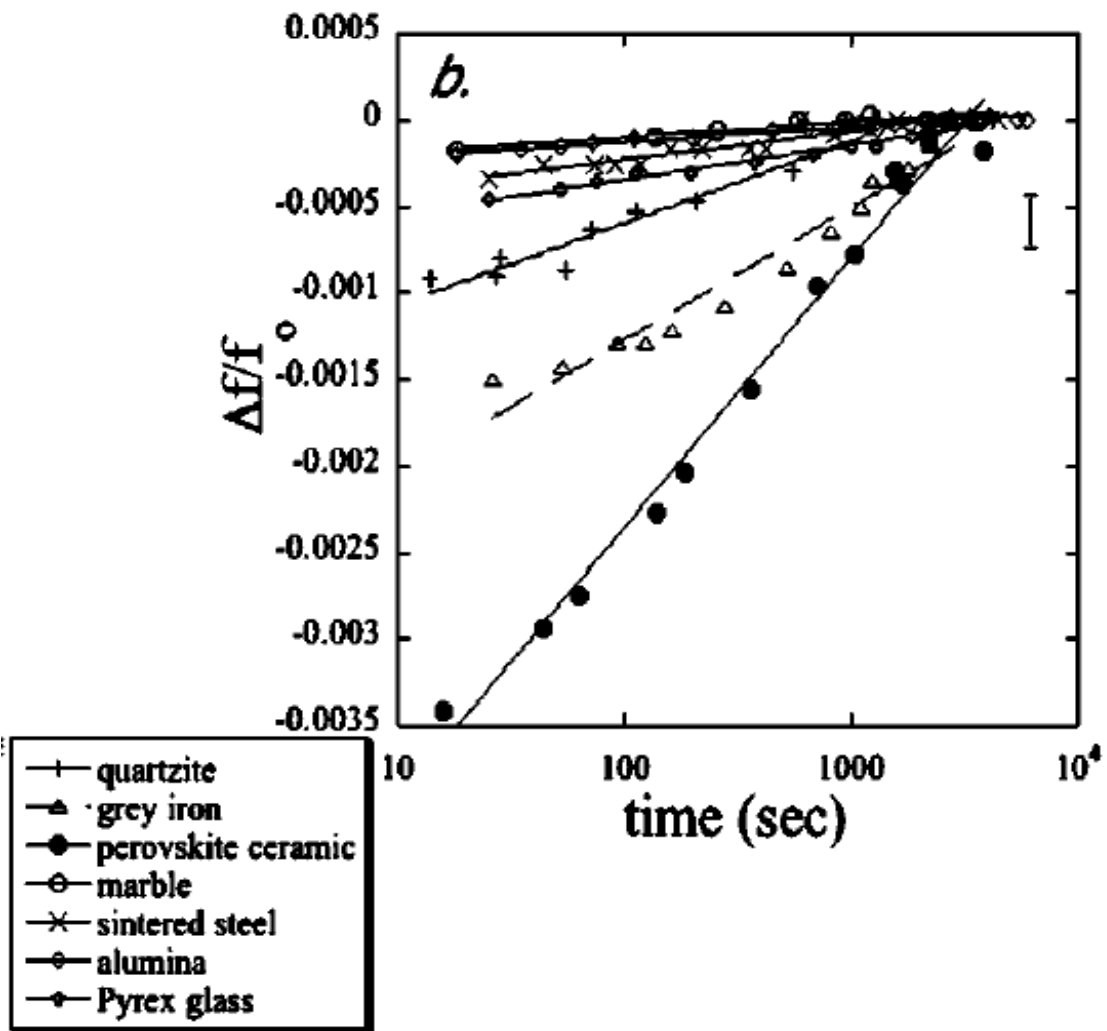


Figure 2.6: Plot of the relative resonance frequency shift vs the logarithm of the time in base 10 during an experiment of slow dynamics for different types of solid materials, the same of Fig. 2.5. Different materials exhibits different recovery times, but all of them with a logarithmic dependence on time itself. Figure taken from Ref. [16]

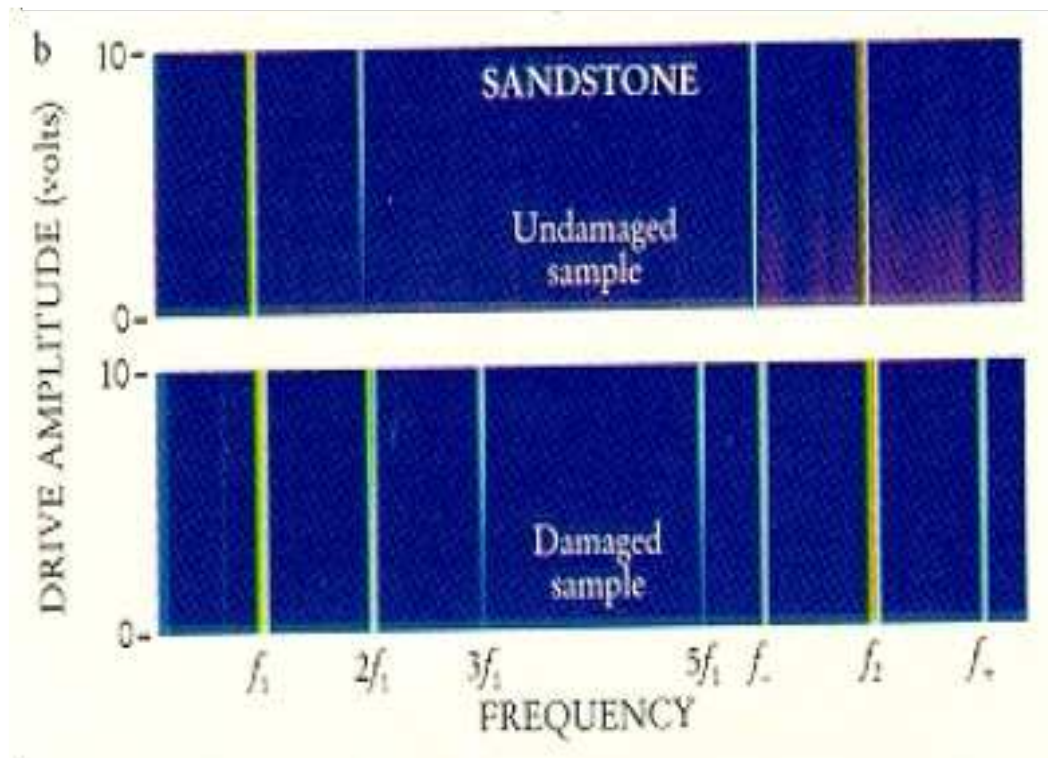


Figure 2.7: Nonlinear wave mixing in a sandstone. The setup and procedure of the experiment is the same of the one of Fig. 2.1 except for the different type of specimen, now a consolidate granular material exhibiting NCNL elastic effects. Already in the undamaged state, the sample exhibits the consequences of harmonics generation (second harmonic generation) and of sidebands generation, in a weak manner and with a weak dependence upon the driving amplitude. After a treatment inducing bulk damage like micro-cracks distributions, the cited effects are more evident and with a stronger dependence on the driving amplitude. In particular, it should be noted the higher level of harmonics generated (up to the fifth order) and the clear evidence of the sidebands. Figure taken from Ref. [6].

while in the case of a CNL material the relationship between the same variables is of the type $C_{\beta\delta} \cdot A_1^2 \cdot A_2$, where $C_{\beta\delta}$ is a parameter depending upon the classical nonlinear elastic moduli for a simple scalar stress-strain constitutive relation for a specimen undergoing only longitudinal deformations. Similarly, for first order sidebands generation at frequencies $\nu_2 \pm \nu_1$, their amplitude are proportional to $\beta \cdot A_1 \cdot A_2$ in the case of a CNL material.

These differences in the spectrum content and in the dependence of the generated signals, from a single frequency input one, on the amplitude of excitation have led to the implementation of such experimental protocol as tools for devising and distinguishing between the type of nonlinear elastic response.

NRUS (Nonlinear Resonant Ultrasound Spectroscopy)⁴ and the Fourier analysis of output signals from nonlinear wave mixing experiments (a technique called **Nonlinear Wave Modulation Spectroscopy, NWMS**) have been named under a unique category of techniques called **Nonlinear Elastic Wave Spectroscopy (NEWS)** (see Ref.s. [22, 10, 11] for an introduction review of the proposed methods). As cited in the Introduction to this Ph.D. thesis (see Chapter 1), two European Research projects NATEMIS (funded by the European Science Foundation, 2000-2005), and AERONEWS (funded by the EC within the FP6, 2004-2008) have been dedicated to the study of NEWS techniques, both from a theoretical and an experimental point of view, for investigating the connections between the NCNL elastic behavior of solids, especially composite materials of interest for construction purposes, and the state of damage of the specimens exhibiting such behavior.

Nonlinear Nonclassical Elasticity and damage

As reported in the Introduction of this Chapter and in Section 2.2, in the last years the numbers of experimental evidences about a correlation between structural damage in certain types of solid materials and NCNL Elasticity has grown considerably. As previously said, some materials, like monocrystalline metals, do not exhibit any kind of NCNL elastic effects except after having undergone damage by quasi-static loading or high amplitude shock wave propagation. The damaging introduces in the initial unperturbed structure of the specimen changes as for example dislocations rearranging the structure of the crystalline lattice itself or distributions of microcracks. The two-phases structural model for materials with NCNL elastic behavior could be used in the case of certain materials only after damaging, e.g. the induction of distributions of microcracks or localized macro-ones introduces interfaces between portions of the specimen which can be filled up by fluids or residual materials and impurities, acting this “network” of interfaces as a “binding” medium between “grains”.

As described briefly in Section 2.2.2, since the identification of structural similarities between NCNL elastic materials, it has been proposed that the two-phases structure of these materials could be at the origin of their anomalous nonlinear elastic behavior. This hypothesis has been recently supported by different types of experimental investigation, in particular it has been confirmed the essential role of the binding medium in the generation of the type and level of NCNL elastic effects.

Damage in composite materials increases their heterogeneity and the complexity of their structure in terms of alternation between grainy regions and binding medium ones, so it has been simply proposed that the NCNL elastic behavior of such damaged specimen increases with the increase of its damaged state [22, 10, 9], as supported by the results of experimental investigations [8, 23, 22, 10, 24, 16], also reported among the original work of this Ph.D. thesis (see Chapter 3 about the NCNL elastic behavior of damaged concrete).

⁴Sometimes, it could be found in the literature reference to Resonant Acoustic Spectroscopy, linear or nonlinear, as for example in Ref. [10]. It depends from the frequency band of operation with elastic waves. The term RUS refers to the original technique proposed and developed by A. Migliori *et al.* [17, 18, 19, 20, 21] so it is usual to refer to a RUS method although it exploits acoustic instead of ultrasonic waves.

2.2.2 Phenomenological models and numerical simulation codes

As previously anticipated, the qualitative and quantitative features of NCNL elastic effects have been associated to the two-phases like peculiar structure of such materials exhibiting such anomalous elastic behavior. Particularly, the differences in the elastic properties of grains and the binding medium portions have been addressed as the physical sources of such elastic nonlinearity.

The first experimental evidence about the role of the interstices and its filling media in the generation of NCNL effects was found out by Gist [25], who measured the wave propagation velocity throughout a specimen of rock before and after having injected liquid epoxy into it (letting the epoxy percolate and fill the interstices between grains). The experiment was performed with the specimen under a quasi-static pressure load, in order to look at the changes in the wave propagation velocity with increasing pressure load. The results indicated essentially a constant velocity for the specimen with the filled-in interstices, while before the injection and after a centrifugation process (performed in order to spin out the liquid epoxy from the rock pores) the velocity had a strong dependence on the loading pressure, being that relation different in the two cases.

NEWS measurements (both NRUS and NWMS types) have been performed in different environmental conditions in order to investigate the role of some environmental parameters in the NCNL elastic behavior. Beyond the role of temperature in acting as a kind of perturbation parameter with similar effects like the ones induced by loading stress [26, 27], it has been found out that humidity and water saturation influence greatly qualitatively and quantitatively the NCNL elastic response [28, 29], so some of the experiments performed at the EES-11 (Geophysics, Non-linear Elasticity Group), Los Alamos National Laboratory, have made use of a special isolation chamber [30]. These experiments confirm the hypothesis that the content of fluids in interstitial regions and pores influences the overall mechanical behavior of rocks.

More recently, new kinds of experiments addressed to study the microscopic structure of sedimentary (consolidated “granular”) rocks have been performed using neutron scattering techniques, particularly time-of-flight spallation neutron sources. These experiments have been conducted at the Lujan Center of the Los Alamos Neutron Science Center (LANSCE), Los Alamos National Laboratory [31, 32]. Neutron scattering measurements using thermal neutron beams provide an approach to learn about the atomic/lattice properties of large volumes of intact rocks due to the very high penetration depth and improved scattering from light elements in respect of X rays.

As described previously, sedimentary rocks exhibiting NCNL elastic effects are generally crystallite aggregates (polycrystalline materials). Usually, the theoretical description and modeling of the composition and mechanical properties of such Earth’s materials never includes viscoelastic solid non-crystalline materials like glassy materials, just because these materials are difficult to detect and their amount is difficult to estimate within a whole specimen.

Stress-strain relation quasi-static measurements have been performed on silica rocks of different types while exposing the specimens to thermal neutron beams. In this way, it has been possible to show that the NCNL hysteretic signature of stress-strain relation is associated to a small fraction of the specimen volume [33]. Other neutron scattering measurements, aimed at obtaining estimates of the Pair Distribution Function (PDF)⁵, have shown clear evidence for the presence of an unexpected glass-like component in Fontainebleau sandstones [32], a typical Earth’s material with NCNL elastic behavior. This last type of measurements have revealed significant local structural deviations from pure quartz (these deviations appear as an excess of 5-10% of nearest neighbour Si-O and O-O chemical bonds, a result consistent with a 5-10% vol-

⁵The PDF method has its origin in the study of materials without long-range order such as glasses and liquids, recently applied also to the study of disordered crystalline and nano-crystalline solids [34]. Essentially, the PDF, $G(r)$, is obtained as the Fourier transform of the total neutron diffraction pattern and describes basically the probability of two atoms being separated by a distance r [34].

ume fraction of vitreous silica), i.e. the existence of other solid materials between the crystalline grains.

These neutron scattering measurements, performed at the LANSCE of Los Alamos National Laboratory, have been among the first direct experiments supporting the previously cited two-phases structural model for NCNL elastic materials, which has been used as a *de facto* assumption, although supported by some phenomenological evidence, for many years in the physical-mathematical modeling of mechanical properties and responses of such materials. Although the structural nature of the binding medium and other microscopic features, like the dimension of the interstices between grains and the structures of materials filling them (inter-grain contacts), have not yet been resolved and imaged (further work in this direction is ongoing at the Los Alamos National Laboratory using Raman microscopy [33]), these experiments finally support the theoretical modeling activities developed in the last 10 years about NCNL elastic materials.

A coherent and complete theory based on a micro-mechanical description of the sources of NCNL effects still does not exist, due to the lack of experimental and phenomenological knowledge at the microscopic scale, as previously said. In the last few years, several physical models of NCNL Elasticity have been proposed, differing for the type of mechanism and material addressed. A review of such theoretical “pictures” can be found in Ref. [12]. It includes:

- the Hertzian contacts-like models, which represent a NCNL material, e.g. a granular rock, as a system of dry contacting grains;
- the “bed of nails” model of distribution of micro-cracks, derived from the Hertzian contact model [12];
- the Granato-Lucke model for internal friction in crystalline metals with networks of dislocations [13].

More recently other three types of physical models have been proposed addressing micro-mechanical issues in order to explain the emergent NCNL elastic behavior of a whole rock or composite damaged material specimen:

- a model which identifies the sources of NCNL effects in dislocation-based incipient kink bands (IKB) [35];
- a model studying the role of adhesion (within an interface between two rough surfaces in contact) in generating hysteretic stress-strain macroscopic constitutive relations and nonlinear scattering effects being at the basis of high-order harmonics generation similar to the one observed in NEWS experiments with Earth’s or composite damaged materials [36];
- a modeling approach based on a realistic nonperturbative form of the macroscopic stress-strain relation and on a description which associates slow dynamics with the experimentally observed memory of peak strain history, both being attributed to strain-induced kinetic changes in concentration of ruptured intergrain and interlamina cohesive bonds, causing a net hysteretic effect on the elastic Young’s modulus; this model manages to explain how enhancement of hysteretic phenomena originates from an increase in equilibrium concentration of ruptured cohesive bonds due to water saturation [37, 38].

Beyond these proposed physical models, I present in what follows a different kind of modeling approach based on phenomenological knowledge and on the use of a description taking advantage of the Preisach-Mayergoyz formalism, developed in the last twenty years for studying systems with hysteretic state equations [39, 40, 41, 42] and derived from the Preisach modeling approach,

first introduced in the field of Magnetism for the study and modeling of magnetization dynamics of ferromagnetic materials [43, 44].

This modeling approach has been, at its origins, developed by M. Scalerandi and P.P. Del-santo at the Dept. of Physics, Polytechnic of Torino [45, 46, 47], and is part of a set of a few phenomenological models based on the Preisach-Mayergoyz formalism that have led to different kinds of mathematical-computational models and codes for simulating quasi-static and dynamic experiments with virtual NCNL elastic materials (for a review of the different models, see Chapters of Ref. [48] and particularly Ref. [49]). This modeling approach has been extended and adapted during my Ph.D. for the development of computational Elastodynamics codes in 1D, 2D and especially 3D in order to simulate acoustic and ultrasonic wave propagation in NCNL materials (see Chapters 3 and 4 and Appendixes I,II,III).

Preisach-Mayergoyz models

The Preisach-Mayergoyz formalism is a mathematical tool for the derivation of the equation of state (first of all a scalar one, then also vectorial and tensorial) of a system whose phase portrait is made by an hysteretic loop. I consider here only the simplest description of the general Preisach-Mayergoyz formalism, the 1D one. Generalization of this description to multi-dimensional equations of state (so multi-dimensional phase spaces) of hysteretic systems can be found in the seminal book by I. Mayergoyz [41].

Considering a generic system characterized by two scalar variables, here defined as ϵ and σ (like in the special case of a solid specimen whose equation of state of interest is the one relating strain and stress), both varying in time, it is supposed that the relation between them, also called the equation of state or constitutive relation of the system, is represented in the $\epsilon - \sigma$ coordinate frame of reference by an hysteretic loop. The σ variable is called the “input” or “control” variable, while ϵ is called the output variable. In an ideal experiment for determining the plot of such equation of state, the control variable is made vary in time, consequently the response of the system in time is measured by measuring the $\epsilon(t)$ signal. Each point in the $\epsilon - \sigma$ plane represents the state of the system at a certain instant of time, so $\epsilon - \sigma$ is a kind of phase or state space (using the terminology of Classical Analytical Mechanics or Dynamical Systems Theory).

The basic assumption of the PM formalism is to consider the equation of state of the system as the mathematical representation of the emergent “behavior” of a multitude of elemental component sub-systems of the main one each of which is characterized by a scalar variable S which can assume only two different values, S_o or S_c . Such sub-systems may or may not be identified with physical components of the main system. They are bi-state systems, each of which is identified by a couple of values (σ_c, σ_o) with $\sigma_c \geq \sigma_o$. It is assumed that the control variable of the main system, σ , determines the state of each component sub-system, that is it determines with its numerical value the one of the variable S . That means that the “macroscopic” variable σ has an influence on each “microscopic” sub-systems, determining if it is in the state $S = S_o$ or $S = S_c$.

The diagram state of each sub-system, characterized by its two couples of values, (S_c, S_o) and (σ_c, σ_o) , is defined mathematically by the subsequent set of inequalities:

$$S = \begin{cases} S_o & \text{if } \sigma \leq \sigma_o, \\ S_c & \text{if } \sigma \geq \sigma_c, \\ S_o & \text{if } \sigma < \sigma_c \text{ and } \sigma > \sigma_o \text{ and } \dot{\sigma} > 0, \\ S_c & \text{if } \sigma < \sigma_c \text{ and } \sigma > \sigma_o \text{ and } \dot{\sigma} < 0. \end{cases} \quad (2.14)$$

Usually, each sub-system has the same couple of values for the parameters (S_c, S_o) , such that it is characterized only by the couple of values (σ_c, σ_o) which act as thresholds in respect of the

value of the macroscopic global variable σ . The ensemble of sub-systems can be visualized, for each system, plotting a point in the plane with Cartesian coordinate system (σ_c, σ_o) for each subsystem and assigning a color to each of them according to the value of its state variable S . In the case the sub-system shares only two possible values for S , the possible colors are two, for example white and black. Such representation of the state of the system, at a certain time, as an ensemble of colored points in the (S_c, S_o) plane is usually called Preisach-Mayergoyz (PM) space representation of the state of the system.

Figure 2.8 shows an example of PM space for a macroscopic systems with microscopic bi-state components sharing the same two possible values for their state variable S and with the same range of values for the thresholds for the control variable, $|\sigma| \leq \sigma_{MAX}$ and both σ_o and $\sigma_c \leq \sigma_{MAX}$ in modulus. The inset figure shows a schematical representation of the state diagram for a single sub-system, which can be in two possible states.

It has been demonstrated that such a formal abstract/mathematical description, whatever the physical meaning of σ and ϵ or the system under analysis, is able to generate a hysteretic relation between the two macroscopic variables and it is also able to describe easily some typical features of hysteretic systems, as end-point memory for example. Figure 2.9 shows a schematic representation of the temporal evolution of such an hysteretic system tracked by the “dynamics” of the states of the multiple sub-units, identified with points in the PM space. At each point of the curve in the σ - ϵ plane it corresponds a “picture” in the PM space made by the distribution of points with different colors indicating the two possible states. The first row of the figure shows the state of the system corresponding to the point A in the σ - ϵ plane, after an increase in the control variable. The PM space picture indicates that all the sub-systems are in the same state because the reached value by the control variable (e.g. σ) corresponding to the state A is bigger than all σ_c thresholds for all the sub-systems. Than (second row), after a complete decrease of the control variable, point B, all the sub-systems are in the other state, just because in this case the control variable (e.g. σ) is zero in point B and every sub-system has a σ_o threshold greater than 0. The third and second rows show the way an hysteretic σ vs ϵ plot is obtained: when the control variable σ increases, it affects some sub-systems, that is it makes some sub-systems change their state from S_o to S_c , particularly those ones having a σ_c value lower than the current σ value. From a graphical point of view it means that the first sub-systems changing state when σ increases are the one filling a right triangle with a lateral side moving from the left to the right, parallel to the σ_o axis, with the increase of σ . When σ decreases and reaches a previously owned value, the sub-systems that first undergoes a change of state are the ones filling in a right triangle with a moving side from the top to the bottom with the decrease of σ . It means that despite the same value of the control variable σ , different portions of the PM space have been affected by its temporal evolution, according to the sign of the first total time derivative of $\sigma(t)$. This means that the state of the system is different in the two cases, because the number of points in the same region of a PM space in certain systems is different in the two cases and its evolution depends from the history of the time evolution of σ . In this way, hysteresis, as a macroscopic feature of the behavior in time of the system, is introduced and explained from a “microscopical” point of view. The last row shows how an inner loop associated to end-point memory is generated, due to the different number of sub-systems that are made to change from state S_o to S_c during the decreasing and increasing phases of the control variable. This schema has been derived from Ref. [12].

The Preisach-Mayergoyz formalism and mathematical description is quite general and it has been thoroughly studied in order to be applied to different types of hysteresis phenomenologies of behavior of systems [41, 39]. As previously said, it has its origins in the field of Magnetism and the study of the magnetization of ferromagnetic materials. For these systems (e.g. a sample of ferromagnetic material), the control variable σ corresponds to the magnetic (induction) field $\|\vec{H}\|$ while the output parameter ϵ could be identified with the magnetization $\|\vec{M}\|$. The

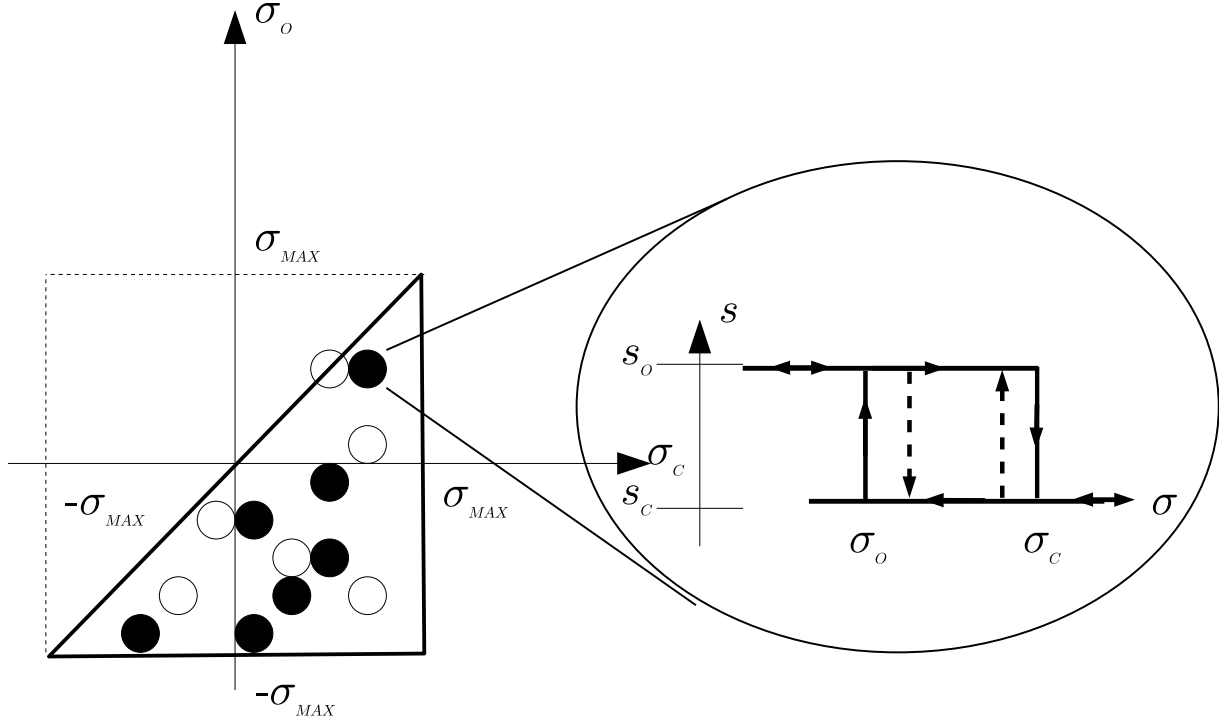


Figure 2.8: Representation of a special kind of Preisach-Mayergoyz space commonly used for the modeling of the NCNL elastic behavior of granular solids. The inset represents a schematical drawing of the diagram state for a single component sub-system of the macroscopic system, with its two possible states, $S = S_o$ or $S = S_c$ according to the value of the macroscopic control variable σ and the microscopic thresholds parameters (σ_c, σ_o) which characterize directly that specific sub-system. Another component sub-system of the main one is represented by another couple of values (σ_c, σ_o) , i.e. another point in the PM space. In this case, it has been assumed that all the components of the macroscopic system share the same values S_o and S_c so that the state of each sub-system, at each time step, can be codified by a color of the point in the PM space, in this case white or black. Such a whole picture represent the state of the overall system, at a generical time step. With the temporal evolution of the control variable σ , the state of each sub-system can change according to its diagram state, i.e. to the relative value of σ in respect of (σ_c, σ_o) and to the sign of the time derivative of σ , i.e. to its history, so that a new state for the macroscopic system corresponds to a different permutation of colors for the set of points distributed in the PM space. The distribution of points in the PM space is a intrinsic feature of the macroscopic system under analysis. In this schematic representation, the dimension of the points have been exaggerated in order to distinguish themselves by their colors and they have not been distributed according to a specific distribution in the PM space.

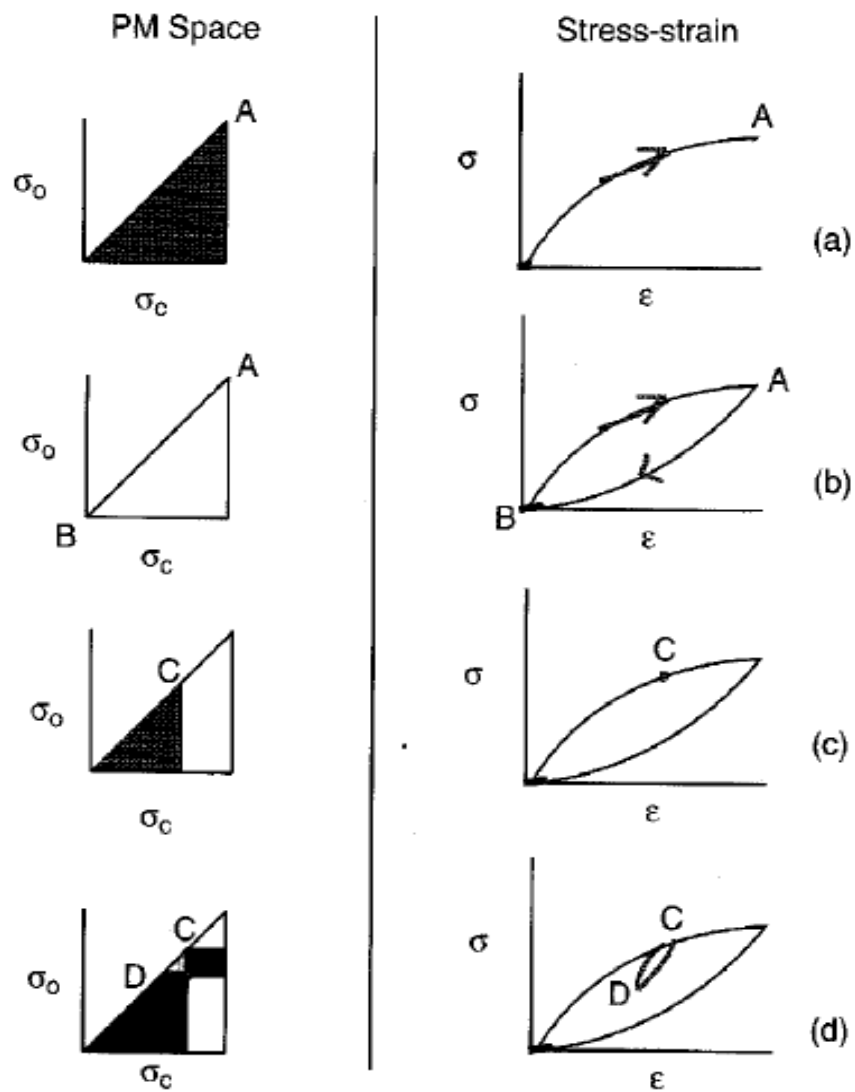


Figure 2.9: Schematic representation of the PM space of an hysteretic system (left column) and of its corresponding equation of state σ vs ϵ , taken at different times (i.e. different states, different rows).

description of the macroscopic system as an ensemble of sub-systems undergoing the influence of the same value of the macroscopic control parameter derives from the identification of such sub-systems, in ferromagnetic specimens, with Weiss domains, each one having its own magnetization vector, with up or down orientation (in the simplest case). The different domains are described as bi-state systems which can interact with the same macroscopic magnetic field and change their magnetization orientation according to thresholds [44].

The PM formalism has been applied in the field of Nonlinear Elasticity for trying to develop a phenomenological description of the mechanisms at the basis of NCNL effects principally identifying the sub-systems of the macroscopic system (for example a specimen of granular rock or a damaged composite material) with the interstitial regions of the specimen itself: as cited before, only recent Research advances have started to prove the connections between the interstices and the medium filling in them (the binding medium) with the NCNL elastic behavior, however, as previously reported, many experimental and phenomenological evidences suggested before such a correspondence.

In this last field, the σ control variable corresponds to the loading stress (mainly a uniaxial pressure in experiments with bar-shaped specimens) and the output variable ϵ with the macroscopic strain of the whole specimen. The two thresholds σ_o and σ_c have been identified with “opening” and “closing” stresses, i.e. different stress to be applied at the sides of the interstices in order to “open” and “close” them. This is one of the first description of the interstices (pores) using the PM approach, with a specific mechanical meaning. Then, other physical interpretations have been proposed, all of them on a phenomenological basis, i.e. without any specific microscopic experimental evidence, interpretations that have led to different mechanical models for the bi-state behavior of the interstices. A review of such proposed descriptions, all of them made by the PM space formalism, can be found, as previously cited, in Ref. [49] and [48] (see particularly Chapter 16 therein for a comparison of different PM descriptions of inter-grain interstices as bi-state sub-systems).

In Section 2.2.2 I present one of these descriptions, used in the modeling approach developed at the Dept. of Physics, Polytechnic of Torino, for realizing a mathematical (complete) model of elastic wave propagation in NCNL materials and implemented in respective computational codes.

It should be finally underlined and reminded that the PM formalism is a mathematical one with only phenomenological relations with the descriptions of hysteretic systems outside the field of Magnetism: the way it is formulated from a mathematical point of view can lead to a variety of models being able to reproduce observed features of hysteretic nonlinear systems (i.e. systems with a nonlinear hysteretic equation of state). This lack of connection with a physical origin for this formalism, except the case of ferromagnetic materials, has been a great asset for its application as a universal mathematical tool for the characterization and modeling of hysteretic systems.

For example, in collaboration with M. Scalerandi, A. Gliozzi, F. Bosia and M. Nobili, we have applied such formalism to the development of a preliminary modeling approach able to reproduce experimental data about the stress-strain relation of solid specimens under cyclic fatigue loading [50]. Such an approach is based on the use of hierarchical PM spaces for different physical variables involved in the Physics of fatigue of materials. Although this is only one of a manifold of applications of the PM formalism to the characterization and modeling of hysteretic systems, the correspondence between sub-systems to real physical microscopic components of a system of interest remains still a main goal, particularly in the application to the modeling of NCNL elastic materials, first of all for associating the PM space parameters to measurable observables.

LISA-Spring model of 1D elastic wave propagation

The **LISA-Spring** model has been developed by M. Scalerandi and P.P. Delsanto at the Dept. of Physics, Polytechnic of Torino, starting from the **LISA (Local Interaction Simulation Approach)** method for the numerical simulation of elastic wave propagation in highly heterogeneous materials [51, 52, 53, 54, 55, 56]. It has been proved that the LISA method is mathematically equivalent to a classical FDTD (Finite Differences Time Domain) approach to the solution of the PDEs (Partial Differential Equations) of Elastodynamics for linear homogeneous or heterogeneous materials [51, 54]. So the LISA approach, which has led to different versions of a mathematical model and corresponding different computational codes for such simulations [56, 57, 58, 59], is basically a FDTD method with the possibility of introducing in the finite difference equations (in time and space) specific terms based on phenomenological knowledge.

The LISA-Spring model has been developed as an extension of the LISA ones formulated for the study of imperfect interfaces between different material regions of a specimen [60]. Particularly, it takes advantage of the mathematical equivalence between the FDTD discretization of the PDEs of Elastodynamics and mechanical-analogical models using tensorial springs (see Appendix II about the 2D LISA-Spring model for the correspondence between FDTD discretization of continuous PDEs of Elastodynamics and FDTD equations written using analogical models involving elastic springs connected between them) for the formulation of phenomenological laws describing the forces acting at the interfaces between different materials. These interfaces have been firstly described as “rigid” then their equations of state have been formulated within the context of a particular Preisach-Mayergoyz (PM) model [47, 46, 45].

The LISA-Spring model has been the first mathematical-physical model aiming at reproducing the typical experimental features of NCNL Elasticity in the simulation of both quasi-static and dynamic (i.e. with traveling waves or standing waves) experiments, using as the main ingredient that PM formulation [47, 46, 45].

Figure 2.10 shows a schematical picture of the structure of a typical material with potentially NCNL elastic behavior, made of grains and interstices filled in with soft poro-viscoelastic media (the so called binding medium or “bond system”, as previously described). Its first formulation has been realized for a 1D case, i.e. in the case of a specimen tailored with a bar shape having a small cross section-to-length ratio. Under these conditions, the main type of elastic wave propagation mode is the one of longitudinal waves, which means, in case of resonance experiments, excitation of the Young’s modes of the bar.

From a geometric point of view, such a bar-shaped specimen can be mapped onto a 1D lattice along the axis x , as shown in Figure 2.11. Each node i of the 1D lattice is considered as the representative point for the cell of material at its left (or centered in it, the formulation is equivalent), as it happens in FDTD discretization of PDEs, where the scalar fields are considered evaluated only on the nodes of the lattice. In order to consider the geometrical interface between the cell of node i and the cell of node $i + 1$ as a physical component with mechanical and geometrical properties (and not only as a geometrical interface), each node i of the lattice is subdivided into two sub-nodes, i^- and i^+ , representing respectively the left and right sides of the interface (or interstice). This means that, according to this formulation, each scalar field (a displacement, a velocity, an acceleration, a stress or strain field) is evaluated not in one point of the lattice (the main node that establishes the separation between two discretization cells of material, with equal or identical physical properties) but in two points, the two sub-nodes and this happens in correspondence of each node of the discretization lattice. Then, for an output representation of the displacement fields calculated by the model, the displacement of the center of mass, u_{cm} , can be calculated from the displacements of the two subnodes.

In this way, the interstitial regions separating different parts of the specimen with different physical properties (e.g. different volumetric mass density or elastic constants) get a direct role

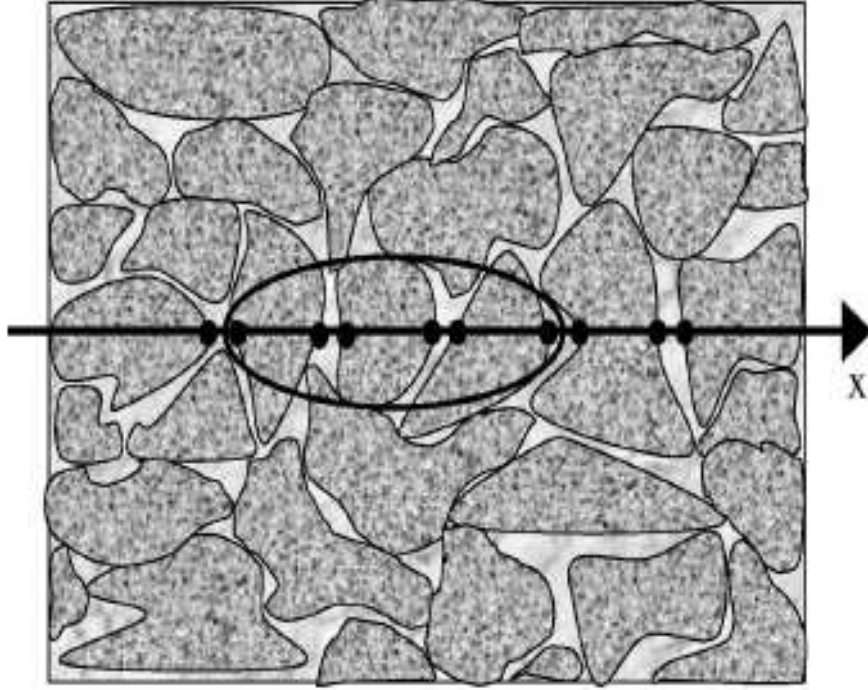


Figure 2.10: Schematization of a 2D slice of a solid “granular” material, e.g. a rock sample or a micro-damaged composite material. A 1D description of the material is chosen, along the x axis, such that the specimen can be formally described, from a physical point of view, in the 1D case, as a succession of grainy regions interfaced between them by interstitial regions. Figure taken from Ref. [45].

in the mechanism of the elastic wave propagation. A rigid interstice corresponds to what has been called a “perfect” interface in the case of the LISA model [60]: the two sub-nodes of a generic node of a portion of the specimen undergoes the same displacement. Calling $u(x, t)$ the continuous longitudinal displacement scalar field, a portion of the specimen with perfect interfaces (or rigid interstices) is such that $u_i^+ = u_i^- = u_i^{cm}$, $\forall t$, where t is the time variable and the label cm identifies the center of mass of the two cells having as side nodes the sub-nodes i^+ and i^- .

As shown in the Appendixes I and II, the case of a rigid interstice is a particular case of a more general description of the interstices as a poro-viscoelastic piece of material (this generalization is presented in detail in Appendix II, in the 2D case, because it has been recently showed by Gliozzi *et al.* that the FDTD equations for the forces acting on the sub-nodes may be expressed by equations corresponding, in the continuum case, to the equations of state of poro-viscoelastic media [61, 62]).

The way through which the LISA-Spring model has been formulated in order to simulate NCNL elastic wave propagation effects is using the PM formalism, identifying the bi-state subsystems, cited in Sections 2.2.2, with the interstices, and using the equations of state of poro-viscoelastic media in terms of stress-strain relation (continuum formulation) or in terms of force-displacement (FDTD formulation, this one deriving consequently by the space and time discretization of the previous one).

In Appendix I the finite difference equations considering forces and displacements are reported as implemented in the computational code, while here I present the corresponding general theoretical formulation of the LISA-Spring 1D model.

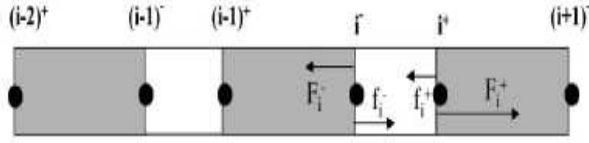


Figure 2.11: Schematic (ideal) 1D representation of a “granular” specimen along the x axis considering a 1D lattice of spatial discretization superposed to it. The index i refers to a generic lattice node, the indexes i^+ and i^- refers to the two sub-nodes obtained by splitting the node i in two components in order to let them identify the boundaries of the interstitial region separating two successive grains. Without such a splitting, the node i is positioned at the interface between two grainy regions and it identifies the portion (cell) of material (grain) at its left. Figure taken from Ref. [45].

Each grainy region is considered as a 1D isotropic linear elastic body with equation of state

$$\sigma = E \cdot \epsilon \quad (2.15)$$

where $\sigma(x, t)$ is the stress scalar field (component along x axis, the only one in a 1D longitudinal wave propagation case), E is the Young’s modulus and $\epsilon(x, t)$ is the strain scalar field. In the actual implemented version of the model for the simulation of NRUS bar experiments, each node is assumed to have the same physical properties, i.e. mass volumetric density ρ and Young’s modulus E , and the same rest-length L_0 . This is a coarse-grain approximation, because in NCNL elastic materials the grains can be different types of crystals or aggregates of crystals. Actually, the theoretical formulation of the model is general, considering grains with different mechanical properties, with the sideback of more parameters for the corresponding implementable model in a FDTD code.

In order to consider attenuative media, the equation of state for the grains can be formulated according to the Kelvin-Voigt’s model of viscoelastic bodies, i.e.

$$\sigma = E \cdot \epsilon + \eta \cdot \dot{\epsilon} \quad (2.16)$$

where η is the first order viscosity coefficient and $\dot{\epsilon}$ is the total time derivative of the strain scalar field.

Regarding this last addition in order to consider attenuative media (many NCNL elastic materials have a low Q factor, which means high levels of attenuation, while others, like micro-damaged Al bars, can be considered low attenuative within a good range of frequencies of propagation) it should be said that in different implementations of the LISA-Spring model (at 1D or at higher dimensions) the attenuation has been modeled in a more phenomenological way, i.e. introducing in the equations of motion derived from Eq. 2.1 and from the stress-strain equation for a pure elastic material a term proportional to the first order total time derivative of the displacement wavefield. As I have described in the Appendix of Ref. [63], in the case of an experimental and simulation study about the NCNL elastic behavior of concrete (see Chapter 3), both formulations of attenuation in NCNL elastic materials do not apply to every kind of material and their use is appropriate only in the case a small range of frequencies of wave propagation is considered (for example, in the simulation of single mode NRUS experiments for tracking the resonance frequency shift due to the increase in excitation amplitude or recovery due to slow dynamics, but not in the simulation of multi-mode NRUS ones). These limitations

are due to the fact that both formulations of attenuation can't reproduce the real attenuative behavior of such materials as rocks, which have a Q factor independent of frequency. Other models should be used in order to consider an appropriate version of the LISA-Spring model for simulating NCNL experiments involving multiply *eigenmodes* of vibration excitation (so different broad ranges of frequencies), e.g. the Robertsson-Blanch-Symes model for the formulation of attenuation in Earth's materials [64].

Regarding each interstitial regions, each of them are described as poro-viscoelastic bodies according to the Biot's theory of elastic wave propagation in porous media [65, 66, 67], i.e. each interstice is characterized by a stress-strain equation of the type

$$\tau = -\frac{a_1}{2} \cdot P + a_2 \cdot \delta + a_3 \cdot \dot{\delta} \quad (2.17)$$

where τ is the stress field localized in the interstice region, δ the corresponding strain field, P is the poro-elastic pression due to the surrounding grains and (a_1, a_2, a_3) are the three parameters characterizing each interstice. As for the grains, each interstice is assumed to have same values of parameters (a_1, a_2, a_3) , so they are treated like identical poro-viscoelastic bodies (this is another coarse grain approximation against the real world interstices of "granular" materials).

The PM formalism is introduced in the model considering the control variable equal to the poro-elastic pressure P acting on the boundaries of the interstices and as the state variable S described in Section 2.2.2 the vectorial parameter (a_1, a_2, a_3) . It means that each interstice is modeled as a linear poro-viscoelastic body whose poro-viscoelastic parameters can assume only two sets of values, $(a_1, a_2, a_3)_R$ and $(a_1, a_2, a_3)_{PE}$. These two vectors define two possible states for the interstice, the first one called "rigid", the second one "poro-elastic" (see Appendix I). The interstice can be in one state or in the other one according to the value of P , compared to the thresholds (P_c, P_o) , and to the sign of its first order total time derivative, as described in Section 2.2.2. As shown in Appendix II, other possible values can be considered for the vector state (a_1, a_2, a_3) and they have been introduced for modeling Acoustic Emission phenomena associated to concentration of stress during wave propagation or quasi-static loading within a specimen [68].

The PM space, according to this formulation, consists in a 2D plane with coordinate axes (P_c, P_o) , with $P_c > P_o$. Every interstice is univocally identified by a couple of values (P_c, P_o) , i.e. by a point in the PM space. At each point can be associated a color, blue and red for example, indicating the state of the interstices.

The interstices have been called **Hysteretic Elastic Elements (HEEs)**, due to the hypothesis (supported by phenomenological evidences and first microscopic measurements, as reported in Section 2.2.2) according to which they are the sources of the NCNL elastic effects. Different models based on a PM formalism consider the interstices as PM units but they differ from the one here presented for the choice of the state variable S : for example, a formulation considers the interstice as rigid with two possible lengths (in this case the interstices are called **Hysteretic Mesoscopic Units, HMUs** [12, 49, 69]). As discussed in Section 2.2.2, also in this case P_c and P_o , for each interstice, are set to be less than or equal to (in modulus) a common value P_{max} .

Another peculiar feature of the PM formalism here applied to NCNL Elasticity modeling is the introduction of the possibility of random transitions between the two possible state of a HEE when the control variable, P , assumes an intermediate value in respect of the thresholds P_o and P_c , i.e. when $P_o < P < P_c$ (see Figure 2.8 for the state diagram of a generic PM unit): in this condition, if the HEE is in the rigid state, it can switch to the poro-elastic state with a probability q_o , while if it is in the poro-elastic state it can switch to the rigid state with probability q_c . q_o and q_c are parameters intrinsic to this specific model so they have been used as degrees of freedom of the model for fitting experimental results. In the computational implementation of the model, at each time step a pseudo-random number is generated within

the interval $[0, 1]$ and compared with the value of q_o if the HEE is in the rigid state or with q_c if it is in the poro-elastic state and if the condition $P_o < P < P_c$ is satisfied. In this way, the switch between the two states may or may not happen

The introduction of such random transitions has been aimed at taking into account random microscopic effects (such as temperature fluctuations) that can change the mechanical properties of the interstices (because they are made by poro-viscoelastic media, usually multi-phase materials including fluids, whose mechanical interaction with the solid phases is greatly influenced by local temperature, humidity, etc... [49]). It has been shown that this formulation is at the basis of the success of the LISA-Spring model in reproducing experimental data not only of fast dynamics but also of slow dynamics [45] (see Chapter 3 for comparison between experimental results about the NCNL elastic effects in concrete samples and the corresponding results of simulations with a modified version of this model).

From a physical point of view, it should be noted at this point that the only ingredient in the formulation of such 1D model connected with a NCNL elastic behavior of a material specimen is the modeling of the interstices as bi-state linear poro-elastic bodies. No other ingredients have been formulated in order to obtain from a whole lattice of inter-chained grains and interstices NCNL effects. The fact that the simulation of bar NRUS experiments (both fast and slow dynamics) made by the implementation of the LISA-Spring 1D model in computational codes has managed to reproduce the results of correspondent real-world experiments is a validation of the modeling approach itself, of the PM formalism but also an important (not definitive) element for supporting the hypothesis about the leading role of the binding medium in the generation of NCNL elastic signatures. The hysteretic and nonlinear elastic behavior of such two-phases materials could stem from dynamic changes of the poro-viscoelastic properties of the media filling in the interstitial regions between grains during the propagation of waves throughout the material or during the quasi-static propagation of a loading stress.

As anticipated above, this is an example of complex behavior in the sense of Complex Systems Theory: the macroscopic behavior results from the collective behavior of a large number of HEEs. In fact, a single HEE is nonlinear only in correspondence with the “state” transition and hysteretic only in a small pressure range around the transition values. Therefore it cannot account sufficiently for the nonlinearity of a whole macroscopic specimen. The switch between mechanical properties occur at different pressures for the various HEEs, providing very large statistics of different switching behaviors, from which the macroscopically observed emergent nonlinear response is obtained.

From a modeling point of view, as previously said, the formulation of the equations of motion for the nodes identifying the grain and interstices regions corresponds to the equations of motion of linear springs (withtout and with changes of viscoelastic parameters, respectively) connected together in a serial way, with a grain spring followed by an interstice one and so on. Different arrangements of the springs representing the HEEs (or eventually combinations of them) have been chosen to describe extended (e.g. in multigrain or extensively damaged materials) or localized (e.g. defects, interfaces, etc.) portions of the specimen with NCNL elastic behavior. The original version of the LISA-Spring 1D model considers only serial arrangements of alternating grains and HEEs. Such a description introduces a specific spatial scale for the nonlinear region, because N HEEs occupy the space of N grains plus N interstices, although the dimension of the interstice can be neglected compared to the one of grains, so not included actually in the modeling. Beyond this fact, the separation of nonlinear from linear zones in the modeling of a real world specimen is implicit. Such a choice is particularly suitable if the nonlinearity is present in a large number of small interstices, which are located between elastic regions (grains). It is not convenient if the nonlinearity is present in a zone that is small compared to the total specimen dimension. This case has been addressed in Ref. [70].

However, more complex arrangements of modeled HEEs has been introduced in successive

implementations of the model, as in the one used for the original Research work presented in Chapter 3. In fact, the nonlinear portions of the specimen can be considered as representative volumes, each of which is described by a large number of HEEs. The behavior of the representative region is obtained by averaging over the behavior of the various HEEs. Two different types of averaging have been used up to now:

- the same external poro-viscoelastic pressure is assumed to act on each HEE of the arrangement in the representative region, but their strains are treated as independent of each other. The total strain calculated for that portion of the specimen (of the lattice) is defined as the average of the strains of the HEEs; this approach yields residual strains at zero stress (as observed in some experiments) due to the HEEs that become rigid during the loading/unloading process;
- the representative portion is considered as a single element in a state defined by parameters (a_1, a_2, a_3) , given by the arithmetic mean of the respective parameters calculated for a large number of virtual HEEs subject to the same external poro-viscoelastic pressure P applied to the interstice; this formulation has been adopted in the development of the version of the model used for the simulations reported in Chapter 3.

In the latter case of LISA-Spring 1D model, a PM space has been associated to each ensemble of virtual HEEs relative to a portion of the specimen/lattice, but the same PM space has been used for each of such regions. A possible improvement in the model should consist in the use of a different PM space for each real interstice (portion in the specimen/lattice between two grains), although it means to add much more parameters in the computational code. Two PM spaces can be different if the distribution of points (P_c, P_o) and the set of their states, at the initial time of the simulation, are different. Up to now, for generating distributions of points in the PM space it has been chosen to use a uniform pseudo-random number generator. A great leap in the evolution of the model should consist in the derivation of such a distribution and a set of initial states from experimental data after solving an Inverse Problem [71].

LISA-Spring model of 2D elastic wave propagation

The LISA-Spring 2D model is an extension to 2D of the formulation of the 1D one, with the introduction of some simplifications in order to reduce the total number of distinct parameters. Figure 2.12 shows a schematical representation of the geometry of the model in 2D. There are two different lattices superimposed to each other: the geometrical lattice, deriving from the discretization of the region of the specimen along the two coordinate axes of a Cartesian frame of reference (x, y) , is individuated by the solid black lines. l_x is the mesh step of spatial discretization along the x axis, l_y along the y axis. In the actual implementations of the model, the two mesh steps are assumed to be equal to a same value l for simplicity. Each node of this geometrical lattice is identified by a couple of integer indexes, (i, j) , indicating its position in respect of the frame of reference, $(i \cdot l_x, j \cdot l_y)$.

Superimposed to this geometrical lattice there is the materials lattice, whose lines are the red dashed ones. Each node of the geometrical lattice identifies a virtual representative mass particle placed at the center of a material cell with the same geometrical dimensions of the one of the geometrical lattice. It means that each cell of the geometrical lattice is subdivided in four sub-cells of four distinct materials, in the most general case. The dashed red lines localize the interfaces between different materials constituting the specimen, in the most heterogeneous case. In order to assign a physical role to the interfaces in the elastic wave propagation mechanism, each virtual representative particle, in the generic node (i, j) of the geometrical lattice, is formally subdivided into four different sub-particles (also called sub-nodes), placed at the corners of the

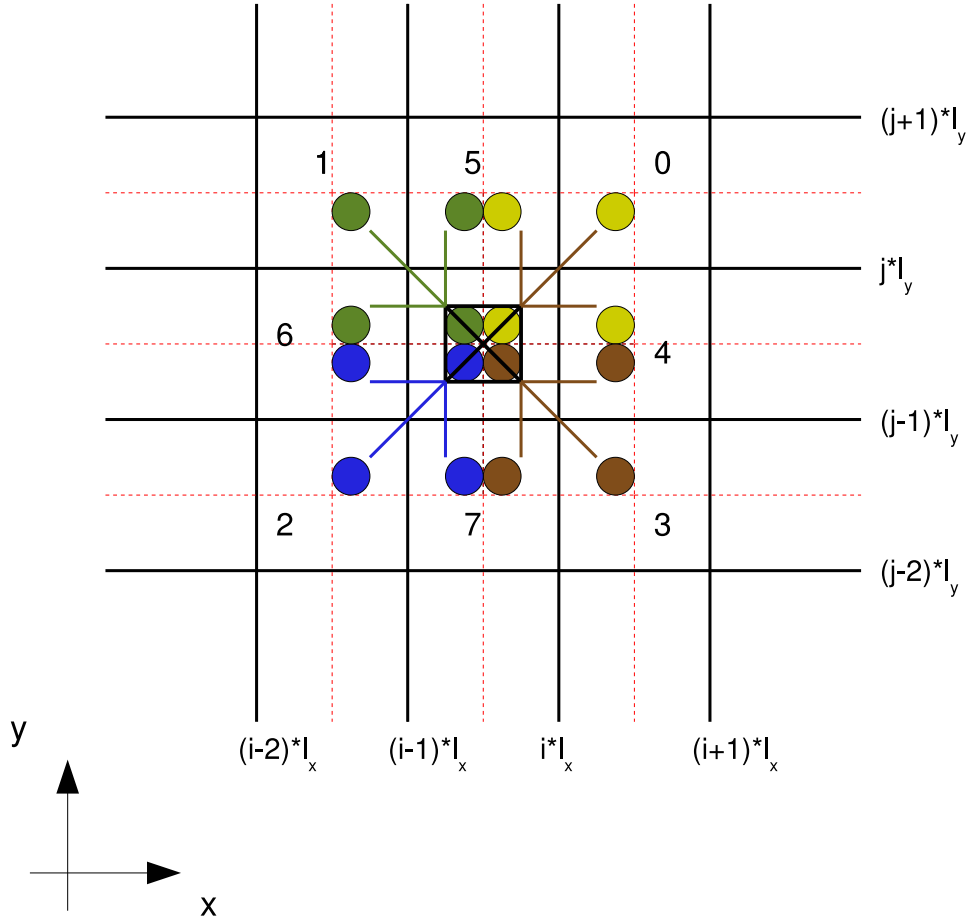


Figure 2.12: Schematical representation of the discretization lattice used for the formulation of the LISA-Spring 2D model. The solid black lines identify the geometric lattice obtained directly by a spatial Finite Difference (FD) scheme of discretization of the equations. l_x is the mesh step along the x axis, while l_y along the y axis. The dashed red lines compose a dual lattice superimposed to the previous one: the cells of this lattice has the same dimensions of the ones of the geometrical lattice, but they correspond to cells of different types of materials, in the most heterogeneous case each cell refers to a different material. A virtual representative particle with the same mass of each material cell is placed in correspondence to each node (i, j) of the geometrical lattice. It is splitted into four sub-particles (or sub-nodes), placed ideally in correspondence of the vertexes of the material cell, to each of which one fourth of the whole mass of the material cell is attributed. The sub-particles referring to the same material cell have the same color and interact among them through linear elastic tensorial springs (of the same color), while sub-particles belonging to different material cells (but to the same geometrical cell) interact among them through special springs across the interfaces between the different material cells. The latter springs express the mechanical features of the interfaces (interstitial regions separating the different material cells identified with the grains)

and are the key elements of the PM description of the HEEs.

material cell having with center the node (i, j) , indicated in Fig. 2.12 as circles with the same color (the color indicates that such sub-particles belong to the same material cell). To each sub-particle of a cell material it is attributed one fourth of the total mass of the material cell itself.

The sub-particles with the same colors interact mechanically between them through **tensorial virtual springs** (the solid lines connecting the four sub-particles and having the same color of the material cell), while the four sub-particles belonging to the four different material cells and placed at the node separating the four material cells interact with them through “internal” springs crossing the geometrical interfaces between the four different material cells. The adjective internal refers to the fact that they are, according to this formalism, the springs for modeling the mechanical behavior of the interfaces/interstices, as in the 1D case there is only one spring. These springs, sources of the NCNL elastic behavior, are schematized as solid black lines connecting the four different sub-particles at the interface between the material cells.

Both the springs connecting sub-particles of the same material type and the interstice ones are tensorial springs, i.e. each spring gives a contribution in the determination of the total force acting on each sub-particles which is calculated from the product of a matrix of elastic constants and a vector of displacements, independently from the fact that in Fig. 2.12 some springs are directed only along the x or y axis (it should be reminded that the Figure is only an ideal schematization, the mathematical formulation of the interacting forces between the sub-particles leads to a description of this type, because each component of the total vectorial force acting on a sub-particle is a linear combination of parameters with the dimension of elastic constants times a component of a displacement vector).

In what follows, I’m going to present a brief overview of the formulation of the model, referring to external forces when speaking about the forces of interaction between sub-particles of the same material type and of internal forces when speaking of the ones due to the interstices, across different material cells⁶.

The 2D model is simply an approximated version of a more general 3D one, presented in Appendix III. The approximation used consists of two assumptions:

- using stress-strain constitutive equation for a crystalline material with cubic symmetry or for an isotropic material;
- considering the specimen as a thin plate with trascurable thickness and using the approximation of plane-stress conditions.

The first hypothesis reduces the total number of elements of the second order elastic constants tensor, C_{klmn} . As for the 1D model, the external forces could be derived by a FD spatial discretization of the stress-strain equation for a perfect linear elastic material. However, the model is set up in order to consider classical nonlinear constitutive equations as well, considering for example third order elastic constants C_{klmnop} , the difference being that the total number of parameters increases considerably for the same material symmetry. Obviously, also for reducing the complexity of the model, each material cell of the specimen is considered of the same crystalline symmetry (cubic or elastically isotropic in the implementations used up to now).

The second hypothesis leads not to consider the dependence of the various scalar fields from the z variable and to a null component ϵ_{33} for the strain tensor field, such that the resulting stress-strain scalar constitutive equations for the specimen are

⁶It should be reminded that only in the most heterogeneous case, each material cell is different from all the other ones, while in more usual setups, only portions of the specimens composed by many material cells differ among them for physical properties. The distinction among material cells is usefull from a mathematical point of view. The specific setup of the simulation to be run establishes which cell refers to which material.

$$\begin{cases} \sigma_{11} = C_{1111} \cdot \epsilon_{11} + C_{1122} \cdot \epsilon_{22} \\ \sigma_{22} = C_{1122} \cdot \epsilon_{11} + C_{1111} \cdot \epsilon_{22} \\ \sigma_{12} = 2 \cdot C_{1212} \cdot \epsilon_{12} \end{cases} \quad (2.18)$$

or written after the explicitation of the strain scalar fields ϵ_{mn}

$$\begin{cases} \sigma_{11} = \sigma \cdot \frac{\partial u_1}{\partial x} + \lambda \cdot \frac{\partial u_2}{\partial y} \\ \sigma_{22} = \lambda \cdot \frac{\partial u_1}{\partial x} + \sigma \cdot \frac{\partial u_2}{\partial y} \\ \sigma_{12} = \mu \cdot \left(\frac{\partial u_1}{\partial y} + \frac{\partial u_2}{\partial x} \right) \end{cases} \quad (2.19)$$

where $\sigma = C_{1111}$, $\lambda = C_{1122}$ and $\mu = C_{1212}$ are the only three independent elastic constants in the case of a crystalline material with cubic symmetry.

Considering a generic node/particle (i, j) of the geometrical lattice, the four sub-particles resulting from the splitting are identified with an integer index $k = 0, 1, 2, 3$, identifying the four sub-cells of the material cell (starting from the top-right cell and following a counter-clockwise turn). Another integer index $n = 0, 1, \dots, 7$ identifies the directions of the eight nearest neighbor particles of the (i, j) particle itself. Each sub-particle k of the particle (i, j) is subjected to a total (vectorial) force \vec{F}^k due to the interaction with the other sub-particles of the same material cell. These vectorial forces are derived from spatial FD discretization of the continuum Eq.s. 2.19 (see Appendix II for a description of the procedure for the algebraic derivations of such forces) and each of them can be written as the sum of three partial vectorial forces \vec{F}_n^k where the index n can assume three of the possible values $0, 1, \dots, 7$ according to the directions of interactions (see in Fig. 2.12 the numbers around the node (i, j)). These forces are the ones that can be identified with tensorial springs forces, just because, as previously cited, each of them can be written as the product of a matrix and a displacement vector, something similar to a tensorial Hooke's law:

$$\vec{F}^k = \sum_{n \in E_k} \vec{F}_n^k \quad (2.20)$$

$$\vec{F}_n^k = M_n^k \cdot \vec{W}_n^k \quad (2.21)$$

where \vec{W}_n^k is defined as

$$\vec{W}_n^k = \begin{pmatrix} u_n^k - u^k \\ v_n^k - v^k \end{pmatrix} \quad (2.22)$$

i.e. a vectorial relative displacement of two sub-nodes of the same material cell connected by one of the virtual external springs, being u^k and v^k the two components of the vectorial displacement field for the sub-particles k and in a similar manner u_n^k and v_n^k the ones of the vectorial displacement field of one sub-particles belonging to the same material cell of the k -th one⁷.

The procedure for deriving such formulae and the explicitation of the matrices M_n^k are presented in Appendix II (further details can be found in Ref. [61, 62]).

The internal forces due to the springs within the interstice region are called f_l^k , where the index k identifies always the sub-particles of a material cell, while the index l plays for these forces the same role of the index n for the external forces, i.e. it identifies the direction of interaction with another sub-particle of another neighboring material cell, through the interstice

⁷ E_k denotes here the set of three possible values of n given k .

region. So for each value of $k = 0, 1, 2, 3$, l can assume three possible values in the finite discrete set $0, 1, 2, \dots, 7$.

As for the external forces, the total internal force acting on the $k - th$ sub-node of the (i, j) main node is the vectorial sum of three of such internal forces associated to the internal springs,

$$\vec{f}^k = \sum_{n \in U_k} \vec{f}_l^k \quad (2.23)$$

where U_k indicates the set of three possible values of l given k .⁸

As for the 1D model, the equations of motions for each sub-node k of each node (i, j) are formulated, remembering that each sub-node has one fourth of the total mass of the material cell associated to itself. In the 2D formulation, the attenuation properties of the specimen have been formulated by the simplest way, consisting in the introduction in the equations of motion of a term proportional to the velocity of the displacement vector field. As discussed in the previous Section dedicated to the 1D formulation, this is one way of formulating attenuation properties of the different media composing the specimen, the other way is using for the grains (the materials cells) a Kelvin-Voigt's like stress-strain equation of state. Although in the 1D case, one formulation is almost equivalent to the other one, in the 2D case, however, the Kelvin-Voigt's constitutive relation introduces several parameters, the elements of the first order viscosity tensor η_{klmn} . So, it has been preferred to use the first formulation, although it should be remembered what has been said in the previous Section about its limits of validity.

Defining m_k the mass of the sub-particle k and avoiding to explicitly mention a specific node (i, j) but considering the subsequent equations referred to a generic one, the equations of motion, in the FDTD forms, result to be

$$\vec{W}^{\rightarrow k, t+1} = \frac{\alpha_1}{\xi_k^+} \cdot \left(\vec{F}^{\rightarrow k} + \vec{f}^{\rightarrow k} \right) + \frac{2 \cdot \rho_k}{\xi_k^+} \cdot \vec{W}^{\rightarrow k, t} - \frac{\xi_k^-}{\xi_k^+} \cdot \vec{W}^{\rightarrow k, t-1} \quad (2.24)$$

where

$$\begin{aligned} \alpha_1 &= \frac{4 \cdot \tau^2}{l_x \cdot l_y \cdot l_z} \\ \alpha_2 &= \frac{2 \cdot \tau}{l_x \cdot l_y \cdot l_z} \\ \xi_k^+ &= \rho_k + \alpha_2 \cdot \gamma_k \\ \xi_k^- &= \rho_k - \alpha_2 \cdot \gamma_k \end{aligned} \quad (2.25)$$

and ρ_k is the volumetric mass density of the sub-cell k multiplied per l_z , the thickness of the quasi-2D specimen⁹.

As for the implementation of the 1D model, also in the 2D case the variables of interest as output signals calculated for each node (i, j) are the components of the displacement vector of the center of mass of the material cell associated to such node (i, j) , defined as

$$\vec{W}_{cm} = \left(\frac{1}{\sum_{k=0}^3 \rho_k} \right) \cdot \sum_{k=0}^3 \rho_k \cdot \vec{W}^{\rightarrow k, t} \quad (2.26)$$

The expression for the interstice internal forces $\vec{f}^{\rightarrow k}$ can be derived imposing different types of conditions, as in the case of the 1D model.

⁸The index l should not be confused here with the l letter used previously for indicating a common value for the mesh steps along the two axes, $l_x = l_y = l$, used in the actual implementation of the LISA-Spring 2D model up to now.

⁹Note that here the time dependence of the forces have not explicitated but these vectorial variables are time dependent too as the displacement vectors.

The original Spring model [60] consider rigid interfaces/interstices between the different material cells imposing the conditions that for each node (i, j) , the acceleration vector of each sub-node k is equal to the one of the mass center, $\vec{W}^{\vec{k},t} = \vec{W}_{cm}^{\vec{t}}, \forall k = 0, 1, 2, 3$, which lead to the following definitions for the internal forces:

$$\vec{f}^k = \sum_{j=0, j \neq k}^3 \frac{\xi_k^+ \cdot \vec{F}^j - \xi_j^+ \cdot \vec{F}^k}{4 \cdot \tilde{\xi}} \quad (2.27)$$

where $\tilde{\xi} = \tilde{\rho} + \frac{1}{4} \cdot \alpha_2 \cdot \sum_{j=0}^3 \gamma_j$ and $\tilde{\rho}$ is the arithmetic mean of the $\rho_k, \forall k = 0, 1, 2, 3$.

It has been shown by Gliozzi *et al.* [61, 62] that a more general condition for a rigid interstice is obtained imposing that the relative velocity of two generic sub-nodes of the same material cell must be null, i.e. $\vec{W}^{\vec{k},t} = \vec{W}^{\vec{j},t}, \forall j = 0, 1, 2, 3$ and $j \neq k$. From these conditions, the formulae for the internal forces can be derived solving a non-homogeneous linear system of algebraic equations:

$$\vec{f}^k = \sum_{j=0, j \neq k}^3 \left(\frac{\xi_k^+ \cdot \vec{F}^j - \xi_j^+ \cdot \vec{F}^k}{4 \cdot \tilde{\xi}} + \frac{1}{\alpha_1} \cdot \frac{\xi_k^+ \cdot \xi_j^- \cdot \Delta_t \vec{W}^{\vec{j},t} - \xi_j^+ \cdot \xi_k^- \cdot \Delta_t \vec{W}^{\vec{k},t}}{4 \cdot \tilde{\xi}} \right) \quad (2.28)$$

where $\Delta_t \vec{W}^{\vec{j},t} = \vec{W}^{\vec{k},t+1} - \vec{W}^{\vec{k},t}$.

Eq. 2.28 can be considered as a limit case of a more general expression for the internal forces acting on sub-particles:

$$\vec{f}_j^{\vec{k}} = a_{1,j}^{\vec{k}} \cdot \frac{\xi_k^+ \cdot \vec{F}^j - \xi_j^+ \cdot \vec{F}^k}{4 \cdot \tilde{\xi}} + a_{3,j}^{\vec{k}} \cdot \frac{1}{\alpha_1} \cdot \frac{\xi_k^+ \cdot \xi_j^- \cdot \Delta_t \vec{W}^{\vec{j},t} - \xi_j^+ \cdot \xi_k^- \cdot \Delta_t \vec{W}^{\vec{k},t}}{4 \cdot \tilde{\xi}} + a_{2,j}^{\vec{k}} \cdot l_z \cdot E_j^k \cdot \vec{W}_j^{\vec{k}} \quad (2.29)$$

Eq. 2.29 is a formulation for the internal forces equivalent to the continuum formulation of the stress-strain relation of HEEs introduced in the previous Section about the 1D model: the first right-hand side term is the poro-viscoelastic term dependent upon the external forces acting on the boundaries of the interface, while the second right-hand side term is the attenuative one and the third right-hand side term is the linear elastic term.

The tuple of three parameters vectors $(a_{1,j}^{\vec{k}}, a_{2,j}^{\vec{k}}, a_{3,j}^{\vec{k}})$ is the 2D version of the set of parameters (a_1, a_2, a_3) characterizing the states of the interstice. In this case, each interstice internal spring have 36 parameters, so its state space is 36-D.

In order to reduce the total number of degrees of freedom of the model, some constraints and assumptions have been introduced [61, 62] for the use of the same type of PM description of the HEE (interstice between grains):

- \forall interstice in the lattice is characterized by the same sets of values for the switching parameters $(a_{1,j}^{\vec{k}}, a_{2,j}^{\vec{k}}, a_{3,j}^{\vec{k}})$;
- given a generic interstice, each internal spring has the same set of values for the switching parameters (the springs have identical states);
- x and y components of the internal forces have the same switching parameters, i.e. $a_{i,j,x}^k = a_{i,j,y}^k, \forall i = 1, 2, 3, \forall k = 0, 1, 2, 3, \forall j = 0, 1, 2, 3$.

With these assumptions, the total number of parameters describing each spring is again three as in the 1D case, (a_1, a_2, a_3) . The 2D HEEs (interstices) are allowed to have two different possible sets of values for their state vector:

- $(a_1, a_2, a_3) = (a_{1,R}, 0, a_{3,R})$, which corresponds to a generalized rigid state in respect of the one identified by the condition that leads to Eq.s 2.27;
- $(a_1, a_2, a_3) = (a_{1,PE}, a_{2,PE}, a_{3,PE})$, which defines, as for the 1D case, the poro-viscoelastic state, being all the values of the parameters positive and less than 1.

The control variable according to whose values each interstice (i.e. each of its internal springs) undergoes a change of state is chosen to be a scalar one among the *eigenstresses* [61, 62] i.e. a deviatoric, a volumetric or a shear stress. In the continuum case, this scalar fields are defined as follows:

$$\begin{aligned}\sigma_V &= \frac{\sigma_{11} + \sigma_{22}}{2} \\ \sigma_D &= \frac{\sigma_{11} - \sigma_{22}}{2} \\ \sigma_S &= \sigma_{12} = \sigma_{21}\end{aligned}\tag{2.30}$$

respectively for the volumetric, deviatoric and shear stress components. These components can be derived from the 2D version of the stress-strain equation of state of an elastic body written in the Voigt's notation, i.e. using a matrix of independent elastic constants, which is a symmetrical matrix, so it can be diagonalized. After finding the orthogonal matrix for the diagonalization of the elastic constants matrix, the stress-strain constitutive relation can be rewritten in that diagonalized form, so the vector of stress components undergoes a transformation which leads to the *eigenstresses*.

The forces correspondent to such *eigenstresses*, for each interstice, can be calculated using the same method for deriving the expression for the external forces \vec{F} (see Appendix II and Ref. [62]).

In different implementations of the LISA-Spring 2D model different control parameters have been chosen in order to compare their role in the dynamics of the HEEs and the consequences on the overall behavior of the simulation of elastic wave propagation in the virtual NCNL specimen. For the simulations used in the Computational Time Reversal Acoustics Imaging technique described in Chapter 4 the control parameter used has been the volumetric *eigenstress*.

Ref. [61, 62] shows some results of simulations of ultrasonic wave propagation through solid specimens with regions modelled with the PM formalism, that is regions containing HEEs. These regions play the role of defects as distributions of micro-cracks. Some other original results about the use of the LISA-Spring 2D model are presented in Chapter 4, where such simulations have been used for validating the cited Imaging technique, realizing numerical forward propagation experiments.

Chapter 3

Nonclassical Nonlinear elastic behaviour of damaged concrete

As seen in the previous Sections, fast dynamics, conditioning and slow dynamics have been shown in the last years to be features shared by the elastic response of several materials, such as rocks, damaged materials, composites, concrete and other ones which have in common structural properties, like the presence of a hard matrix made by several grains surrounded by a soft bond system.

It has been suggested that the nonclassical nonlinear elastic behaviour should emerge as a consequence of the interactions among grains through the bond system during deformations due to waves (dynamic regime) or loads (quasi-static regime). The soft bond system can be a natural structural component of the type of material or it can be created within the material after strong perturbations such as ones generating damage in the form of, e.g., localized or distributed microcracks, dislocations networks, creeps, flaws.

As discussed above, although an understanding of the mechanisms responsible for the mentioned anomalous elastic behavior might shed light on the comprehension of the link between nonclassical nonlinearity and damage state [22], with a consequent wealth of applications in the field of Materials Characterization, nonlinear signatures are among the first manifestations of the presence of damage in materials [10], so some drawbacks for application of techniques based on fast and slow dynamics are immediately evident and exploitable.

For example, a large elastic energy may usually be injected in the specimen (which is not always easy) to obtain small effects, hardly measurable *in situ*, e.g. a resonance frequency shift of a few percentage points. Furthermore, the nonlinear properties of hysteretic elastic media are very sensitive to environmental conditions, such as temperature [26], humidity, confining pressure [72], etc. On the other hand, it is much easier to perform measurements based on the detection of slow dynamics effects, which seem to be equally (or even more) sensitive to damage [16]. Here parameters as the typical time scale of the recovery process are expected to be optimal indicators for damage detection.

This chapter is dedicated to the presentation of an investigation I conducted along with M. Scalerandi (Dept. of Physics, Polytechnic of Torino) and M. Bentahar and R. El Guerjouma (both formerly at the GEMPPM, *Groupe d'Etude en Metallurgie Physique and Physique des Matériaux*, UMR CNRS 5510 and INSA, *Institute Nationaux des Sciences Appliquées*, de Lyon at the time this work was done) about the nonclassical nonlinear elastic behaviour of concrete specimens by NEWS techniques, in particular resonance frequency experiments.

Concrete has been known to be slightly nonlinear and hysteretic even when not damaged [73, 24]. In Section 3.1, a brief review of the structure of concrete materials is presented in order to show that they share the previously cited structural model hard matrix-bond system.

However, the aim of the work was to compare the sensitivity and accuracy of fast and

slow dynamic measurements to the presence of damage in concrete sample, which increases its nonlinear elastic behaviour.

To do so, resonance frequency experiments probing fast and slow dynamics typical effects have been conducted at the laboratories of INSA Lyon. The setups and results of these experiments are presented in Section 3.2.

The analysis of the sensitivity and accuracy of both types of experiments has been performed with numerical simulations of the corresponding real-world experiments (see Section 3.4), based on an adapted version (see Section 3.3) of the LISA-Spring 1D model described in Section 2.2.2 and with more details in Appendix 5.3.2. The best fitting of the experimental data via the LISA-Spring 1D-based numerical simulations has also led to one of the first complete validation of that model¹.

As a result of the best fitting of the experimental data via the model, an interpretation of the experimental results has been conducted.

3.1 Structure of concrete and its elastic behaviour

Concrete is one of the most used materials in the world: every year about 5.5 billion tons of it are produced, it has been estimated a $\frac{1}{10}$ ratio of consumption between steel and concrete. Among the reasons for its widespread use as a fundamental material for structured components, there are:

- an excellent resistance to water, in fact some of the earliest known applications of the material consisted of aqueducts and waterfront retaining walls constructed by Romans; from this point of view, it has been widely used for building structural elements exposed to moisture, usually with the form of a *reorced concrete*, i.e. a concrete containing steel bars designed on the assumption that the two materials act together in resisting forces; reinforced concrete is also called *pre-stressed concrete* because, by tensioning steel tendons, prestress of such magnitude and distribution is introduced so that the tensile stresses resulting from the service loads are counteracted to a desired degree;
- structural concrete elements can be formed into a variety of shapes and sizes, because freshly made concrete is of a plastic consistency, which permits the material to flow into prefabricated frameworks; after a number of hours, the framework can be removed for reuse when the concrete has solidified and hardened to a strong mass;
- concrete is among the cheapest and most readily available materials on the job; its principal ingredients are relatively inexpensive and more commonly distributed in most areas of the world.

From a structural point of view, concrete can be defined as a **composite material** that consists essentially of a **binding medium** within which are **embedded** particles or fragments of aggregates. For example, in one type of concrete called hydraulic cement concrete the binder is formed from a mixture of hydraulic cement and water.

An aggregate can be defined as a granular material such as sand, gravel, crushed stone or iron blast-furnace slag, used with a cementing medium to form hydraulic-cement concrete or mortar (the other most known and use type of concrete). The aggregate is usually subdivided into two main categories: **coarse aggregate**, i.e. aggregate particles with a typical linear

¹Refs. [46, 45, 27] do report first results of validation of the LISA-Spring model in the simulation of nonclassical nonlinear elastic wave propagation in solid materials. However, those papers do not report any kind of systematic validation of that modeling and simulation approach upon one complete set of experimental data referring to one single type of material exhibiting nonclassical nonlinear elastic behaviour.

dimension larger than 4.75 mm; **fine aggregate**, with particle having a typical linear dimension lower than 4.75 mm. Some examples of aggregates and their use: gravel is a coarse aggregate resulting from natural disintegration and abrasion of rocks or processing of weakly bounded conglomerates; sand is a fine aggregate resulting from the same previous type of processing on Earth materials; crushed stone results from industrial crushing of rocks, boulders or large cobblestones; iron blast-furnace slag is a by-product of the iron industry.

The **cement**, i.e. the binding medium, is a finely pulverized material which by itself cannot act as a binder but does develop the binding property as a result of hydration, i.e. from chemical reactions between the cement minerals and water. The most used type of cement is called hydraulic cement when hydration products are stable in an aqueous environment. The most commonly used hydraulic cement is called **portland cement**, consisting essentially of hydraulic calcium silicates, responsible for its adhesive characteristics.

So far introduced, concrete can be obtained as a mixture of an hydraulic cement, water and aggregates. A fourth ingredient is usually adjunct, an admixture, for obtaining special mechanical/thermal features in the final product.

At a macroscopic scale, i.e. at the scale of resolution of the eye (about 200 μm), concrete can be considered as a **two phase material**: one phase is the ensemble of the aggregate particles, the other one is the binding medium, composed of an incoherent mass of hydrated cement paste (from now on called HCP).

At a microscopic scale, i.e. at a scale of resolution of modern scanning electron microscopes, for example, the two phases of this composite material result to be neither homogeneously distributed with respect to each other nor are themselves homogeneous. For example, in some areas, the HCP may be as dense as the aggregate while in other ones it may be very porous.

For a well-hydrated cement paste, the inhomogeneous distribution of solids and voids can perhaps be ignored when modeling the behavior of the material. In the presence of aggregate, the HCP structure in the vicinity of large aggregate particles is usually very different from the structure of the bulk paste. Many aspects of concrete behavior under stress can be explained only when the cement paste-aggregate interface is treated as a third phase of the concrete structure. This third phase is usually called the **transition zone**, i.e. a thin shell typically 10 to 50 μm thick around a large aggregate, generally weaker than either of the two main phases, therefore exercising a far greater influence on the overall mechanical behavior of concrete than is reflected by its size.

Each of these three phases, always at the cited microscopic scale, is itself a multiphase material in nature. For instance, each aggregate particle may contain several minerals in addition to microcracks and voids. Both the HCP and the transition zone generally contain an heterogeneous distribution of different types and amounts of phases, pores, microcracks.

So, concrete results to be a complex composite material from a structural point of view but also from the point of view of its elastic-plastic behavior.

The quasi-static stress-strain constitutive equation for concrete has been unsuccessfully formulated considering two phases material models. Under quasi-static compressive loading, above the linear regime stress threshold, both the aggregate and the HCP, if separately tested, would fail elastically whereas concrete itself shows inelastic behavior before fracture. Some other peculiar features have been observed: the quasi-static stress-strain constitutive relation is independent of the loading time; concrete undergoes creep, i.e. a gradual increase in strain with time under a sustained constant stress; strain can arise even in unloaded specimens as a result of changes in the environment humidity and temperature. Concrete quasi-static stress-strain relation also exhibits hysteresis at loading stress values above the linear regime threshold.

Its quasi-static and dynamic visco-elastic behavior can be studied only considering models taking into account its multi-phase structure, particularly the differences in the elastic behavior of aggregates and the binding medium/transition zone. Both at the macroscopic and at the

microscopic scales defined before, its structure shares common features with mesoscopic granular materials described in Section 2.2.1. Its nonclassical nonlinear elastic behavior has been found out in different experimental investigations [14, 73, 24] including the one reported in this Section.

The LISA-Spring model approach, as reported below, has been proven to be successful in describing and reproducing by numerical simulations the nonlinear dynamic elastic behavior of concrete, due to its basic description of a specimen as a succession of alternating linear visco-elastic bodies interfaced between them by nonlinear bi-state visco-elastic regions. In this case, the HEE of this modeling approach corresponds to binding medium/transition zone complexes of real concrete specimen while hard grains correspond to aggregate particles, as shown below in Section 3.3.

3.2 Fast and slow dynamics experiments with undamaged and damaged concrete samples

The experiments conducted at the laboratories of the GEMMPM, INSA Lyon, have involved small cylindrical concrete bars of cross section $\Sigma = 10 \text{ mm}^2$ and length $L = 61 \text{ mm}$. Several specimens have been produced with an identical treatment. One of them (intact specimen) has been used for reference, while other ones have been damaged through compression tests, up to the yield rupture, determined to be about 65 MPa. Longitudinal and transverse velocities in the intact sample have been measured to be $c_P = 3389.6 \text{ m/s}$ and $c_S = 2217.3 \text{ m/s}$, corresponding to a Young's modulus of value 24 GPa and Poisson ratio of value 0.126. Volumetric mass density of the specimen is $\rho = 2167.6 \text{ Kg/m}^3$.

A porosity meter has been used to determine the density of voids. The resulting volume fraction has been 14% and voids sizes has been noticed to vary between 0.5 and 315 μm . Concrete samples have no preferential grain orientation. Cracks, which have been shown to be present even in the intact state, could have lengths up to 2 mm with an opening corresponding to few μm . It follows that interstices have been assumed to be much smaller than grains (of the order of one with respect to tens of μm).

Nonlinear properties of concrete samples have been previously investigated by several authors [14, 24, 73, 74, 75]. Nevertheless, most of the experiments performed so far were aimed at analysing the elastic properties of the sample in propagation conditions, e.g. through a spectral (non-linear) analysis [24, 74] or using actively modulated acoustic signals [75]. Only few experiments have been performed in resonance conditions [14]. In [14], however a complete analysis of damage effects have not been addressed.

The experimental setup used in our experiments conducted at the laboratories of the GEMMPM, INSA Lyon, is presented in Figure 3.1. It has been designed according to the following principle: a gain-phase analyzer, controlled by a computer, generates a continuous sinusoidal wave, while performing frequency sweeps to excite the material around its natural vibrating modes. The signal amplitude is controlled by the analyzer and amplified with a constant gain. At one end of the sample (suspended to have free boundary conditions at both ends) we have attached one piezoelectric transducer to produce in the sample ultrasonic vibrations, which have been revealed at the other tip through a laser vibrometer. The gain-phase analyzer displays the received signals and transmits them to the computer for data processing. The method could be readily adapted to samples having particular geometries.

As one of the aims of this work was to detect material nonlinearities for weak strains (vibrations), we have taken great care to minimize nonlinearities due to electronics, in particular, by using a high power ultra-broadband coupler connected to a spectrum analyzer. Indeed, the latter displays the spectrum of reflected and transmitted signals through the coupler, allowing to control possible distortions due to electronics, which can lead to a better adjustment of the

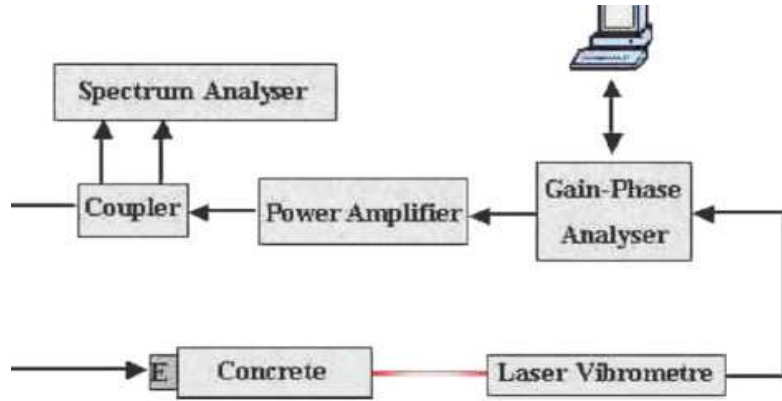


Figure 3.1: Schematic view of the experimental setup used for resonance frequency experiments on concrete specimens.

experimental device.

The linearity of the experimental device has been also tested on an intact aluminum sample whose nonlinearity is of the “atomic order”. For an accuracy corresponding to 0.1 Hz, the reference material has proved to be linear up to an excitation corresponding to a longitudinal strain $|\varepsilon| = 10^{-5}$, beyond which the resonance frequency shifts for electronics reasons (i.e. influence of the electronics chain on the measurements). This threshold is sufficient to study the nonlinear behavior of concrete, since most of the heterogeneous materials behave nonlinearly for lower strains (see Section 2.2.1 and Ref. [15]). Indeed, measurements on concrete samples have always been performed well below such threshold, with an additional check provided by the coupler (not used in previously reported experiments [76]), which warrants a careful test of the linearity of the electronic chain.

In the performed experiments, the resonance frequency of the first Young’s *eigenmode* of vibration (due to longitudinal stationary waves) of the specimen (damaged and undamaged) has been measured under different conditions, as discussed below. Resonance curves have been obtained by sweeping the frequency around the sample first compressional vibrating mode (located at about 26) KHz and recording the vibration velocity of the tip of the bar opposite to the one on which the transducer has been attached. Data processing then has allowed to extract the averaged-in-time vibration velocity at the sample tip.

Two sets of experiments have been performed.

- Fast dynamics experiments, i.e. successive resonance curves have been measured for different excitation amplitudes, without letting the system relax during the experiment. In this case, voltages from 10 mV to 100 mV have been amplified before exciting the material. To obtain enough energy in the sample, we have used a constant gain corresponding to 52 dB. As the input channel of the gain phase analyzer was conceived for small voltages, the output signals have been divided by a factor of ten, which corresponds to an attenuation of 20 dB.
- Slow dynamics experiments: the gain phase analyzer has been set at a fixed tension of 10 mV. For a short time duration, the amplifier has been switched on (52 dB amplification) to obtain a large amplitude signal in the sample, which induces conditioning. Afterwards, the amplifier has been switched off and the resonance frequency has been tracked in time every 50 (10-100) s in the case of intact (damaged) samples.

In the chosen conditions the experimental device has been shown to be linear. Thus the stress σ_{ext} applied by the PZT transducer on the specimen surface has been linearly dependent on the tension V generated by the gain phase analyzer. In this case it would be possible to define an efficiency coefficient “ g ” and link the stress to the tension as:

$$\sigma_{ext} = g \cdot V \quad (3.1)$$

It should be noted that the coefficient “ g ” depends on the considered set-up. Indeed, the acoustic impedance of the system may change either by switching on the amplifier or by changing sample (damaged and undamaged in our study). As such, it does depend on the elastic properties of the specimen (density and Young modulus), on the properties of the full electronic chain and on the quality of the specimen surface. It follows that the transduction efficiency has been altered and should not be taken as unchanged for the different experiments or dependent only on the acoustic impedance of the specimen.

3.3 Setups of the numerical simulated resonance experiments

As discussed in the previous Section, experiments have been performed on small concrete bars with negligible cross-section Σ to length L ratio. Since continuous compressional (plane harmonic) waves have been (and are usually) generated via rather large circular piezoelectric transducers (with a radius of the same order degree of the radius of the cross section of the bars), a 1-D description has been considered sufficient to model wave propagation.

Furthermore, concrete is known to have a complex microstructure, in which grains alternate with interstitial regions, as shown, for example in Figure 3.2 (a). Then, the LISA-Spring 1D model, which schematizes the material as a sequence of alternating hard (grains) and soft (interstices) portions, with different equations of state (see Figure 3.2 (b)), has been used in order to describe the concrete bars and develop a code to simulate the previously described resonance experiments.

It should be noted that the porosity of the specimens considered is about 14%. It follows that interstices have been assumed to be much smaller than grains (of the order of one with respect to tens of μm): the basic assumptions of the LISA-Spring model fit successfully the physical system to be modelled.

The LISA-Spring 1D simulation code used in this work has been implemented following the general formulation reported in Section 2.2.2 and in Appendix 5.3.2.

However, with respect to that general formulation, which has been based on previous approaches [45, 27], it has been considered in this case, for the probabilities of transition from one state to another of each HEE, a dependence on the shape of the bi-state diagram described in Figure 3.3 (d). Indeed, if the HEE is kept at a pressure P , jump probabilities should depend on the differences $|P - P_{c/o}|$. In fact, relaxation probabilities depend on the difference between the energy levels of the two states and, in a first approximation, it has been assumed they vary linearly with the external loading (P in our case). Therefore, since transitions from one state to the other are expected to be easier when the pressure is close to the corresponding deterministic transition, the following definition for the effective transition rates has been adopted:

$$\bar{q}_{c,o} = q_{c,o} \cdot \left(1 - \frac{|P - P_{c,o}|}{2P_{\max}}\right) \quad \text{when } P_o < P < P_c \quad (3.2)$$

The transition rates are schematically reported in Figure 3.3 (d) for one HEE as a function of P . $\bar{q}_{c,o}$ are not defined in the regions outside $P_o < P < P_c$, where only one state is allowed (see

Fig. 3.3 (a)). Here, e.g. for $P > P_c$, the HEE is always in the rigid state and transitions are no longer allowed (equivalent to $\bar{q}_c = 1$ and $\bar{q}_o = 0$).

It should be also noted that dependencies on temperature have been neglected in this case, only isothermal thermodynamic transformations have been considered associated to the corresponding mechanical deformations within the concrete specimen.

The relaxation process defined allows the introduction of the initial configuration of the system in a non arbitrary way. Considering that numerical experiments have been assumed to be performed, as in experiments, on a completely relaxed specimen (i.e. kept at $P = 0$, constant temperature and humidity for a very long time), with this formulation all the HEEs have been set initially at their restlength state. Units with $P_o < P_c < 0$ are in the closed state, while units with $P_c > P_o > 0$ are open. The remaining elements are in the closed/rigid state with probabilities $\bar{q}_{c/o}/(\bar{q}_c + \bar{q}_o)$, respectively.

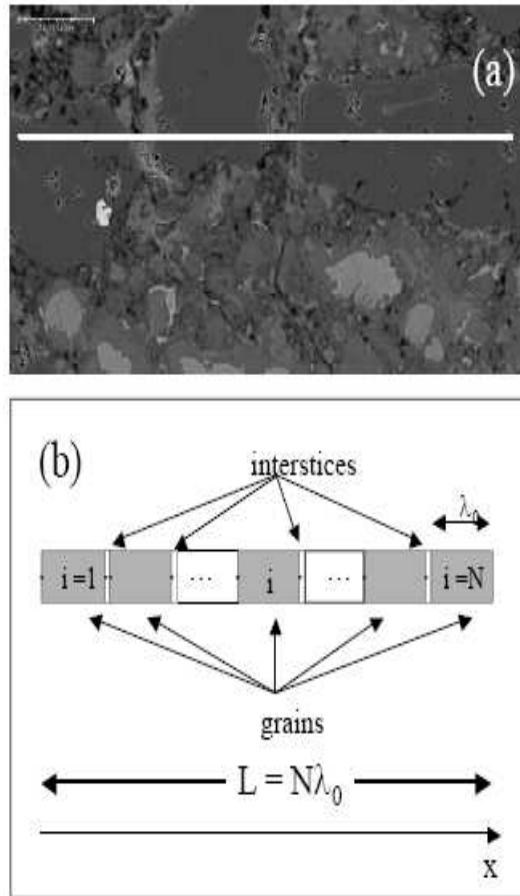


Figure 3.2: Correspondence between the microstructure of a typical concrete specimen with the description of a mesoscopic nonlinear elastic material according to the LISA-Spring 1D model. (a): microphotograph of a $110 \times 40 \mu\text{m}^2$ section of the intact concrete bar used in the experiment. (b): schematized/idealized 1D representation of the specimen according to the formulation of the LISA-Spring 1D model, with the grains alternated by thin interstices whose length is uncomparable with the length λ_0 of the grains. L is the total length of the cylindrical bar, N the total number of grains.

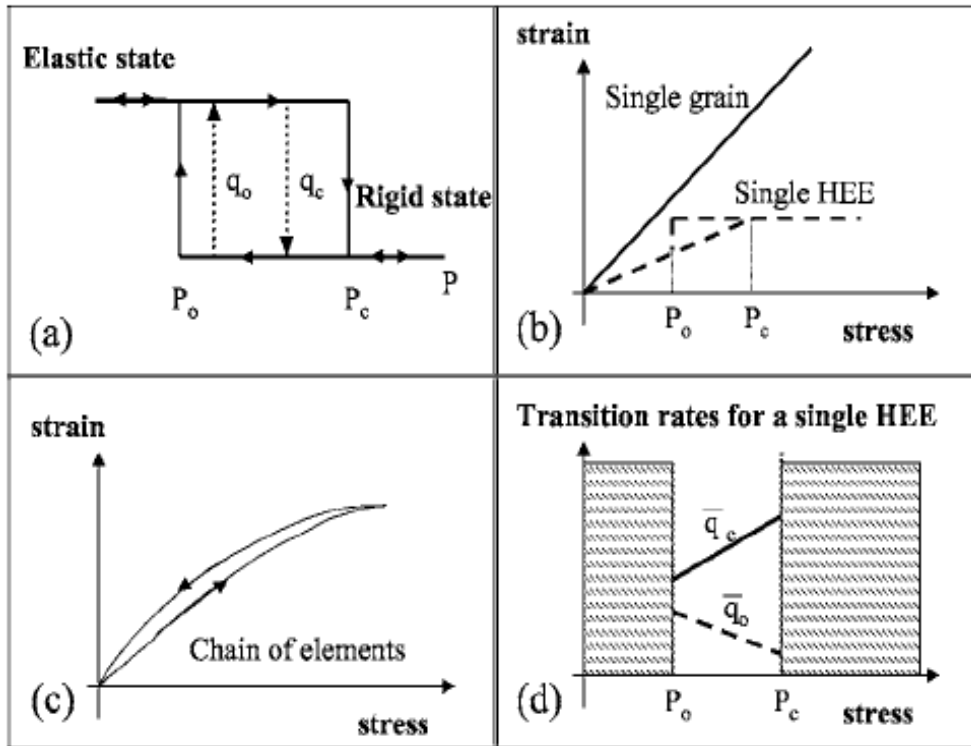


Figure 3.3: (a) Representation of the bi-state protocol adopted for the hysteretic elastic elements (HEEs). (b) Stress-strain constitutive relation for a single modelled grain (linear 1D Kelvin-Voigt's like visco-elastic body) and a single HEE (bi-state visco-elastic system). (c) Stress-strain relation for a chain of alternating grains and HEEs. (d) Representation of the transition rates between the two possible states for a HEE as a function of the pressure applied to the HEE from outer. Transition rates (probabilities of transition per unit of time) can not be defined in the dashed regions, where only one state for the HEE is allowed.

3.4 Comparison between numerical simulations results and experimental data

In this Section, both simulation and experimental data are shown, both in the case of an intact and a damaged concrete sample. The linear parameters of the specimen have been measured and have been resulted to be: bar cross section $\Sigma = 10 \text{ mm}^2$; sample length $L = 61 \text{ mm.}$; Young's modulus $E = 24 \text{ GPa}$, density $\rho = 2167.6 \text{ Kg/m}^3$. Furthermore we have considered a linear Q -factor of 600, reasonable for concrete. Note that attenuation will be influenced also by nonlinear contributions already at low excitation amplitudes. We consider grains and interstices with typical dimensions $\varepsilon_0 = 75 \text{ }\mu\text{m}$ and $\delta_0 = 1.5 \text{ }\mu\text{m}$, respectively, for a total of $N = 810$ discretization nodes in our numerical approach.

The set of parameters to describe the nonlinearity have been chosen to obtain a best fitting of the experimental data. As a result of an extensive analysis, the coefficients in the poroelastic state have been chosen as $a_{1e} = 0.4995$, $a_{2e} = 48 \cdot 10^{-5} \text{ GPa}$; $a_{3e} = 14 \text{ Pa}\cdot\text{s/m}$ for the intact state (i.e. a small nonlinearity). For the damaged state, to simulate more nonlinearity, $a_{1e} = 0.48725$, $a_{2e} = 156 \cdot 10^{-5} \text{ GPa}$; $a_{3e} = 7 \text{ Pa} \cdot \text{s/m}$ have been chosen. Furthermore, the relaxation parameters used in the simulations are $q_o = 5.4 \cdot 10^{-6}$, $q_c = 8 \cdot 10^{-4} \text{ s}^{-1}$ (probabilities per unit time).

The choice of the “best fitting” set of parameters has been performed by first adjusting them in order to fit the resonance curve at the lower excitation amplitude. The resonance angular frequency (ω_r) is sensitive only to a_{1e} and a_{2e} , it decreases with decreasing a_{1e} or a_{2e} , while a_{3e} plays only to define the amplitude at resonance. We have also observed that the curve width is sensitive only to a_{2e} . Fitting of the curves at larger amplitude values gives then only a slight adjustment of the parameters a_{1e} and a_{2e} . It is important to observe also that numerical results are very sensitive to the choices of the parameters. For instance, a 1% change in a_{1e} gives a change in the resonance frequency ω_r of about 10% [70].

In the experiments, the various curves correspond to different voltages applied to the function generator (varying from 10 mV to 100 mV) as described above. We have assumed, for the intact case, an efficiency conversion factor $g = 54 \cdot 10^3 \text{ N/m}^2\text{V}$ (see Eq. (3.1)). It follows that the driving amplitude σ_{ext} used in the simulations varies from 540 to 5400 N/m².

During the damage process, i.e. when the sample have been put under stress, some areas have behaved as stress concentration zones characterized by a high strain level comparing with the rest of the other regions. This may have allowed creation and nucleation of micro-cracks in the bulk and near the surface even for moderate stress values, which can cause a change in the material's impedance and can decrease the efficiency of the coupling effect. As a consequence, in the simulation for the damaged case we have used a smaller efficiency $g = 27 \cdot 10^3 \text{ N/m}^2\text{V}$.

3.4.1 Fast dynamics experiments and simulations

In Fig. 3.4, results from a fast dynamics experiment, i.e. the determination of the resonance frequency for different values of the driving amplitude A_{ext} , are reported. The experimental data and simulation results (first two columns) show a good quantitative agreement, for both the undamaged and damaged samples, as highlighted in the third column where some of the experimental (solid lines) and simulation (dots) curves have been superimposed.

Data shows that already in the intact case (first row), the sample is slightly nonlinear. Both experiments and simulations show in fact a small shift of the resonance frequency towards lower values (see also Fig. 3.5) when increasing the forcing (larger A_{ext} values). More evident is the contribution of nonclassical nonlinearity to attenuation: the ratio of the peak amplitudes at resonance for the lower and higher injection amplitudes is about 9 (considering offsets), i.e. well different than the ratio of 10 of the corresponding injected amplitudes. Further evidence of

nonclassical nonlinear attenuation is given by the increase of the curve width with increasing the excitation amplitude. The simulation results agree well with experimental data. In particular, the resonance frequencies and the peak velocity values are very well estimated, even from a quantitative point of view. Slightly more approximate is the prediction of the curve width, which, in the simulations, is slightly smaller at low amplitude and larger at high amplitude. Nevertheless the agreement is satisfactory (see below the comments about Fig. 3.6).

Similar considerations are valid for the damaged specimen (second row of Fig. 3.4). In this case, however, the effect is much larger and more easily distinguishable (note the different scale in the angular frequency scale). Also, besides the shift and increase in attenuation, resonance curves are considerably distorted from the classical Lorentzian shape, as qualitatively captured from the simulations. Again, optimal quantitative agreement is found for the peak values and resonance frequencies at the different values of A_{ext} , while satisfactory agreement is found for the width of the curves.

The same observations are reported in Figs. 3.5 and 3.6 in a more quantitative way. Here we plot, as a function of the peak amplitude (averaged velocity at resonance), the relative resonance frequency shift (Fig. 3.5) and relative Q-factor change (Fig. 3.6), defined as

$$\frac{\Delta\omega_r}{\omega_r} = \frac{\omega_r(A_{ext}) - \omega_{r0}}{\omega_{r0}} \quad (3.3)$$

$$\frac{\Delta Q}{Q} = \frac{Q(A_{ext}) - Q_0}{Q_0} \quad (3.4)$$

where $\omega_r(A_{ext})$ is the resonance frequency at excitation amplitude A_{ext} and ω_{r0} is the resonance frequency at the minimum excitation amplitude used ($A_{ext} = g \cdot 10 \text{ mV}$). The Q-factor has been estimated by the ratio between the resonance frequency and the width of the resonance curve at $\sqrt{2}/2$ peak amplitude. Both quantities behave linearly (note the linear fitting of the experimental data reported as a solid line) with a good agreement between experimental (squares) and simulation (triangles) results. Both in the damaged and undamaged cases, the material softens with increasing amplitude and the Q-factor decreases (more attenuation). Non linear effects are however much larger in the damaged case (slopes of the fitting curves are reported in the Figures). It is remarkable to note that the change in slope with respect to the intact case is about 400 for the resonance frequency shift and only 3.5 for attenuation.

Finally in Fig. 3.7 we report the strain (normalized to the input amplitude) vs. frequency curves for the damaged and undamaged samples at 10 mV and 50 mV excitation amplitudes. Results allow to appreciate the huge effect on attenuation and resonance frequency caused by the damage process. Note that the apparent discrepancy in the tails of the curves for the undamaged case is emphasized by the log scale used.

3.4.2 Slow dynamics experiments and simulations

As reported in Section 2.2.1, in a slow dynamics experiment, the resonance frequency is tracked in time at a fixed small excitation amplitude (linear regime of elastic response) after a larger amplitude wave has been applied to condition the specimen. In Fig. 3.8, the response of the system during relaxation is reported for a simulation case referring to the damaged concrete specimen excited at 10 mV. In the reported simulation, conditioning is applied at $t = 0$ with a 40 mV driving amplitude. Resonance curves are reported at successive times after conditioning. As expected, the material is softened by the large amplitude perturbation, but the effect is completely reversible and the resonance frequency slowly recovers its unperturbed value, i.e. the value assumed before conditioning.

The agreement between numerical and experimental data is quite good for both the undamaged and the damaged case. In Fig. 3.9, the resonance curves at three selected times (for both

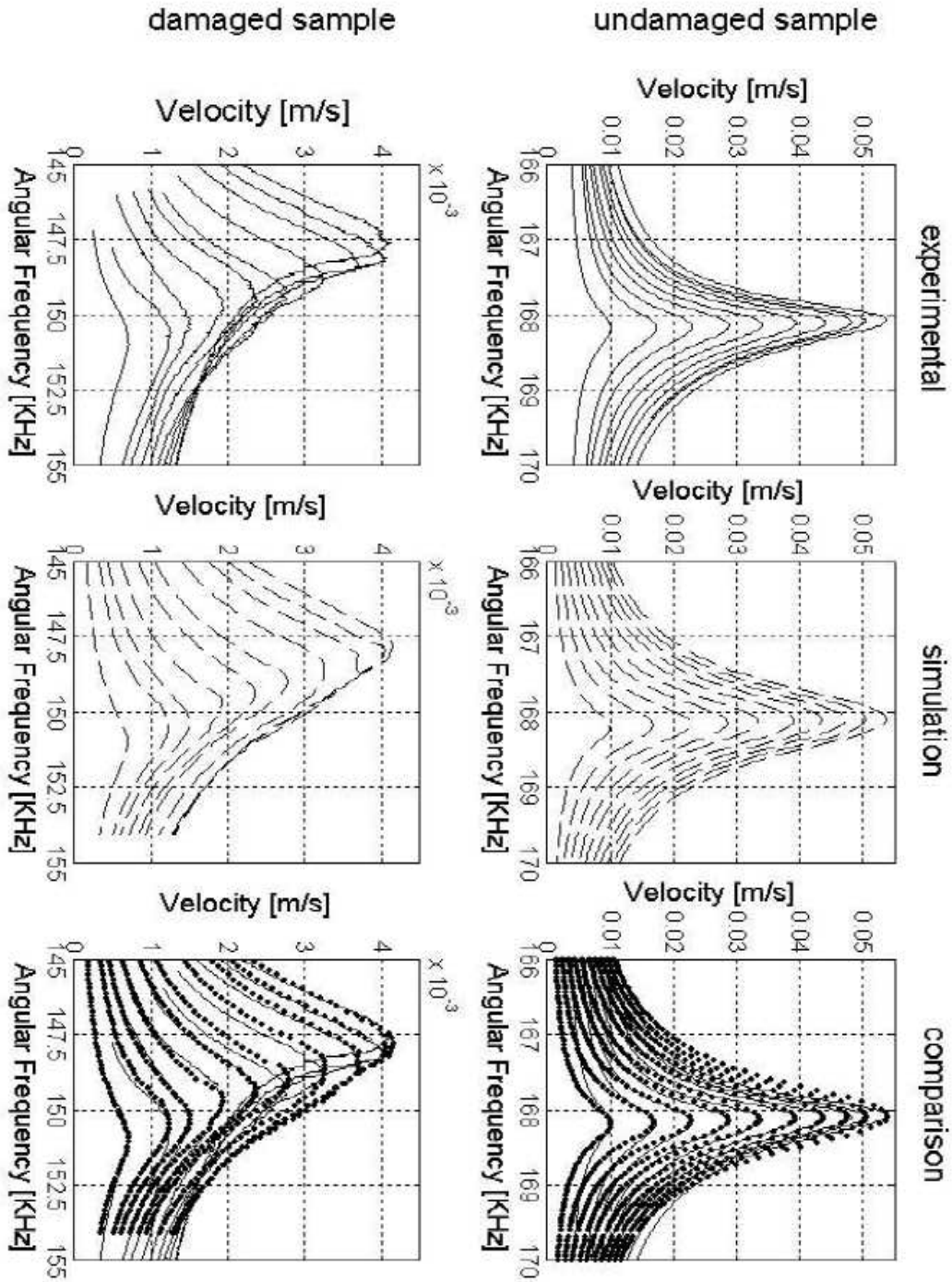


Figure 3.4: Experimental and simulated resonance curves for an undamaged (first row) and corresponding damaged (second row) sample at 10 different excitation amplitudes (from 10 mV to 100 mV). For better visualisation a comparison is presented superimposing, in the last column, experiments and simulation data for only one every two amplitudes.

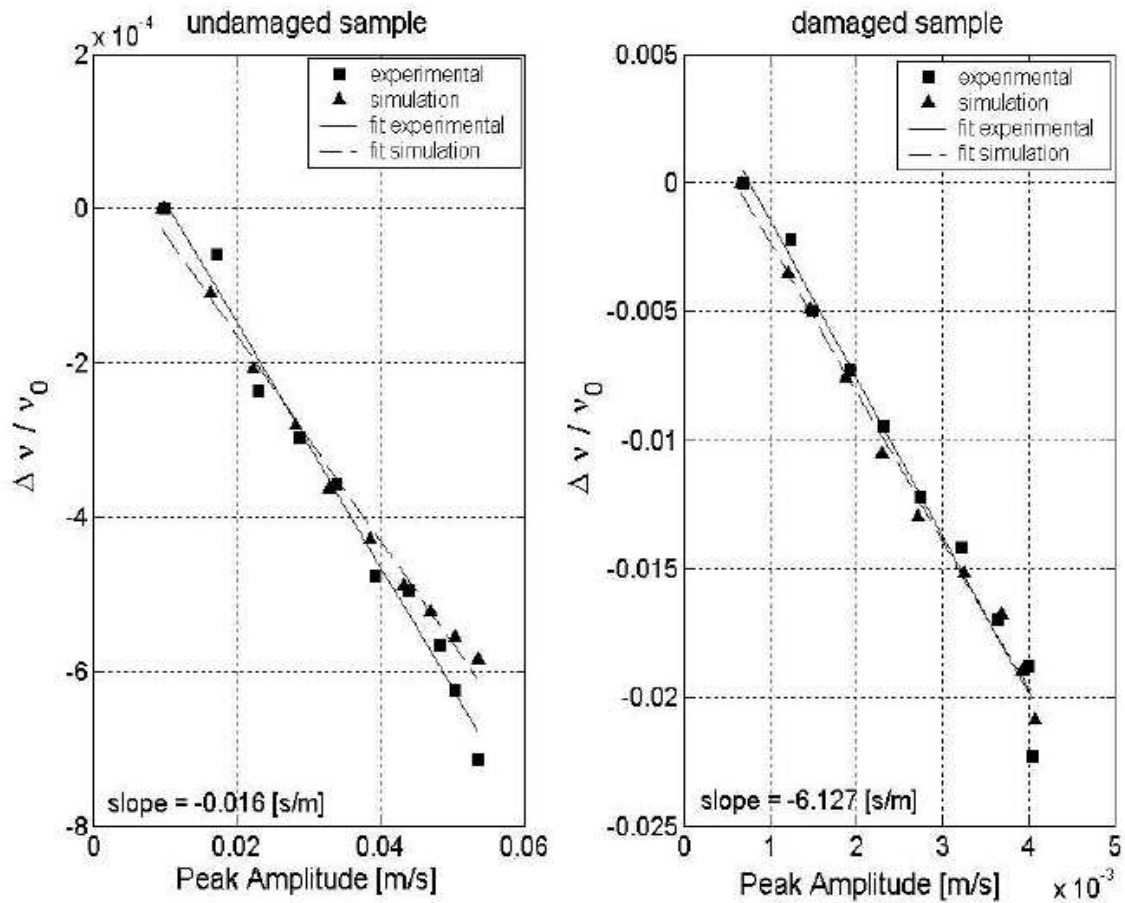


Figure 3.5: Relative resonance frequency shift as a function of the amplitude of the peak of the resonance curve, for each injected amplitude (see Fig. 3.4). Experimental (squares) and simulation (triangles) data are fitted by a straight line (with slope reported in the plot) for both the undamaged and damaged samples, in order to show the agreement with the typical nonclassical nonlinear elastic effect phenomenology.

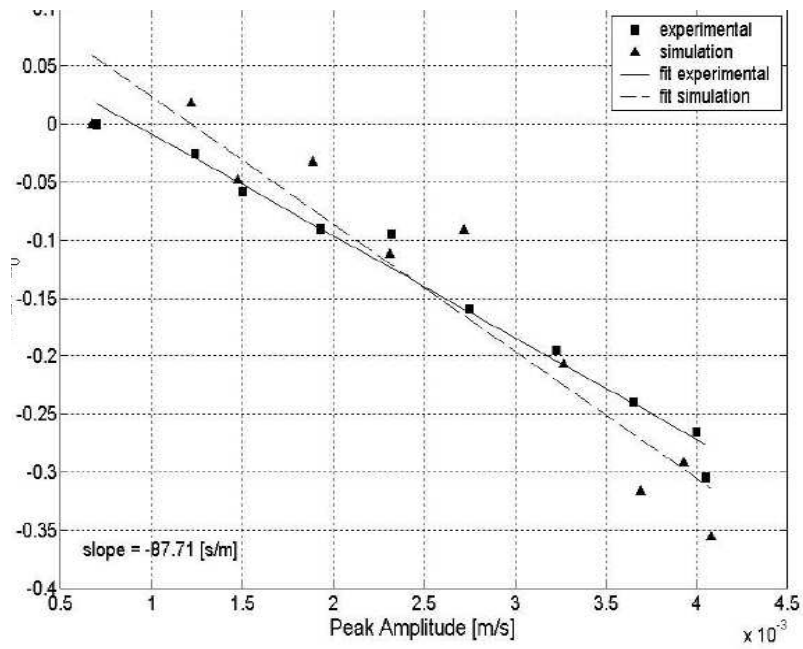


Figure 3.6: Q-factor change as a function of the peak amplitude. Experimental (squares) and simulation (triangles) data are fitted by a straight line (with slope reported in the plot) for the damaged sample.

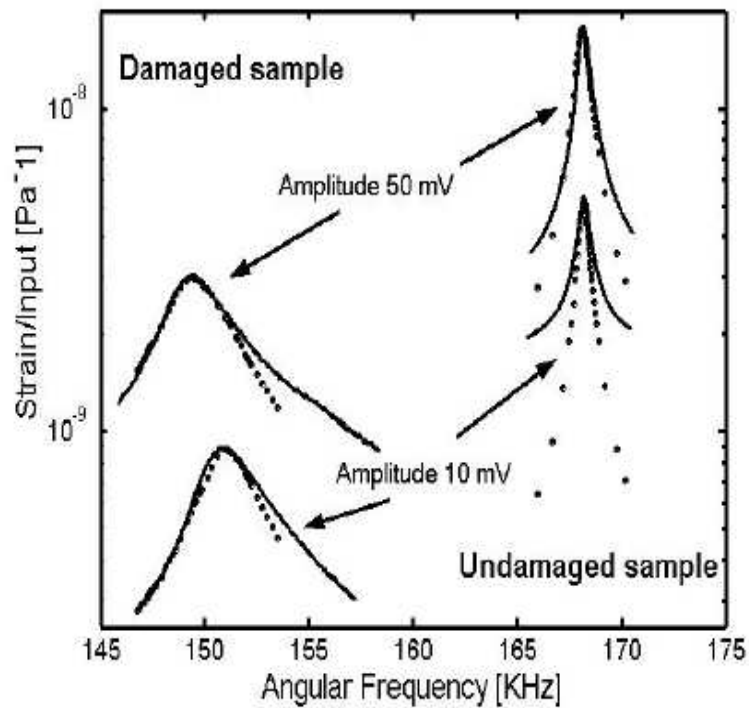


Figure 3.7: Strain vs. frequency curves for the damaged and undamaged samples at 10 *mV* and 50 *mV* excitation amplitudes.

intact and damaged samples) are reported. Simulations have captured well the recovery of the resonance frequency (which is well predicted at all times). Qualitatively the reduction of non-linear attenuation with increasing time has also been well reproduced by the model proposed, even though with some approximation, as already discussed about fast dynamics experiments. Qualitatively the behavior looks very similar for the undamaged and damaged case, due to the slight hysteretic nonlinearity generated by cracks which are already present in the undamaged concrete specimen.

Quantitatively, however, the effect is considerably more evident for the damaged case, as shown in Fig. 3.10, where the resonance frequency is plotted vs. time. The shift after conditioning increases from 0.02 % (about 30 Hz) to 0.7 % (about 1 KHz) and the recovery time from 5000 to 8000 s when damage is present. It is to be noted that the recovery, in both experiments and simulations, is logarithmic with time, as found in slow dynamics experiments on several other types of solid materials [16].

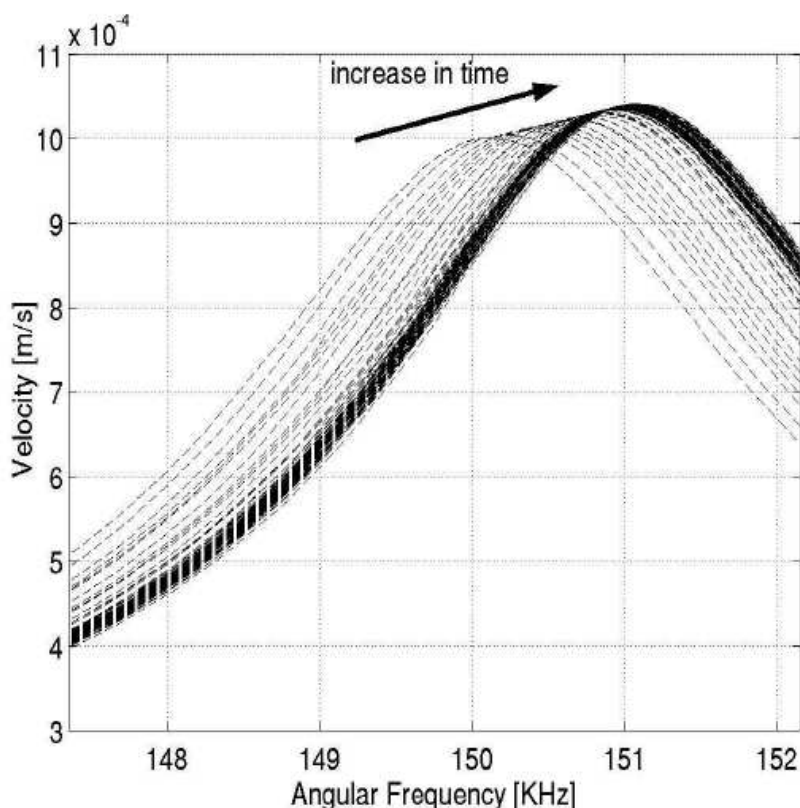


Figure 3.8: Resonance frequency curves (simulation) for the damaged sample during recovery after a large amplitude perturbation. The various curves have been obtained in successive time windows (the arrow indicates increasing time) during slow dynamics.

3.4.3 Comments on the experimental and simulation results

To sum up, Sections 3.4.1 and 3.4.2 show experimental results about resonance frequency measurements in concrete performed to compare the response of intact and damaged concrete specimens. Fast and slow dynamics typical effects have been recognized in the elastic response of damaged materials to external excitations and this fact is evidence of anomalous (hysteretic) elastic behavior. The LISA-Spring 1D model, used for performing corresponding numerical simulations of Young's first *eigenmode* excited vibration, has been showed with this work to

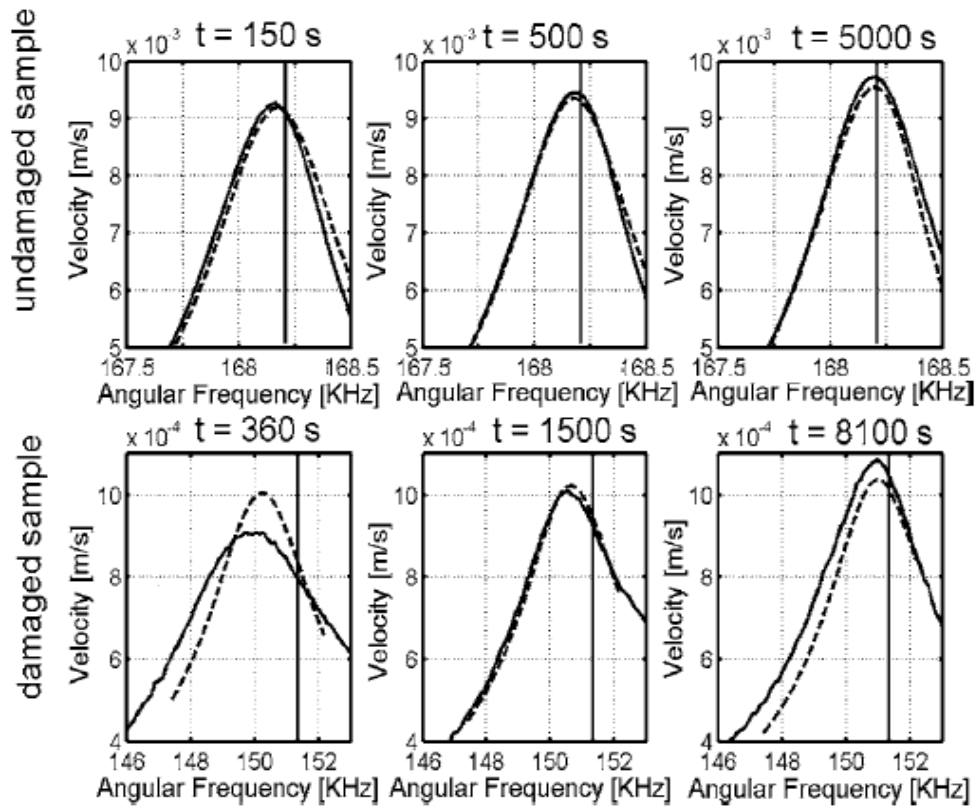


Figure 3.9: Experimental (solid line) and simulation (dash) resonance frequency curves at selected times during recovery for both intact (upper row) and damaged (lower row) samples.

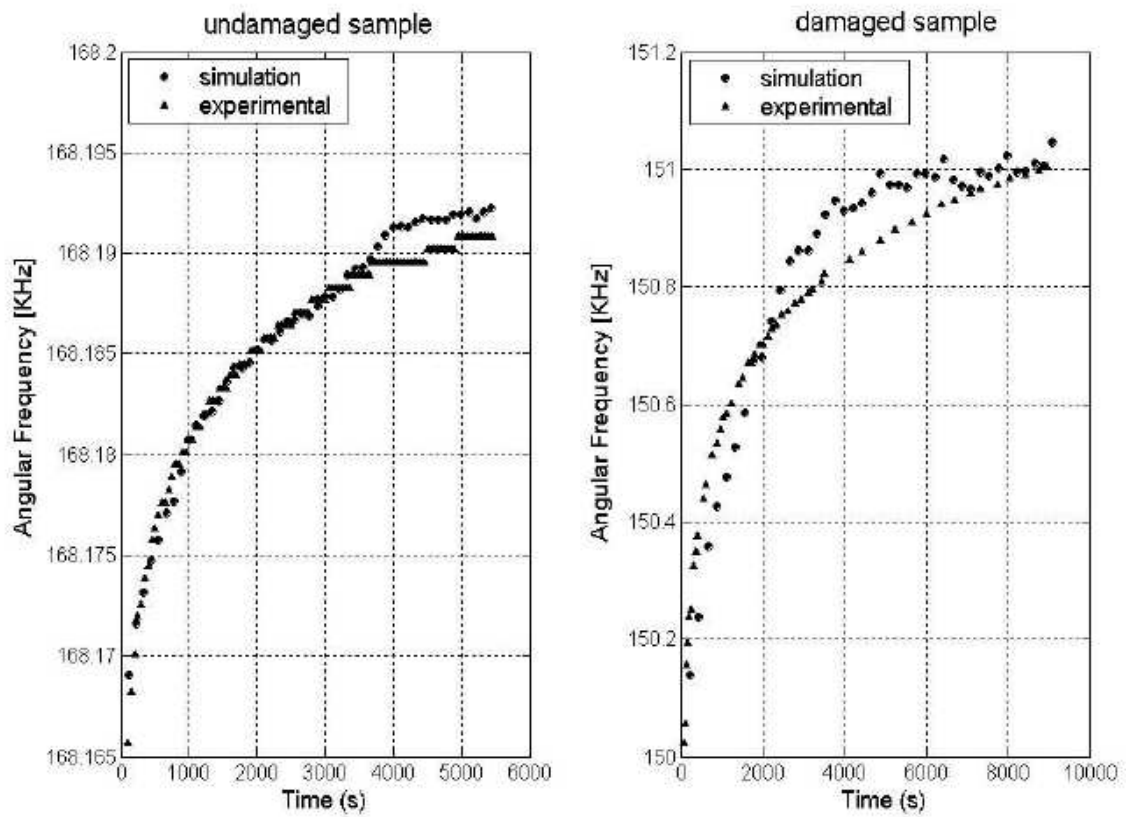


Figure 3.10: Resonance frequency vs. time during the recovery phase of the slow dynamics experiment. Simulation and experimental data are compared for both intact and damaged sample. Note the different scales on both x- and y-axes.

capture quantitatively the observed phenomenology, both in fast and slow dynamics experiments. Numerical results have been compared with experimental data, showing a reasonably good agreement. Improvements in the best fitting of experimental data could of course be obtained, in particular for what concerns the prediction relative to attenuation. However, a finer search in the parameter space becomes reasonable only once a direct connection of the model parameters with physical properties of the damaged zones is proposed and this was not the purpose of this investigation.

Experiments conducted at the INSA Lyon laboratories highlight the large sensitivity of the hysteretic nonlinearity to the presence of damage. Indeed, even though concrete presents hysteresis already in its intact state [73], these kinds of effects are much enhanced for damaged specimens. In particular, we have found a change of about 400 of the slope of the resonance frequency vs. amplitude curve when damage is present. Similar changes, albeit less huge, have also been found for the measured Q-factor. Likewise, the parameters characterising conditioning and slow dynamics (frequency drop and recovery time) are also hugely influenced by the presence of damage: about a factor 35 and 2 for the mentioned parameters.

As far as fast dynamics experiments are concerned, it should be noted that, at the lowest amplitude, a considerable change (about 10 %) of the resonance frequency may be observed in the damaged specimen (see Fig. 3.9). This result suggests good sensitivity of a linear measurement to the presence of damage. Nevertheless, it should be noted that a linear measurement of this kind implies a comparison with an “identical” reference specimen, which may not be easy to make available. For instance, small variations during the specimen production may well cause variations of the resonance frequency which might be taken as evidences of small damaging. An example is reported in Fig. 3.11, where the resonance frequency has been plotted vs. amplitude for two distinct intact concrete bars, which should indeed be identical. From Fig.3.11 it can be easily evinced that the low amplitude resonance frequency drops for the second specimen of about 0.8 %, while the slope of the curve vs. amplitude is mostly unaffected.

Experiments have also showed that slow dynamics measurements are easier to perform than fast dynamics ones, but are equally sensitive to the presence of damage. It follows that the drop of the resonance frequency due to conditioning may be a good indicator of damage, together with the recovery time, which however is more time consuming to measure.

From a theoretical point of view, it should be reminded that the LISA-Spring 1D model is only phenomenological. Nevertheless, if at this stage it does not include any physics, some hypotheses may be formulated from the approach adopted. In particular, about the role of conditioning, i.e. of small (fully reversible) changes of the microstructure when even small amplitude waves are injected in the specimen. Such modifications, corresponding in the model to a modification in the distribution of the initial states of the Hysteretic Elastic Elements composing the specimen, are reflected into a modification of the elastic properties of the material, since the two states of the HEE have a different effective elastic constant (for more details see [27]).

It follows that, in the model proposed, conditioning effects are also responsible of the anomalous fast dynamics effects, i.e. the resonance frequency at a given amplitude depends on the microstructure as it is “conditioned” at that forcing amplitude. Such hypotheses about the mechanisms at play seems to be confirmed by recent experimental data [15], which point out the impossibility to separate fast dynamics and conditioning in rock samples. Then, slow dynamics follows as a natural relaxation of the system, in which the original microstructure is recovered. Note that in this context recovering is intended as a recovery to an equivalent, rather than to the very same initial structure [77]. At the moment I am aware of only one alternative proposed mechanism [37, 38] able to account for slow dynamics.

Finally, it should be remarked that additional experimental studies have been performed by M. Bentahar and R. El Guerjouma [78], showing very similar effects in composite materials.

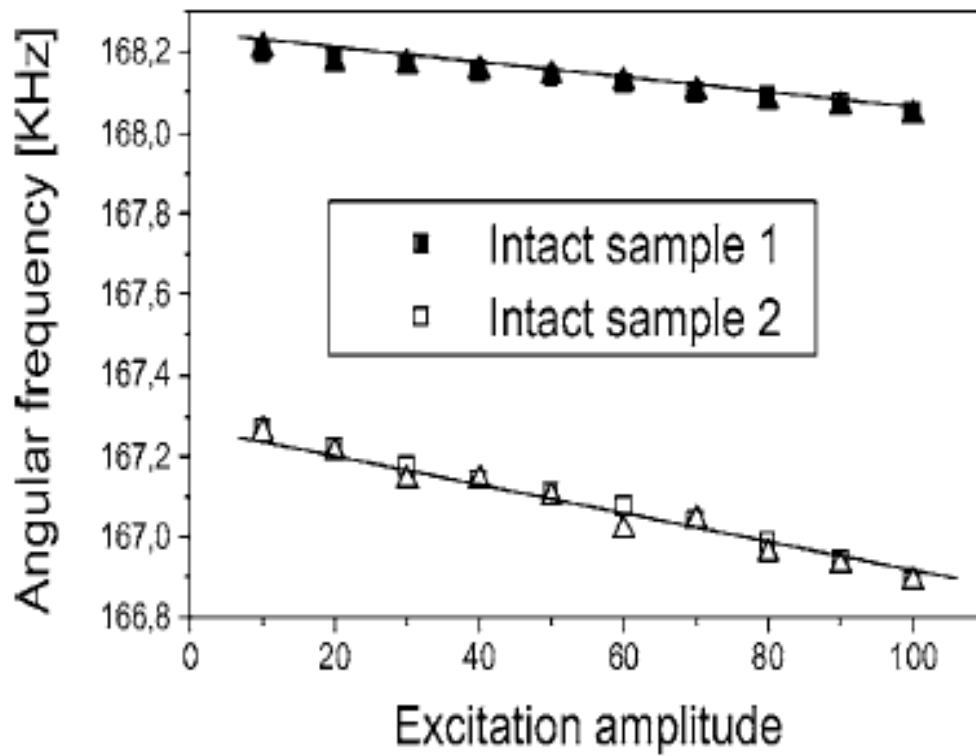


Figure 3.11: Resonance frequency vs input amplitude for two intact concrete specimens. Experimental (squares) and simulation (triangles) data are compared. For both specimen, a linear fitting is also reported.

At the same time, experimental studies have been conducting to link slow dynamics with the intensity of Acoustic Emission events during the processing of damaging of the specimen under investigation. Likewise, from a theoretical point of view, several applications of the LISA-Spring model have been proposed elsewhere, e.g. to validate from a qualitative point of view, the validity of the approach to capture other aspects of the observed phenomenology. Nevertheless, far more important from the physical point of view, is the progress towards a connection of the proposed approach with physical models [36, 79, 80].

Chapter 4

Time Reversal Elastic Wave Propagation for the localization and characterization of nonlinear scatterers in damaged materials

4.1 The Physics of Time Reversal Elastic Wave Propagation

4.1.1 Theoretical and historical considerations

Time reversal (TR) invariance is a fundamental symmetry that holds nearly everywhere in microscopic physics. In macroscopic physics it can be exploited with wavefield but not with macroscopic particles.

TR symmetry is substantially coded in the second Newton's law of motion for a body, due to the direct proportion between forces and acceleration, which is defined as the second ordinary time derivative of the displacement. Although Classical Mechanics laws are covariant under the transformation $t \rightarrow -t$, it is nearly impossible to observe its validity when considering the dynamics of macroscopic objects.

TR invariance implies the reversal of the motion of an object, which can be ascribed to a change in initial conditions of the motion itself. An illustrative *gedanken* experiment which can explain how difficult would be the realization of the time-reversed motion of a complicated systems as, e.g., a set of classical particles, interacting only with the Earth gravitational field, is presented in [81]. Consider a block of matter that undergoes an internal explosion during its motion in a static fluid. An experimental apparatus for producing its time-reversed motion will need a device interacting with the pieces of the object, scattered away from its center after the explosion, when they go through a closed surface surrounding the initial object. For each piece, the device should measure its arrival time on a region of the closed surface, its position of arrival and its velocity vector, so at least seven variables. Thereafter, that device, at appropriate time, should apply to each piece a velocity with the same module but opposite direction. Such a device would rely on its precision and ability to measure the cited seven variables. However, it is known that macroscopic physics, particularly the dynamics of sets of particles, is affected by the sensitivity to initial conditions so that any slight error in measurements or perturbation to the system leads to a significant change of the dynamics itself: many macroscopic systems follow a **nonlinear dynamics**. Regarding the *gedanken* experiment just described, a small perturbation in the reconstruction of the velocity vector field on the closed surface, for each piece, implies that the pieces still do not follow the same path with the reversed direction, so they do not reconstruct

the initial block (irreversible thermodynamics considerations have not been introduced so far in the treatment because the limitations due to chaos are sufficient in explaining why such an experiment could not be realized).

However, in linear wave physics, to the extent of adiabatic processes (so without changes of entropy of the medium considered for propagation), TR invariance holds and is, conceptually, comprehensible because the amount of information to describe and reconstruct a wavefield is limited in respect to the one needed for particle systems: the smallest scale of the wavefield fluctuations is of the order of the wavelength. The wave vector (three variables) is sufficient for reconstructing a simple wavefield. Wave propagation in media, for example elastic or electromagnetic wave propagation, is less sensitive to perturbations of initial conditions, so an ideal experiment as the one proposed above could be imagined as realizable, given the adequate technology.

TR invariance in elastic wave propagation has been experimentally verified and used for the realization of many applications since the 1990s, but from a theoretical point of view it has been known since ever due to the fact that the basic laws of Continuum Mechanics derive from Newton's ones. If we consider a linear elastic isotropic homogeneous infinite medium, without attenuation, the wave equation for the displacement vector field \vec{u} can be written as

$$\rho \cdot \frac{\partial^2 \vec{u}}{\partial t^2} = (\lambda + G) \cdot \vec{\nabla} (\vec{\nabla} \cdot \vec{u}) + G \cdot \Delta \vec{u} \quad (4.1)$$

where λ and G are the two Lamé constants and ρ is the volumetric mass density.

Considering simple harmonic plane wave propagation, as usual the displacement vector field \vec{u} can be considered as the sum of two vector fields, one (\vec{u}_P) irrotational ($\vec{\nabla} \times \vec{u}_P = \vec{0}$) and the other (\vec{u}_S) solenoidal ($\vec{\nabla} \cdot \vec{u}_S = 0$). These two components correspond to the compressional and shear waves which usually constitute a general wave in an isotropic medium. The corresponding two wave equations for the two displacement vector fields, \vec{u}_P and \vec{u}_S , as it can be derived from Eq. 4.1.1, can be written in the general form

$$\left(\Delta - \frac{1}{c^2} \cdot \frac{\partial^2}{\partial t^2} \right) \vec{u}_i = \vec{0} \quad (4.2)$$

where the index i can assume the values P or S and c is the wave propagation phase velocity, different for the two types of waves.

Eq. 4.1.1 is the typical D'Alembert wave equation without a source. The TR invariance of elastic wave propagation stems directly from the presence of the 2nd order partial time derivative operator. It should also be noticed that the presence of the Laplacian differential operator guarantees also the covariance of those eq.s under the transformation $\vec{r} \longrightarrow -\vec{r}$, a kind of **spatial reciprocity**.

From a physical point of view, TR invariance in elastic wave propagation means that it is theoretically possible to arrange for a backpropagation of waves towards their sources. Using a geometrical optics approach, TR invariance means that the waves can follow the same path in the reversed order.

This feature of elastic wave propagation is shared also by electromagnetic wave propagation. Historically, this invariance of the wave phenomena have been proved and exploited in different applications first in Optics since the 1980s. In Optics, monochromatic waves are usually used in experimental setups called phase-conjugation mirrors. Such devices actually produce time-reversed versions of the original source field, backpropagating light to its localized source. The time-reversed EM (Electro-Magnetic) field propagates in a manner reciprocal to the original field and focuses onto the original source even when the intervening path includes complicated and unknown aberrations, due to inhomogeneities of the index of refraction of the medium.

Optical phase-conjugation mirrors rely on nonlinear effects in the bulk of some medium in order to measure and to conjugate the phase information of a monochromatic wavefield [82, 83]. Information on the amplitude and phase distribution of the signal wave can be recorded during its nonlinear interaction with one or two pump waves. Measuring the phase and realizing a conjugate version of the original simple harmonic wavefield correspond to time reversal of the field itself. This mathematical equivalence between time-reversal of a broad-band field ($t \rightarrow -t$) and its phase conjugation can be seen with the help of Fourier transforms: if $f(\vec{r}, t)$ is a scalar wavefield and $F(\vec{r}, \omega)$ is its Fourier transform from the time domain to the frequency domain, the Fourier integral representation of $f(\vec{r}, t)$ shows that the TR transformation corresponds to take the complex conjugate of the corresponding Fourier transform: the Fourier transform of $f(\vec{r}, -t)$ is $F^*(\vec{r}, \omega)$.

In Optics, one of the most used techniques for realizing phase-conjugation, so back-propagation, of a simple harmonic EM wavefield is known as the four-wave mixing: three input monochromatic waves at the same frequency propagates in a medium with a cubic non-linearity. Two wavefields (with respective wavevectors \vec{k}_1 and \vec{k}_2) are counter-propagating ($\vec{k}_1 = -\vec{k}_2$) and used as pump waves, while the third one is the wavefield to be conjugated. Due to counterpropagation of the first two waves, the phase matching condition is satisfied at all incidence angles for the third wave, so the nonlinear mixing between the three waves gives as output a wave which is the phase conjugate version of the third input one.

During the 1990s, some principles of optical phase-conjugation were applied to elastic wave propagation, in order to realize ultrasonic phase-conjugation mirrors or phase-conjugation arrays, with the aim of focusing ultrasonic beams propagating in an aberrating media [84, 85, 86, 87].

However, the significant leap in validating and exploiting TR invariance in elastic wave propagation was realized by the group of M. Fink at the Laboratoire Ondes et Acoustique of the CNRS/ESPCI/Université de Paris VII *Denis Diderot* during 1990s. They developed a first theoretical description of an ideal experimental setup for realizing the focusing of elastic waves onto their sources by the propagation of their time-reversed versions. This theoretical treatment and analysis of a *gedanken* experiment is called the theory of the **Time Reversal Cavity** and is presented in Section 4.1.2 with some details because it contains the most important physical features of TR elastic wave propagation Physics. However, they also developed many different experimental setups both for studying other interesting features of these wave phenomena and for realizing devices that actually manage to focus elastic energy on spatial regions within a specimen. Section 4.1.3 present some of these pioneering techniques and devices.

4.1.2 Theory of the Time Reversal Cavity (TRC)

The **Time Reversal Cavity (TRC)** is an idealized setup for an experiment exploiting the Physics of TR elastic wave propagation in order to focus a wave packet on a specific target within a specimen, overcoming the problems connected with the distortion of wavefronts and the change in propagation direction due to inhomogeneities within the specimen. It was introduced by D. Cassereau and M. Fink in a seminal paper [88] which analyzes a *gedanken* experiment with such a setup and all the respective consequences from a theoretical point of view. The results of the developed theory are very important for understanding the basic features of TR elastic wave propagation, its potentialities and limits at the experimntal level.

Starting from the TR invariance of basic elastodynamics equations for lossless media, as presented in Section 4.1.1, it is straightforward that if it was possible to measure the wavefunction $\Psi(\vec{r}, t)$ ¹ in each point \vec{r} of a 3D volume surrounding the source of an elastic pulse, then it would

¹It may be a component of the displacement vector field or of the potential vector field through which the

be possible to generate the time-reversed version of such field, $\Psi(\vec{r}, -t)$, so it would be possible to realize the backpropagation of the original wave function towards the source. Although this is not possible, the Huygen's principle suggests that the reconstruction of $\Psi(\vec{r}, t)$ in a generic point \vec{r} of the volume can be realized by knowing its sources on a 2D surface. From this basic principle of wave interference theory, it derives the idea of a closed time-reversal cavity, an ideal experimental setup for backpropagating a wave towards its original source.

The TRC *gedanken* experiment is subdivided into two steps

During the first step, also called **forward propagation step**, an initial (for example) point-like source embedded in an inhomogeneous medium generates a wavefield $\Psi(\vec{r}, t)$ ² which propagates within the medium; an ideal closed surface surrounding both the source and the inhomogeneities (which are assumed to be bounded in a closed region too) is considered and it is assumed that at each point on this 2D surface the experimenter can measure the wavefield $\Psi(\vec{r}, t)$ and its normal partial directional derivative, $\frac{\partial \Psi}{\partial \vec{n}}(\vec{r}, t)$, where \vec{n} is the vector field normal to the closed surface in each of its points, directed outward. As an another ingredient of the ideal experiment, it is assumed that the closed surface and the measurement, which lasts in time for an interval of amplitude T , do not perturb the wave propagation, as they did not exist and the wavefield could propagate in an unbounded medium. It should be reminded that the considered inhomogeneous medium is lossless, otherwise, from a theoretical point of view, the TR invariance will not be a symmetry property of the elastodynamics wave equations for the type of Eq.s 4.1.1. In Section 4.1.4 the partial validity of TR elastic wave propagation also in weakly attenuative and nonlinear media is considered and treated.

The second step of the TRC experiment, also called the backward propagation step, considers the sudden removal of the original source of the elastic waves or its silencing (it remains passive). It is assumed to be possible to create secondary sources (monopole and dipole types) on the closed surface surrounding the cavity that exactly correspond to the time reversed versions of the recorded signals $\Psi(\vec{r}_c, t)$, where \vec{r}_c is a generic point of the closed surface. These sources act as new initial and boundary conditions for a wave propagation inside the cavity which should correspond to the backpropagation of the one occurred during the first step of the experiment. The theoretical treatment below shows that this is not completely exact and that other ingredients are needed in order to realize an actual TR elastic wave propagation. Although this need of new ingredients, the current described ideal setup leads to a partial backpropagation that focuses waves into the position of the spoint-like source of the forward propagation.

Many considerations can be realized at this point of analysis of the TRC ideal experiment:

- a TRC is not realizable experimentally, first of all because it is not possible to record the values of the wavefield Ψ in each point of a closed 2D surface, the real-world transducers have finite dimensions, so only a discrete set of such points could be considered for measurements; that means that spatial filtering (i.e. information loss about the wavefield) is unavoidable;
- also in the case of ideal point-like transducers, it is difficult to realize an experimental setup with transducers arranged on a closed surface surrounding the whole volume of propagation; only a small solid angle can be covered in respect of the center of the volume (see Section 4.1.3 for actual experimntal setups realized by the group of Fink *et al.*);
- experimentally, it is not possible to fix specific boundary and initial conditions in the emitting mode on a surface;

displacement vector field of a shear wave is defined or it can be the scalar potential field through which the displacement vector field of a compressional wave is defined.

²To be added, specifying the type of wavefield is considered here, from a physical and dimensional point of view

- acoustic/ultrasonic transducers, in receiving mode, can not measure simultaneously the wavefield and its normal partial derivative; the electrical signal they produce is usually a linear combination of both quantities, with relative weights that are specified in addition to the transducer;
- the TR wave propagation process requires a completely lossless medium, but, historically, experiments in biological tissues (which are very inhomogeneous and attenuative) showed that TR ultrasound waves focusing through backpropagation works well also in weakly attenuating media in the frequency range used;
- the TRC model is not realizable experimental but its theoretical study, as said previously, leads to the investigation of the theoretical potentialities and limits of TR elastic wave Physics;
- the TRC gedanken experiment could not be used for imaging purposes directly; reconstruction algorithms or numerical simulations of TR propagation must be used for imaging within the interior of the volume, as explained in Section 4.1.5.

In [88] the theoretical analysis of the TRC problem is presented through an extensive use of the Green's functions theory. This theoretical treatment is made for three different types of media enclosed in the volume: homogeneous, general inhomogeneous and weakly homogeneous. In what follows, the basic and most relevant results of such treatment are reported because they lead to understanding many TR wave Physics features.

The wave equation governing the forward propagation is of the type of Eq. 4.1.1, considering an isotropic elastic medium without attenuation. In [88], the wavefield Ψ is assumed to be the pressure field, in the case that the propagation occurs in a non viscous fluid and the inhomogeneities are solid immersed in the fluid. However, the same treatment here developed can be generalized to the case of an elastic isotropic solid with solid inhomogeneities. In this case, Ψ may be any component of the compressional or shear displacement vector field. For these reasons, the treatment here reported does not consider in detail the type of propagating wavefield Ψ .

$$\square_c \Psi(\vec{r}, t) = -\phi(t) \cdot \delta(\vec{r}) - \hat{A}(\vec{r}, t)(\Psi(\vec{r}, t)) \quad (4.3)$$

Eq. 4.3 is the wave equation for the forward propagation step of the experiment: \square_c is the D'Alembert differential operator with phase velocity c as defined in Eq. 4.1.1; $\phi(t)$ is the signal emitted by the point-like source positioned in the center of the Cartesian reference system; $\hat{A}(\vec{r}, t)$ is a functional operator which, applied to the wave function, describes the interactions of the propagating wavefield with the inhomogeneities, which act as secondary sources (i.e they do not input new energy in the medium), also called scatterers. For causality reasons, $\phi(t)$ is defined as followed:

$$\phi(t) = \begin{cases} 0 & \forall t < 0 \\ \phi(t) & \forall t \in [0, T_\phi] \\ 0 & \forall t > T_\phi \end{cases} \quad (4.4)$$

Due to the point-like nature of the source, it should be expected that the propagating wave is a spherical one. The Green's function of Eq. 4.3 is defined as

$$G_d(\vec{r}, \vec{r}_0, t) = \frac{1}{4\pi \cdot \|\vec{r} - \vec{r}_0\|} \cdot \delta\left(t - \frac{\|\vec{r} - \vec{r}_0\|}{c}\right) \quad (4.5)$$

assuming that the point-like source starts to emit at $t = 0$. Eq. 4.5 is the typical Green's function representing a diverging spherical Dirac's pulse.

Considering the whole volume V in which the forward propagation occurs, including both the primary and the secondary sources, the solution of Eq. 4.3 can be written as

$$\Psi(\vec{r}, t) = \int \int \int_V d\vec{r}_0 G_d(\vec{r}, \vec{r}_0, t) \ast_t [\phi(t)\delta(\vec{r}_0) + \hat{A}(\vec{r}_0, t)(\Psi(\vec{r}_0, t))] \quad (4.6)$$

where \ast_t is the symbol for the convolution operator over time. Eq. 4.6 shows that the wave function for the forward propagation is the sum of two components, the pulse emitted by the source and the wavelets generated by scattering:

$$\Psi(\vec{r}, t) = \frac{1}{4\pi \cdot \|\vec{r}\|} \cdot \phi\left(t - \frac{\|\vec{r}\|}{c}\right) + \int \int \int_V d\vec{r}_0 G_d(\vec{r}, \vec{r}_0, t) \ast_t \hat{A}(\vec{r}_0, t)(\Psi(\vec{r}_0, t)). \quad (4.7)$$

The recorded signals on each point \vec{r}_c of the closed surface S are defined as:

$$\Psi_{R_1}(t) = \Psi(\vec{r}_c, t) \cdot W(t) \quad (4.8)$$

$$\Psi_{R_2}(t) = \frac{\partial \Psi}{\partial \vec{n}}(\vec{r}_c, t) \cdot W(t) \quad (4.9)$$

where

$$W(t) = \begin{cases} 1 & \text{if } 0 \leq t \leq T \\ 0 & \text{otherwise} \end{cases} \quad (4.10)$$

is a windowing function introduced in order to represent a finite sampling of the wavefield on the surface. The hypothesis made previously is the possibility of recording both signals in each point of the surface S continuously.

After that, the second step of the experiment starts and the hypothetical secondary sources on the surface S are considered able to create in each of its points the exact time-reversed versions of the received signals during the first step, i.e.

$$\begin{cases} \sigma_1(\vec{r}_c, t) = \Psi(\vec{r}_c, T - t) \cdot W(T - t) \\ \sigma_2(\vec{r}_c, t) = \vec{n}(\vec{r}_c) \cdot \vec{\nabla} \Psi(\vec{r}_c, T - t) \cdot W(T - t) \end{cases} \quad (4.11)$$

According to the initial hypothesis about the experiment, the source of the first step is considered silent, passive or removed. The wave function of the backward propagation, Ψ_{tr} then will satisfy the wave equation

$$\square_c \Psi_{tr}(\vec{r}, t) = -\hat{A}(\vec{r})(\Psi_{tr}(\vec{r}, t)) \quad (4.12)$$

whose solution can be searched for using a special representation of $\Psi_{tr}(\vec{r}, t)$ through an adapted version of the Kirchhoff-Fresnel integral,

$$\Psi_{tr}(\vec{r}, t) = \int \int \int_V d\vec{r}_0 G_d(\vec{r}, \vec{r}_0, t) \ast_t \hat{A}(\vec{r}_0)(\Psi(\vec{r}_0, t)) + \int \int_S [G_d(\vec{r}, \vec{r}_0, t) \ast_t \sigma_2(\vec{r}_0, t) - \vec{n}(\vec{r}_0) \cdot \vec{\nabla} G_d(\vec{r}, \vec{r}_0, t)]. \quad (4.13)$$

In Eq. 4.13, the surface integral represents the pure Kirchhoff-Fresnel integral developed within the theory of wave interference. This surface integral can be transformed into a volume integral using the second Green's identity. Also with this transformation, Eq. 4.13 is not yet a self-consistent equation for the representation of the solution of Eq. 4.12, i.e. for $\Psi_{tr}(\vec{r}, t)$ and the final objective is finding such a solution and comparing it with $\Psi(\vec{r}, T - t)$ in order to check

for TR elastic wave propagation as a result of the TR invariance of the elastodynamic equations for lossless media.

However, Eq. 4.13, in the form with only volume integrals, can be used within Eq. 4.12. This implies computing the partial time derivatives of $\sigma_1(\vec{r}_c, t)$.

Due to the introduction of the time windowing function $W(t)$ (Eq. 4.10) in the definition of the received signals on the close surface during the forward propagation (see Eq. 4.9), it results that $\sigma_1(\vec{r}_c, t)$ and $\sigma_2(\vec{r}_c, t)$, as functions of time, have a singularity point in $t = T$. Then, the partial time derivative of $\sigma_1(\vec{r}_c, t)$ can only be done using the theory of distributions. The results of computing (omitted here for brevity but developed [88]) lead to

$$\frac{\partial^2 \sigma_1}{\partial t^2}(\vec{r}_c, t) = W(T - t) \cdot \frac{\partial^2 \Psi}{\partial t^2}(\vec{r}, T - t) + \varepsilon(\vec{r}) \cdot \dot{\delta}(t) - \eta(\vec{r}) \cdot \delta(t) \quad (4.14)$$

where

$$\begin{cases} \varepsilon(\vec{r}) &= \Psi(\vec{r}, t)|_{t=T} \\ \eta(\vec{r}) &= \frac{\partial \Psi}{\partial t}(\vec{r}, t)|_{t=T} \end{cases} \quad (4.15)$$

and $\dot{\delta}(t)$ is the time ordinary derivative of the Dirac's δ distribution. Using Eq. 4.15 and the fact that $\Psi(\vec{r}, T - t)$ satisfies the subsequent elastodynamics equation

$$\square_c \Psi(\vec{r}, T - t) = -\phi(T - t) \cdot \delta(\vec{r}) - \hat{A}(\vec{r})(\Psi(\vec{r}, T - t)) \quad (4.16)$$

it results that (see Appendix of [88])

$$\begin{aligned} \Psi_{tr}(\vec{r}, t) = & \frac{1}{4\pi \cdot \|\vec{r}\|} \cdot \phi(T - t - \frac{\|\vec{r}\|}{c}) \cdot W(T - t) - \\ & - \frac{1}{4\pi \cdot \|\vec{r}\|} \cdot \phi(T - t + \frac{\|\vec{r}\|}{c}) \cdot W(T - t + \frac{\|\vec{r}\|}{c}) + \\ & + W(T - t) \cdot \int \int \int_V d\vec{r}_0 G_c(\vec{r}, \vec{r}_0, t) \ast_t \hat{\vec{r}}_0 (\Psi(\vec{r}_0, T - t)) - \\ & - \int \int \int_V d\vec{r}_0 G_d(\vec{r}, \vec{r}_0, t) \ast_t \left[W(T - t) \cdot \hat{\vec{r}}_0 (\Psi(\vec{r}, T - t)) \right] + \\ & + \int \int \int_V d\vec{r}_0 G_d(\vec{r}, \vec{r}_0, t) \ast_t \hat{\vec{r}}_0 (\Psi_{tr}(\vec{r}_0, t)) + \\ & + \frac{1}{c^2} \cdot \int \int \int_V d\vec{r}_0 \frac{1}{4\pi \cdot \|\vec{r} - \vec{r}_0\|} \cdot \\ & \cdot \left[\eta(\vec{r}_0) \cdot \delta(t - \frac{\|\vec{r} - \vec{r}_0\|}{c}) - \varepsilon(\vec{r}_0) \cdot \delta(t - \frac{\|\vec{r} - \vec{r}_0\|}{c}) \right]. \end{aligned} \quad (4.17)$$

Eq. 4.17 is not yet a self-consistent representation for Ψ_{tr} but it is a good start point for obtaining it in different cases analyzed below. The focus remain to establish if $\Psi_{tr}(\vec{r}, t) = \Psi(\vec{r}, T - t)$ under the initially assumed conditions for the Time Reversal Cavity ideal experiment.

If the medium is completely homogeneous, without scattering inhomogeneities, then the functional operator $\hat{A}(\vec{r}) = \hat{O}$, i.e. the null operator. In this case, Eq. 4.17 assumes a self-consistent form:

$$\begin{aligned} \Psi_{tr}(\vec{r}, t) = & \frac{1}{4\pi \cdot \|\vec{r}\|} \cdot \phi\left(T - t - \frac{\|\vec{r}\|}{c}\right) \cdot W(T - t) - \\ & - \frac{1}{4\pi \cdot \|\vec{r}\|} \cdot \phi\left(T - t + \frac{\|\vec{r}\|}{c}\right) \cdot W\left(T - t + \frac{\|\vec{r}\|}{c}\right). \end{aligned} \quad (4.18)$$

If Eq. 4.18 is compared with the first right-hand-side term of Eq. 4.7, then it can be seen that the backpropagation wavefield is the superposition of two basic wavefields: one wave function represents an isotropic wave converging towards the position of the source of the forward propagation, $\vec{r} = \vec{O}$, with the same features of the forward propagated wave but reversed in time; the other wave function represents an isotropic wave diverging from the origin of the reference frame. Eq. 4.18 can also be written as

$$\begin{aligned} \Psi_{tr}(\vec{r}, t) = & G_d(\vec{r}, \vec{O}, T - t) \ast_t \phi(t) - \\ & - G_d(\vec{r}, \vec{O}, t) \ast_t \phi(T - t) \end{aligned} \quad (4.19)$$

while the wave function of the forward propagating field can be re-written as follows starting from Eq. 4.6,

$$\Psi(\vec{r}, t) = G_d(\vec{r}, \vec{O}, t) \ast_t \phi(t). \quad (4.20)$$

The comparison between Eqs. 4.20 and 4.19 makes more clear the differences between the two wave functions and leads to these conclusions on what happens, in the case of an homogeneous medium, during a TRC experiment:

- the setup of the TRC, although ideal, does not manage to realize the perfect time-reversed correspondent version of the propagation of a wave in the medium; the TR covariance of the elastodynamics equations is broken by some unfit boundary and/or initial condition;
- the backpropagated wavefield has a component which is the exact time-reversed version of the forward propagated wavefield, but it has also a second component diverging isotropically from the position of the source of the forward propagation wave; although the TR symmetry of the ideal experiment is not obtained, the experimental setup can focus waves back on the position of the source of the signals registered during the forward propagation.

Eq. 4.19 can also be written in a more compact form:

$$\Psi_{tr}(\vec{r}, t) = K(\vec{r}, t) \ast_t \phi(T - t) \quad (4.21)$$

where

$$K(\vec{r}, t) = \frac{1}{4\pi \cdot \|\vec{r}\|} \cdot \delta\left(t + \frac{\|\vec{r}\|}{c}\right) - \frac{1}{4\pi \cdot \|\vec{r}\|} \cdot \delta\left(t - \frac{\|\vec{r}\|}{c}\right) \quad (4.22)$$

is its kernel. The modulus of the Fourier transform of $\Psi_{tr}(\vec{r}, t)$ gives the minimum scale of fluctuations of the backpropagated wavefield:

$$|\tilde{\Psi}_{tr}(\vec{r}, \omega)| = 2\pi \cdot |\tilde{K}(\vec{r}, \omega)| \cdot |\tilde{\phi}(\omega)| \quad (4.23)$$

where the $\tilde{\cdot}$ symbol indicates the Fourier transform from the time to the frequency domain of the respective functions. Apart from the $|\tilde{\phi}(\omega)|$, which depends from the type of injected signal during the first step of the experiment, the plot of $|\tilde{K}(\vec{r}, \omega)|$ versus the normalized wavenumber,

$k \cdot \|\vec{r}\|$, of the generic harmonic component of the wavefield $\Psi_{tr}(\vec{r}, t)$ has the typical profile of a diffraction curve with a central peak interference fringe of half-width $\|\vec{r}\| = \frac{\lambda}{2}$. This value is the maximum resolution obtainable through the focusing of the backpropagated wave.

This result about the limit of resolution in focusing elastic waves through a TRC is coherent with the basic results of the classical diffraction theory. In Optics, this result is called the **diffraction limit of optical holography** [89].

The same type of results is obtained in the case of $\hat{A}(\vec{r}) \neq \hat{O}$, i.e. in the presence of inhomogeneities. In [88], a basic treatment has been proposed under the specific assumptions that the inhomogeneities come as spatial variations of the compressibility ($\chi = \chi(\vec{r})$) modulus and/or of the mass volumetric density ($\rho = \rho(\vec{r})$). In this case, the scattering operator $\hat{A}(\vec{r})$ assumes the expression

$$\hat{A}(\vec{r}) = \frac{1}{c^2} \cdot \gamma_\chi(\vec{r}) \cdot \frac{\partial^2}{\partial t^2} + \vec{\nabla} \cdot (\gamma_\rho(\vec{r}) \cdot \vec{\nabla}) \quad (4.24)$$

where $\gamma_\chi(\vec{r})$ and $\gamma_\rho(\vec{r})$ are the relative variations of the compressibility modulus and density, respectively, compared to the values of the corresponding homogeneous medium. It should be noted that in this case-study it still valid the assumptions made at the beginning of the treatment on the TRC experiment, that is all the inhomogeneities are enclosed by a volume contained in the volume V . Eq. 4.17, which is the general representation, yet not self-consistent, for $\Psi_{tr}(\vec{r}, t)$, can be used for the determination of a self-consistent equation for $\Psi_{tr}(\vec{r}, t)$ itself, although computing the volume integrals is quite complicated. The approach used in [88] leads to a final expression for Ψ_{tr} of the type

$$\Psi_{tr}(\vec{r}, t) = (h(\vec{r}, -t) - h(\vec{r}, t)) \ast_t \phi(T - t) \quad (4.25)$$

where $h(\vec{r}, t)$ is the Green's function of Eq. 4.3.

Eq. 4.25 still represents the wave function of the wave propagating during the second step of the experiment as the superposition of a converging isotropic wave towards the center of the reference frame (the position of the forward propagation source) and of a diverging isotropic wave from the center itself. $h(\vec{r}, -t)$ exactly corresponds to the time-reversed version of $h(\vec{r}, t)$, due to causality reasons, so during the first step of the TRC cavity experiment the effects of the diverging wave from the point-like source are received and observed before the effects of the scattering inhomogeneities acting as secondary sources; during the second step of the experiment, the experimenter may observe first the effects of the scattering by the inhomogeneities, then the converging waves may come out and focuses into \vec{O} . For causality reasons too, the second term of Eq. 4.25 due to $h(\vec{r}, t)$ is null as long as the impulse spherical wave has not perfectly converged into the initial source position, thus generating a singularity in \vec{O} for the reconstructed wavefield. Then, the first term of Eq. 4.25 vanishes and only the second one exists, regenerating the same diverging propagation observed during the first part of the experiment. The onset of the second wavefront immediately after the end of the first, in the second step, avoids the singularity of the resulting wavefield in \vec{O} . Considering the term $h(\vec{r}, -t) - h(\vec{r}, t)$, it can be seen that the two associated wavefronts are completely separated in time, except in the neighborhood of \vec{O} .

From a theoretical point of view, it should be noticed that, having considered a lossless medium, the wavefield $\Psi(\vec{r}, t)$ attenuates with time but should never vanish. Experimentally, one could record the signal during the forward propagation only on a finite time interval of amplitude T . As it results from the theoretical treatment, T plays an important role as a parameter of the ideal experiment: referring to Eq. 4.15, the time window of recording during the forward propagation must be chosen such that $\varepsilon(\vec{r})$ and $\eta(\vec{r})$ are as small as possible,

because they act in the wave equations as perturbing terms in respect of the usual form of these equations. Considering inhomogeneous media, the choice of a useful value of T depends on the medium features: for example, weakly inhomogeneous media produce negligible effects from multiple scattering, while in the case of strong inhomogeneities the temporal duration of signals during forward propagation may be very large due to multiple scattering.

The importance of T for the focusing of time-reversed back-propagating waves on the source position of the forward propagation has been verified in real experiments described in Section 4.1.3 below. T plays a fundamental role also in computational TR elastic wave imaging as it is reported in Section 4.2. The physical reasons of its relevance are discussed briefly in Section 4.1.3 too. At this point, it is worth noting that the individuation of this aspect, which is shown below to be one of the most critical in realizing real-world TR elastic wave propagation experiments and consequent applications, is a first relevant result of the theoretical analysis of the TRC problem.

Another important result of the theory of the TRC developed by Cassereau and Fink in [88] is the evidence that the initial hypotheses of the TRC *gedanken* experiment are not sufficient for obtaining a correct TR elastic wave propagation. The theory of the TRC suggests immediately why such a TR symmetry break occurs.

The symmetry break happens during the second step of the ideal experiment, near the focus region, due to the creation of the diverging isotropic wave from $\vec{r}=\vec{0}$. A complete TR backward propagation should consist of only a wave converging into the position of the source of the first step. The reason why this fact does not occur, in the theoretical treatment but also in real experiments and simulations too, is quite easily understandable from a physical point of view but also from a mathematical point of view.

From a mathematical point of view, if the flow of argumentations previously reported is analyzed in details, it becomes clear that Eq. 4.12 is the correct wave equation for the propagation during the second step of the experiment, according to all hypotheses done about the experiment setup, particularly according to the assumption of a removed or passive source in $\vec{r}=\vec{0}$, but the correct time-reversed wavefield $\Psi_{tr}(\vec{r}, t)$ corresponding to $\Psi(\vec{r}, t)$ can not obey to that equation, it obeys to an equation like Eq. 4.16. That means that during the second step of the experiment, in order not to break TR symmetry, in the position $\vec{r}=\vec{0}$ a signal $\phi(T - t)$ must be injected.

In fact, from an experimental point of view, the conditions for realizing a TR wave propagation must include a time-reversed version of the source acting during the forward propagation. If this artificial time-reversed source is introduced in the setup of the experiment, the TR symmetry is not broken because it acts as an **acoustic sink**. The concept of an acoustic sink explains, from a thermodynamical point of view, why TR symmetry is not broken: the energy injected in $\vec{r}=\vec{0}$ during the first step of the TRC experiment is likely absorbed in the same position during the second step. In [90] de Rosny and Fink reports a simple mathematical treatment showing that, assuming $\phi(t) = A \cdot e^{-i\omega t}$ and considering a longitudinal wave propagation case as a particular one, if the solution to Eq. 4.16 in the homogeneous case is searched for, then it yields a wavefield which is exactly the time-reversed version of the forward propagation one. In the case of an inhomogeneous medium or a more complicated type of wave propagation, the calculations are more complicated but still lead to the same results. More important, de Rosny and Fink shows in [90] the results of an experiment, described below in Section 4.1.3, in which an acoustic sink is implemented and the focusing, on the position of the initial source, of the back-propagated waves is not affected by the effects of diffraction, i.e. the creation of the diverging wave. They also managed to show, with that experiment, a fascinating physical effect deriving from the TR symmetry by the use of an acoustic sink: the resolution of the focused back-propagated waves was of the order of one fourteenth of the smallest wavelength, i.e. less

than the limits imposed by the theory of diffraction.

The fact that the assumptions about the setup of the TRC experiment are not sufficient, as formulated, for realizing theoretically a TR elastic wave propagation experiment could come out as soon as they are formulated. However, their formulation, as proposed in [91], is fully understandable and reasonable taking into account the main interest in TR elastic wave propagation Physics, i.e. focusing waves not in a position known in advance (as in the case of the TRC case, the initial source position) but in unknown regions within a specimen where scatterers are placed. A scatterer, if illuminated by a pulse or quasi-monochromatic wave, acts as a secondary source. The back-scattered waves can be considered the only signals of interest: if they are collected and re-injected, time-reversed, in the medium, they would back-propagate focusing on its source, the scatterer. Focusing waves on scattering leads (and has led, as briefly showed in Sections 4.1.3, 4.2 and 4.3) to many possible applications in imaging techniques based on elastic wave propagation (mainly in the ultrasound frequency band but not only), in characterization of secondary sources within a specimen or in concentrating elastic energy in certain parts of a specimen, e.g. in bio-tissues for therapeutic objectives.

The TRC problem has been instrumental in developing parts of the basic theory of **Time-Reversed Acoustics**, also known as **TRA**, (or **Time-Reversed Elastic Wave Propagation**) and has suggested the existence of many phenomena of TR wave Physics then observed and characterized experimentally and exploited for applications.

4.1.3 Time Reversal Elastic Wave Propagation Experiments

Time Reversal Mirrors (TRMs)

As underlined in Section 4.1.2, the TRC setup, as described, does not let realize a complete TR elastic wave propagation experiment (TR symmetry is broken by the absence of the time-reversed version of the forward propagation source acting during the backward propagation step) but is sufficient for obtaining focusing of elastic energy on the position of the source. In this setup the source is a primary one. However, the same results of the theoretical treatment of Section 4.1.2 apply in the case the source is a secondary one, that is a scatterer within a specimen illuminated by a propagating wave. Focusing back the scattered waves on the scatterer position (or the scatterer itself in real experiments) is an important results for many application purposes.

It was a specific application, in the field of medical therapy, that first led the group of Fink *et al.* to realize experimental setups able to focus back-scattered waves on the scatterers themselves exploiting TR wave Physics[92, 91, 93]. These setups were called **Time Reversal Mirrors (TRMs)** and have been used both for the investigation of the TR linear wave Physics and for implementing different kinds of applications, first of all the destruction of kidney stones in the bio-medical field of lithotripsy[93].

The first experiments with TRMs suggested a number of questions and issues to be addressed at the theoretical level, so the TRC theory was developed. However, in the reverse order, a TRM can be considered the natural experimental implementation of a TRC considering all the limitations of a TRC setup as cited in Section 4.1.2.

TRMs have not been the only technological solutions for the realization of experiments on TR elastic wave propagation. As reported in Section 4.1.1, many ideas about TR wave Physics were first developed in Optics, with the idea of **Phase Conjugated Mirrors (PCMs)**. Many temptatives have been done for exporting the same approaches and techniques from TR electro-magnetic wave propagation into TR elastic one. They are essentially based on the idea of exploiting classical nonlinear effects and wave mixing for the phase conjugation of quasi monochromatic waves or on the use of delay lines. However, they have been used only in specific cases, while TRMs have demonstrated a wider range of applicability, first of all because they work with broad band elastic pulses.

A TRM consists in an array of transducers that can function both in transmit and receive modes and that have a linear transfer function. Each transducer is connected to a dedicated electronic measurement chain made by (in sequence) an amplifier, an Analog-to-Digital Converter (ADC), a storing memory and finally a programmable transmitter. The transmitter is then connected, along another line, to a DAC (Digital-to-Analog) device which feeds another amplifier connected to the same transducer. The programmable transmitter can be driven by a waveform generator controlled by a computer.

A typical TRM experiment consists in two steps: receiving an elastic wavefield on the array surface, sampling the wavefield on each transducer (functioning in a receive-mode) on a finite time interval of amplitude T , recording the signal in each TR channel memory; then, by the use of the programmable transmitter, produce a time-reversed version of the stored signal and re-emit it through the transducer, acting now as an emitter. This two-step procedure is executed for each TR channel simultaneously. The wavefield received by the transducer array during the first step may be a back-scattered wavefield emitted by a scatterer after being illuminated by a primary wavefield generated by the array itself (or a small part of it) or it may be a wavefield emitted by an active source. This second case corresponds to the TRC setup and it has been the less implemented one, while the first case is the typical one for a TRM experiment.

The first experimental studies with TRMs have been dedicated to the focusing of elastic waves through an inhomogeneous medium on a reflective target that behaves as an elastic source after being insonified. TRMs have progressively taken advantage of piezoelectric transducers features, first of all both transmit and receive capabilities, linearity in the response function and the possibility of instantaneous measurements of pressure (stress) or velocity waveforms. They have been usually arranged as 1D linear array or according to more complicated patterns on 2D surfaces.

The limitations of TRMs can be summarized in the following list of features:

- diffraction effects, due to the finite dimensions of each transducer, act as a low-pass filter on the spatial frequency spectrum of the emitted or back-propagated wavefields; it means that the image of a point is actually a spot with typical dimensions depending upon the central wavelength λ_{centr} of the wavefield;
- as reported in Section 4.1.2, it is very difficult to realize a 2D surface surrounding a region as much as possible; the transducers are usually arranged on plane or weakly curved 2D surfaces; it means that they have a *finite aperture* as “elastic mirrors” and this feature implies a point-spread function whose width is related to the angular aperture of the mirror observed from its focal point;
- grating lobes are produced by the finite dimensions of the transducers and by their separations; the array pitch must be reduced of the order of $\frac{\lambda_{centr}}{2}$ for reducing the side lobes;
- secondary grating lobes can be avoided by using a time period between two sampling greater than $\frac{T_{centr}}{8}$, where T_{centr} is the central period of the wavefield;
- in the case of propagation within a weak inhomogeneous medium, the procedure satisfies the conditions under which the first Born approximation can be assumed valid in the mathematical description of the scattering processes, so for each inhomogeneous region a single scattering process can be considered to occur; in this case, the TRM is able to compensate exactly for the wavefront distortion whatever the position of the aberrator in respect of the elastic beam; however, in the case of presence of strong inhomogeneities, multiple scattering processes may occur, it is then necessary to measure the wavefield

during the first step of the experiment for a very long time interval, in order to take into account the multiple scattered waves that decay slowly; when multiple scattering is present, the scattered field is radiated along all directions and the TRM can not measure the complete information needed to realize a procedure as close as possible to a complete TR.

TRMs are said to realize optimal focusing through inhomogeneous media in the sense that they are able to provide input to the transducer emitters that maximize the pressure/stress (in liquid or in solid respectively) wavefield at the target location, during the second step of their use. This feature has been extensively studied from a theoretical point of view by Fink et al. in [91] showing that, from a mathematical point of view, a TRM experiment realizes the spatio-temporal matched-filter to the inhomogeneous Green's function of the medium containing the array and the scatterers.

Beyond this definition of optimal focusing, which makes reference to the theory of matched-filter in Signal Processing [94], many experiments were conducted during the 1990s in order to investigate the properties of the TRMs in focusing elastic waves (mainly acoustic and ultrasound ones) propagating in inhomogeneous media [93, 95]. The first important results from these studies are summarized in the list below.

1. TRM focusing is **self-adaptive** and automatically accomplishes **compensation for geometrical distortions of the transducer array**. A basic experiment, described in [93], was conducted using a transducer array made of 64 elements arranged on a weakly curved 2D surface in order to obtain a prefocused cylindrical elastic mirror. Each transducer was rectangular, 0.5 mm wide and 10 mm high. The array pitch was fixed to be 0.6 mm. The transducers were placed on cylindrical backing of 80 mm radius curvature. The resultant total aperture of this elastic mirror is thus equal to 40 mm and the natural (i.e. in the absence of any aberrating medium) focal length is 80 mm. Due to the curvature of the surface, this TRM setup suffers of geometrical distortion. A needle point hydrophone was used both as a passive scatterer and as an active source or as a movable receiver. All the apparatus was immersed in water. The TRM experiment was conducted in two different ways. In the first case, the hydrophone was positioned 40 mm away from the array surface and 10 mm off the central axis, far away from the natural focal point. It was used first as an emitter. The received signals were time-reversed and re-emitted, using as a receiver the needle hydrophone fixed in the same position of emission. The time-reversed signal of each transducer was emitted independently (in time) from the other ones. It resulted that all the time-reversed wavefields, in the hydrophone position, reached their maximum values at the same time after their initial re-emission. This was a first demonstration of compensation of the distortion due to transducers with different inclinations. In the second case, the same experiment was conducted with the simultaneous re-emission of all the time-reversed signals, now moving the hydrophone in receive mode along a line on the plane at 40 mm from the array surface. The directivity pattern, in the form of a plot of the temporal maximum of the wavefield versus the distance from the central axis, confirmed that constructive interference was maximized in the original position of the hydrophone when it acted as source.
2. A TRM is able to compensate for distortion induced by an inhomogeneous layer. This feature was probed with an experiment, described in [93], very similar to the previous one but with the addition of a silicon prism with weak parabolic curvature and variable thickness in the lateral direction (maximum thickness about 15 mm). Two cases were investigated. In the first configuration, the aberrating silicon layer was positioned at 40 mm from the TRM weakly parabolic transducer array, while the needle hydrophone was

used as a mobile receiver scanning along a line in the focal plane (at 80 mm far from the array). The transducers acted as emitters and injected into water identical short pulses. The resulting focusing point was showed to be displaced of 4 mm from the array central axis, on which lies the natural focal point. This focal point displacement was due to the silicon layer with variable thickness. In the second configuration for the experiment, a classical TRM procedure was implemented, with the hydrophone acting as a passive point-like scatterer placed in the natural focal point of the mirror. It was illuminated by the transducer array, the back-scattered signals were processed according to the TR techniques and re-emitted. During the re-emission stage, the hydrophone was used as a movable receiver scanning along a line the focal plane. The resulting directivity pattern showed that the time-reversed waves focused on the natural focal point although they crossed the aberrating silicon layer. The TR procedure compensates for the refraction effects on the back-scattered waves.

3. A TRM is able to compensate for aberrating effects due to an inhomogeneous layer placed at different distances from the transducer array. This is an important property of TRM experiments: an aberrating layer (a rubber layer with randomly modulated thickness, in the example of the configuration described in [93]), placed at different distances from the array, refracts in different ways an emitted beam. If it is positioned very close to the array, the elastic beam is widely spread and on the average, it corresponds to the beam produced by a smaller transmitting aperture with a dimension equal to the coherence length of the random profile. If the layer is far from the array, the beam intercepts a smaller area of the aberrator so the beam spreading is reduced. This is what was probed with the first part of one experiment described in [93]: the transducer array, this time, was arranged as a 1D-like plane array with 128 elements, each 10 mm high and 0.6 mm wide, with an array pitch of 0.75 mm and a central working frequency ν of 3.5 MHz. Actually, during the first part of the experiment, only 64 elements of 128 were used, located in the middle of the array, corresponding to a 48 mm maximum aperture mirror. These 64 transducers transmitted synchronous identical pulses while the needle hydrophone scanned over a line of the focal plane in receive mode. This procedure was repeated four times, each with a different distance of the rubber layer from the plane array (0, 27, 47 and 67 mm). The focal point resulted to be displaced 9.75 mm over the natural focal point of the mirror. The directivity patterns along the scanning line for the maximum-in-time pressure wavefield showed that side lobes and peak width diminished in correspondence to a larger distance of aberrator from the array. The second part of the experiment was dedicated to the usual TR procedure as described for the other experiments. The relevant result was that the directivity profiles for the focusing time-reversed waves did not change with the distance of layer, the peaks were all placed 9.75 mm over the natural focal point in the focal plane and the peak widths were comparable. The TR focusing managed to compensate for the different beam refraction due to the different positions of the aberrator.
4. A TRM mirror can selectively focus elastic waves onto a scatterer with the highest reflectivity within a set of different scatterers, if the propagation medium do not contain too many scatterers or if inhomogeneities are not too much distributed. The experimental configuration for reaching such a result is essentially the typical one for a TRM, the protocol differs only in the fact that the TR procedure is iterated many times. In [93], the authors report the results of an experiment with the same TRM setup discussed at the point above (a quasi 1D plane array). Two metallic wires of different materials and diameters were placed on a plane 110 mm far from the array plane, directed along the transducers length axis. The first wire was placed 13 mm above the central axis of the array, while the second one 7 mm below it. The first one was a brass wire with 0.7 mm di-

ameter while the second one a copper wire 1.5 mm diameter. These wires acted as passive scatterers, the needle hydrophone was used as a mobile receiver and scanned the plane of the wires along line for obtaining the directivity profile of the maximum-in-time pressure time-reversed wavefield. The graphs in [93] show that two peaks are localized at distances from the central array axis equal to the ones of the wires, although they did not stand in the natural focal plane of the mirror. At the second time-reversed back-propagation, the peak corresponding to the wire with smaller diameter reaches a smaller value and so on with the number of iterations of the TR process. Physically, this is clearly understandable: the wire with lower reflectivity produces a weaker back-scattered wave and this happens at each reflection. With increasing numbers of iterations, the TR process focuses on that wire even more less elastic energy. This special protocol of operation is called the **Iterative Time Reversal Mirror (ITRM)**. It has been experimentally and theoretically studied extensively [96, 97, 95, 98], also for its important role in applications. For example, a ITRM protocol has been used in model experiments for lithotripsy, in order to probe its exploitation for the localization of kidney stones with higher reflectivity in the presence of an aberrating medium interposed between the stones location and the array (for simulating the complicated structure of media the kidney stone are embedded in for real-world cases, i.e. biological tissues) [93, 99].

All these preliminary experiments were aimed at investigating the basic physical properties of TRMs and their limits in retro-focusing elastic pulses travelling through inhomogeneous regions. One of the common features of these experiments is that the TRM and the target scatterer (the point needle hydrophone) were immersed in water and the refracting media were placed in between the two. The water was chosen as the “matrix” medium in order to reduce the impedance mismatch with the inhomogeneous specimens acting as aberrating media. Another common feature is the free lateral boundary conditions for the region of propagation.

In what follows, three other types of experiments with TRMs are described, all of them realized between 1990s and 2000s by researchers of the group of M. Fink at the Laboratoire Ondes et Acoustique of the CNRS/ESPCI/Université de Paris VII. The presentation of these experiments capture relevant features of TR elastic wave propagation in lossless media and let address topical issues of TR linear wave Physics.

The first two experiments have in common some characteristics of the experimental setup: a point-like ultrasonic transducer is placed in front of a 1D plane TRM array; the elements of the TRM are of the same type of the source transducer; the source emits a quasi isotropic wave packet (2-3 cycles of a sine wave with frequency equal to 3.5 MHz). The emitted pulse is very short in time (about 1 μ s). Like in the previously described experiments, a medium with a certain geometry is inter-posed between the source and the TRM. The wave packet travels through the medium, reaches the TRM, made of up to 128 elements. Each TRM element (channel) has its own amplifier, an 8 bit ADC working at 20 MHz sampling rate and storage memory. After time-reversal of the digitized signals, the backward emission is performed through a 8 bit DAC followed by a linear power amplifier. The resolution of the TRM can be estimated by using the following formula derived by the classical theory of diffraction:

$$R_{es} = \lambda_{centr} \cdot \frac{z}{a} \quad (4.26)$$

where λ_{centr} is the central wavelength of the backpropagated waveform, z is the distance between the source of the forward propagation and the array, finally a is the length of the 1D plane TRM array, where $a = N_{trsd} \cdot a_{trsd} + (N_{trsd} - 1) \cdot a_{pitch}$ with N_{trsd} the total number of TRM elements, a_{trsd} the linear dimension of a single transducer and a_{pitch} the array pitch. It should be noted that Eq. 4.26 is the resolution of the TRM in such configuration in the absence of any inhomogeneous medium or boundary condition in between the single source and the TRM itself,

i.e. in the case of propagation in water (the entire experimental apparatus is still immersed in water).

The first two experiments show that the resolution of the TRM can be increased in the presence of an intermediate highly disordered random scattering medium (first experiment) or in the case of reflecting lateral boundary conditions (second experiment), as if the mirror aperture was enlarged. The first result to be underlined is that introducing an intermediate inhomogeneous medium and/or lateral reflecting boundary conditions in the typical experimental setup of a TRM not only does not reduce its focusing capabilities but, on the contrary, does enhance them exploiting physical processes that are typical of linear wave propagation.

The third experiment was conducted by Fink et al. with a different setup, about elastic wave propagation occurring in a bounded finite solid medium. The results of that experiment are still more surprising in demonstrating robustness and special features of TR elastic wave propagation phenomena.

TR elastic wave propagation through random scattering media: the pseudo-lens effect

The basic experimental setup is schematized in Figure 4.1 below: the ultrasonic wide-band transducer S transmits a sine-wave pulse of frequency 3.5 MHz that propagates through a layer of lateral thickness $L = 45$ mm. This layer is a set of randomly distributed parallel steel rods, each of which with diameter 0.8 mm. The average spacing between two rods is 3.6 mm, the total number of rods used is about 900 and the total area covered is $150 \cdot 75\text{mm}^2$. Each transducer has a linear size $a_{trsd} = 387\mu\text{m}$, the array pitch $a_{pitch} = 417\mu\text{m}$ and the distance between the array and the source S $z = 180$ mm. The TRM is made of 96 such transducers.

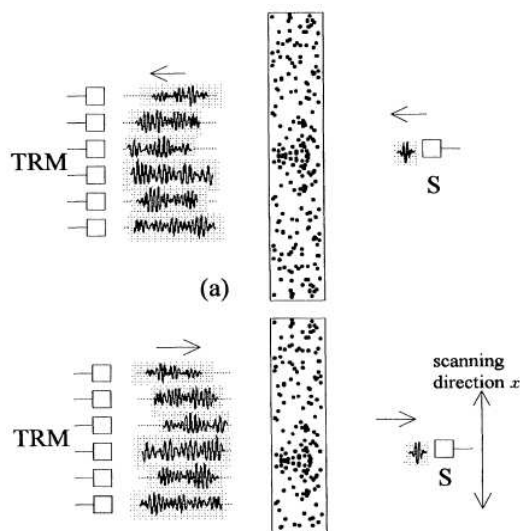


Figure 4.1: Setup of the experiment described in [100] about the TR elastic wave focusing through a multiply scattering highly disordered medium. Figure taken from [100], Fig. 1 page 4207

The steel rods behave as linear elastic media ($c_P = 5.9\text{mm}/\mu\text{s}$, $c_S = 3.2\text{mm}/\mu\text{s}$, $\rho = 7.85\text{g}/\text{cm}^3$) and as scatterers. A small part of the wave packet crosses the disordered layer with a weakly distorted wavefront and impacts firstly the TRM array (**ballistic wavefront**), while the greatest part of the emitted wave packet undergoes multiple scattering inside the layer. As

a result, a bunch of incoherent waves emerges from the random scattering layer over a long time interval. Each TRM transducer records a signal $s_j(t)$, with j being the identification index of the transducer, during a time window of amplitude $T = 80\mu s$. Figure 4.2 shows an example of such a signal, the one received at transducer # 46: apart from a narrow pulse at initial times, maybe due to the ballistic wavefront, the wave form consists in a series of small amplitude pulses at random times for a long time interval, about $120\mu s$, due to the interactions of the different wavefield emerging from the layer at different times, at random, after multiply scattering. Figure 4.3 presents a B-scan³ image of the wave forms incident on the TRM array both in the case without the random scattering layer and with it: in the first case, a), it should be noted only a spherical wavefront due to the point-like nature of the emitting transducer S , while in the second case, b), the same spherical wavefront is followed by a random pattern of signals.

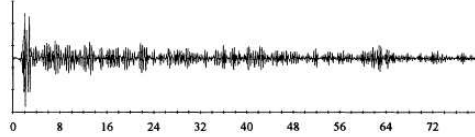


Figure 4.2: Wave form received on one of the transducers of the TRM, the element # 46. The signal is the superposition of an initial pulse (due to the ballistic wavefront) with a noise-like signal, due to the multi-scattering inside the disordered medium. Figure taken from [100], Fig. 3a page 4208.

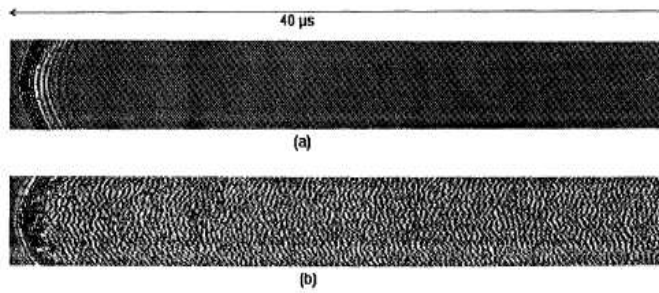


Figure 4.3: B-scans of the pressure field received on the TRM during the forward propagation in two different cases, a) without the aberrating layer, b) with the layer inserted. Figure taken from [100], Fig. 2 page 4208.

A fundamental parameter of the setup of such an experiment with a highly disordered and multiply scattering aberrating medium interposed between the source and the TRM is the mean free path l [101]. It is defined as the coherence radiation energy decay length: when a wave undergoes multiple scattering as it goes through a slab of thickness L the transmitted intensity is composed by two parts, a coherent term which corresponds to the remainder of the incident wave and an incoherent term due to multiple scattering, as cited above. In many cases, the intensity transmission coefficient T_I is found to be dependent from the slab thickness according to an exponential decay law, $T_I = e^{-\frac{L}{l}}$. As a consequence, if the ratio $\frac{L}{l}$ is large enough, almost all the incident energy of the wave is transferred to the multiply scattering process and its transport across the aberrating layer may be better described as a diffusion process, which is

³A B-scan is obtained collecting time series in different positions along a line, in this case along the TRM transducer array. Each signal $s_j(t)$ can be considered a set of values of a 2D spatio-temporal scalar field sampled in a specific space position x_j , corresponding in this case to the central point of the transducer j along the x -axis, directed along the array longitudinal axis, see Fig. 4.1.

a irreversible thermodynamic process. However, if $\frac{l}{\lambda}$ is not too large, a small amount of coherent radiation energy is transported out of the slab, resulting in a ballistic wavefront as shown in Fig. 4.3. In case such this experiment, l can be estimated by measuring $T_I(L)$ varying L and fitting data according to the exponential law. For the experiment reported in [100] it resulted $l = 9 \pm 0.5$ mm. Obviously, what determines a complete multiply scattering regime of energy transport or a partial one is the wavelength of the incident radiation.

The received and stored signals on the TRM were time-reversed using two different time windows, with the same amplitude equal to $80\mu s$: over an overall interval of $120\mu s$, the first and the last $80\mu s$ of the wavefield emerging from the aberrating layer were used for the TR process, in order to include or not the ballistic component of the wavefield itself.

In both cases, the time-reversed signals were re-emitted and the a B-scan was conducted along a line parallel to the TRM array longitudinal axis in the position of the initial source S , so the set of data $S(x_i, t)$ were recorded (x_i is the position of the transducer that acted as the source S during the forward propagation phase of the experiment along such new x -axis; $x_i = 0$ for the original position of S ; this B-scan-mode signal recovery was performed repeating many times the TR wave propagation from the TRM). Figure 4.4 shows the signal $S(0, t)$ recorded in the position of the original source S : inset b) refers to the TR of the first $80\mu s$ of the signals received on the TRM, inset c) to the last $80\mu s$ and d) one to the case without the random scattering layer. The relevant result is that in both three cases the signal in S original position has the same features of the emitted one during the forward propagation, in particular it is very narrow in time, about some μs , comparable with the $1\mu s$ duration of the original source signal. A finer comparison of the inset d) with the other two shows that the reconstruction in time of the original S signal seems better with the presence of the aberrating layer than without it. This analysis underlines one relevant feature of TRMs and TR elastic wave propagation: although the TR symmetry is broken because a TRM is not a TR cavity and the time-reversed version of the forward propagation source signal is not injected during the backward propagation, as shown in Section 4.1.2, a TRM can reconstruct an emitted signal with a high degree of **temporal compression** despite the propagation occurs through a strongly scattering medium.

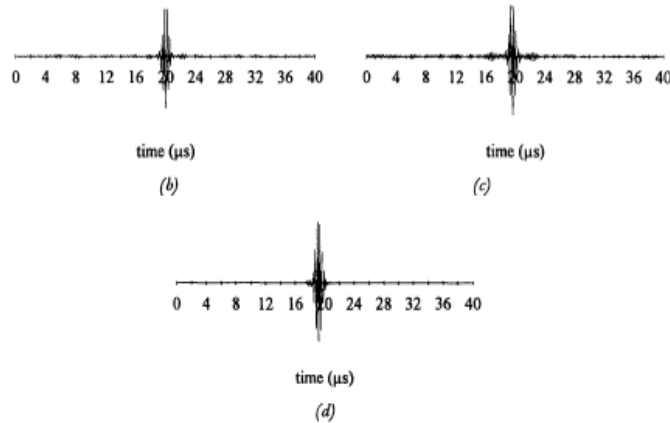


Figure 4.4: Signal received in the position of the forward propagation source S after TR back-propagation. Inset (b) and (c) show the same signal obtained with two different TR time windows (the first and last $80\mu s$ of the received signals on the TRM have been recorded and time-reversed respectively), while (d) one shows the same signal but in the case of absence of the aberrating layer. Figure taken from [100], Fig. 3 page 4208

The set of signals obtained with the B-scan during the backward propagation step of the experiment, $S(x_i, t)$, let the authors of [100] calculate and plot the directivity profile of the TRM along a line on the plane of the forward propagation source, i.e. $S(x_i) = \max_t S(x_i, t)$. Figure 4.5 is the plot of such a function, with the 0 corresponding to the original position of the source S . This plot shows the second relevant property of TRMs: the **spatial focusing** of the TRM improves with the presence of the multiply scattering layer (thick line) in respect of propagation in a homogenous medium as water (dashed line). According to Eq. 4.26, the theoretical resolution of the TRM, without the aberrating layer, would be $R_{es} \simeq 0.994$ mm, which has to be compared with the half width at half maximum of the directivity profile. It can be seen from Fig. 4.5 that the actual resolution of the TRM is about 1.2 mm, but it increases with the presence of the random scattering layer, about 0.6 mm. A similar result is showed by Fig. 5, page 4209, in Ref. [100], which refers to the same type of experiment conducted with a larger number of steel rods, about 2000. Increasing the multiply scattering within the slab implies an increase in the duration of the signals received on the TRM and their incoherence. However, the focusing during backpropagation seems to improve, a counter-intuitive result: the highly disordered scattering medium acts as a kind of “lens” for the time-reversed backpropagated waves.

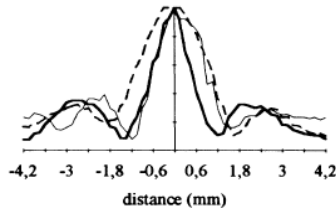


Figure 4.5: Directivity profile of the TRM apparatus along a line on the plane of the forward propagation source, obtained in the case of absence of the multiply scattering medium (propagation in pure water, dashed line), with the presence of the aberrating layer made of steel rods (thick line) and in the presence of another aberrating layer made with glass spheres. The reference point along that line has been fixed in the original position of the source S . Figure taken from [100], Fig. 4 page 4209.

TR elastic wave propagation in waveguides

Figure 4.6 shows the experimental setup of an experiment of TR elastic wave propagation in a waveguide, described in Ref. [102]. The TRM has similar features of the one described in the previous part and used with the highly disordered multiply scattering medium. Instead of interposing an aberrating layer between the point-like source S and the TRM 96 elements array, the space between the two was limited by two interfaces, one water-air, the other one water-steel. The distance between the source S and the TRM plane was fixed to be $L = 740$ mm. The source S was positioned at the mid vertical distance between the top water-air interface and the bottom water-steel one (20 mm from both interfaces). The system was considered invariant along the z -axis (see Fig. 4.6). The depth of the waveguide was fixed as $H = 40$ mm. The experiment followed the typical protocol: the source S emitted a sine-wave short pulse with central frequency about 3 MHz. The propagated wavefield was recorded by the TRM over a long time window ($T = 100\mu s$), time-reversed and emitted many times in order to let two types of measurements (the reconstructed signal in the position of the forward propagation source S and the directivity profile on a line centered on that position and lying on the source plane).

Figures 4.7 and 4.8 let to describe some features of the forward propagation of the experiment: the wavefield was composed by a cylindrical wave propagating directly towards the TRM and

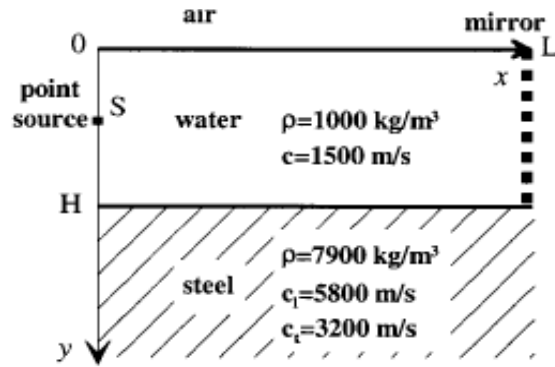


Figure 4.6: Experimental setup of TR in a ultrasonic waveguide: a TRM with the similar properties of the one illustrated in Fig. 4.1 is opposed to a point-like source S consisting in one transducer of the type used for the TRM itself; the TRM has 96 channels; the distance L between source and TRM plane is 740 mm, while the vertical length of the mirror is $H = 40$ mm. The propagating medium is water, bounded along the y -axis by reflecting interfaced (top, water-air - bottom, water-steel). The medium is considered invariant along the out-of-plane (z -axis) direction, as infinitely extended therein. The source S is positioned at $(0, 20)$ according to the frame of reference on the $x - y$ plane. This Figure has been taken from [81], Fig. 7 page 1951.

by a set of wavelets generated by reflections at the two interfaces (the wavefield emitted by S was a spherical one). Figure 4.8 shows the signal received at one single transducer of the TRM: it spreaded over a long time interval and was made by many different narrow pulses received at different time steps, with amplitudes decreasing with the time of arrival at the TRM plane. These pulses were generated by the iterated reflections at the two interfaces, just like many similar pulses hit the TRM of the experiment with the multiply scattering layer previously described. The difference in this case is that the arrival times of the different pulses could be calculated knowing the geometry of the waveguide, while in the previous one they were random. In Figure 4.7, the B-scan-like plot shows at early times the wavefront of the cylindrical direct wave, while at later times the different reflected wavelets arriving at the TRM channels.

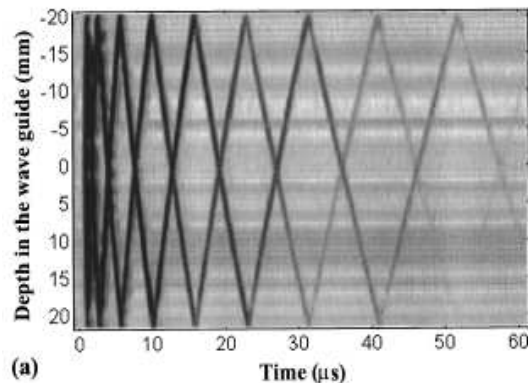


Figure 4.7: B-scan-like plot of the different signals received on the TRM during the forward propagation phase of the experiment. Figure taken from [102], Fig. 2a page 1812.

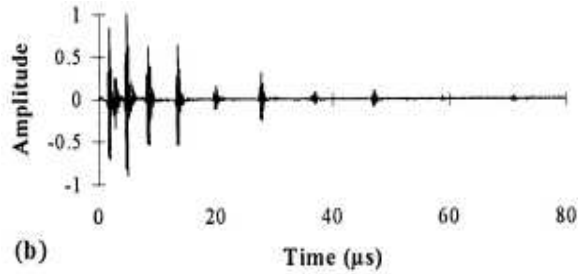


Figure 4.8: Signal recorded in one element of the TRM during the forward propagation. Figure taken from [102], Fig. 2b page 1812.

The TR process was performed as in the previously described experiment and the same type of measurements were performed. Figure 4.9, inset (a) shows the backpropagated (pressure) wavefield measured at different times along a line passing through the position of the source S , while the inset (b) shows the wavefield in the position of S itself. Although the multiple reflections, the TRM has been able to focus back the waves onto the source position, recreating a signal in S which had the same features of the emitted one (a narrow-in-time sine-wave pulse, lasting some μs). Also in this case, the TRM compensated for the geometric limitations to wave propagation: the reflecting boundaries transformed spatial information, which could have been obtained with TR transducer in a TRC, into temporal one, in the form of different pulses hitting the TRM array at different times according to the paths they followed.

The spatial focusing ability of such a configuration for a TRM was also probed calculating the directivity profile of the pressure wavefield measured along the same line of the B-scan in Fig. 4.9 (a). Also in this case, the limitations to isotropic wave propagation did not affect the spatial focusing capabilities of the apparatus but increased them, as demonstrated by the comparison of the directivity profile of this experiment with the one in open space and water (Fig. 4.10). The effective resolution of the TRM, calculated as the half width at half maximum of the directivity profile, was greatly enhanced. In [102] it is shown that this effective resolution increased taking longer TR recording windows during the forward propagation. This is in agreement with the idea of spatial information converted in temporal one. Using a small value for T , the amplitude of the TR windows, implies receiving less pulses due to multiple reflections, i.e. parts of the propagated wavefield are wiped out and they can not contribute to the time-reversed backpropagation and retro-focusing. An effective increased resolution of the mirror is equivalent to an effective mirror aperture greater than the real one. In [102] a description of this effect is presented using the theory of mirror images in a medium bounded by two mirrors (the two reflecting interfaces of this experiment), derived from Geometric Optics: for an observer located in S (see Fig. 4.6) the TRM can be considered as a periodic array along the y -axis; each pulse received by the TRM and generated by multiple reflections corresponds to one virtual image of the TRM array displaced along the y -axis. From a theoretical point of view, this means that if the TR recording window lets receiving a pulse generated by ten reflections (the first ten echoes are received) then the effective TRM aperture is nine times larger than the actual one, because the first received pulse is the one directly propagated from S to the mirror without reflections (ray path orthogonal to the TRM plane). In practice, this proportion is not exactly respected for a multiply reflected pulse impacting the TRM has an amplitude which decreases with the number of reflections undergone.

This experiment confirmed the temporal compression and spatial focusing capabilities of a TRM also in restricted geometric conditions for wave propagation. Elastic wave propagation

in a waveguide is a useful model for describing real-world wave propagation in several situations and contexts of interest for applications, from Non Destructive Evaluation of materials to acoustic wave propagation in shallow water in the ocean. The investigation of TR elastic wave propagation in a waveguide has suggested many other investigations in similar conditions for solving problems of interest, for example in acoustic communication in oceanic environments [103, 104, 105, 106].

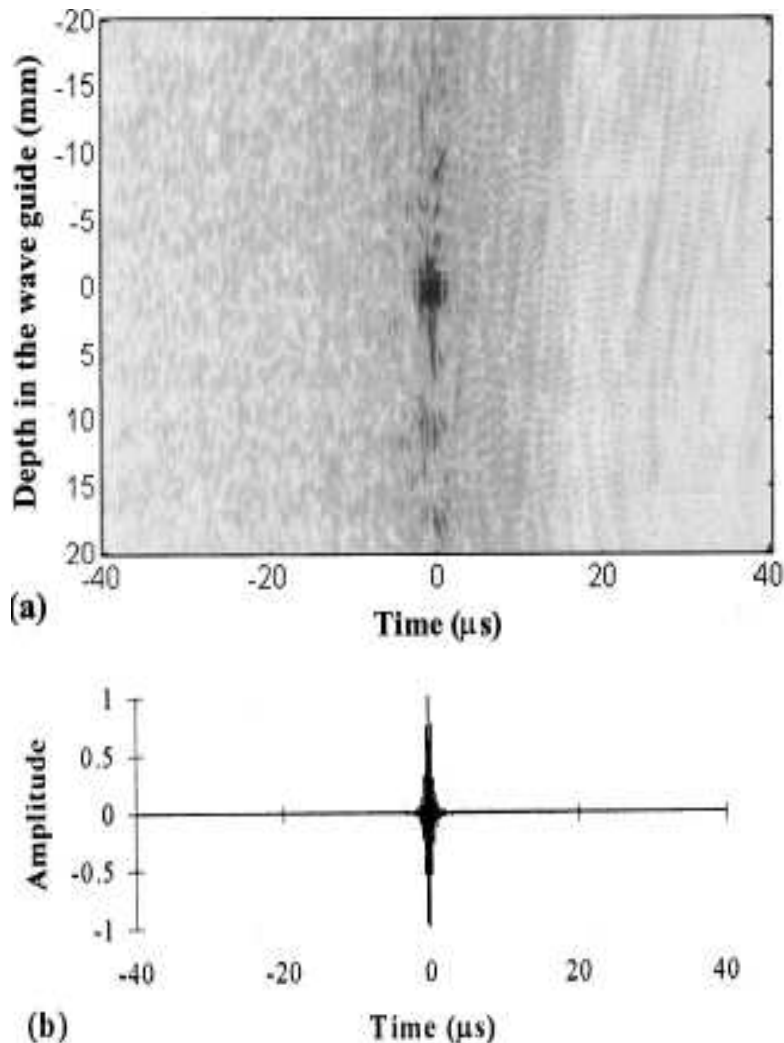


Figure 4.9: Reconstruction of the forward propagation source signal in S . Inset (a) shows a B-scan image obtained along a line in the plane of the source position, moving the transducer acting as a receiver. Inset (b) shows the temporal signal in the position of the source. Figure taken from [102], Fig. 3 page 1812

TR elastic chaotic cavities

The third relevant type of TR elastic wave propagation experiment was conducted within a monocrystalline silicon wafer with a shape of a circular disk having one segment cut off. Figure 4.11 shows the experimental setup used by Draeger and Fink. The disks used in the experiment

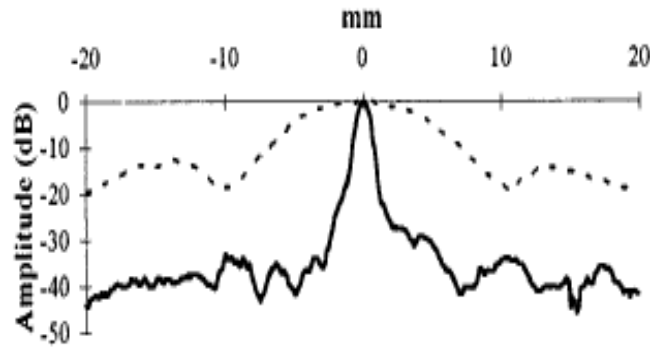


Figure 4.10: Directivity profile calculated from the B-scan of the time-reversed backpropagated pressure wavefield on a line passing through the position of the forward propagation source S , assumed to be the 0 of the corresponding axis. Figure taken from [102], Fig. 5 page 1813

had a thickness of $525\mu\text{m}$, a diameter between 100 and 125 mm. The monocrystalline silicon material was chosen for its weak attenuation (decay periods of the order of 10 to 20 ms). Two aluminum cones were attached to two respective transversal transducer, each of which connected to a TR electronic channel as usual. Each was posed in gently contact with the surface of the disk. The shape of the cut disk was chosen because it was demonstrated mathematically that classical particles moving within such a cavity with perfectly reflecting boundaries have a non-periodic dynamics, that is they move according to a chaotic regime [107]. Chaos guarantees ergodicity for such a classical “billiard” and this result can be used also for the description of the rays dynamics of elastic wave reverberating inside the cavity. Ergodicity guarantees that multiple reflected wavelets explore all points of the cavity boundaries.

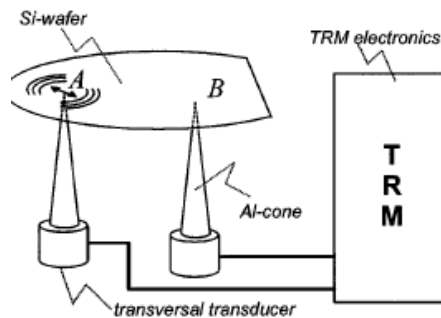


Figure 4.11: Setup for an experiment of TR elastic wave resonance within a closed cavity with reflecting boundaries and chaotic ray dynamics. A is the point of injection of a wave disturbance within the cavity. This waves propagates and after some time multiple reflections excite some eigenmodes of vibration of the cavity itself (resonance conditions). The reverberating wavefield is measured in point B over a long time interval of amplitude T . The resultant signal is processed, time-reversed and recreated in B , generating the backpropagating time-reversed waves. Figure taken from [108], Fig. 2 page 408

The cone tip in A was made vibrate according to a specific type of polarization and frequency band in order to excite some vibration modes of the thin disk. Different modes of resonance

were excited, particularly the one due to SH, A0 and S0 Lamb wave propagation modes. The injected signal used for such excitation in A was a narrow pulse with central frequency 1 MHz and duration $0.5\mu s$. The signal in B was recorded for a long time interval of amplitude $T = 1.5$ ms, in order to let multiple reflections (from 80 to 400) of the pulses. Then, that signal was time-reversed and used for exciting again the disk in B , thus generating the backpropagating waves, being a superposition of the different modes, SH, A0 and S0 Lamb.

The signal in A during backward propagation and the wavefield in the nearby of A were recorded using optical (laser) interferometry, due to the fact that the A0 Lamb propagation produces an out-of-plane displacement. The relevant result was that it was showed that TR focusing not only works in such a setup but its resolution is better than the one obtainable with a multi-channel TRM.

In this case, the physical phenomenon of transformation of spatial information into temporal one, described for the TR elastic waveguide experiment, plays a more relevant role, due to the high number of multiple reflections and to the chaotic rays dynamics, which implies mixing.

Figure 4.12 shows the excitation pulse during the forward propagation (inset (a)) applied by the cone in A , the signal received in B during a time interval (inset (b)), the time-reversed backpropagated wavefield received in A in the case of two different TR window amplitudes used (inset (c) and (d) respectively). It could be seen that despite the signal in B is completely noisy, the TR process manages to focus back on the source waves and to reconstruct the original forward propagation source signal. This reconstruction, through temporal compression, is as better as the TR window amplitude T is larger (inset (c) $T = 40\mu s$, inset (d) $T = 1.5$ ms).

It has been shown in [108, 109] that the time-reversed backpropagated wavefield evaluated in A (the position of the forward propagation source), $\Psi_{tr}(\vec{r}_A, t)$, converges to a signal proportional to an asymptotic signal $s_\infty(t)$ as T increases and that the proportionality constant is T itself. As a result, its amplitude increases with the TR window amplitude, an interesting feature from an application point of view because it means this experimental setup can focus elastic energy in a point with increasing amplitude without the need to increase the amplitude of the forward propagation excitation. It is sufficient to use a larger emission time and a longer TR window.

Despite this relevant property, it should be noticed from Fig. 4.12d and from Fig. 4.13 (which reports the 2D time-reversed wavefield amplitude distribution in a square region of lateral side equal to 15 mm centred on point A) that the focusing is not perfect, side-lobes persist also in the case of higher values of T .

A theoretical analysis and description of these side-lobes has been presented by Draeger, Aime and Fink in [110] along with an explanation of the existence of an asymptotic form for $\Psi_{tr}(\vec{r}_A, t)$ and its proportionality to T for high finite value of T itself. Basically, the sidelobes are due to the multiple reflections passing over the locations of the TR transducers (A and B). A quantitative formulation and expression for the side-lobes signals and fields have been proposed using the wavefunctions of the excited eigenmodes of vibration of the disk [110].

From summarizing the relevant properties of this experimental setup, it could be said that the TR elastic wave propagation can be performed also using only one point-like transducer (while it has been shown in the two previous experiments that the number of TR channels used in the TRM influences greatly its focusing performance): in a closed reflecting cavity with ergodic and mixing properties, all the spatial information contained in the waves emitted by a point-like source will reverberate throughout the whole volume and thus can be collected in only one single location.

In all the three experiments cited up to this point, the TR process has been implemented without consideration of the actual TR symmetry break described in Section 4.1.2 about the TRC theory. It has been said previously that the TR chaotic cavity last presented has better focusing properties than TRMs in a bounded space, so it is a good approximation of the TRC setup. In fact, the chaotic ray dynamics guarantees the focusing of the time-reversed backprop-

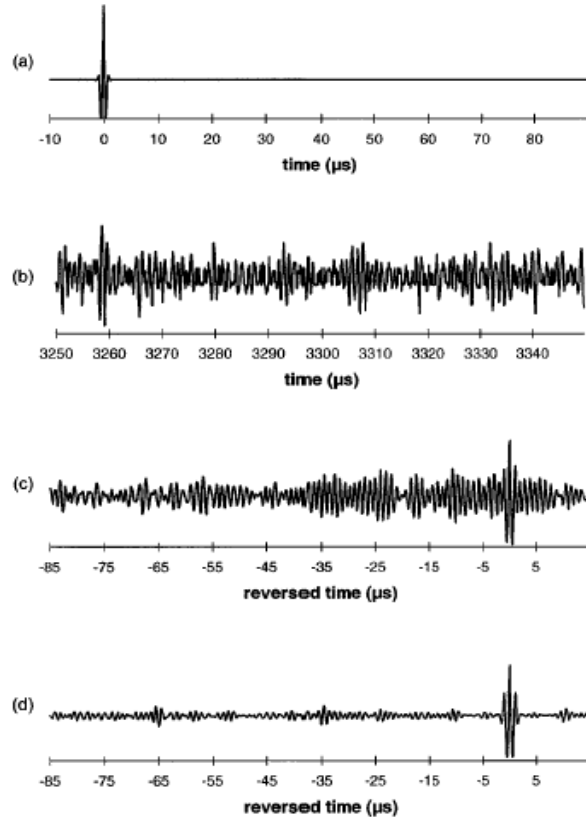


Figure 4.12: Signals during the two phases of the TR experiment. Inset (a) shows the signal used during the forward propagation phase to excite the specimen. It is a narrow gaussian-like pulse of central frequency 1 MHz. Inset (b) reports the signal received during forward propagation in B : it is a noise-like signal, due to the multiple reflections that generate resonance conditions inside the cavity. Insets (c) and (d) are two examples of time-reversed backpropagated wavefield measured in A in correspondence of different TR window amplitude T : in both cases, a sharp peaks is present at time $t = T$ form the beginning of the backward propagation, however in the first case the signal-to-noise ratio is very high, in the second one is reduced, showing a better focusing on the source position A . Figure taken from [108], Fig. 3 page 409

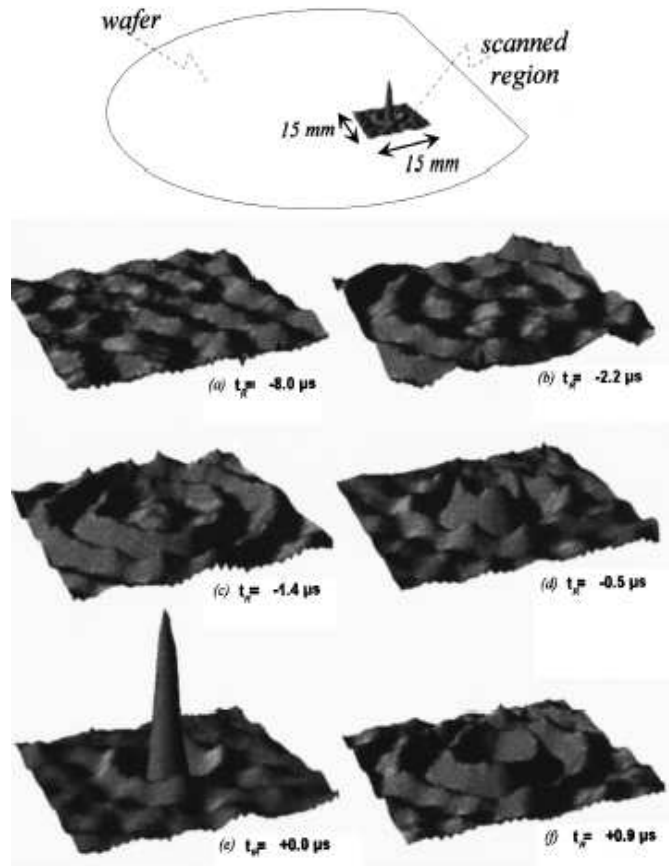


Figure 4.13: 3D plots of the wavefunction (displacement field) $\Psi_{tr}(\vec{r}, t)$ at different times t during the backpropagation phase of the experiment, obtained by laser interferometry scanning over a square region of lateral side 15 mm centred on A position. It should be noted that as time goes on, a peak located in the center of the scanning square emerges from a noise-like field and increases its amplitude up to a time $t = T$ from the beginning of the backpropagation (insets (a)-(e)). After that time, the peak disappears due to TR symmetry break described in Section 4.1.2 and the wave propagation starts again as if the forward propagation phase was repeated. Figure taken from [109], Fig. 5 page 620

agated waves emitted by only one TR channel. The robustness of TR elastic wave propagation has been even more probed with this experimental setup.

However, as cited in Section 4.1.2, a slightly modified version of the chaotic cavity was used for confirming the predictions and suggestions of the TRC theory about how implementing a complete TR process. This experiment is reported in a paper by de Rosny and Fink [90]. It was conducted just for demonstrating the correctness of the TRC theory and for probing the possibility of avoiding TR symmetry partial break. It should be remembered here what reported in Section 4.1.2: in typical TR elastic wave propagation experiments, the source of the forward propagation is passive or artificially removed during the typical backpropagation phase of the experiment. In real applications of TRMs for nondestructive characterization of materials or imaging of bulk features of specimens, the source of the forward propagation is usually a scatterer whose position is not known in advance and it is the actual objective of the whole procedure. In order to realize a complete TR process, the TR version of the source should be artificially created during the backward propagation phase in the exact position of the source. This is not possible from a practical point of view and the consequent partial TR process is robust enough in focusing waves onto the secondary sources of interest, as demonstrated by the previously described experimental results.

In the experiment reported in [90] the TR version of the source was recorded during the forward propagation and added to the emitted signal during the backpropagation phase. A chaotic cavity made of transparent glass and with the shape of a quarter stadium (80 mm lateral side and 1.9 mm thickness) was used. Again, this shape was chosen for it would lead to a non-periodic chaotic dynamics for classical particles bouncing off its reflecting boundaries. Only one brass cone was used both as source and TR transducer. A heterodyne laser interferometer was used for scanning a square region centred on the position of the transducer. The face of the stadium plate in contact with the brass cone was covered with a thin aluminum layer in order to be reflective for the laser radiation.

The dimension of the contact zone between the cone transducer and the plate was less than $100\ \mu\text{m}$. The central working frequency of the pulse emitted during the forward propagation was 500 KHz, corresponding to a central wavelength 14 times the contact area linear dimension: a complete, not broken, TR elastic wave retro-focusing should produce a focal spot with dimensions of the order of this contact area linear dimension, well below the diffraction limits which fixes the resolution at half the central wavelength.

For realizing the forward propagation, a $5\ \mu\text{s}$ long pulse was injected into the plate. The created wavefield reverberated into the cavity for 2 ms. The laser interferometer spot was initially placed on the position of the source, in order to record such short initial pulse plus the subsequent signals in that point due to multiple reflections inside the cavity. The reverberating wavefield was recorded in that point over a TR window with amplitude $T = 1.750\ \text{ms}$. Then, the TR process was conducted in two different ways: using the overall TR window, which included the source, and using a restricted subset of it, starting from the time $t = 250\ \mu\text{s}$. In both cases, during the backpropagation the laser interferometer scanned the cited area around the source position, in order to measure the amplitude of the out-of-plane component of the displacement time-reversed wavefield.

Figure 4.14 shows the results of the two backpropagations: column (a) refers to the case with the TR source as in typical TRMs experiments, while column (b) the one with the TR source added. In both cases, it could be seen that the time-reversed waves backpropagate and focus onto the center, the position of the source. However, from a certain time step, a diverging wave is created after focusing in (a), while in (b), at the same time step, the converging wave disappears into the center, as it would happen in the case of perfect TR of the forward propagation. The TR source acts as an **acoustic sink**, a concept described in Section 4.1.2. Figure 4.15 shows the comparison between the directivity profiles of the time-

reversed backpropagated wavefields, measured along a line passing through the source position and having it as the 0 of the corresponding axis: it can be seen that the resolution taken as the half width at half maximum is greater in the case with the TR source added, about $\frac{\lambda_{centr}}{14}$, where λ_{centr} is the central wavelength, well below the diffraction limit of $\frac{\lambda_{centr}}{2}$ but in agreement with the linear dimension of the contact area between the plate and the cone transducer.

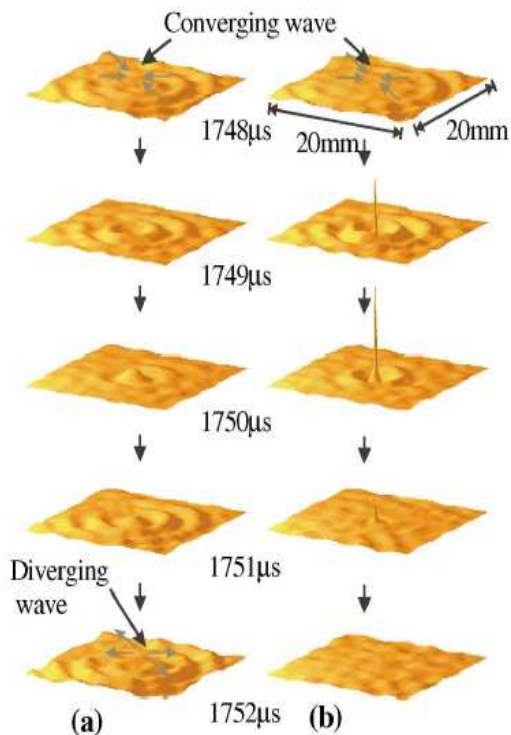


Figure 4.14: 3D plots of the time-reversed backpropagated displacement wavefield (out-of-plane component of the vector field) taken at different times at the end of the backpropagation phase. Column (a) refers to the case with a shorter TR window not including the TR source signal, while column (b) to the one including it (full TR window including the time-reversed version of the source signal). The wavefield has been measured via an heterodyne laser interferometer. At time step $1750\mu s$, at the end of the TR window period, in both cases the wavefield is focused onto the center corresponding to the source original position. At subsequent times, a diverging wave from the center can be seen in (a) while in (b) the peak vanishes, due to the presence of the TR source that compensates for the diffraction effects present in (a) and acts as an **acoustic sink** (see Section 4.1.2). Figure taken from [90], Fig. 3 page 124301-3

4.1.4 TR elastic wave propagation in attenuative and nonlinear media

TR symmetry holds in elastic wave propagation only in the case of lossless media, as reported in Section 4.1. From a theoretical point of view, the basic feature of an elastodynamics wave equation that suggests the TR invariance is the presence of even-order time partial derivative operators in the expression of the equation, mainly of the 2nd order as a derivation from the Newton's laws.

The different types of TR elastic wave propagation experiments exposed in Section 4.1.3 have showed the different degrees of robustness of the TR process realized through TRM-like

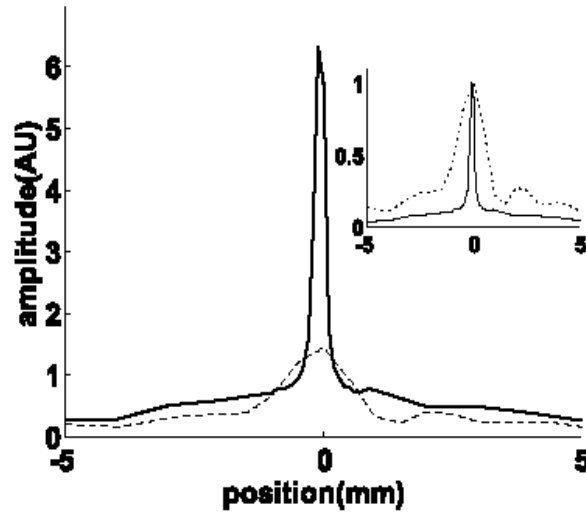


Figure 4.15: Directivity profile of the time-reversed backpropagated wavefield measured along a line passing through the forward propagation source position (the 0 on the line). The thickness line refers to the Tr backpropagation with TR source, the dashed one without. The inset shows the two profiles normalized to their respective maximum value. It can be easily seen that the resolution in the case with the TR source is greatly enhanced in respect of the other case. Figure taken from [90], Fig. 4 page 124301-4

apparatus, although they do not let implementation of a complete TR (obtainable only with a TRC as showed in Section 4.1.2): focusing of time-reversed backpropagated waves on the position of sources (being them primary or secondary ones) has been obtained through highly disordered multiply scattering media, through waveguides and within chaotic reflecting cavities. All these experimental setups have shown that boundary conditions or aberrating intermediate media not only do not interfere with the retro-focusing process but, on the contrary, they enhance their focusing capabilities, in some cases letting overcome the diffraction limits.

In any type of experiment described up to this point, the media considered have been lossless or weakly lossy, as in the case of the monocrystalline silicon chaotic cavity (Section 4.1.3), and elastically linear. The use of water as the “environment” and coupling medium of propagation is justifiable due to its high linearity and lossless behaviour in propagation regimes with low level amplitudes.

However, since the beginning of the study of TR elastic wave propagation in different conditions, in order to test the limits of its validity and its exploitation for application purposes, it has been necessary to consider what happens in media and experimental setups where attenuation or nonlinear elastic behaviour are unavoidable.

For example, TR ultrasounds focusing for medical applications in the fields of lithotripsy and hyperthermia for cancer therapy faces with many limitations of this kind: the focusing of time-reversed US waves within a small portion of brain tissues through the skull in order to produce ablation of neoplastic cell populations have required a specific experimental apparatus for amplitude compensation, because backpropagation through the skull is strongly affected by attenuation. A specific model of the propagation conditions have been proposed, with a wave equation that does not hold TR covariance because the skull has been modelled as a thin random absorbing phase screen located close to the TRM array. The skull does act as an amplitude modulator due to strong absorptions losses. In order to compensate for these losses, a two phase TR process have been devised, with the first one based on computational TR backpropagation (see Section 4.1.5 for its definition) and the second one on a real-world TRM retro-focusing

[81, 111, 112].

Another example comes from the application of TRMs in the nondestructing evaluation of solid specimens and localization of bulk defects as distributions of microcracks, localized macroscopic cracks, inclusions, flaws and delaminations. TR elastic wave propagation in solids may be affected by nonlinearity (classical and/or nonclassical) due to defects (as it will be showed in Section 4.1.5), by strong diffraction effects and conversion of propagation mode due to interfaces with solid media having different mechanical impedances [113].

However, nonlinear elastic behaviour of solids with weak attenuation properties, seems not to impede TR focusing but strongly influences its quality, for example its resolution or the possibility of selecting scatterers with different nonlinear responses (see Section 4.2), first of all for the spatial reciprocity is not yet granted. From a theoretical point of view, the validity of TR invariance is in agreement with wave equations for classical/nonclassical elastic media due to the presence of the 2nd order time partial derivative operator, $\frac{\partial^2}{\partial t^2}$ but this formulation for nonlinear elastodynamics equations remains valid in absence of shock formation, whose mathematical description requires other types of equations (see chapter 4 of [114]).

In presence of classical nonlinear elastic behaviour, even if elastic energy is transferred from an injected sine wave of a given frequency, for example, to its harmonic components self-produced during forward propagation of a TR experiment, the TR invariance ensures that, after the TR process at the transducer array (single or multi-channel), that energy, during the time-reversed backpropagation, comes back to the fundamental frequency. This TR symmetry holds only as long as the shock distance of the wave in the propagating medium is not reached, otherwise the formation of a shock discontinuity implies an irreversible change in entropy (the elastic deformations no longer correspond to adiabatic thermodynamic transformations) and thus TR invariance does not hold yet.

Probing TR symmetry for elastic wave propagation in media with classical/nonclassical elastic behaviour is very difficult from an experimntal point of view, for the enrgy spreading on different harmonic components generated during propagation requires piezoelectric transducers with large frequency bandwiths, while they usually are very narrow.

Tanter et al. report in [115] the result of TR experiments within weakly viscous media with high level amplitude regimes of operation, up to the formation of shock waves. The setup of the experiment is described in Fig. 1, page 1420, of [115]. The whole apparatus is immersed in water. A quasi-plane wave has been generated with a particular arrangement of 61 transducers (disks of 8 mm in diameter, central frequency 1 MHz, 10 mm step distance between each of them) arranged according to an exagonal pattern on a plane piston 0.9 m in diameter. The piston configuration guarantees collimation and that amplitude losses are only due to diffraction at the edges of the piston during forward propagation emission. In such conditions, forward propagation occurs mainly in a 1D way along the axis orthogonal to the plane piston. In order to achieve TR, an anti-symmetric wavefield is emitted, i.e. $\Psi(\vec{r}, -t) = -\Psi(\vec{r}, t)$, so a plane free interface between water and air is realized with a 13 μm thick Mylar sheet stretched on a hollow cylindrical shell. This sheet has been placed at 0.8 m from the array plane. For a pressure wavefield with initial amplitude of 1.7 atm, the shock distance is calculated to be 1.1 m, so beyond enough the Mylar free interface. When the wavepacket arrives at this interfaces, the total pressure field is zeroed ($\Psi(x_{int}, t)_{inc} + \Psi(x_{int}, t)_{refl} = 0$, where x_{int} is the coordinate of the interface along the propagation axis, $\Psi(x, t)_{inc}$ is the incident presure field and $\Psi(x, t)_{refl}$ the reflected one) and the velocity one is double. A bilaminar htdrophine placed at an intermediate position between the piston and the interface has been used for recording the wavefield in different position along the x -axis. Figure 3, page 1421, of [115] shows that a plane sine wave has been generated. During the forward propagation, its profile has been modified by classical nonlinear effects (harmonic generations and wavefront distortion). After reflection at the Mylar interface, a kind of time-reversed wave profile has been created and propagated up to the piston,

where the profile has resumed the shape of a sine wave. The same experiment have been repeated with an inject amplitude of 5 atm, for a corresponding shock distance of 0.33 m, so well before the water-air interface. In this case, in the nearby of the interface, a shock wave have been recorded before reflection. After reflection, the wavepacket did not recovered the corresponding waveform but propagated according to another shock wave-like profile.

The results reported in [115] show that with high level finite amplitudes, the classical non-linearity of wave propagation breaks completely the TR symmetry. Other experimental investigations about TR elastic wave propagation with finite amplitudes show similar nonlinear propagation distortion effects that affect the focusing of time-reversed backpropagated waves. These experiments have been conducted with phase-conjugation-like techniques based on nonlinear wave mixing (see Section 4.1.1), particularly on parametric interaction of an incident sound beam, after transmission into a magnetostrictive ferrite specimen, with an oscillating magnetic field [116]. A theoretical study and numerical simulations described in [113] take into account the amount of such TR symmetry break effects, due to nonlinear distortion, thermoviscous absorption of shock waves and diffraction of both the incident and time-reversed sound beams. This works underlines the fact that even in presence of shock formation, the phase-conjugation process seems still able to retarget most of the acoustic energy on the source or focal region of the incident beam, confirming the robustness of TR elastic wave propagation, although it is strongly perturbed in these cases.

4.1.5 Imaging techniques by TR elastic wave propagation

Imaging techniques exploiting elastic wave propagation have been mainly based on the ability to focus such waves inside zones of interest of a specimen. Acoustic and US imaging nowadays make use of transducer arrays. The procedure for obtaining an image of an object embedded in a medium might be summarized by the following list of steps:

1. a sound or US beam is focused at a given point within a zone of interest;
2. a transducer array records the back-scattered field by the object in the zone of interest;
3. the brightness of the image at the selected focus point is calculated as, e.g., the correlation coefficient between the back-scattered field and the beam emitted by the focusing source;
4. the focusing source is setup in order to generate another beam propagating and focusing at another point of interest in the selected zone to be imaged, so that the procedure can start again from point (1) of this list.

The overall procedure iterates as many times as the number of spatial points/elements by which the image is made (pixels in 2D, voxels in 3D).

As the focusing source it has been used an adapted delay-lines-based array. To reduce the run time of the scanning and obtain images in real time, only a few delay lines are used and a fundamental assumption is made for modeling the wave propagation process: the time of arrival of the back-scattered echoes are directly correlated to the depth of the scatterer within the medium via the elastic wave phase velocity.

In a complete homogeneous and linear medium, the quality and resolution of the image depend entirely on the source array aperture, according to the classical law of diffraction introduced in Section 4.1.2: the size of the focal spot is inversely proportional to the array aperture.

In heterogeneous, multiply scattering media, delay-lines-based arrays do not permit to focus through multiple scattering and the assumption previously described can no longer be valid.

In the previous Sections, the capabilities and robustness of TR techniques in focusing elastic beams at positions of primary or secondary sources have been reported and described taking as

examples some of the most important experimental apparatus, such as TRMs, in open space or inside waveguides, and solid chaotic cavities. It has been demonstrated that focusing through highly disordered multiple scattering media or in regions limited by reflecting boundary conditions (as happens in solid specimens or biological tissues) is not only granted via TR techniques but also the resolution obtained is usually better than with other techniques.

In [117], Roux *et al.* define a new US imaging apparatus constituted by a multi-channel TR array plus a layer of multiply scattering medium (made as the one described in Section 4.1.3) positioned closed to the array surface. This setup has been designed for exploiting the pseudo-lens effect studied in Section 4.1.3: a TR technique is exploited for generating a focusing beam instead of the more traditional delay-lines technique. The specimen to be imaged is positioned in front of the apparatus from the side of the scattering layer. In order to obtain an image, a calibration procedure (to be performed before the specimen of interest is put in front of the imager) has been devised. This calibration constitutes of three steps:

- the size and resolution of the future image is fixed, subdividing a reference plane in front of the multiply scattering layer into different pixels;
- an artificial point-like source is placed at each pixel position on the reference plane, it emits a pulse which is recovered by each TR array transducer, stored and time-reversed as in a common TR experiment;
- for each pixel, the time-reversed signals are emitted and the back-scattered field produced by the close aberrating layer is recored by the same TR transducer array; this field is called the **reference field**.

After the calibration, the specimen is exposed to the imager, the set of time-reversed signals associated to each pixel of the calibration phase is backpropagated, one at a time, through the aberrating layer and the specimen, the back-scattered wavefield produced by the specimen is recorded by the TR array and the reference field is subtracted from it. Then the cross-correlation between this last field and the wavefield recorded during the first step of the calibration process is calculated. A correlation coefficient is thus obtained in correspondence of each TR channel and their arithmetic mean is used as the brightness level for the selected pixel of the image. The procedure is executed for each pixel, i.e. with each set of signals obtained with the calibration source of step 1 in a specific position of the reference grid. Figures 5 and 6, pages L11-L12 in [117], show the 2D image of a phantom specimen made with gel and containing 9 aluminum rods as the ones constituting the multiply random scattering layer. Figure 5 therein refers to the case with the presence of the aberrating layer in front of the array acting as a pseudo-lens, while Figure 6 without it. From the comparison of these two figures, it can be seen that the multiply random scattering highly disordered layer improve the resolution of the image in locating the different rodes immersed in the gel.

Another example of imaging apparatus that takes advantage of TR elastic wave propagation features, particularly of focusing with improved resolution, is presented in [118] and in [119]. It is based on a imaging procedure similar to the one presented above but instead of using an aberrating multiply scattering layer it exploits the properties of a leaky reflective Sinai chaotic cavity (obtained from an aluminum solid cube with a spherical hole in the middle) in retro-focusing elastic beams after a long time interval over which multiple reflections occur within the cavity itself. Also in this case, after a calibration procedure, the apparatus (the cavity plus a TR transducer array attached to one of his surface) is placed in contact with the specimen to be imaged and the time-reversed signals obtained during calibration are used to produce acoustic/US wave packets focusing on a specifing region of the specimen (a voxel); the back-scattered wavefield from the specimen, correlated with the reference wavefield, measured during the calibration, leads to the calculation of the correlation coefficient used as the brightness value

of the voxel considered. The image thus produced is 3D and can be obtained without the use of complicated 2D transducer array (usually difficult to be implemented because they require up to thousands of elements, so an expensive electronic multiplexing hardware setup), improving the resolution via the exploitation of the focusing capabilities of a 3D TR chaotic cavity.

The two examples of imaging techniques just reported use TR elastic wave propagation as a means for generating a highly focused sound/US beam, to be used for scanning the object. However, imaging techniques have been devised relying directly on TR techniques rather than on the classical scheme underlined by the enumerated list above

In [120], Prada *et al.* illustrate two techniques entirely based on the use of TRMs for the detection of defects, acting as scatterers, embedded in solid specimens with an heterogeneous microstructure that yields a strong scattering noise. The specific case considered therein is a specimen of a specific type of titanium alloy (Ti6-4) with a shape of an emi-cylinder (125 mm radius) containing three flat bottom holes on its plane face, spaced 15 mm apart. Titanium billets are the primary source for the fabrication of rotating parts of aircraft engines. The non-destructive inspection of these specimen in search for defects is very difficult because the a strong speckle noise is induced by the polycrystalline microstructure during the insonification and that noise can hide the echo from the defects. This is also the case for all grain materials such as steel and ceramics or composite materials (fibers act as speckle noise sources in this case). For most of these materials, the average distance between scatterers is smaller than the central work wavelength ($\simeq 0.5$ mm for typical US frequencies), so the speckle noise received by the TR arrays makes the target detection complicated.

The first technique is based on the **Iterative Time Reversal Mirror (ITRM)** approach described in Section 4.1.3, which allows to focus selectively on the strongest scatterer. The second technique derives from the mathematical analysis of the ITRM process and, in contrast to TRMs, does not require programmable generators in the TR array and allows the simultaneous detection and separation of several defects. This last technique is called **DORT**[121, 122, 81], a French acronym that stands for “decomposition of the time-reversal operator”.

Both techniques, which relies on different signal processing methods, bring distinct advantages in the detection of defects other than small scale distributed scatterers due to the distributed heterogeneity of the specimen. For the localization within the specimen of interest of such defects the backpropagation of time-reversed wavefields must be performed and must be tracked in time and space in order to realize an image of the interior or sub-surface structure of the specimen.

As pointed out in [123], the backpropagation of time-reversed wavefields, focusing back onto scatterers, more or less selectively according to the technique used in the TR signal processing, may be **physical** or **virtual**. Physical backpropagation occurs as in typical TR experiments and its use for imaging purposes is restricted to specific situation when it is possible to measure on the surface of the specimen the effects of the backpropagating time-reversed wavefield, as in thin plates. Virtual backpropagation is performed by numerical simulation: the time-reversed signals emitted from the arrays are used as input data for a numerical simulations of elastic wave propagation within a **reference medium** with the same geometry and same background features of the real one. This modelled fictious specimen do not contain information about the defects or strong scatterers positions, information that may be obtained as a result of the simulation itself.

Physical TR backpropagation for imaging purposes does not need any information about the specimen, while the virtual one needs a bunch of data about it but is easier to be implemented. That is the main reason for its increasing use as an alternative imaging technique, also know as **computational TR imaging**, applied both for nondestructive evaluation of defects in solids [120, 123, 124, 125, 126, 127] and for imaging of structures in biological tissues and organs..

It should be underlined that physical TR backpropagation imaging, whenever possible from an experimental point of view (see for example [128]), may lead to a better resolution in the localization and characterization of defects or of inhomogeneous structures/interfaces in a complicated specimen, than computational TR imaging. The reason of this difference consists in the fact that in computational TR imaging the simulated backpropagation cannot include the defects/strong scatterers into the simulation setup. This feature implies that the focusing of the backpropagated time-reversed waves is perturbed, it is simulated within the reference fictitious medium which is different from the actual one, i.e. the one where the forward propagation has occurred [129]. So, the reliability and resolution capabilities of computational TR imaging rely on the information about the geometry and physical features of the real specimen that can be obtained and used for the description and coding (in the simulation program) of the reference fictitious one.

In Sections 4.2 and 4.3 results of original work conducted by me, A. Gliozzi and M. Scalerandi (Dept. of Physics, Polytechnic of Torino) about computational TR detection and imaging of defects within solid specimens are reported. This work has been addressed towards the issue of selective detection and imaging of defects that may contribute to the nonlinear (classical and nonclassical) elastic behaviour of specimens. Such defects, in real-world specimens, may be difficult to be detected and characterized for the same reasons cited above: small scale distributed inhomogeneities generate speckle noise that can hide the typical features of back-scattered signals by localized defects such as small cracks, flaws, delaminations, inclusions. Speckle noise is created by multiple random scattering within the disordered heterogeneous structure of such specimens cited above. Typically, it affects TR elastic wave propagation when the central work wavelength of a TRM-like apparatus of measurement, λ_{centr} , is of the same order of the correlation length l of the microstructure, being this one very low in respect of the array aperture a and the mean distance between the array and the zone containing the defects, L :

$$\lambda_{centr} \simeq l \ll a \ll L. \quad (4.27)$$

4.2 Computational Nonlinear TR imaging of scatterers in 2D

One major task in nondestructive evaluation of materials via TR elastic wave propagation techniques is nowadays their optimal application into cases of nonlinear elastic behaviour, stretching their focusing capabilities as much as possible up to limit conditions where the TR focusing breaks down completely. One important issue is the discrimination between images produced by real defects, which, as seen in Sections 2.1.2 and 2.2.1, confers a compressive nonlinear elastic behaviour to the specimen, and images due to linear inclusions, local changes in the elastic constants or boundaries conditions, all of them acting as scatterers as well as the defects.

The Iterative Time Reversal Mirror and the DORT techniques, cited in Section 4.1.5, have been probed in focusing selectively on different scatterers. However, for early damage detection, it is often necessary to focus on extremely weak scatterers, a very difficult task in the case of real-world specimen with high degree of small scale distributed or localized inhomogeneities.

I have developed, in collaboration with A. Gliozzi and M. Scalerandi (both at the Dept. of Physics, Polytechnic of Torino), a novel signal processing procedure to be applied to back-scattered wavefields during a kind of TRM experiment, before the TR processing. In [130], we have reported such proposed procedure and tested with an *in silico* experiment of computational TR imaging, i.e. we have used numerical simulations both for the forward and for the backward propagation. We have considered therein the case of a specimen whose surfaces, or part of them, could not be accessed directly, e.g. via laser interferometry. As a consequence, we have studied such procedure in a case in which the experimenter could not take advantage of all information of the received signals along, for example, a given direction which may be one side of a plate

or a radial circumference (for cylindrical specimens). We have chosen a model experimental setup with a geometry that does not have any partial/complete symmetry and with reflecting boundary conditions that play a significant role in multiple scattering.

Our simulated experiment makes use of computational TR backpropagation for imaging purposes and could be applied to real-world experiments in which the forward propagation occurs actually in a real-world specimen, while the backpropagation of processed and time-reversed signals is still performed by a numerical simulation with a similar reference specimen.

After the processing (mainly a special kind of filtering) of signals obtained from the forward propagation in a damaged specimen (simulated in our case), the results of the TR backpropagation lead to the localization and characterizations of regions within the specimen where the scatterers are located.

For the forward propagation simulation, we have set up a 2D aluminum plate with dimensions $12 \times 6 \text{ cm}^2$, considered, in a first case, as an elastically isotropic and homogeneous specimen with Lamé constants $\lambda = 51.08 \text{ GPa}$ and $\mu = 26.32 \text{ GPa}$ and volumetric mass density $\rho = 2700 \text{ Kg/m}^3$. The corresponding longitudinal and shear wave velocities are then $c_P = 6176 \text{ m/s}$ and $c_S = 3122 \text{ m/s}$ respectively. Attenuation in the material have been chosen to be quite significant, in order to simulate a bad situation for the exploitation of TR elastic wave propagation properties. The boundaries of such a specimen have been considered fixed (as in the case of closed chaotic cavities presented in Sections 4.1.3 and 4.1.5) and not accessible to receivers, in order to simulate propagation within a specimen embedded in a larger one, as it usually occurs in structured components used in aircraft or automotive industry. The not weak level of attenuation in the medium have implied the damping of multiply reflected waves within the specimen, which should be considered as a kind of closed cavity without ergodic properties, due to the rectangular shape (see Section IV of [109] for experimental probe).

Two regularly-shaped scatterers have been added to the virtual specimen setup. The larger one is a square-shaped linear inclusion with dimensions $5 \times 5 \text{ mm}^2$, with the same volumetric mass density previously defined but with Lamé constants values reduced of an amount equal to 20 % of the values of bulk previously reported. The second scatter has been set up as a small region with rectangular shape, length 10 mm and width 0.1 mm, with the same elastic and physical properties of the bulk but with nonclassical nonlinear elastic behaviour, implemented according to the modeling presented in Section 2.2.2 and Appendix 5.3.2. Figure 4.16 shows the geometrical setup of the specimen, with the linear inclusion and the nonlinear thin defects, along with the configuration of the virtual transducers used for the TR experiment.

As it can be seen from Fig. 4.16, the two scatterers have been located in arbitrary positions, each far from the other, with a configuration that is quite different from an optimal one for their localization (for example, the defects placed in the center of the specimen or equidistant from the receivers).

Fig. 4.16 shows at position $x = 2 \text{ cm}$ the presence of three thin embedded transducers (length 10 mm, width 1 mm) used as emitters during the forward propagation, while a network of N point-like transducers is displaced around the two scatterers. These last transducers act as receivers during the forward propagation and as emitters of the time-reversed signals during the backward one, being the equivalent elements of a 2D TRC array retina (see Section 4.1.2). Each of the three extended transducers have been designed to emit, during the simulated forward propagation phase of the TR experiment, a Gaussian modulate sine waveform with central angular frequency $\omega = 1.2 \text{ MHz}$. We have chosen this setup with three equal extended emitters in order to have a uniform coverage of the specimen cross section by the forward wavefield.

As previously cited, both for the forward and for the backward propagation simulation, we have used the LISA-Spring 2D model described in Section 2.2.2 and in Appendix 5.3.2: while during the forward propagation the specimen contains both the linear inclusion and the nonlinear thin scatter, which may mimic a flaw in a plate, during the backpropagation of the

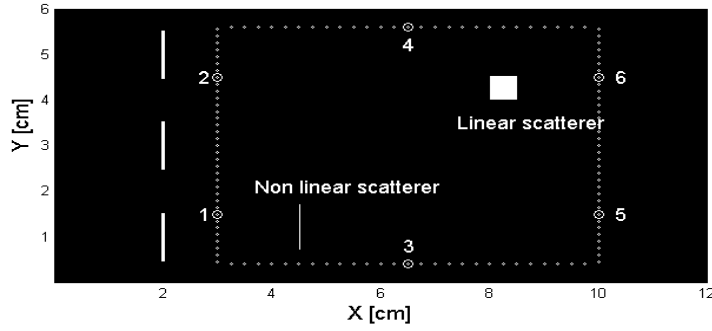


Figure 4.16: Schema of the setup of the 2D virtual specimen used for the simulated forward propagation. Three extended thin transducers are placed along the line $x = 2$ cm, while a network of transducers is placed around the linear inclusion and the nonlinear defect (small white points). These transducers act as receivers during the simulated forward propagation, but as emitters of the time-reversed signals during the backward propagation. Some of them have been selected and indicated with numbers from 1 to 6 in order to sample therein the signals obtained during the forward propagation for showing the effects of the two scatterers during that phase of the *in silico* experiment

time-reversed signals received by the network a reference specimen has been setup, identical to the one of the forward phase but without the linear inclusion, the nonlinear defects and the three extended transducers. As discussed in Section 4.1.5, although this method of performing the computational backpropagation is the standard one, because in real-world situations the positions of the scatterers would not be known and because the source of the forward propagation is usually removed or made passive during the backpropagation according to the theoretical treatment presented in Section 4.1.2, it should be underlined that the reference medium should not guarantee a precise focusing on the actual scatterers positions, because the configuration of the closed cavity is not the same as in the forward propagation. However, in this case, the changes between the two configurations are very small, the absence of the scatterers during the backpropagation, as it is showed below, has not modified significantly the wave propagation inside the cavity, so the TR focusing has been preserved with a high level of reliability.

Figure 4.17 shows the temporal evolution of the norm of the velocity vector wavefield within the specimen during the forward propagation. It can be seen therein the three wave packets emitted by the three extended transducers (first row-left column), their propagation towards the right side of the specimen and their component reflected by the left side (first row-right column and second row-left column). At successive time steps, it can be seen that the propagating wavefront do not interact in a strong enough manner with the linear inclusion and the nonlinear thin defect, so they do not produce high level contrast during the forward propagation. Figure 4.18 reports two signals recorded during the forward propagation by the rectangular-shaped network of receivers, in two specific positions of the array (see Fig. 4.16). They are compared with the corresponding signals recorded in the same positions during another simulation with the same setup (boundary and initial conditions, specimen) but the absence of any scattering region. The arrivals of the waves after multiple scattering from the defects and the boundaries can be seen, for example, at $10\mu s$ for the receiver #1 (the second pulse in that time series might be due by reflection of the emitted wave packets at the left side of the specimen) or at $22\mu s$ for the receiver #6 (the main pulse might corresponds to the superposition of the waves reflected both from the left and the right sides). The good correspondence with the signals obtained in

the scatterers-free specimen confirms that the effects of the linear inclusion and of the nonlinear defect might be buried in the overall forward propagating wavefield. A slight mismatch is only visible at the receiver #6, as it is reasonable to expect for it has been placed very close to the linear scatterer.

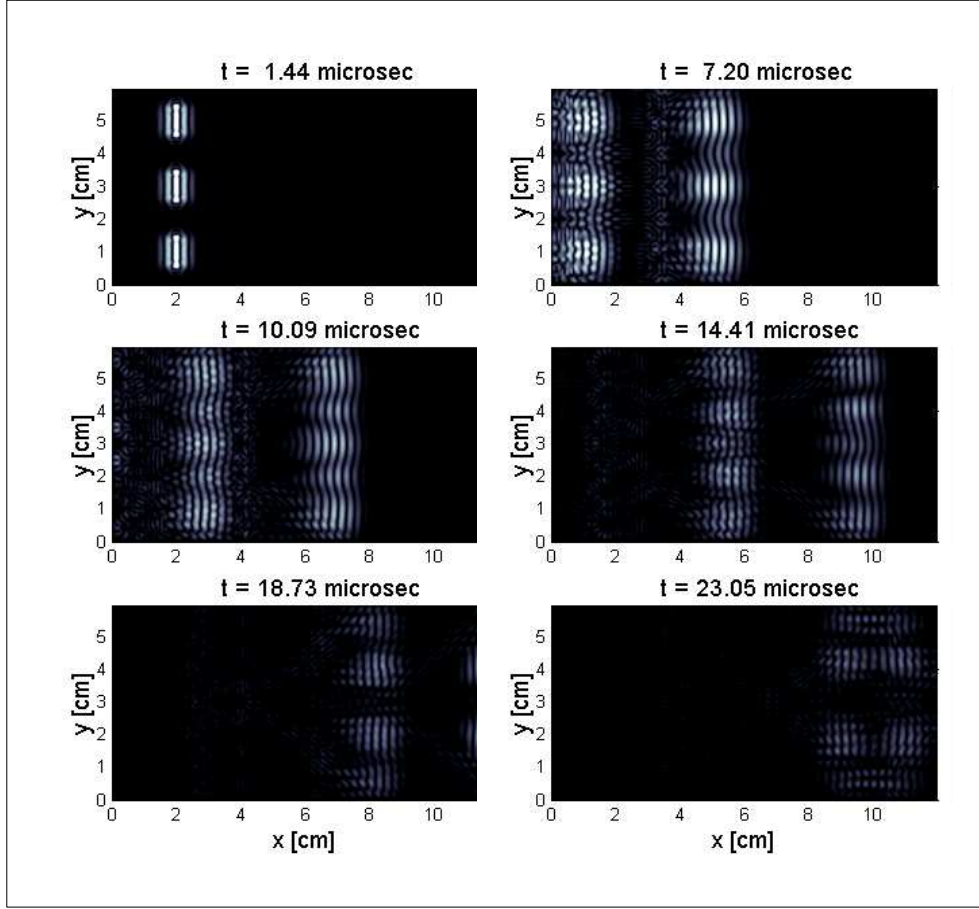


Figure 4.17: Snapshots taken at different time steps of the norm of the velocity vector wavefield during the simulated forward propagation. Lighter grey tones refers to higher values, of the order of 0.8 cm/s. See Figure 4.18 for the actual scale of such computed wavefield.

We have chosen a TR time window of amplitude $T = 18 \mu s$ and a starting time of recording during the forward propagation $t_0 = 7 \mu s$. During the overall work with such *in silico* TR experiment, great attention has been paid to the role of the amplitude of the TR window. We have noticed that, at least in principle, a different value of T should be used for each receiver, in order to account for the different distances between the receivers and the sources (primary or secondary). However, we have not investigated so far this issue.

Calling $\vec{u}_j(t)$ the vectorial signal recorded at each receiver $j = 1, \dots, N$ during the forward propagation, before the time-reversal of the signal we have processed each of them using mainly two different techniques and compared the results obtaining from the numerical backpropagation starting from the correspondent different time-reversed signals, called $\vec{v}_j(t)$ for each transducer j of the network acting as an emitter during the backward propagation. It should be underlined the fact that the processing techniques may be easily implemented in real-world experiments, although with real transducers it is difficult to measure a vectorial signal $\vec{u}_j(t)$ and in many occasions it is still quite difficult to understand the polarization of the scalar signal recovered,

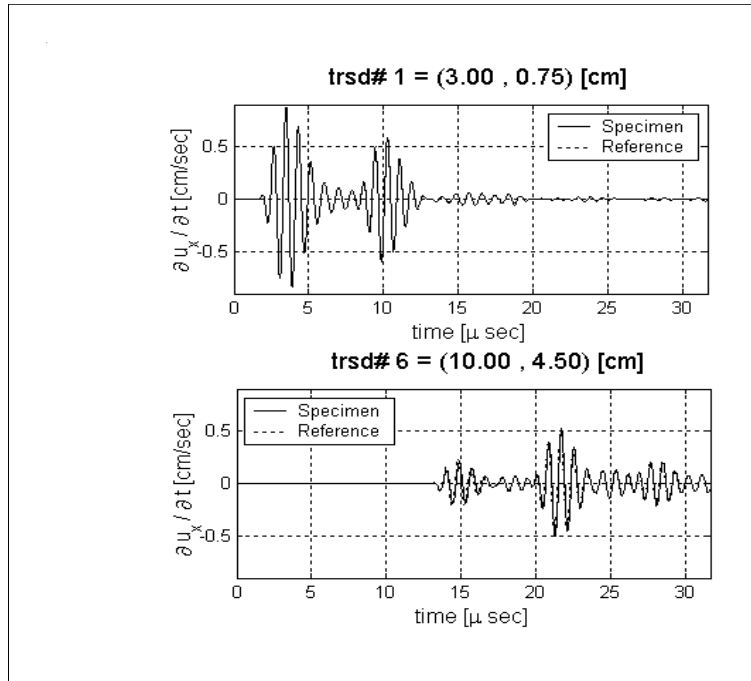


Figure 4.18: Time signals recorded at the receivers number #1 and #6 of Fig. 4.16 during the simulated forward propagation. The recorded signal type is the x component of the velocity vector wavefield. The dash line refers to the signals obtained in a similar simulation without any scatterer, while the continuous one to the forward propagation in the specimen described above

i.e. which projection of the real vectorial signal it is, while in numerical simulated forward propagation the vector fields in the locations of the receivers can be calculated directly.

As said in the introduction of this Section, the processing stage we have devised has had as its main objective the selective detection and imaging of the scatterers, in particular of the nonlinear one, via the computational backpropagation.

The first processing technique consists in the simple time reversal of the received signal $\vec{u}_j(t)$, for each receiver j , so $\vec{v}_j(t) = \hat{TR}(\vec{u}_j(t))$, where $\hat{TR}(\cdot)$ indicates mathematically the time-reversal operator/operation. The second processing technique implements the difference between the received signal $\vec{u}_j(t)$ and the one obtained in the same receiving positions by a forward propagation in a corresponding homogeneous specimen, $\vec{u}_{j,0}(t)$, so $\vec{v}_j(t) = \hat{TR}(\vec{u}_j(t) - \vec{u}_{j,0}(t))$. The third processing methods exploits a high-pass-like filter applied to $\vec{u}_j(t)$ in order to remove from the received signal all the components due to multiple reflections at the boundaries and to the scattering by the linear inclusion, leaving the part of the signal actually generated by the nonlinear scatterer, which generates high order harmonics due to its nonclassical nonlinear behaviour (see 2.2.2). In then last case, $\vec{v}_j(t) = \hat{TR}(\vec{u}_j^F(t))$ where $\vec{u}_j^F(t)$ is the signal resulting from the filtering of $\vec{u}_j(t)$; we have used a band pass filter cutting all the Fourier components of $\vec{u}_j(t)$ with angular frequency less than $1.8 \cdot \omega_{central}$ and greater than $4 \cdot \omega_{central}$, where $\omega_{central} = 1.2$ MHz is the central angular frequency of the injected signal.

A comparison between the signals received, processed and time-reversed at two different Tr transducer of the network according to the three processing techniques are presented in Figure 4.19. The selected transducers are #5 and #6 of Fig. 4.16. The first row of Fig. 4.19 shows the x component of the force vector field (expressed in N) calculated via the LISA-Spring 2D model at that receiving point⁴. The second column shows the corresponding time-reversed signal, remembering that the TR window is $[t_0; t_0 + T]$. The third row reports the time-reversal of the subtracted signal while the fourth one the time-reversal of the filtered signal, for each selected transducer.

It can be seen that the processed signals are similar when only a reversal is performed, reflecting the symmetry in the placement of the three transducers. On the contrary they are very different in the other two cases (bottom two rows), reflecting the asymmetries in the placement of the scatterers. Indeed, the signal at the TR transducer #5, which is aligned with the nonlinear scatterer (see Fig. 4.16), is almost null when the subtraction processing is applied, while rather large when filtering. The opposite occurs for the signal at the transducer #6, aligned with the linear inclusion. It should be noticed the different ranges on the y-axes in Fig. 4.19: while after subtraction about 25% of the signal is used for reversal, only about 2% remains after filtering. It then follows that noise may play a crucial role.

The final step of the computational TR imaging experiment has consisted in the injection of the processed signals $\vec{v}_j(t)$ back into the specimen for each j simultaneously. Simulations of the propagation of the time-reversed wavefield have been performed using the homogeneous linear specimen (without scatterer), in order not to introduce any bias from an a priori knowledge of the defect location. Note that here the vectorial form of the reversed signal has been maintained in the injection (i.e. both components of the received signals have been reinjected). Receivers in experiments may not be able to keep the vectorial information.

In Figure 4.20, the norm of the velocity vector wavefield (expressed in cm/s), taken at the time corresponding to best focusing during the backward propagation, is plotted, for the three

⁴There is no discrepancy between this Fig. and Fig. 4.17, where the received signal is a velocity signal. Within the LISA-Spring 2D model, the injected signals are calculated as forces, so in this Fig. we have reported the force signals calculated from the correspondent velocity ones.

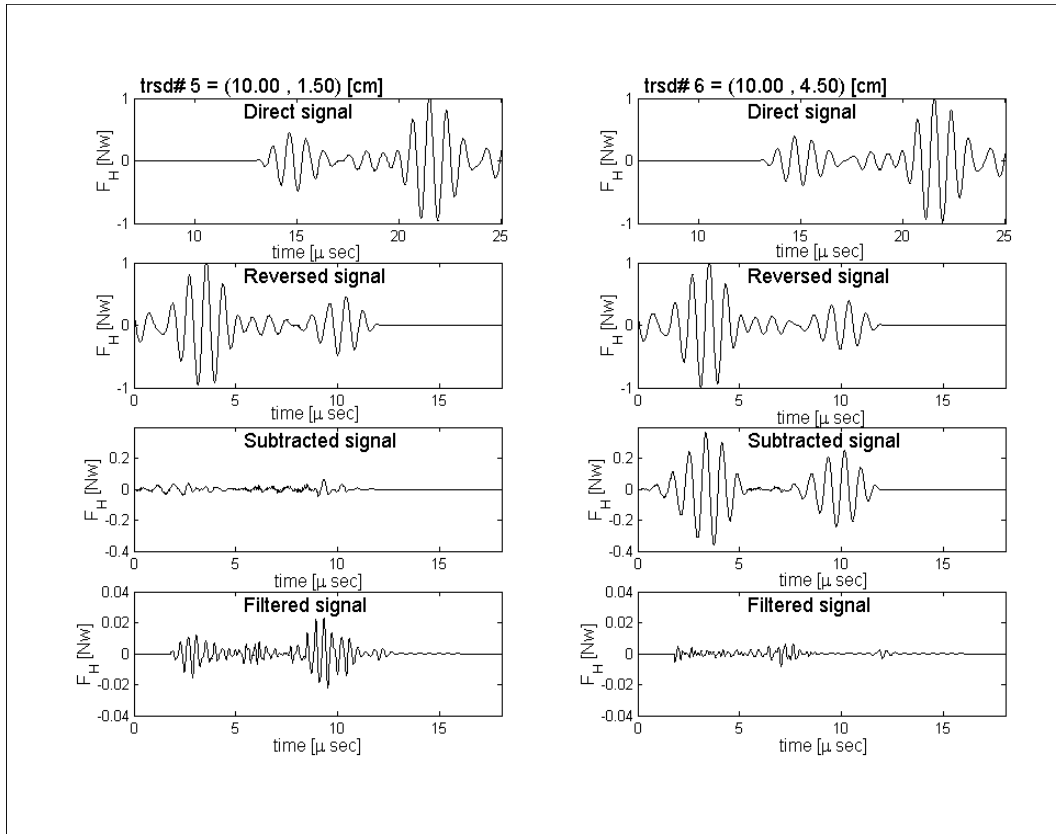


Figure 4.19: Results of the processing of the signals at transducers #5 and #6 (see Fig. 4.16) before reinjection into the specimen. The horizontal component of the force per unit surface is reported in the selected time window. First row: received signal. Second row: reversal of the received signal. Third row: reversal of the signal obtained subtracting the reference signal. Fourth row: reversal of the band-pass filtered received signal

processing procedures described previously: pure time-reversal, subtraction+time-reversal and filtering+time-reversal, from top to bottom. As expected, albeit at different times, best focusing is obtained on the three transducers, on the linear inclusion and on the nonlinear scatterer, respectively. In each of them, the temporal evolution of the wavefield does not indicate evidence of focusing on other sources except the ones indicated in the plot. A very slight evidence of focusing on the nonlinear inclusion is only present in the wavefield corresponding to the subtracted reversal process, which indeed was to be expected. The reduced focusing of energy on the central transducer in the upper plot is due to the choice of the distribution of receivers.

Great attention in this work has been paid to the last proposed procedure only, which is novel, to our knowledge, with respect to existing TR approaches and does not require any reference signal. In Figure 4.21, we have reported snapshots of the norm of the velocity vector field taken at selected times during the backpropagation. Therein, the time-reversed wavefield appears at positions farther from the source (the nonlinear scatterer) first, i.e. the upper and right rows of receivers. At a later time ($14 - 15 \mu s$), the receivers close to the defect start playing a role, but the wavefield remains unfocused. Progressive focusing occurs between 16 and $18 \mu s$ revealing a reasonably good image of the scatterer. At later times, due to the absence of the time-reversed forward propagation source, as explained in Section 4.1.2, the propagation starts again as if the forward pulse is started again. No evidence of focusing in regions far from the scatterer (i.e. phantom images) is present.

Images of the wavefield at the time corresponding to best focusing (see Fig. 4.20) constitute a first indicator of the quality of the imaging procedure. In these plots, however, several pieces of information are lost. For example, the possible focusing on other scatterers and the images of the ray paths from the receivers to the focusing point. To capture these details an alternative mapping of the wavefield data have been proposed. Defining $f(x, y; t)$ the scalar field describing the observable whose values are plotted at fixed times for realizing an image (it could be vibration velocity, strain, stress, etc.), we have introduced the following scalar field,

$$M(x, y) = \max_{t \in \Delta t} \{f(x, y; t)\}, \quad (4.28)$$

which represents, in any position, the maximum value the variable f assumes within the time interval Δt . The function M is expected to present maxima wherever focusing occurs and also secondary maxima where the unfocused paths from the N receivers interfere coherently towards the focusing point, hence identifying the ray paths. In [130] we have chosen the variable f to be the norm of the local displacement vector field. An image of the map M corresponding to the same simulation of Fig. 4.21 is reported in the upper row of Fig. 4.22. The map clearly indicates focusing on the nonlinear scatterer and a maximum in the position of the receivers which are mostly contributing to the reconstruction (i.e. receivers close to the scatterer). Some ray paths are also identified, although not particularly meaningful here. To improve the imaging procedure, it should be noticed that Fig. 4.22 shows that only few transducers contribute to the reconstruction of the image. Also, the time series in Fig. 4.19 illustrate that some transducers reinject a signal of very small amplitude (e.g. the TR transducer #6). Since focusing is determined mostly by keeping proper phase delays between signals injected from different positions, independent of amplitudes, we have introduced the possibility of amplifying the injected signals differently at different positions. Therefore, we have added a further signal processing step: $\vec{z}_j(t) = A_j \cdot \vec{v}_j(t)$, where A_j is the amplification factor for the j -th TR channel. To obtain equal contributions from all transducers, we have defined

$$A_j = \frac{1}{\max_{t \in \Delta t} \{ \|\vec{v}_j(t)\| \}}. \quad (4.29)$$

The corresponding signals, components of $\vec{z}_j(t)$, are therefore each normalised to one and expressed in arbitrary units (a.u.). Results of the backpropagation simulation using normalised

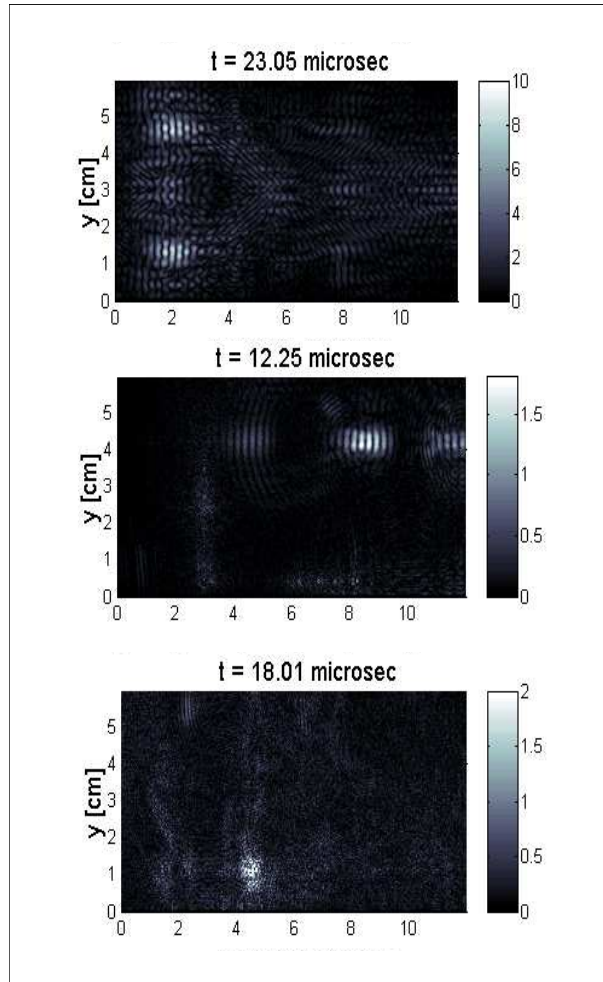


Figure 4.20: Snapshots of the norm of the velocity vector wavefield as obtained by the simulated backpropagation, taken at the time step of the simulation at which the best focusing is obtained. The different rows refer to the three distinct processing of signals before TR: first row, pure time-reversal; second row, reference signal subtraction and time-reversal; third row, band pass filtering and time-reversal. The lighter tones correspond to higher values. It should be remarked that the scales of tones in the three snapshots have a different maximum: 1 cm/s for the first row, about 1.75 for the second one, 2.0 for the third one.

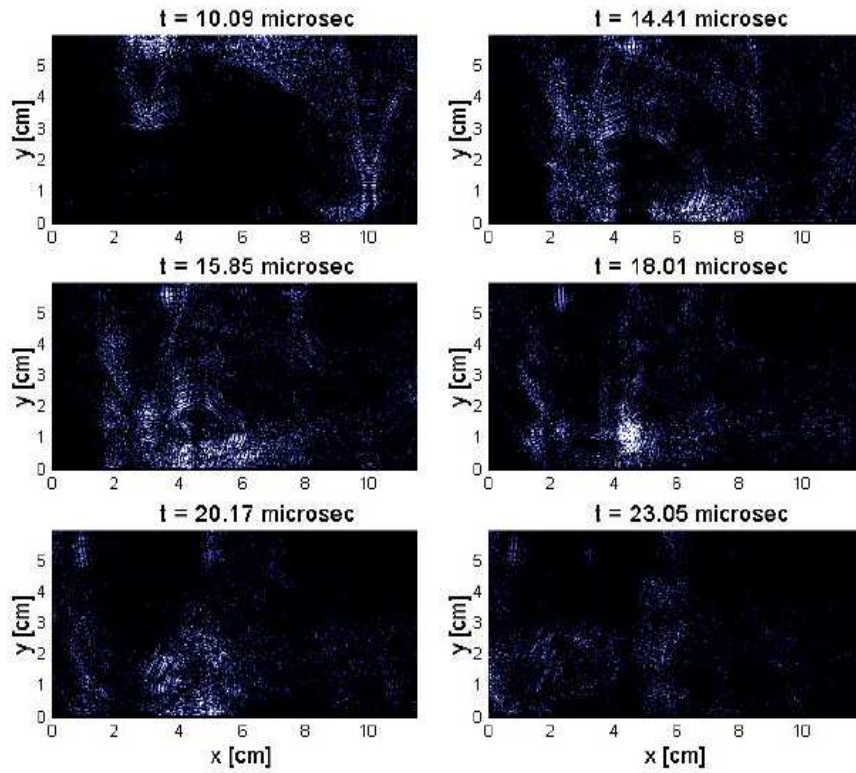


Figure 4.21: Snapshots of the norm of the velocity vector wavefield at successive times, calculated during the backpropagation, in the case of the filtering procedure applied to the signals received from the forward propagation. The lighter tones correspond to higher values, the maximum of the scale being 2 cm/s.

signals are reported in the second row of Figure 4.22, where the map of the function M is reported. The improvement of the reconstructed image is evident, with a much larger energy being focused on the scatterer than that being injected at the transducers. Ray paths are more meaningful and give indication of the progressive focusing. With the third row of Fig. 4.22 we have also analysed the effect of reinjecting normalised signals using only one component of the recorded wavefield (in particular the x-component). The reconstructed map remains reasonably good, albeit with a deterioration of the image with respect to the previous case. Finally, in the bottom row of Fig. 4.22 it is shown how a mathematical smoothing on the map M leads to a significant improvement of the quality of the image of the nonlinear scatterer location. This plot corresponds to the same image of the second row, but averaged on a square of size corresponding to the distance between two adjacent receivers (3 mm).

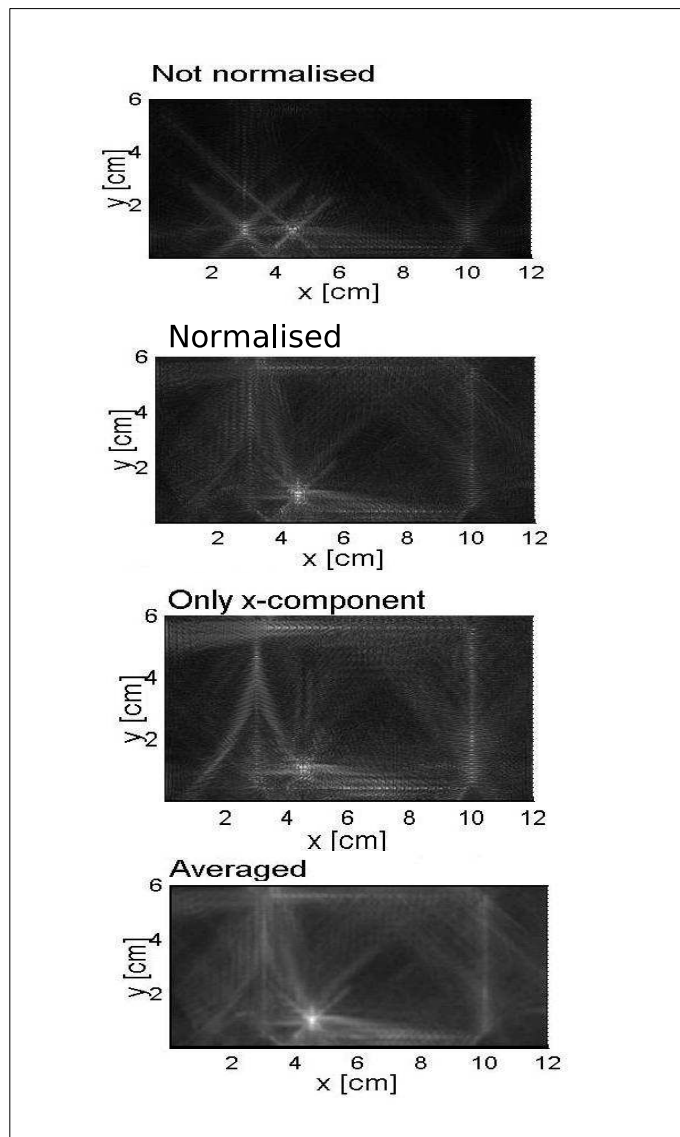


Figure 4.22: Maps of the maximum in time of the norm of the displacement vector field. Different rows refer to the distinct processing procedures. The lighter tones correspond to higher values. The tones scale are expressed in nm for the first row, while in arbitrary units for the other three scales, due to normalization of the displacement vector field used to calculate the maps M according to Eq. 4.28.

The Figures presented up to this point suggest that the combination of the band-pass filtering of the wavefield received on the TR transducer network at the end of the forward propagation, the TR of such signals at each receiving transducer including an amplification different for any transducer, finally of the normalization of each time-reversed vectorial signal to the maximum in time of its norm, leads to a selective localization of the nonlinear scatterer. The plots of M have been chosen as the best way for realizing such images of the nonlinear defect position within the specimen.

In order to test the robustness of this overall method for the imaging of nonlinear scatterers, we have investigated the effects of various constraints/errors, actually present if the forward propagation was performed experimentally and not with a simulation with the previously introduced setup, on the resolution property and quality of the images themselves thus obtained. All the results reported in what follows refer to plots of the scalar field $M(x, y)$ (see Eq. 4.28), obtained implementing the filtering procedure, with normalized signals and maintaining the vectorial information in the backward injection. Also in these cases, we have used numerical simulations of forward propagation with different setups (obtained with some modifications introduced in the one presented above) of the specimen or of the initial/boundary conditions of the propagation problem.

First of all, we have studied the efficiency of the same method just described when the number of elements of the TR transducer network, N , is lower than in the previous setup ($N = 124$, a large number for a closed transducer array). This setup change is equivalent to reduce the total number of TR channels in a typical TRM experiment. As cited in Section 4.1.3, the number of TR channels is a fundamental parameter along with the amplitude T of the time reversal window for optimizing the focusing (so imaging) capabilities of TR elastic wave propagation experiments.

Fig. 4.23 shows the reconstructed images obtained using different values of N . The entire simulation and processing procedure has been repeated as described above using only different values of N and consequent different distributions of the TR transducers within the specimen. We have maintained the same geometry for the transducer network (it covers the same rectangular path), changing only the array pitch (distance between two nearest neighbour transducers). The processing procedure has been the same in all cases, the last one described above (filtering + amplification + time-reversal + normalization + plot of $M(x, y)$). Finally, it should be reminded that the amplitude of the TR window T has been kept fixed.

Except for the plot in the bottom-right corner, the transducers are always taken equidistant on the four sides of a square. In the bottom-right plot, only transducers localized on the two vertical arrays have been used, which may be an easier configuration from an experimental point of view.

As expected, it can be seen that the quality of the image decreases with a decrease of N . In fact, lowering N , the maxima of energy become more and more focused on the transducers positions: fewer transducers mean fewer rays converging on the defect location and, consequently, less constructive interference. Nevertheless partial focusing is still evident in the case $N = 22$. It could be noticed that the need of a quite large number of transducers should not be considered a technical obstacle. Indeed, receivers for the forward propagation may be easily substituted by a scanning laser interferometer, as mentioned. Emitters in the reversed propagation are used only in the numerical simulation, where an arbitrarily large number of emitters can be used without difficulties.

The second test we have conducted about the robustness of the signal processing method proposed for the computational TR localization and imaging technique has been concerned with the presence of a random noise component in the signals obtained from the forward propagation.

Synthetic forward propagation data are not affected by noise. On the contrary, in every experimental system, noise is present, it may derive from the measurement apparatus and devices

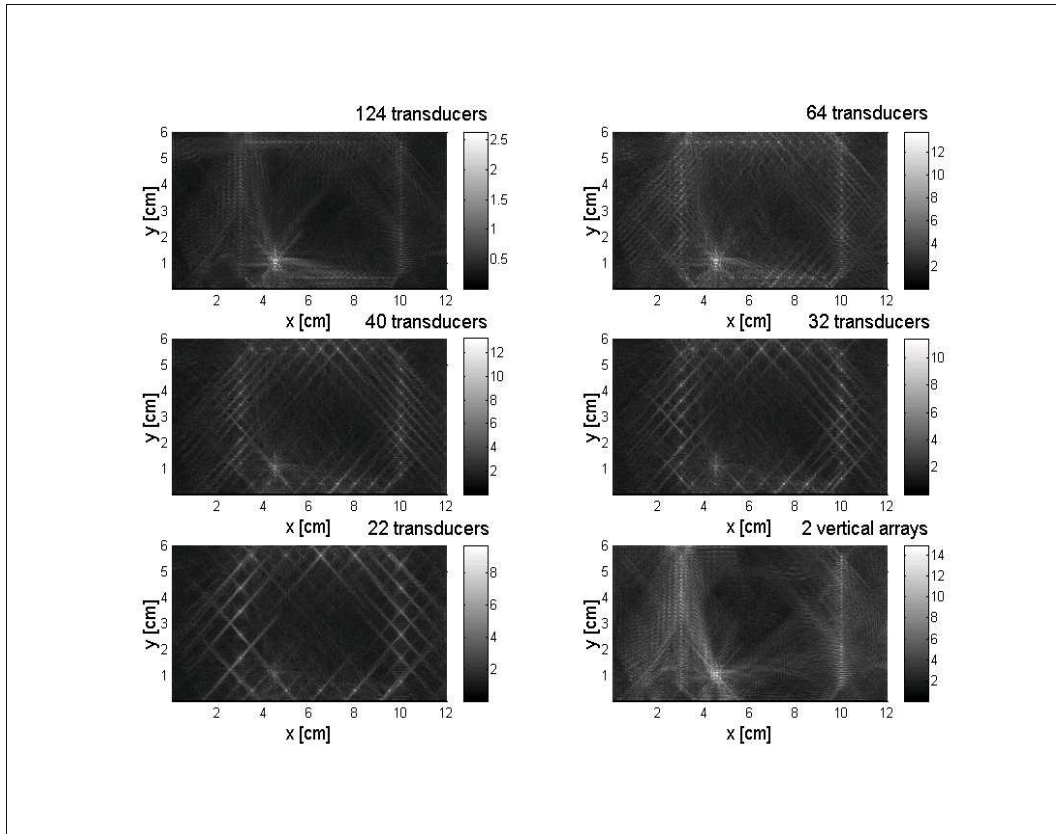


Figure 4.23: 2D plots of the maximum-in-time of the norm of the displacement vector field obtained through numerical backpropagation with a different number N of TR transducers. Each plot, except the right-bottom one, refers to the same type of transducers arrangement within the specimen (rectangular closed path around the scatterers); decreasing N , the array pitch (distance between two nearest neighbour elements) increases. The plot at the right-bottom refers to a configuration with only two vertical 1D arrays each in front of the other.

and/or from the wave propagation itself, due to small scale (below the central wavelength of the waves) distributed inhomogeneities, finally it contaminates the received signals. To simulate a realistic condition, we would have had to choose two possible approaches: describing the specimen as a random inhomogeneous one, with a random distribution of values for the Lam constants or with a more complex model [] for its elastic parameters; using a simpler specimen model as we have done and artificially perturbing the received signals with a randomly generated additive noise before processing.

Chosen the second approach, we have performed the usual forward propagation simulation, obtained the vectorial signals $\vec{u}_j(t)$, for $j = 1, \dots, N$, we have added to each of them a white vectorial stochastic process $\vec{\gamma}_j(t)$ with the properties

$$\begin{aligned}\langle \gamma_{j,k}(t) \rangle &= 0 \\ \langle \gamma_{j,k}(t) \cdot \gamma_{j,k}(t') \rangle &= \left(\frac{\gamma_0^2}{4}\right) \cdots \max_t \{u_{j,k}(t)\} \cdots \delta(t, t')\end{aligned}\quad (4.30)$$

$\forall k = 1, 2, 3$, being $u_{j,k}(t)$ and $\gamma_{j,k}(t)$ the components of $\vec{u}_j(t)$ and $\vec{\gamma}_j(t)$ respectively, thus obtaining a final forward propagation signal $\vec{u}_j^n(t) = \vec{u}_j(t) + \vec{\gamma}_j(t)$ at the TR channel j , $\forall j = 1, \dots, N$.

Figure 4.24 shows the effects of this white noise on the signals received at the receiver #1 (see Fig. 4.16) for two different values of the noise parameter γ_0 .

It can be noticed that the effect on the received signals (upper row) is small, while it increases enormously in the filtered signal (second row). In the case of a large value of γ_0 , its effect is comparable with the original signal (see third row). Despite these effects, the reconstructed images of the nonlinear defect remain acceptable up to a noise level of $\gamma_0 = 0.1$ (see Figure 4.25). Not surprisingly, the procedure does not work any longer at the largest value for γ_0 , where no evidence of focusing is observable. Rather unexpected is the robustness of the procedure for $\gamma_0 = 0.1$, considering the noisy features of the injected signals. This result is an indicator that noise, albeit very large, produces an unfocused wavefield superimposed to the wavefield generated by the nonlinear scatterer. The former is distributed on the full specimen, resulting in a local energy which is very small compared to that which focuses on the scatterer.

Finally, we have tried to test the robustness of the procedure in the presence of a distributed nonlinearity: we have introduced into the modeling of the specimen additional several weak nonlinear scattering regions with about the 5-10% of the values of the nonlinearity parameters of the already considered nonlinear defect. These regions have been distributed randomly within the specimen area. To quantify such distributed nonlinearity, we have used a parameter, α , which defines (as a percent area) the zone in which nonlinear scatterers are distributed, hence giving the surface density of nonlinear scatterers. Different forward propagation simulations and corresponding TR back ones have been run for different values of α . This last set of computational TR imaging *in silico* experiments have been conducted in order to investigate the efficacy of the processing procedure in case of multiply scattering media.

The signals obtained from the simulation of the forward propagation differ only very slightly from the ones obtained in the absence of weak scatterers. On the contrary, such a nonlinearity has an enormous influence on the filtered and reversed signals already at $\alpha = 5\%$ (see Figure 4.26). Despite the huge effect on the injected signals, reconstruction of the defect image remains good up to $\alpha = 10\%$ (see Figure 4.27). It should be remarked that part of the elastic energy focuses close to the transducers used in the forward problem. Such focusing is due to the fact that, in the forward propagation problem, nonlinear scatterers close to the source have been excited at a larger amplitude than scatterers far from it.

As a final summary, it could be stated that the filtering processing of the forward propagation signals seems to guarantee the selective focusing of time-reversed wavefields on the scatter with nonclassical nonlinear behaviour, although it does not behave as a strong scatterer, as suggested

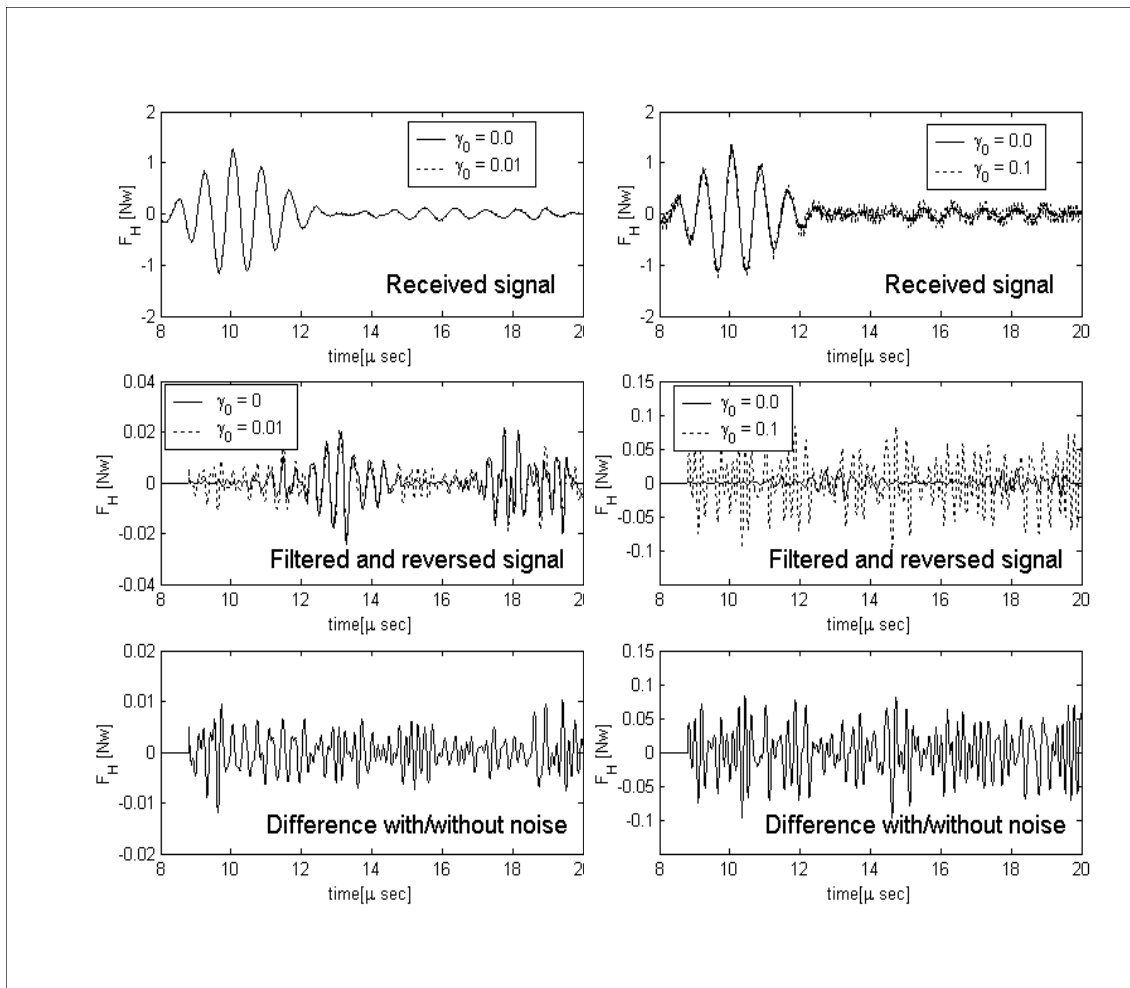


Figure 4.24: Effects produced by the addition of white noise to the signal obtained at receiver #1 (see Fi. 4.16) from the forward propagation. The first four insets show the comparison between the same type type of signals in presence and absence, respectively, of noise. The first row reports the forward signal received at the TR transducer #1 before its processing: increasing the amplitude of white noise fluctuations the signal is slightly perturbed. The second row show, for the same two noise amplitudes, the filtered and time-reversed corresponding signals: the greater the level of noise (right column) the greater the randomness of the signal to be backpropagated. The third row, in each column, reports the difference of the signals plotted in the second row, corresponding column, in order to show that when the amplitude of noise fluctuation is quite large ($\gamma_0 = 0.1$., right column), the noisy component of the signal is the predominant one in the time-reversed signal.

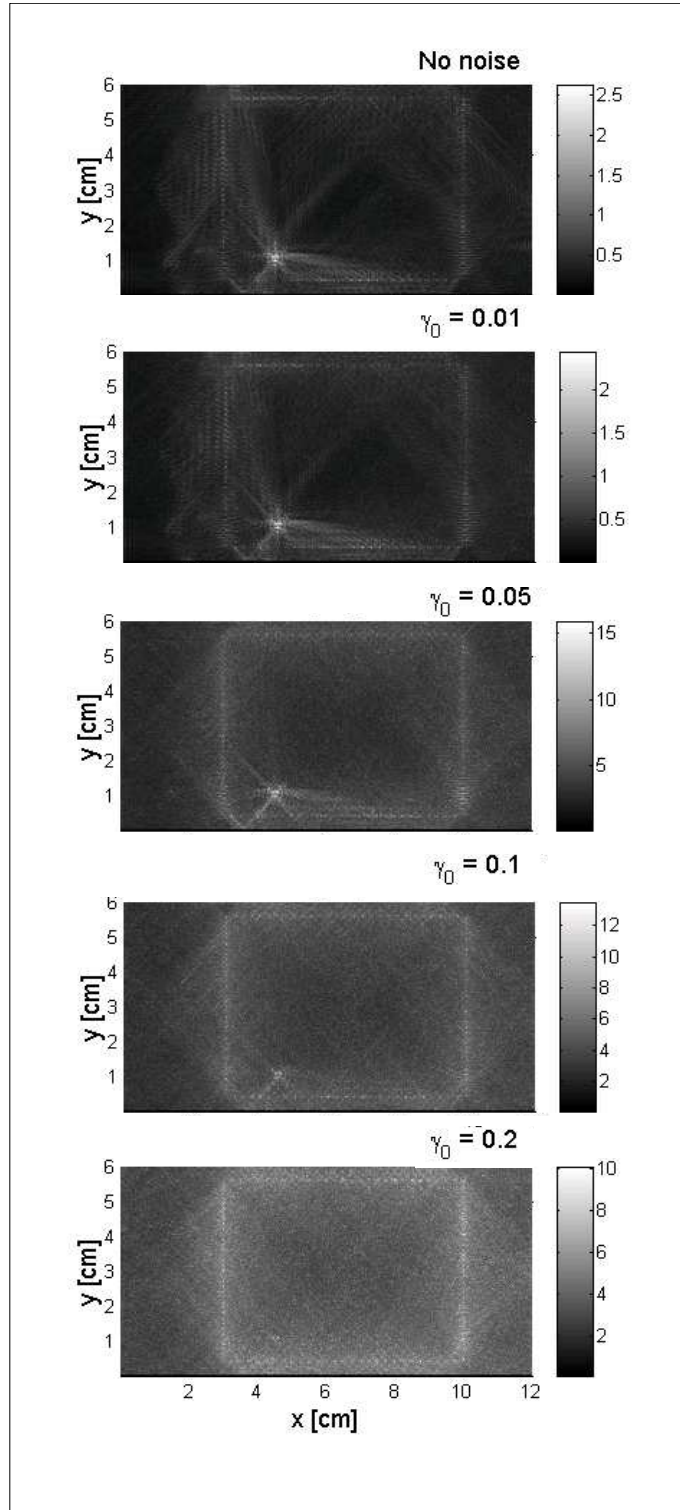


Figure 4.25: Plot of $M(x, y)$ for different simulations with different values of the added noise amplitude γ_0 . It should be noted that the focusing of the time-reversed backpropagated waves in the region of the nonlinear scatterer persists up to a value of $\gamma_0 = 0.1$. Above that value, the noise dominates the re-injected signals, without any possibility of producing ray paths converging back to the original source.

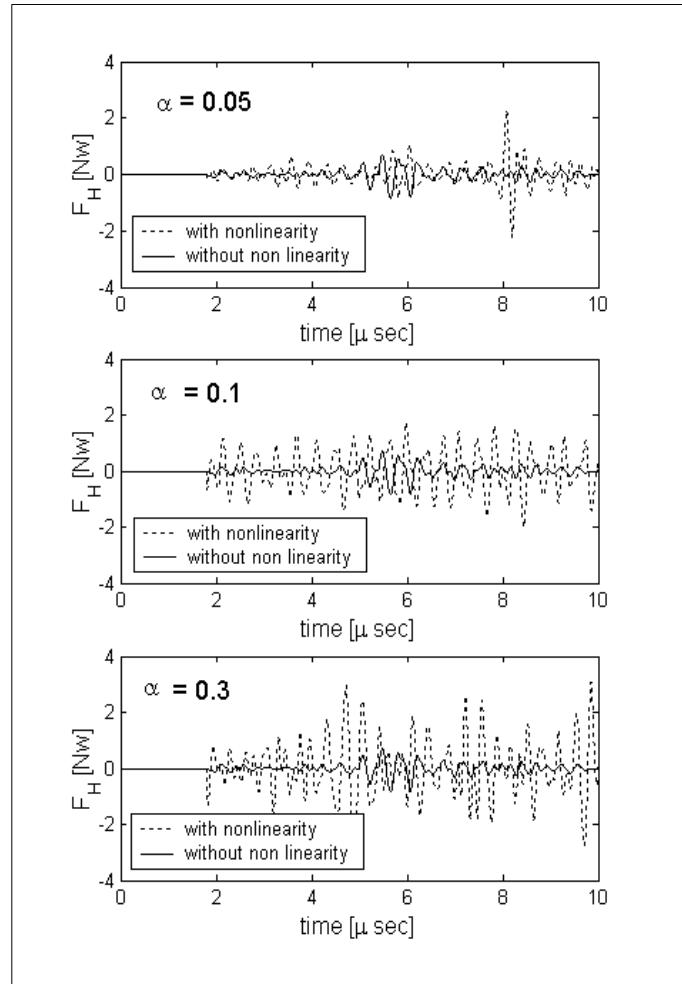


Figure 4.26: Time series recorded at the position of the TR transducer #1 during the simulated forward propagation in presence of different distributions of nonclassical nonlinear scattering zones with different densities codified by distinct values of the parameter α . In each case, the corresponding signal obtained without the distributed nonlinear zone is also showed. The signal reported is the x component of the total force acting on the basic surface element of the node where the receiver #1 is placed.

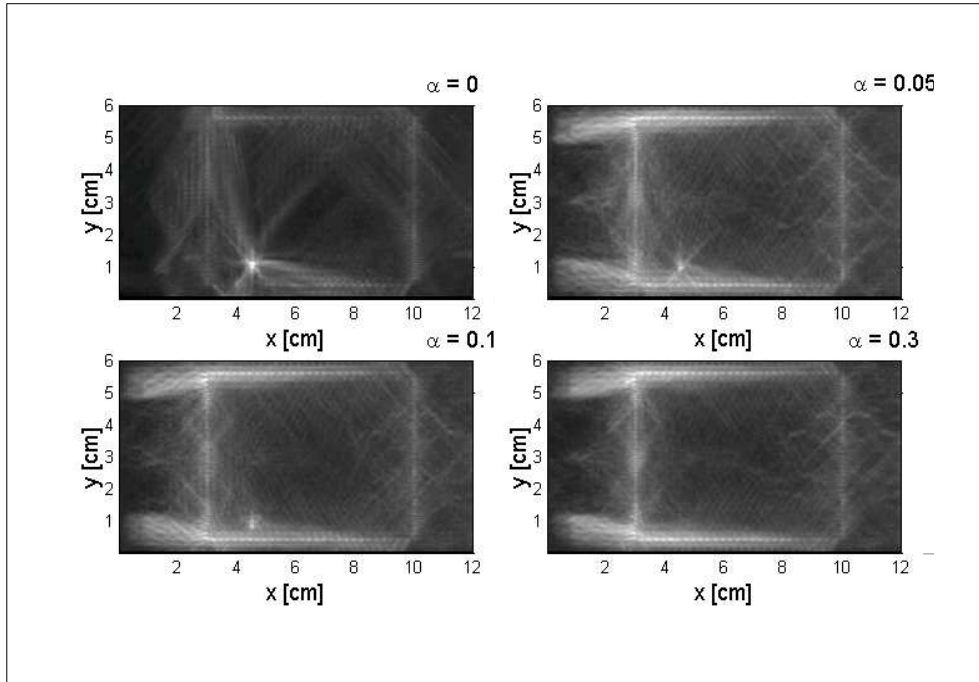


Figure 4.27: 2D plots of $M(x, y)$ without distributed weak nonlinear scattering regions (first row-first column) and with them. The amount of distributed nonlinearity is expressed by the parameter α .

by our forward propagation simulations (see Fig. 4.17). The processing technique might be implementable at the experimental level, in order to perform real-world forward propagation measurements and using then simulated backpropagation as a tool for the localization of the scatterers, particularly the ones with nonlinear elastic behaviour which might be associated to defects of great importance from a nondestructive evaluation point of view.

4.3 Computational TR imaging of scatterers in 3D

In Section 4.2, a special kind of computational TR imaging technique has been introduced. It has been called “nonlinear” because it is addressed to the localization and imaging of scatterers that induce nonlinear elastic wave propagation properties in solid specimens they are embedded in.

We have used the 2D LISA-Spring model for elastic wave propagation simulation both for the computational backpropagation (which is the second phase of the overall imaging process) and for obtaining the forward propagation signals at the TR array (the first phase). The core of the proposed imaging technique consists in the procedure for processing these forward propagation signals before TR and in the processing of calculated values of the backpropagating wavefield, in order to increase the contrast of the image.

The 2D LISA-Spring model has showed to be a useful “toolbox” for the simulation of the elastic wave propagation through specimens with NCNL behaviour, as reported in Section 2.2.2, so it has served as a first “platform” for the study of the signal and image processing approach in computational TR Imaging.

2D simulations of wave propagation for realizing computational TR imaging experiments may be used only in restricted cases where the plane-stress propagation can be assumed as a good approximation of the real-world forward propagation type in the considered specimen. 2D

simulations both of the forward and of the TR backward propagation have been used by many other Researchers in order to prove the feasibility and the main features of imaging methods based upon numerical simulation and processing of real data [125, 126, 127, 123, 131, 132, 133].

However, a thorough analysis of the reliability of such processing methods can be done only using forward propagation signals obtained in real-world experiments or by 3D numerical simulations which could take into account more details about the propagation mode. So, in collaboration with A. Gliozzi and M. Scalerandi (Dept. of Physics, Polytechnic of Torino), I have been involved in the extension of the 2D LISA-Spring code to a 3D one in order to test the same type of signal and image processing proposed in Section 4.2 onto forward propagation data obtained by 3D simulations (see Section 4.3.1 below).

Regarding my PhD work, I have been focused towards the 3D extension and the realization of a parallel version of that code to be run on parallel supercomputers. As a first step, I have worked on the development of a 3D (linear) LISA parallel code (see Appendix III), avoiding to include the modeling of NCNL elastic behaviour typical of the LISA-Spring model (see Section 2.2.2 and Appendix I). This last task would require the development of a multi-dimensional PM space modelization of the stress-strain constitutive relation for the interfaces between grains (see Section 2.2.2) or at least an extension to a 3D code of the formulation used for the 2D LISA-Spring code (see Section 2.2.2 and Appendix II), which however is still very reductive. Work for the development of a 3D full LISA-Spring code being able to simulate elastic wave propagation through NCNL media is under development at the Dept. of Physics, Polytechnic of Torino, by M. Scalerandi and A. Gliozzi.

Another principal reason for limiting to the development of a linear LISA parallel code has been the opportunity to start a collaboration with Dr. Paul A. Johnson, EES-11 (Geophysics), Nonlinear Elasticity Group, Los Alamos National Laboratory (Los Alamos, New Mexico, USA) and his group during the last two months of my Ph.D. on computational TR Imaging techniques for nondestructive evaluation and characterization of defects in solid specimens and for the 3D localization and characterization of seismic sources. This ongoing collaboration has given the opportunity of obtaining real forward propagation data of TR Imaging experiments. So, in the final months of the PhD, I have started to work on the modeling of such experiments, in order to study a series of topical issues addressed to the support of the analysis of the experimental results obtained by Dr. Johnson and his collaborators, with the final goal to use the 3D LISA parallel code for performing the numerical backpropagation phase of such TR imaging experiments, including the forward propagation signals processing proposed in Section 4.2. For this target, the 3D linear LISA code is sufficient, being its use restricted to the TR backpropagation, which is simulated through a corresponding homogeneous reference specimen with the same geometry, boundary conditions and matrix properties of the one used in the real-world forward propagation. (see Section 4.1.5). Section 4.3.2 is dedicated to preliminary results of such analysis targeted to the application of the computational TR imaging method presented in Section 4.2 to data obtained by real-world forward propagation experiments.

4.3.1 Test of the computational TR imaging method with 3D numerical simulations

To test the computational TR imaging and processing technique proposed in Section 4.2 under less restricted conditions of wave propagation, it has been performed a forward propagation simulation in a 3D thin plate with dimensions $10 \cdot 2.5 \cdot 1 \text{ cm}^3$ (x -, y -, z - axes, respectively), with parallelepiped shape, elastically isotropic (Lamé constants $\lambda = 106 \text{ GPa}$ and $\mu = 71 \text{ GPa}$), volumetric mass density $\rho = 8 \cdot 10^3 \text{ Kg/m}^3$. A small parallelepiped area with dimensions $5 \cdot 3 \cdot 2 \text{ mm}^3$ and classical nonlinear (CNL) elastic properties has been located within the plate starting from the position ($x = 5, y = 1.5, z = 0.5$) cm. One extended virtual transducer has been

localized on the upper surface of the plate starting from the location ($x = 4, y = 1.2, z = 2.5$) cm. A Gaussian amplitude modulated sine wave with center angular frequency $\omega_{centr} = 0.7$ MHz has been used as source for the forward propagation. Forty-five TR transducers have been fixed on the lower surface of the plate ($z = 0$ cm), disposed according five parallel 1D arrays (nine elements per array).

After the simulation of the forward propagation, the signal processing at the forty-five TR virtual transducers and the execution of the time-reversed numerical backpropagation have been performed according to the same procedure described in Section 4.2. The filtering + time-reversal + normalization sequence of processing have been followed and during the backpropagation the scalar field $M(x, y, z)$, still defined as the maximum in time of the norm of the displacement vector field, has been sampled on the simulation grid.

Figure 4.28 shows 2D plots of the function M taken on $z = \text{const.}$ planes, for different values of the quote z . In such 2D slices of the 3D graph of $M(x, y, z)$, the tone scale has been fixed such that darker grey tones correspond to higher values for M , lighter tones to lower values.

It could be seen that on the lower surface of the plate, at $z = 0$ cm, the only regions with significant contrast are the ones where the TR transducers are placed (they act as emitters during the time-reversed backpropagation, so they are sources of elastic energy). Considering the other slices, corresponding to increasing quotes z , it could be seen that the higher concentration of elastic energy, due to wave focusing, has occurred on the plane $z = 0.5$ cm, around the point of coordinates (5, 1.5) cm, corresponding to one corner of the nonlinear region (see the third row-right column of Fig. 4.28). Above that plane, there is no other evidence of focusing (last row of Fig. 4.28).

Figure 4.29 shows a 3D partial representation of the graphs of $M(x, y, z)$, using a collection of some of its 2D slices (four planes, three of them being the coordinates planes $z = 0, y = 0$ and $x = 0$ cm, respectively, the fourth plane being a diagonal one passing through the central point of the nonlinear region, intersecting the plane $z = 0.5$ cm). This 3D plot shows clearly the focusing of the time-reversed backpropagated waves onto the nonlinear region. It should be reminded that this Fig. as the previous one represents the maximum values in time of the norm of the displacement vector field, so they catch its maximum values point-by-point, corresponding to the values at the time focusing has occurred.

These 3D results confirm the reliability of the processing approach used in the computational TR imaging technique. It should be reminded that, in this case, the simulated forward propagation has occurred in a specimen with only a classical nonlinear elastic region. However, this setup has been sufficient for a rapid validation of the method developed for improving computational TR imaging and otherwise proved only via 2D synthetic forward propagation data. Further ongoing work by me, M. Scalerandi and A. Gliozzi is addressed to extend such test to cases with forward propagation simulations including the effects of nonclassical nonlinear scatterers.

4.3.2 3D numerical simulations of real-world TR imaging experiments

The last two months of my Ph.D. have been dedicated to start to validate the developed and proposed Computational TR Imaging technique with real-world problems of defects identification and localization within solid specimens. This work has been ongoing at the time this Ph.D. Thesis has been written, mainly in collaboration with the Group of Dr. Paul A. Johnson, EES-11 (Geophysics), Nonlinear Elasticity Group, Los Alamos National Laboratory (Los Alamos, New Mexico, USA), under the framework of the Project “Image Reconstruction with Time Reversal Mirrors”, funded by the Department of Energy of USA and which I’m involved in.

Two main issues have been addressed for the moment:

- implementation of the 3D LISA-Spring model and computational code for the simulation of forward and, most important, backward propagation through specimens with complicated

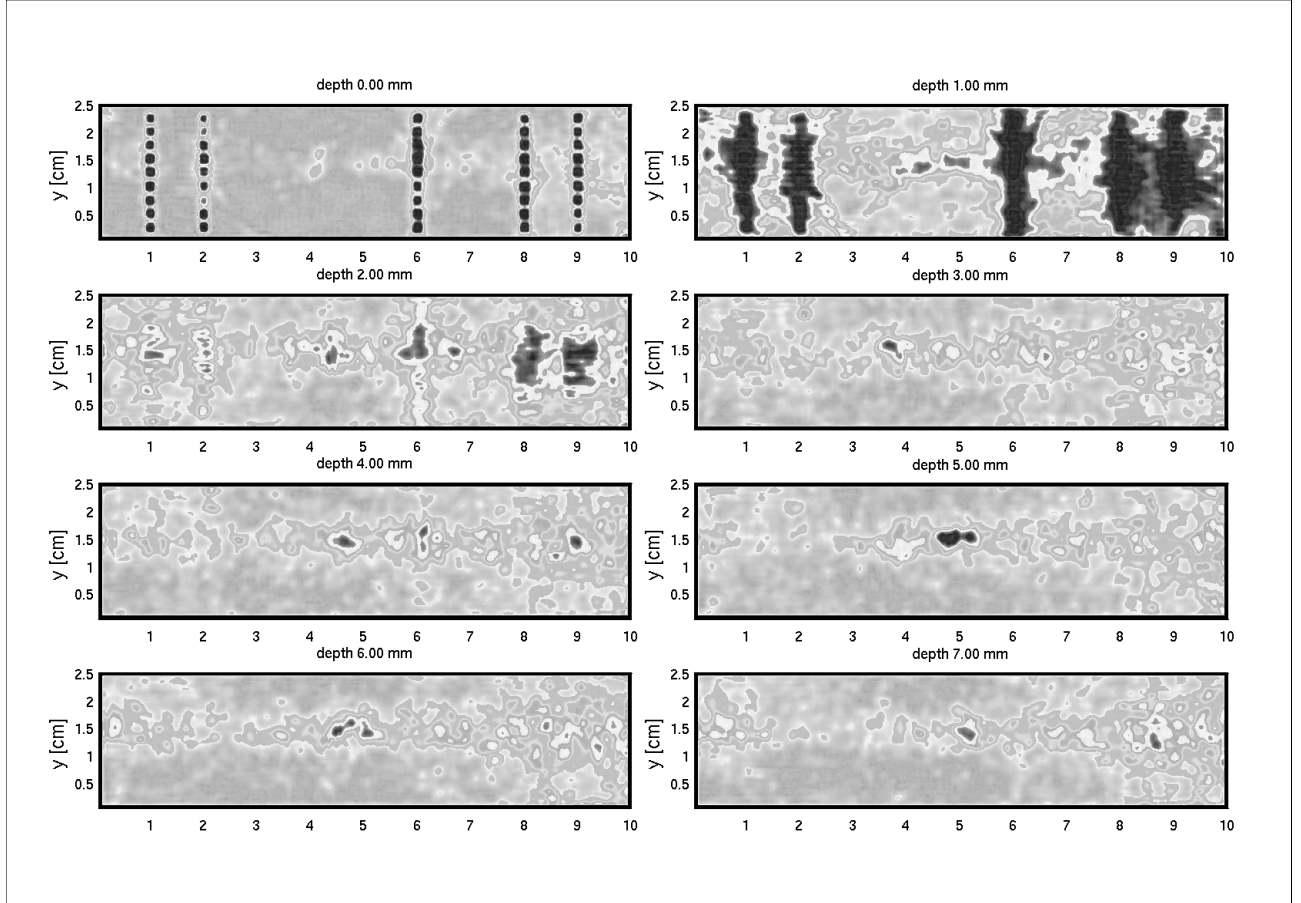


Figure 4.28: 2D slices taken as planes orthogonal to the z -axis from the 3D graph of the scalar field $M(x, y, z)$, calculated as the maximum in time of the norm of the displacement vector wavefield of the time-reversed backpropagation. Each inset corresponds to a 2D slice taken at a different value of z , called “depth” in the pictures. Lighter tones refer to lower values of the scalar field, darker tones to higher values. Apart from the plane $z = 0$ cm, where the TR transducers are positioned and from where they emit the time-reversed signals (see first row-first column inset), it can be seen that, on the plane $z = 0.5$ cm, the focusing occurs in a region in the neighbourhood of the point with coordinates $(5, 1.5)$, which is the position of one vertex of the parallelepiped nonlinear region simulating a classical nonlinear scatterer.

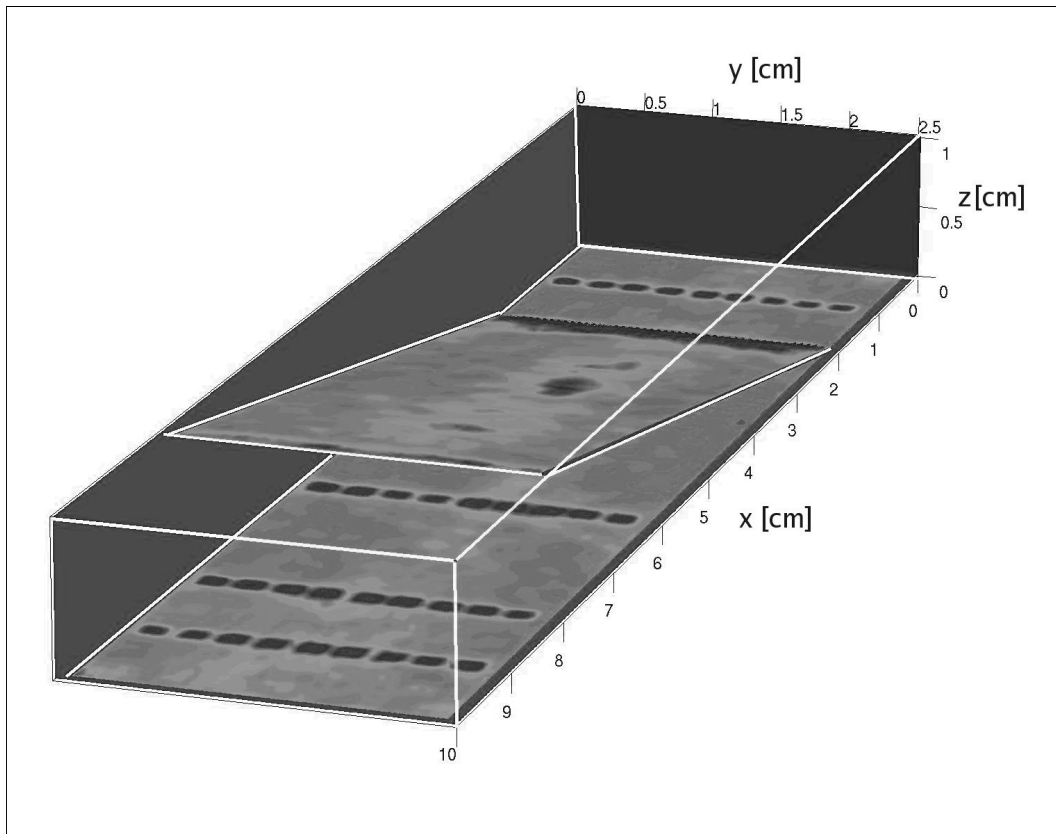


Figure 4.29: 3D partial representation of the scalar field $M(x, y, z)$ made by 2D plane slices from its 3D graphs. Four slices have been used: three of them are the coordinate planes $x = 0$, $y = 0$, $z = 0$ cm, the fourth one is a diagonal plane passing through the point of coordinates $(5.0, 1.5, 0.5)$ cm, one vertex of the nonlinear scatterer. It could be seen a clear spot localized in the region hosting the nonlinear scatterer.

geometry, shape and boundary conditions;

- use of virtual forward propagation experiments and corresponding backward propagation simulations in order to study the role of multiple sources in the retro-focusing.

Regarding the first issue, it has been introduced in the code the possibility of setting up specimens with a more complicated geometry than a simple parallelepiped (see Appendix III for details about the implementation). A first case study has been proposed by the cited Group of the Los Alamos National Laboratory, regarding a bearing cap used in the aircraft industry, with a visible surface macro-cracked area. Figure 4.30 shows two photos of the specimen and the respective coordinate axes used for its description within the computational code (first row): the left photo shows the $x - y$ face of the specimen, with transducers bonded on its surface at some locations, used by the researchers of the Los Alamos National Lab Group for physical TR Imaging experiments; it could be seen that the specimen presents two curved regions; the right photo shows the $x - z$ view of the specimen, revealing two quasi-cylindrical cavities with symmetry axis equal to the y axis.

After the implementation of the geometry and (free) boundary conditions of the specimen within the LISA-Spring 3D code, a simulated forward propagation experiment with one virtual point-like source placed in the $z = 0$ cm plane has been run, with 6 TR transducers placed also on the $z = 0$ cm face of the specimen. A region with classical nonlinear elastic behavior has been modelled and implemented in the computational code, placed in the neighborhood of the top of the internal arch. After that, the Computational TR Imaging technique has been applied in order to validate the ability of the method in the localization of the forward propagation source position.

Figures 4.31, 4.32, and 4.33 show some results of the TR backward simulated propagation: each plot is a 2D plot of the maximum-in-time of the norm of the displacement vector wavefield on a plane of the type $z = \text{const.}$, i.e. 2D slices of the graph of the scalar field $M(x, y, z)$, defined previously, at different depths (z positions).

Starting from the face $z = 0.25$ mm and going in depth within the specimen, the plots show that retro-focused elastic energy is localized mainly in eight points on the upper surface of the specimen: six points corresponds to the positions of the six TR transducers acting as sources for the backward propagation (they correspond in the first plot of Fig. 4.31 to the aligned bright spots, divided into two groups of three spots each); another point, localized in the neighborhood of the point with coordinates (10.1, 2.41, 0) cm, corresponds to the actual position of the point-like source of the forward propagation experiment. The eighth point, just in the neighbourhood of the top of the internal arch, corresponds to the position of the region with classical nonlinear elastic behavior, so acting as a stationary scatterer during the forward propagation part of the virtual experiment. The 2D slices other than the first two show no evidence of energy focalization. However the boundaries between the specimen and the environmental atmosphere (simulated as air) are well remarked due to the mechanical impedance mismatch between the two different media.

These results constitute another validation of the technique, using virtual experiments for the forward propagation part of the method. Work is ongoing in order to apply the technique to the real-world signals of real-world experiments of forward propagation performed at the Los Alamos National Laboratory by the cited Research Group.

This latter virtual TR Imaging experiment, although very simple, exemplifies the issue regarding the presence of multiple primary (or secondary, i.e. scatterers) sources during the forward propagation part of a real-world experiment: in the simple case just described, a primary source and a single classical nonlinear region acting as a secondary source during the forward propagation can be easily distinguished in the final images obtained by the simulated backward propagation, but it is possible to do so due to the simplicity of the setup and to the fact that it

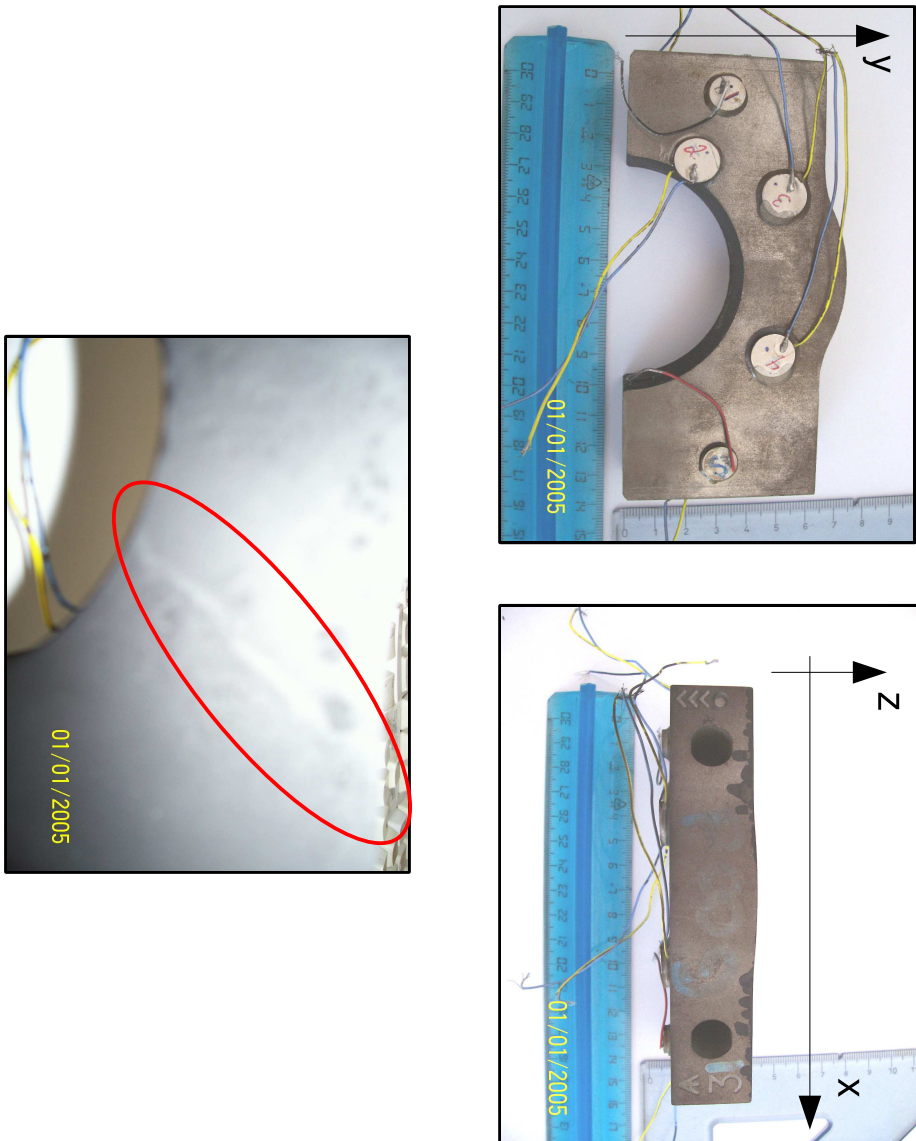


Figure 4.30: Three photographs of a damaged bearing cap used in the aircraft industry. The photos in the first row show the specimen from two different views, corresponding to two different planes of the frame of reference used for designing the specimen geometry and implementing it within the LISA-Spring 3D computational code. The third photo is a magnified image of a region in the neighborhood of the internal arch that shows the superficial signs of a macro-crack. The specimen has been made available courtesy by Dr. P.A. Johnson, EES-11 (Geophysics), Nonlinear Elasticity Group, Los Alamos National Laboratory (Los Alamos, New Mexico, USA).

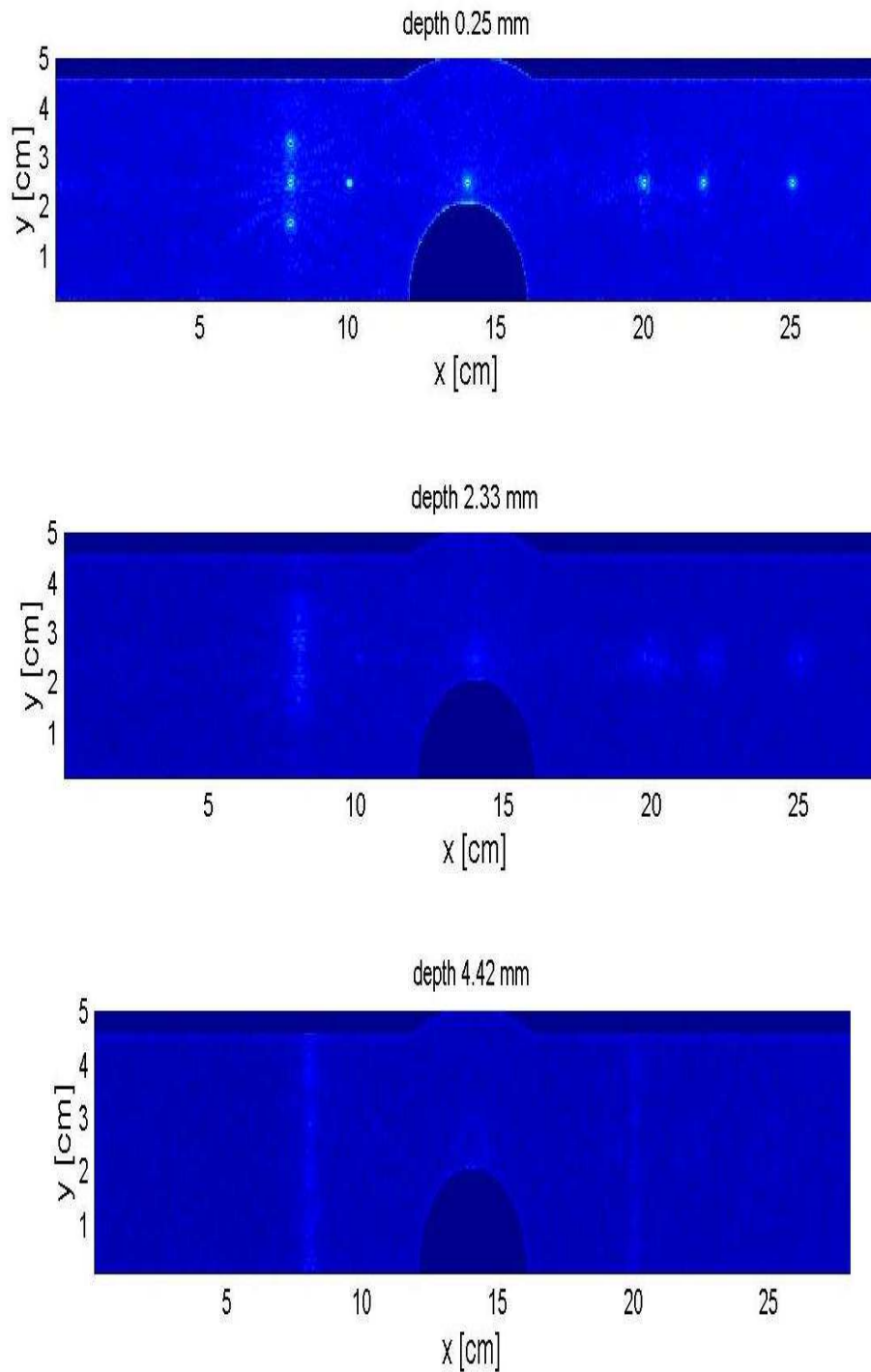


Figure 4.31: Results from a virtual experiment of localization of the source position via the Computational TR Imaging technique described above in the case of a solid damaged specimen with non-trivial geometry. 2D slices from the graph of the scalar field $M(x, y, z)$, i.e. the maximum-in-time of the norm of the displacement vector wavefield calculated during the TR backward propagation, are presented in correspondence of three different depths along the z axis, starting from the nearby of the $z = 0$ cm surface, where the TR transducers are placed. The elastic energy is focused on eight points, six of which correspond to the positions of the TR transducers, that act as sources for the simulated backward propagation (that is why energy retro-focuses on these positions), another point corresponds to the position of a point-like classical nonlinear defect, while the brightest point in the nearby of (10.1, 2.41, 0) cm is the actual position of the source of the forward propagation.

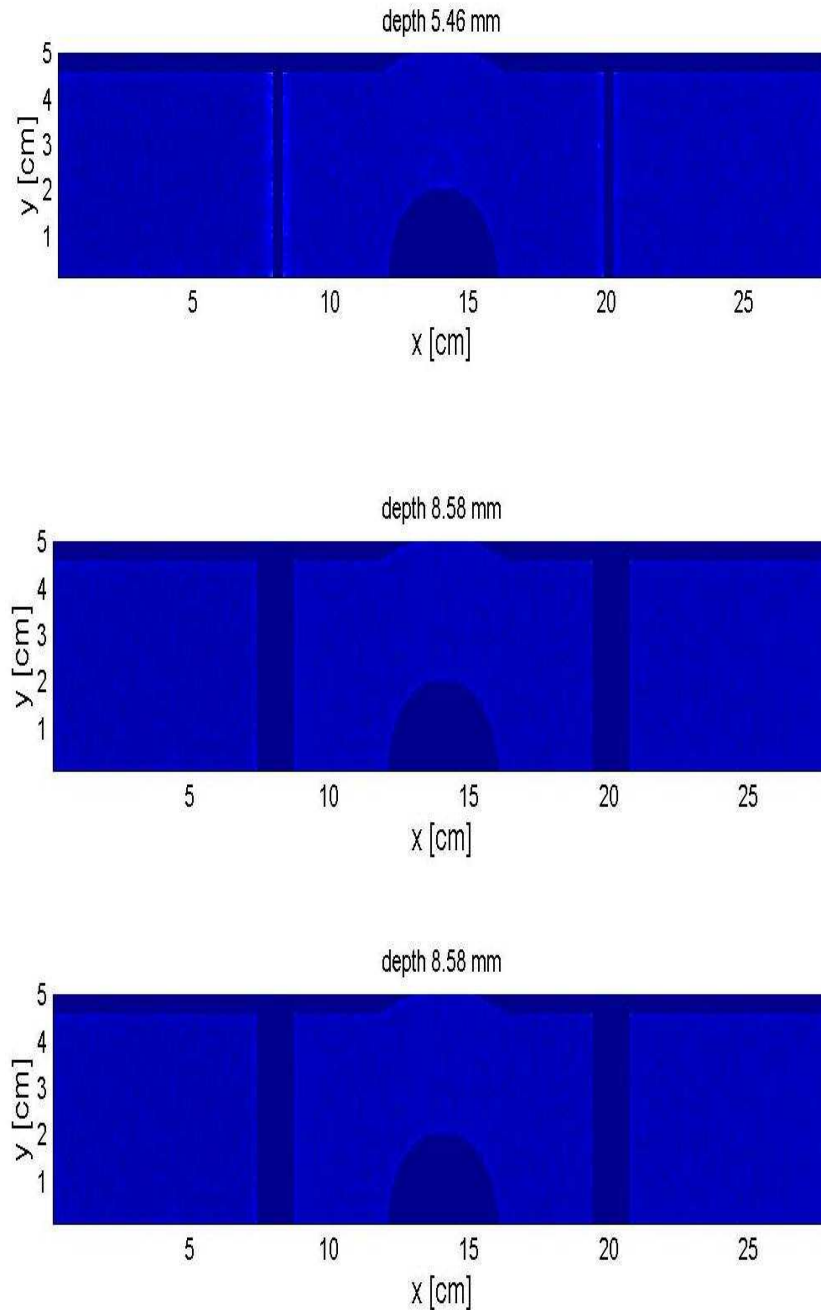


Figure 4.32: As in Fig. 4.31, 2D slices from the graph of $M(x, y, z)$ taken at inner depths within the specimen are presented: there is no evidence of elastic energy focusing, as it should be, because the defect (scatterer, i.e. secondary source) and the sources of the TR backward propagation are placed on the surface $z = 0$ cm. It could be noted how the simulation can distinguish and resolve the boundaries of the specimen, which are curved (theoretically) interfaces between the solid specimen and air, so in their regions there is an high impedance mismatch that generates such contrast in the images. Going in depth within the specimen, the width of the hollow cylinders increases, then it starts to decrease (see Fig. 4.33) due to the cylindrical shape itself.

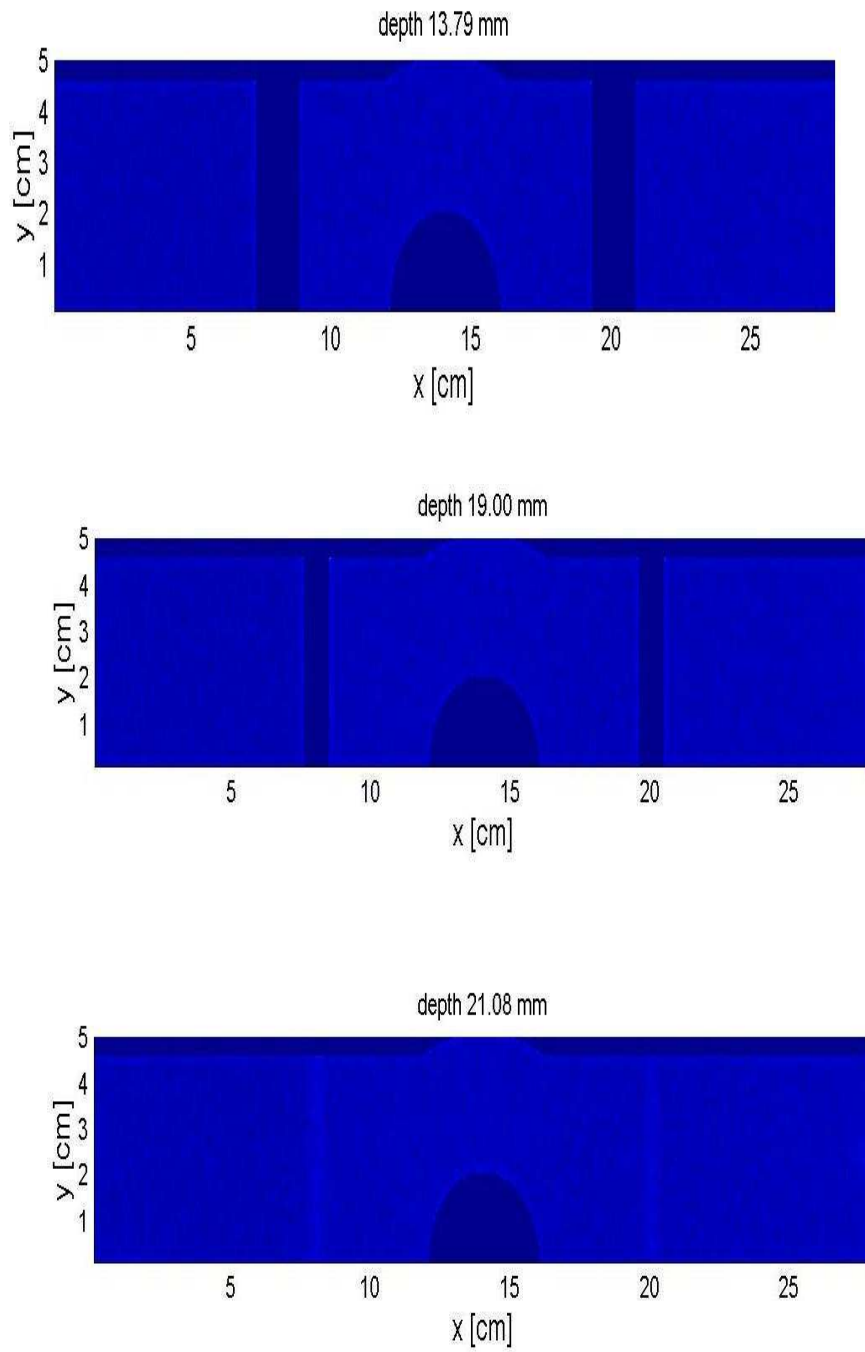


Figure 4.33: Other 2D slices from the graph of $M(x, y, z)$ at higher depths within the specimen, with no evidence of elastic energy focusing. The width of the hollow cylinders decreases due to their shape, correctly imaged by the computational technique.

is a virtual experiment, with the classical nonlinear region implemented by the programmer, so known in advance (as it should be in virtual experiments, useful only for validating and analyzing the method, not for its application). In the case the forward propagation signals derive from a real-world experiment and the only information at hand is the position of the TR transducers and of the forward propagation primary source, used for probing the specimen, the distinction and characterization of the focusing spots, present in the simulated backward propagation images, may be very difficult or in some cases such spots may be due to particular patterns of TR wave interference due to the presence of multiple secondary sources or secondary sources active at different times (but simultaneously) during the forward propagation.

Defects in an investigated specimen, behaving like scatterers, are expected either to be additional sources in the wave propagation or to additionally break TR Wave Physics properties. Experiments conducted at the Los Alamos National Laboratory has suggested that TRA can be implemented to observe damage in solids already in the early stages of its evolution, by exploiting the nonlinear features of early stage cracks and microinhomogeneities. TR-NEWS Imaging techniques [134], in particular, exploits the modulation of two acoustic waves and the sidebands generation in order to filter the signal before TR and obtaining selective focusing on the nonlinear scatterers. Use of TRA for defects imaging is, however, a more complex problem due to the presence of multiple sources, as discussed. Indeed, each scatterer behaves as a source in the propagating medium, in addition to the transducer which is, by far, the strongest one. Obtaining selective focusing is possible and several methods have been already developed by the group of Fink. Among them there are the “Decomposition de L’Operateur Temporel” (DORT) [121, 122] method or other decomposition methods [123]. Nevertheless, multiple sources may become a serious problem in the presence of nonlinear effects due to scatterers. Here, indeed, sources with up to one order of magnitude different amplitude (e.g. two nonlinear scatterers or the nonlinear scatterer and the transducer itself) can be present within the specimen and also sources which are active cyclically in time or for a long time window, hence somehow equivalent to multiple sources. For instance, in the case of low attenuative media with nonlinear scatterers, the amplitude of the ultrasonic wave may remain large enough to excite the nonlinearity of the scatterer for a long interval of time.

Ongoing work by me, M. Scalerandi, A. Gliozzi (Dept. of Physics, Polytechnic of Torino) and the Group of P.A. Johnson at the Los Alamos National Laboratory is addressed to show how the presence of multiple sources, either as located in different positions or active in different time windows, affects the reconstruction of the primary source signal. In particular, this work has as its main objective the analysis of the effects on phase coherence of the signals retro-focused from TR transducers localized in different positions and the advantages of using longer time signals to be time-reversed or a larger number of TR channels. The efficiency of different methods for visualising and reconstructing the signals is under analysis at the time this Ph.D. thesis has been written. The analysis has been performed using both synthetic and experimental data, considering a typical experiment with specimens having simple geometries. Virtual forward propagation experiments and correspondent simulated backward propagation have been performed using the LISA-Spring 3D computational code. Preliminary results have been undergoing a first study and analysis.

Chapter 5

Conclusions and future developments

Here, I try to make a short resume of the work presented in this Thesis, underlying the topical issues, the problems that have arisen during the work, the achieved results, the problematic issues still to be solved and the ongoing and future developments on these topics

5.1 Summary of achieved results

The main original achieved results of my Ph.D. work can be collected in two different sets having a common objective: the exploitation of NCNL elastic effects due to damage in order to characterize and localize it.

The first set of results regards the basic investigation of the NCNL elastic behavior of concrete with and without damage in the form of distributions of micro-cracks and/or extended macro-cracks. The experimental measurements about slow and fast dynamics in quasi-intact and damaged concrete samples and the best fitting of the resulting data by numerical simulations made with the LISA-Spring 1D model have led to one of the first complete study about the connection between damage and NCNL Elasticity of concrete. Also, this study has been one of the most complete test-bed for the validation of the LISA-Spring modeling approach in the simulation of elastic wave propagation in NCNL elastic materials.

The second set of results regards the development of a technique for the spatial localization of defects (behaving as scatterers) in solid specimens, especially the selective imaging of such defects that induce NCNL elastic responses in the overall elastic behavior of the specimens. The technique exploits Time Reversal Acoustics (TRA) methods and numerical simulations at the same time, being the numerical simulations used instead of real experiments in the second part of the typical TRA probing experiments, because they let the formation of 3D images of bulk scattering regions.

The novelty of the technique consists in a signal processing approach to the forward propagation signals in order to realize a selective focusing of elastic wavefronts on NCNL scatterers (defects of interest for nondestruction evaluation purposes) instead of inhomogeneities or primary sources of forward propagation. This method has been validated with virtual experiments, i.e. simulated forward propagation experiments.

Although numerical simulations code are used only as tools for reaching such objectives, their development and implementation have constituted a fundamental part of the Ph.D. work, especially for what regards the 3D parallel LISA-Spring code: without a parallel code, it would have been impossible to setup and realize backward simulations of real-world specimens with typical dimensions of up to tens of cm.

5.2 Supplementary work to be done

As cited in Section 4.3.2, up to now the 3D simulations have been realized with a LISA-Spring code that treats, as it is formulated, interstices according to the LISA-like approach, i.e. as rigid elements, not as HEEs. This formulation is sufficient for the use of the code for TR backward propagation simulations (the actual Imaging tool). However, as it has been shown previously, virtual TRA experiments may be useful support tools for analyzing complicate TR Wave Physics phenomena in damaged solid specimens that make difficult a selective focusing on defects of interest. So, one of the needed developments of the 3D LISA-Spring model consists in the appropriate modeling of HEEs in 3D, a difficult task due to the trade-off between sufficient completeness of the modeling for describing poro-viscoelastic behavior of interstices in 3D and the total number of parameters, related to a vectorial Preisach-Mayergoyz formulation, added to the model, most of all cannot be associated to measurable observables, so they are free degrees of freedom of the model.

5.3 Ongoing and future developments

Along the last two Sections of Chapter 4, I have cited the ongoing collaboration between Dr. M. Scalerandi, Prof. P.P. Delsanto (Dept. of Physics, Polytechnic of Torino) and the Research group of Dr. P.A. Johnson, EES-11 (Geophysics), Nonlinear Elasticity Group, Los Alamos National Laboratory (Los Alamos, New Mexico, USA), dedicated to the further development of Nonlinear TRA Imaging techniques and to their applications in nondestructing evaluation of solid specimens and in their exploitation for suggesting novel seismic computational imaging methods for the 3D localization and spatial/temporal characterization of Earthquake sources. Within the context of such collaboration and of the ongoing project at the Los Alamos National Lab (which I'm involved in), the main future developments of my Ph.D. work can be outlined.

5.3.1 Selective localization and characterization of defects in solid NCNL elastic materials

The Computational TR Imaging method described in Sections 4.2 and 4.3 finds its natural application in the nondestructive evaluation of defects in solid laboratory specimens. The 3D LISA-like code must be considered as an imaging tool having as input data the collected signals of a probing forward propagation experiment throughout the specimen under investigation. However, virtual TRA experiments are being used for supporting the analysis of experimental results with complicated patterns of interference between TR propagated waves. One of the main issue under study at the moment of the writing of this Ph.D. thesis regards the presence of multiple primary and secondary sources emitting waves during the forward propagation during the same TR temporal window. The big deal is to extend or devise a new signal processing approach in order to be able to selectively retro-focusing elastic energy on one scatterer instead of other ones. Parametric studies about the role of transducers dimensions, near- or far-field regime of propagation, influence of geometric position of TR transducers and of their total number are other subjects of ongoing Research, both experimentally and theoretically, with the use of Green's functions approaches and with LISA-Spring simulations.

5.3.2 Spatial and temporal characterization of Earthquake sources and physical mechanisms

As presented in Chapter 2, Earth materials have been among the first materials shown to exhibit NCNL elastic behavior and they have served as testbeds for the development of many experimental techniques and theoretical approaches for studying such anomalous nonlinear elastic

effects, experimental and theoretical tools then used for the study of NCNL Elasticity of other types of solid materials.

As reported in Section 2.2, from an historical point of view it was a pure interest in Earth Sciences issues that led to the investigation of the quasi-static stress-strain constitutive relation of rocks. It should be added to what exposed there that another basic issue in Earth Sciences suggested to study in a thorough way the nonlinear elastic behavior of Earth's materials, i.e. the imaging of Earthquake sources.

Citing from Ref. [30]: «In Seismology, “acoustic approximation” is frequently used. In fact much of the world's early seismic imaging is based on acoustic approximation. It was thus only natural to examine the nonlinearity of the Earth and Earth's materials with nonlinear acoustics analogues. These nonlinear experiments were performed to explore and potentially develop techniques commonly used in Nonlinear Acoustics for seismic imaging applications. Early experiments at the Los Alamos National Laboratory were carried out to create a parametric array in the Earth (using an array of seismic sources). Although the results were inconclusive, the fact that Earth's materials were highly nonlinear was unmistakable. Nonlinear research in Earth materials was thus scaled down to the laboratory ([135, 136, 137]) and nearly ten years of Research into the nonlinearity of Earth's materials resulted. Over this period, various types of rocks were studied and all were found to be highly nonlinear; notably, sedimentary rocks (which are oil and gas bearing) showed the largest and most interesting nonlinearities».

So, while during the 1980s Research interests in Earth Sciences (particularly Seismic Imaging) led to basic investigations of the anomalous nonlinear elastic behaviors in Rocks using laboratory experiments taking advantage of the “acoustic approximation”, i.e. the use of ultrasound and acoustic waves instead of seismic ones due to the appropriate scaling in the dimensions of the material specimens, during the 1990s such investigations were extended to the field of Nondestructive Evaluation and (recently) Imaging of damaged solid materials.

In the last few years, a reverse path has been leading to exploit the considerable amount of knowledge obtained by laboratory experiments and modeling again for Earth Sciences issues, in particular for the spatial and temporal characterization of Earthquake sources and physical mechanisms.

One recent Research subject is the study of the role of the (nonclassical) nonlinear elastic behavior of unconsolidated granular media in strong ground motion and Earthquake Physics. Indeed, during an Earthquake, strong ground motion is induced and broad-frequency band elastic (seismic) waves propagate from hypocentral depths of the order of 10 Km to the Earth's surface. Sediments at the surface, composed by granular media, can respond by ringing at their vibration *eigenmodes*. The shear *eigenmodes* are particularly dangerous because of the possibility of their coupling with buildings and infrastructures *eigenmodes*, then inducing damage or failure of the structures themselves.

The NCNL elastic behavior of near-surface sediments during an earthquake was demonstrated by the analysis of data about the 1994 Parkfield (California) earthquake: due to such nonlinear elastic responses, it has been showed that the large earthquake, occurred in the Los Angeles Basin site, induced a 75% decrease in the surface-layer resonance frequencies of certain vibration *eigenmodes* [138].

Recently, it has been proposed that a phenomenon known as **dynamic earthquake triggering** [139, 140] could be due in part to the NCNL elastic behavior of Earth's materials [3].

Dynamic earthquake triggering consists in the manifestations of aftershocks events at hundred of kilometers from a mainshock at the time or soon after the seismic waves emitted by the mainshock encounter a distant fault ¹, thus inducing a new seismic event of small-intermediate

¹The mainshock is the large intensity seismic event whose magnitude is usually reported for characterizing an earthquake, using either the Richter's or the Mercalli's scale, while other seismic events of smaller magnitude, thus usually not reported to the general public, take place just before and after the mainshock, called respectively

magnitude. It has been demonstrated that dynamic earthquake triggering takes place although it is triggered by strain waves with amplitude levels of the order of $10^{-7} \div 10^{-6}$, i.e. small strains compared to the intensity of such aftershocks [139].

It has been suggested that, under proper conditions, the triggering of the aftershocks may be due to a NCNL softening and weakening of the fault core, i.e. of the gouge granular material that is created by a fault as it progressively slips over the history of the fault. The strain waves inducing the aftershocks may reduce temporarily the core elastic constants, so the material strength, up to a sufficient order for inducing a fault slip, so other hierarchic triggering events [3].

Laboratory experiments on composite materials and sedimentary rock specimens under execution at the EES-11 (Geophysics Group) Division of the Los Alamos National Laboratory and 3D numerical simulations reported in Section 4.3.2 about the selective localization and characterization of multiple active secondary sources due to defects in solid specimens via the developed computational TRA Imaging technique, described in Section 4.2, are subjects of further and thorough investigation within the framework of the Project “Image Reconstruction with Time Reversal Mirrors” funded by the Department of Energy of USA and hosted by the Los Alamos National Laboratory itself, into which I’m involved. The targets of such studies are not only the applications of the TRA Imaging techniques in the field of Nondestructive Evaluation and Imaging of defects in laboratory solid specimens but also the use of such methods for developing analog techniques for the characterization in time and the localization in space of earthquake sources. Particularly, part of this project is devoted to the implementation of 3D computational TRA Imaging methods similar to the one proposed in this Ph.D. thesis in new 3D computational codes for seismic imaging purposes [141] using different numerical methods (Spectral Element Methods [142, 143, 144, 145, 146, 147]).

foreshocks and aftershocks.

Appendix I. LISA-Spring 1D model and computational code

The 1D LISA-Spring model formulation is based on the equivalence between the FDTD numerical solution of the Elastodynamics equation² and the description of the 1D bar-shaped specimen like a chain of viscoelastic analog mechanical springs.

The discretization of the bar-shaped specimen (with a circular or rectangular cross section) along its symmetry/longitudinal axis leads to the individuation of the nodes of the 1D lattice, in which the physical observables of interest are evaluated. I choose a formulation so that each node i corresponds to the position $x_i = l \cdot i$, where $i = 0, 1, \dots, N$, one side of the bar being in position $x_0 = 0$ and the other one in $x_N = l \cdot N$. Each node i , $\forall i = 1, 2, \dots, (N - 1)$, is connected to its two nearest neighbours by a 1D “scalar” spring (see Appendix II for the definition of tensorial springs). The portion of material between x_{i-1} and x_i is considered as associated to the node i , so that the specimen is divided in N cells: all the physical properties of the j -th, $\forall j = 1, 2, \dots, N$ cell are considered associated to the a virtual representative particle placed in the node i (position x_i). The first node, $i = 0$ is considered too as a physical node with mass.

At the initial time, the representative particles are considered at rest at their positions $x_i^0 = i \cdot l$, except for the application of a force into some of their positions. The total length of the specimen is equal to $L = l \cdot N$.

Starting from the simplest case of an homogeneous specimen, the elastic constants of each spring are assumed to have the same value K . After the perturbation of the state of the system of chained mass springs at the initial time, each particle i undergoes a displacement calculated as

$$u_i^t = (x_i^t - x_i^0) \quad (1)$$

Considering linear springs, then Hooke’s law can be used to calculate the forces acting on each particle of the node i :

$$F = -K \cdot \Delta l$$

where F is the force and $\Delta l = (l^t - l)$ is the variation of the distance between the particle i and the particle $(i - 1)$ at the time t . It could be easily derived that $\Delta l = u_i^t - u_{i-1}^t$.

The particle i , except for $i = 0$ and $i = N$, is subjected to two forces along the x axis:

$$\begin{aligned} F_i^{t,-} &= K \cdot (u_{i-1}^t - u_i^t) \\ F_i^{t,+} &= K \cdot (u_{i+1}^t - u_i^t) \end{aligned} \quad (2)$$

respectively from the left and right nearest neighbor.

The equation of motion for the i -th particle is thus set up:

$$m \cdot \frac{d^2 u_i}{dt^2} = F_i^{t,+} + F_i^{t,-} \quad (3)$$

where m is the total mass of the i -th cell, equal for each cell to the homogeneity hypothesis. Using a 1st order FDTD discretization scheme, the finite difference coupled equations of motions result to be

$$u_{i+1}^t = 2 \cdot (1 - c) \cdot u_i^t + c \cdot (u_{i-1}^t + u_{i+1}^t - u_i^{t-1}) \quad (4)$$

where c is called the Courant’s number, it is equal to $c = \frac{m}{\tau^2}$, where τ is the time-discretization step (t is an integer index from 0). This parameter is very important for convergence and stability of the finite difference equations, it has been showed theoretically that it must have a value $\simeq 1$.

²in the case of the 1D longitudinal wave mode of propagation the Elastodynamics equations reduce to only one equation of motion, the one for the component of the displacement vector wavefield along the axis of the bar, assumed from now on to be the x axis of the Cartesian frame of reference

The same equations of motion can be obtained starting from a Continuum Mechanics formulation, i.e. from the equation of motion 2.1 and from a linear stress-strain equation $\sigma = E \cdot \epsilon$. Using always a first order spatial and time FD scheme, Eq.s. 4 are derived, where the Courant's number is defined as

$$c = \frac{E}{\rho} \cdot \frac{\tau^2}{l} \quad (5)$$

where l (the rest-length of each spring in the spring model) is the mesh step and ρ is the volumetric mass density, $\rho = \frac{m}{\Sigma \cdot l}$, where Σ is the cross-section area of the bar, finally E is the Young's modulus of the bar.

Starting to consider the possibility of an heterogeneous bar-shaped specimen, a new lattice is super-imposed to the previous one such that now the virtual representative particle i is placed, at rest, at the center of the cell i , i.e. in the position $x_i = l \cdot (i + \frac{1}{2})$. It means that each cell i is now separated, by the position of the mass particle, in two different parts having different physical parameters ρ , S , etc. At rest (i.e. in a condition of mechanical equilibrium), each representative particle has still two nearest neighbors (except again for the ones at the sides of the bar) with which it interacts through virtual springs having different mechanical properties in principle. The particle identifies the position of the interfaces between two different homogeneous cells made of two distinct materials, in general.

In order to introduce the interface between such cells of different materials as physical components influence the dynamics of the chain of springs, the particle i (at rest in the position of the node i of the lattice) is split into two virtual subnodes, i^- at left and i^+ at right, each identifying the corresponding lateral side cell of material. Although it could be avoided to assign a dimension to the interface, i.e. a distance at rest between the two sub-nodes, it is assumed that each sub-particles interacts with its nearest neighbours, i.e. forces internal to the interstices are assumed to exist (see Fig. 2.11 for a schematization of the lattice with original nodes splitted in couples of sub-nodes.). This assumption corresponds to considering the existence of an analog spring within each interface region.

Instead of having equations of equations of motions for each particle i , the set of coupled FDTD equations regards the sub-particles i^- and i^+ :

$$m_i^- \cdot \frac{d^2 u_i^-}{dt^2} = F_i^- + f_i^- \quad (6)$$

$$m_i^+ \cdot \frac{d^2 u_i^+}{dt^2} = F_i^+ + f_i^+ \quad (7)$$

where m_i^- and m_i^+ are the masses of the two sub-particles (i.e. the two half-cells, one of the cell $i - 1$, the other one of the cell i , interfaced by the two sub-particles),

$$\begin{aligned} m_i^- &= \frac{1}{2} \cdot \Sigma \cdot \rho_i^- \cdot l_i^- \\ m_i^+ &= \frac{1}{2} \cdot \Sigma \cdot \rho_i^+ \cdot l_i^+ \end{aligned} \quad (8)$$

u_i^- and u_i^+ are the displacements of the two sub-particles, F_i^- and F_i^+ are the external forces acting respectively on the two sub-particles due to the springs of the homogeneous cells of materials, f_i^- and f_i^+ are the internal forces due to the spring representing the interface, ρ_i^- and ρ_i^+ are the respective volumetric mass densities of the material of the two half-cells, l_i^- and l_i^+ are the rest-length of the two half-cells.

The external forces are formulated and calculated using the usual Hooke's law, while the expression of the internal forces depends from the modeling of the mechanical behavior of the

media of the interfaces:

$$F_i^- = \frac{\Sigma \cdot S_i^-}{l_i^-} \cdot (u_{i-1}^+ - u_i^-) \quad (9)$$

$$F_i^+ = \frac{\Sigma \cdot S_i^+}{l_i^+} \cdot (u_{i+1}^- - u_i^+) \quad (10)$$

At this point of the formulation, it could be observed that the linear springs at the basis of the external forces are extended across homogeneous regions of materials (cell material), while the spring internal at an interface connects the two sub-particles of the two pieces of the two distinct materials. In the case of the “grainy” media with NCNL elastic behavior, the linear elastic springs are correspondent to the grains while the internal springs are correspondent to the poro-viscoelastic media filling in the interstices (see Section 2.2.2).

The FDTD equations of motions for the sub-particles are

$$u_i^{\pm, (t+1)} = (2 - c_i^{\pm}) \cdot u_i^{\pm, t} + c_i^{\pm} \cdot u_{i\pm 1}^{\mp, t} + \overset{\approx \pm, t}{f}_i u_i^{\pm, (t-1)} \quad (11)$$

where c_i^{\pm} is the Courant’s number for the respective two hal-cells of the two neighboring material cells and are defined as

$$c_i^{\pm} = \frac{E_i^{\pm}}{\rho_i^{\pm}} \cdot \frac{2 \cdot \tau^2}{(l_i^{\pm})^2} \quad (12)$$

being E_i^{\pm} and ρ_i^{\pm} the Young’s moduli and volumetric mass densities of the two half-cells of the two neighboring materials, finally $\overset{\approx \pm, t}{f}_i$ are re-scaled internal forces defined as

$$\overset{\approx \pm, t}{f}_i = \tau^2 \cdot \frac{2 \cdot f_i^{\pm}}{\rho_i^{\pm} \cdot l_i^{\pm} \cdot \Sigma}. \quad (13)$$

In the implementation of the LISA-Spring model into a computational code, the main variable of interest is the displacement of the virtual centre of mass of each couple of sub-particles each initial particle is splitted into,

$$u_i^{cm} = \frac{m_i^- \cdot u_i^- + m_i^+ \cdot u_i^+}{m_i^- + m_i^+}. \quad (14)$$

A perfect rigid interface is defined imposing the two conditions

$$\begin{aligned} f_i^+ &= f_i^+ \\ u_i^{cm} &= u_i^+ = u_i^- \end{aligned} \quad (15)$$

which lead to the subsequent definitions of the internal forces for each interstice i ,

$$\begin{aligned} f_i^+ &= \frac{-m_i^- \cdot F_i^+ + m_i^+ \cdot F_i^-}{m_i^+ + m_i^-} \\ f_i^- &= -f_i^+. \end{aligned} \quad (16)$$

These conditions correspond to the case of rigid interfaces whose thickness does not change in time³. They do not interact and influence the elastic wave propagation throughout the bar, they transmit instantaneously the perturbation from the left side i^- to the right one i^+ . So

³In actual implementations of the model, with rigid or elastic interstices, their real thicknesses are not used in calculating the total length of the specimen because very low compared with the grains lengths, while their change in time influence how the sub-particles oscillate, so how the waves propagate through the specimen

these conditions for the model are used in regions of the specimen where there are interfaces between different media but the elastic propagation through them is fully linear [60].

In order to model the interstices as Hysteretic Elastic Elements (HEEs) as described in Section 2.2.2, the internal forces associated to the internal springs are defined as [45, 46]

$$f_i^{+,t} = -f_i^{-,t} = f^t = -\frac{a'_1}{2} \cdot P_i^t + a'_2 \cdot (u_i^{+,t} - u_i^{-,t}) + a'_3 \cdot (u_i^{+,t} - u_i^{+,t-1} - u_i^{+,t} + u_i^{+,t-1}) \quad (17)$$

where the vector parameter (a'_1, a'_2, a'_3) is th equivalent of the one for the continuum formulation, a_1, a_2, a_3 and can assume two values for describing two possible elastic behaviors of the interstice, $(a'_1, a'_2, a'_3)_R$, corresponding to a generalized “rigid” state with $a'_2 = 0$, and $(a'_1, a'_2, a'_3)_{PE}$, corresponding to a poro-viscoelastic state. The switching between the two states is regulated by the PM formalism described in Section 2.2.2, where the poro-viscoelastic pressure P is defined as $F^+ - F^-$ or a linear combination of the two external forces with the coefficient of F^- being negative (see 2.2.2).

It should be noted that the rigid state in this case has a more general form, including a term of attenuation of the perturbation transmitted instantaneously through the interstice.

The expression for the internal forces in the case of the LISA-Spring 1D model for specimens including regions with interstices defined as HEEs, so for the simulation of elastic wave propagation through specimens with NCNL elastic features, was first introduced on a phenomenological manner by Scalreandi *et al.* [45, 46, 69], then it has been showed (with a reversed path, first for the 2D case, then for the 1D one) by Gliozzi et al. that this way of formulation is a simple generalization of the expression that can be obtained for the internal forces under the condition for a constant-in-time deformation of the interstice, which is a different definition of the rigid state as defined by Eq.s. 15 that imply that the interstices does not undergo any kind of deformation (its tickness remain constant in time).

Appendix II. LISA-Spring 2D model and computational code

As described in the part of Section 2.2.2 dedicated to the LISA-Spring 2D model, the components of the total external (vectorial) force on a sub-particle of a cell material are given by the sum of all stress components in the contiguous material cell that tear in the respective direction multiplied by the area, on which they act. Figure 1 shows where the material cell stresses are calculated.

As expressed by Eq. 2.21, the total external force acting on the sub-node k of a cell material is the sum of the three forces due to the linear elastic interactions with the other three sub-nodes of the same material cells. Such forces can be formulated as the product of a matrix times the vectorial relative displacement of the two sub-nodes, just as a consequence of the calculations of stress tensor components. It results that such forces can be theoretically thought as due to “tensorial” springs connecting the sub-nodes. However, I would like to remind that the tensorial springs are “ideal” springs useful for the description of the formulation of the model, their meaning being only on a mathematical basis and not a physical one.

Eq.s 10 are written with such vectorial formulation, where the matrixes M_n^k are defined as follows:

$$M_n^k = l_z \cdot \begin{pmatrix} 0 & \psi_k \\ \psi_k & 0 \end{pmatrix} \quad (18)$$

$$\forall k = n = 0, 1, 2, 3, \text{ where } \psi_k = (-1)^k \cdot \frac{\lambda_k + \mu_k}{4},$$

$$M_n^k = l_z \cdot \begin{pmatrix} \frac{\sigma_k}{2} & -\chi_k \\ \chi_k & \frac{\mu_k}{2} \end{pmatrix} \quad (19)$$

$$\text{for } n = 4, k = 0, 3 \text{ or } n = 6, k = 1, 2, \text{ where } \chi_k = (-1)^k \cdot \frac{\lambda_k - \mu_k}{4},$$

$$M_n^k = l_z \cdot \begin{pmatrix} \frac{\mu_k}{2} & \chi_k \\ -\chi_k & \frac{\sigma_k}{2} \end{pmatrix} \quad (20)$$

for $n = 5, k = 0, 1$ or $n = 7, k = 2, 3$.

The first type of matrixes defines the tensorial diagonal springs, the second type the tensorial horizontal springs while the last one the tensorial vertical one. It should be remembered, as reported in Section 2.2.2, that σ_k , λ_k and μ_k are the three independent elastic constants of the k -th sub-node, having developed a formulation only for crystalline materials with cubic symmetry or elastically isotropic.

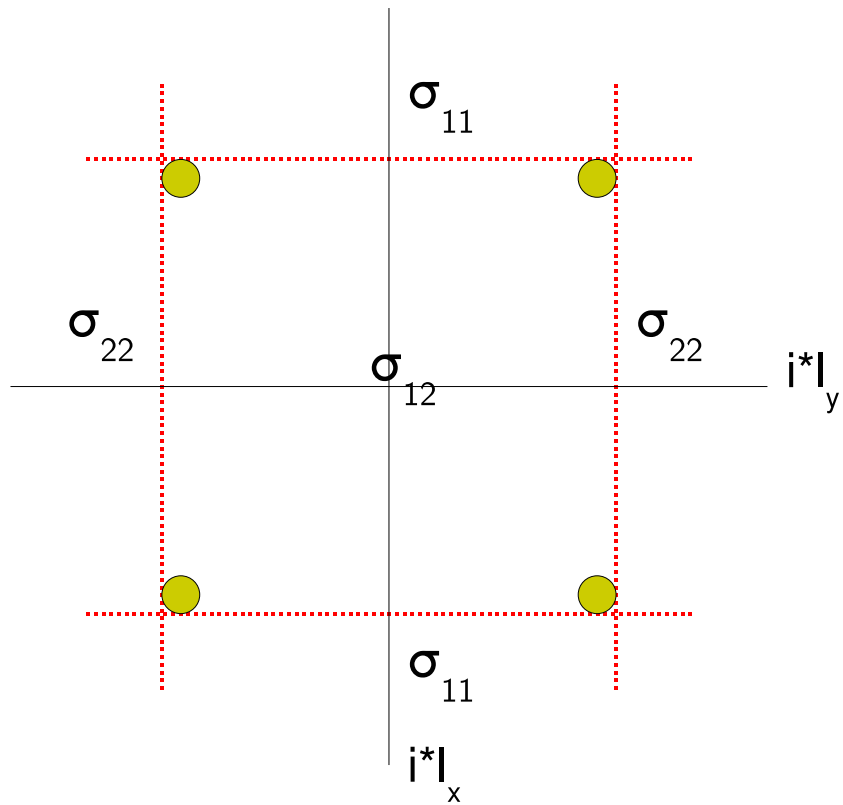


Figure 1: Schema about the locations where the elastic stresses in a material cell are calculated. The mass of the cell is shared by the four contiguous sub-nodes, ideally placed at the vertexes of the material cell and indicated in the schema with the same colour. As for Fig. 2.12, the solid dark lines belongs to the geometric lattice, while the dashed red ones to the materials lattice.

Appendix III. LISA-Spring 3D model and computational code

The LISA-Spring 3D model has been developed as a natural extension of the 2D one, due to the fact that the latter is already an approximated version of the former (see Section 2.2.2 entitled “LISA-Spring model of 2D elastic wave propagation” and Appendix II for the description of the 2D correspondent model and the approximations used to derive it from a 3D case).

The 3D model has been implemented without any kind of approximation about the elastic anisotropy of the material, so using for the grains (materials cells) linear stress-strain equations with all the 21 second order elastic constants (and also the correspondent third order elastic constants for the cells belonging to the regions with classical nonlinear behavior).

Regarding the modeling of the attenuative behavior of the specimens, it has been made the same choice of the 2D case: the attenuation has been introduced in the formulation directly with a term proportional to the first order total time derivative of the displacement vector field in the equations of motion instead of using for each material cells Kelvin-Voigt’s stress-strain equations of state. The reason for such a choice is the same already reported in Section 2.2.2: avoiding to introduce too many parameters due to the elements of the first order viscosity tensor.

For the formulation of the internal forces, the 3D version of the Eq.s. 2.28, which means considering each interstice in a rigid state as formulated by the LISA modeling approach. So, the 3D model, up to now, does not let simulate NCNL elastic effects. Two main reasons are at the basis of such a 3D implementation:

- after a preliminary validation of the computational TR Imaging approach described in Section 4.2 (see Sections 4.3,4.3.1), the main purpose of the ongoing work is its validation using real-world forward propagation signals, in order to apply the method itself to defects imaging in real-world specimens of interest, e.g., in the nondestructive evaluation problems within the AERONEWS project; having this objective in mind, it is sufficient to use a 3D LISA-like computational code, because the simulated backpropagation is made through an elastic linear specimen with the same geometrical and physical properties of the real one except for the presence of nonlinear scatterers (e.g. defect regions, sources of NCNL elastic behavior);
- a 3D extension of the LISA-Spring 2D model is very complicated, first of all because the it requires a thorough study of how to implement the PM description of HEEs in 3D; particularly, a good choice of the control parameter(s) is necessary, the use of one among the three *eigenstresses* (see Section 2.2.2 about the 2D LISA-Spring model) might be not sufficient for a full modeling of NCNL elastic behavior in 3D; however, such a formulation is very complicated from a theoretical point of view and it necessary requires the use of Preisach-Mayergoyz vector models [148, 149, 150, 41], which imply a huge number of additional parameters not directly correlated to experimental measurable observables, so degrees of freedom for the model.

Regarding the latter point, I would like to remark that an application of multi-dimensional Preisach-Mayergoyz model to the description of NCNL elastic behavior of 3D solids have been developed by Helbig *et al.* [151, 152], but it is doubtful implementing such theoretical formalism due to the high numbers of new parameters to be considered in the 3D code, in addition to the ones already used. A tentative new approach to the solution of such problem is under development by M. Scalerandi and A.S. Gliozzi (Dept. of Physics, Polytechnic of Torino).

So, I have developed a 3D LISA-Spring model with rigid interstices modeling and I have implemented it in a 3D parallel code (written in C language) to be run on distributed shared-memory parallel supercomputers, using the version 1.2.5 of the MPICH implementation of the MPI (Message Passing Interface) standard.

The parallel code, as developed, assumes as x axis the one along which the specimen to be modelled has its longest dimension. A data parallel-like approach has been used, with subdivi-

sion of the specimen in 3D slices along the x axis, assigned during the computing to different processing units (different process within the parallel job). However, the approach used for parallelization is actually not of the type data-parallel, due to the dependences of the variables evaluated in the nodes belonging to the boundary of each slice, orthogonal to the x axis, from the values of the respective variables evaluated on the nodes of the respective boundaries of the nearest neighbour slices. So, a typical “phantom” boundary layers algorithm [153] has been used such that the message passing routines of the parallel code are mainly dedicated to the exchange of such boundary values along the x axis of the different slices of the specimen.

The 3D model has been developed with an extension input module in order to implement non-trivial geometry of the investigated specimen. The module starts from a parallelepiped-shaped specimen made of the main material (the matrix), then it substitutes (by set operations) solid or plane regions of such parallelepiped specimen with solid or plane objects of a different material. Hollow object are modelled as solid or plane sub-domains made of air.

The resultant 3D parallel code have been run on Linux cluster-like parallel supercomputers, mainly the Biocluster (a eight nodes, two AMD Opteron 232 CPU/per node, Linux cluster), operated at the Bioinformatics and High Performance Computing Labs of the Bioindustry Park of Canavese (Colleretto Giacosa), the IBM 1350 Linux Cluster and the Cray XD1 cluster, both operated at Cineca (Consorzio InterUniversitario per l’Elaborazione e il Calcolo Automatico, Casalecchio di Reno, Bologna).

Bibliography

- [1] H.M. Jaeger and S.R. Nagel. Granular solids, liquids and gases. *Rev. Mod. Phys.*, 68(4):1259–1273, 1996.
- [2] H.M. Jaeger, S.R. Nagel, and R.P. Behringer. The physics of granular materials. *Phys. Today*, 49(4):32–38, 1996.
- [3] P.A. Johnson and X. Jia. Nonlinear dynamics, granular media and dynamic earthquake triggering. *Nature*, 437(6):871–874.
- [4] C. Campos-Pozuelo, C. Vanhille, and J.A. Gallego-Juarez. *The Universality of Nonclassical Nonlinearity (with application to Nondestructive Evaluation and Ultrasonics)*, chapter 28, pages 441–463. Springer, New York, 2006.
- [5] L.D. Landau and E.M. Lifshitz. *Theory of Elasticity*, volume 7 of *Course in Theoretical Physics*. Pergamon, Oxford, 1986.
- [6] R. A. Guyer and P. A. Johnson. Nonlinear mesoscopic elasticity: Evidence for a new class of materials. *Phys. Today*, 1999.
- [7] P.A. Johnson, B. Zinszner, and P.N.J. Rasolofosaon. Resonance and nonlinear elastic phenomena in rock. *J. Geophys. Res.*, 101:11553–11564, 1996.
- [8] P.A. Johnson. The new wave in acoustic testing. *Mater. World, J. Inst. Mater.*, 7:544–546, 1999.
- [9] P.A. Johnson. *The Universality of Nonclassical Nonlinearity (with application to Nondestructive Evaluation and Ultrasonics)*, chapter 4, pages 49–69. Springer, New York, 2006.
- [10] K. van Den Abeele, J. Cameliet, J. Tencate, and P.A. Johnson. Nonlinear elastic wave spectroscopy (news) techniques to discern material damage, part ii: Single mode nonlinear resonant acoustic spectroscopy. *Res. Nondestruct. Eval.*, 12(1):31–42, 2000.
- [11] A.S. Gliozzi, M. Nobili, and M. Scalerandi. Modeling localized nonlinear damage and analysis of its influence on resonance frequencies. *J. Phys. D Appl. Phys.*, 39(17):3895–3903, 2006.
- [12] L.A. Ostrovsky and P.A. Johnson. Dynamics nonlinear elasticity in geomaterials. *Riv. Nuov. Cim.*, 24(7):1–46, 2001.
- [13] A. Granato and K. Lucke. Application of dislocation theory to internal friction phenomena at high frequency. *J. Appl. Phys.*, 27:798–805, 1956.
- [14] James A. TenCate, Eric Smith, , and Robert A. Guyer. Universal slow dynamics in granular solids. *Phys. Rev. Lett.*, 85:100–1023, 2000.

- [15] J. A. Tencate, D. Pasqualini, S. Habib, K. Heitmann, D. Higdon, and P. A. Johnson. Nonlinear and nonequilibrium dynamics in geomaterials. *Phys. Rev. Lett.*, 2004.
- [16] P.A. Johnson and A. Sutin. Slow dynamics and anomalous nonlinear fast dynamics in diverse solids. *J. Acoust. Soc. Amer.*, 117(1):124–130, 2005.
- [17] A. Migliori and J.L. Sarrao. *Resonant Ultrasound Spectroscopy: applications to Physics, Materials Measurements and Non-Destructive Evaluation*. John Wiley and Sons Inc., New York, 1997.
- [18] B. Zadler, J.H.L. Rousseau, J.A. Scales, and M.L. Smith. Resonant ultrasound spectroscopy: theory and application. *Geophys. J. Int.*, 156:154–169, 2004.
- [19] J. Maynard. Resonant ultrasound spectroscopy. *Phys. Today*, 49(1):26–31, 1996.
- [20] R.G. Leisure and F.A. Willis. Resonant ultrasound spectroscopy. *J. Phys. Condens. Matter*, 9:6001–6029, 1997.
- [21] A. Migliori and T.W. Darling. Resonant ultrasound spectroscopy for materials studies and non-destructive testing. *Ultrasonics*, 34:473–476, 1996.
- [22] K. van Den Abeele, A. Sutin, and P.A. Johnson. Nonlinear elastic wave spectroscopy (news) techniques to discern material damage, part i: Nonlinear wave modulation spectroscopy (nwms). *Res. Nondestruct. Eval.*, 12(1):17–30, 2000.
- [23] A. Moussatov, V. Gusev, and B. Castagnede. Self-induced hysteresis for nonlinear acoustic waves in cracked material. *Phys. Rev. Lett.*, 90:124301, 2003.
- [24] K. van Den Abeele and J. De Vissche. Damage assessment in reinforced concrete using spectral and temporal nonlinear vibration techniques. *Cem. Concr. Res.*, 30, 2000.
- [25] G. Gist. Fluid effects on velocity and attenuation in sandstones. *J. Acoust. Soc. Amer.*, 96:1158–1173, 1994.
- [26] T.J. Ulrich and T.W. Darling. Observation of anomalous elastic behaviour in rock at low temperatures. *Geophys. Res. Lett.*, 28:2293–2296, 2001.
- [27] M. Nobili and M. Scalerandi. Temperature effects on the elastic properties of hysteretic elasti media: modeling and simulations. *Phys. Rev. B*, 69:104105, 2004.
- [28] K.E.A. Van Den Abeele, J. Carmeliet, P.A. Johnson, and B. Zinszner. Influence of water saturation on the nonlinear elastic mesoscopic response of earth materials and the implications to the mechanism of nonlinearity. *J. Geophys. Res.*, 107, 2002.
- [29] J. Carmeliet and K.E.A. Van Den Abeele. Application of the preisach-mayergoyz space model to analyze moisture effects on the nonlinear elastic response of rocks. *Geophys. Res. Lett.*, 29(7), 2002.
- [30] J.A. TenCate, T.J. Shankland, and P.A. Johnson. *The Universality of Nonclassical Nonlinearity (with application to Nondestructive Evaluation and Ultrasonics)*, chapter 25, pages 409–414. Springer, New York, 2006.
- [31] T.W. Darling, J.A. Tencate, D.W. Brown, B. Clausen, and S.C. Vogel. Neutron diffraction study of the contribution of grain contacts to nonlinear stress-strain behavior. *Geophys. Res. Lett.*, 31:L16604, 2004.

- [32] K.L. Page, T. Proffen, S.E. McLain, T.W. Darling, and J.A. TenCate. Local atomic structure of fontainebleau sandstone: Evidence for an amorphous phase? *Geophys. Res. Lett.*, 31:L24606, 2004.
- [33] T.W. Darling, J.A. TenCate, S. Vogel, T. Proffen, K. Page, C. Herrera, A.M. Covington, and E. Emmons. Localizing nonclassical nonlinearity in geological materials with neutron scattering experiments. In A.A. Atchley, V.W. Sparrow, and R.M. Keolian, editors, *Innovations in Nonlinear Acoustics: 17th International Symposium on Nonlinear Acoustics*, pages 19–26. American Institute of Physics, 2006.
- [34] T. Proffen, S.J.L. Billinge, T.T. Egami, and D. Louca. Structural analysis of complex materials using the atomic pair distribution function - a practical guide. *Zeits. fur Kristall.*, 218(2):132–143, 2003.
- [35] M.W. Barsoum, M. Radovic, T. Zhen, P. Finkel, and S.R. Kalidindi. Dynamic elastic hysteretic solids and dislocations. *Phys. Rev. Lett.*, 94:085501, 2005.
- [36] C. Pecorari. Adhesion and nonlinear scattering by rough surfaces in contact: beyond the phenomenology of the preisach-mayergoyz framework. *J. Acoust. Soc.Am.*, 116(4):1939–1947, 2004.
- [37] O.O.Vakhnenko, V.O. Vakhnenko, T.J. Shankland, and J.A. Ten Cate. Strain-induced kinetics of intergrain defects as the mechanism of slow dynamics in the nonlinear resonant response of humid sandstone bars. *Phys. Rev. E*, 70:015602, 2004.
- [38] O.O.Vakhnenko, V.O. Vakhnenko, and T.J. Shankland. Soft-ratchet modeling of nd-point memory in the nonlinear resonant response of sedimentary rocks. *Phys. Rev. B*, 71:174103, 2005.
- [39] M.A.Krasnosel'skii and A.V.Pokrovskii. *Systems with hysteresis*. Springer-Verlag, 1989.
- [40] I.D. Mayergoyz. Hysteresis models from a mathematical and control theory points of view. *J. Appl. Phys.*, 57:3803–3805, 1985.
- [41] I. D. Mayergoyz. *Mathematical Models of Hysteresis*. Springer-Verlag, 1991.
- [42] G. Bertotti and I. Mayergoyz, editors. *The Science of Hysteresis*. Elsevier, 2006.
- [43] F. Preisach. über die magnetische nachwirkung. *Z. Phys.*, 94:277–283, 1935.
- [44] G.Bertotti. *Hysteresis in Magnetism*. Academic Press.
- [45] P.P.Delsanto and M.Scalerandi. Modeling nonclassical nonlinearity, conditioning, and slow dynamics effects in mesoscopic elastic materials. *Phys.Rev. B*, 68:064107, 2003.
- [46] M.Scalerandi, V. Agostini, P.P. Delsanto, K. Van Den Abeele, and P.A. Johnson. Local interaction simulation approach to modelling nonclassical, nolineare elastic behavior in solids. *J. Acoust. Soc. Amer.*, 113(6):3049–3059, 2003.
- [47] M.Scalerandi, P.P.Delsanto, and P.A.Johnson. Stress induced conditioning and thermal relaxation in the simulations of quasi-static compression experiments. *J. Phys. D. Appl. Phys.*, 36:288–293, 2003.
- [48] P.P. Delsanto, editor. *The Universality of Nonclassical Nonlinearity (with application to Nondestructive Evaluation and Ultrasonics)*. Springer, New York, 2006.

- [49] R.A. Guyer. *The Science of Hysteresis*, volume III, chapter 6. Elsevier, 2006.
- [50] M. Scalerandi, M. Nobili, M. Griffa, A. Gliozzi, and F. Bosia. A preisach-mayergoyz approach to fatigue induced irreversibility. *Phys. Rev. B*, 73:092103, 2006.
- [51] P.P. Delsanto, T. Whitcombe, H.H. Chaskelis, and R.B. Mignogna. Connection machine simulation of ultrasonic wave propagation in materials. i. the one-dimensional case. *Wave Motion*, 16(1):65–80, 1992.
- [52] P.P. Delsanto, R.S. Schechter, H.H. Chaskelis, R.B. Mignogna, and R. Kline. Connection machine simulation of ultrasonic wave propagation in materials. ii. the 2-dimensional case. *Wave Motion*, 20(4):295–314, 1994.
- [53] P.P. Delsanto, R.S. Schechter, , and R.B. Mignogna. Connection machine simulation of ultrasonic wave propagation in materials. iii. the three-dimensional case. *Wave Motion*, 26(4):329–339, 1997.
- [54] R.S. Schechter, H.H. Chaskelis, R.B. Mignogna, and P.P. Delsanto. Real-time parallel computation and visualization od ultrasonic pulses in solids. *Science*, 265(5176):1188–1192, 1994.
- [55] N. Cretu, P.P. Delsanto, G. Rosca, M. Scalerandi, and I. Sturzu. Ultrasonic pulse propagation in inhomogeneous one-dimensional media. *J. Acoust. Soc. Amer.*, 104(1):57–63, 1998.
- [56] V. Agostini, P.P. Delsanto, I. Genesio, and D. Olivero. Simulation of lamb wave propagation for the characterization of complex structures. *IEEE Trans. Ultrason. Ferr. Freq. Contr.*, 50(4):441–448, 2003.
- [57] M. Hirsekorn, P.P. Delsanto, N.K. Batra, and P. Matic. Modelling and simulation of acoustic wave propagation in locally resonant sonic materials. *Ultrasonics*, 42(1-9):231–235, 2004.
- [58] M. Hirsekorn, P.P. Delsanto, A.C. Leung, and P. Matic. Elastic wave propagation in locally resonant sonic materiasl: comparison between local interaction simulation approach and modal analysis. *J. Appl. Phys.*, 2006.
- [59] E. Ruffino and P.P. Delsanto. Scattering of ultrasonic waves by void inclusions. *J. Acoust. Soc. Amer.*, 108(4):1941–1945, 2000.
- [60] P.P. Delsanto and M. Scalerandi. A spring model for the simulation of the propagation of ultrasonic pulses through imperfect contact interfaces. *J. Acoust. Soc. Amer.*, 104(5):2584–2591, 1998.
- [61] P.P.Delsanto, A.S. Gliozzi, M. Hirsekorn, and M. Nobili. A 2d spring model for the simulation of ultrasonic wave propagation in nonlinear hysteretic media. *Ultrasonics*, 44(3):279–286, 2006.
- [62] M. Hirsekorn, A.S. Gliozzi, M. Nobili, and K.V.D. Abeele. *The Universality of Nonclassical Nonlinearity (with application to Nondestructive Evaluation and Ultrasonics)*, chapter 18, pages 285–306. Springer, New York, 2006.
- [63] M. Bentahar, H. El Aqra, R. El Gurjouma, M. Griffa, and M. Scalerandi. Hysteretic elasticity in damaged concrete: Quantitative analysis of slow and fast dynamics. *Phys. Rev. B*, 73:014116–1/10, 2006.

- [64] J.O.A. Robertsson, J.O. Blanch, and W.W. Symes. Viscoelastic finite-difference modeling. *Geophysics*, 59(9):1444–1456, 1994.
- [65] M.A. Biot. Propagation of elastic waves in cylindrical bore containing fluid. *J. Appl. Phys.*, 23(9):997–1005, 1952.
- [66] M.A. Biot. Theory of the propagation of elastic waves in a fluid-saturated porous solid. i. low-frequency range. *J. Acoust. Soc. Amer.*, 28(2):168–178, 1956.
- [67] M.A. Biot. Theory of the propagation of elastic waves in a fluid-saturated porous solid. ii. higher frequency range. *J. Acoust. Soc. Amer.*, 28(2):179–191, 1956.
- [68] M. Nobili, F. Bosia, A. Gliozzi, M. Griffa, and M. Scalerandi. Acoustic emission and nonlinear elasticity in fatigue induced damage. In *Proceedings of the 12th International Congress on Sound and Vibration (ICSV12)*, July 2005.
- [69] A.S. Gliozzi, M. Nobili, and M. Scalerandi. *The Universality of Nonclassical Nonlinearity (Applications to Non-Destructive Evaluation and Ultrasonics)*, chapter 16, pages 249–266. Springer, New York, 2006.
- [70] M. Scalerandi, M. Nobili, M. Griffa, A.S. Gliozzi, and F. Bosia. *The Universality of Nonclassical Nonlinearity (Applications to Non-Destructive Evaluation and Ultrasonics)*, chapter 17, pages 267–284. Springer, New York, 2006.
- [71] V. Aleshin and K. Van Den Abeele. Micro-potential model for stress-strain hysteresis of microcracked materials. *J. Mech. Phys. Solids*, 53(4):795–824, 2005.
- [72] B. Zinszner, P. A. Johnson, and P. N. J. Rasolofosaon. Influence of change in physical state on elastic nonlinear response in rock: significance of effective pressure and water saturation. *J. Geophys. Res.*, 102:8105–?, 1997.
- [73] J.C. Lacouture, P.A. Johnson, and F. Cohen-Tenoudji. Study of critical behavior in concrete during curing by application of dynamic linear and nonlinear means. *J. Acoust. Soc. Amer.*, 113:1325–1332, 2003.
- [74] K. Warnemuende and H.C. Wu. Actively modulated acoustic nondestructive evaluation of concrete. *Cem. Concr. Res.*, 34(4):563–580, 2004.
- [75] H.C. Wu and K. Warnemuende. Nonlinear acoustic nondestructive testing for concrete durability. In A.E. Aktan and S.R. Gosselin, editors, *Proceedings of SPIE. Nondestructive Evaluation of Highways, Utilities, and Pipelines IV*, volume 3995, pages 501–507. The International Society for Optical Engineering, 2000.
- [76] J. A. Tencate and T. J. Shankland. Slow dynamics in the nonlinear elastic response of berea sandstone. *Geophys. Res. Lett.*, 1996.
- [77] P. P. Delsanto, M. Nobili, and M. Scalerandi. Temperature dependence of the elastic properties of hysteretic materials.
- [78] M. Bentahar and R. El Guerjouma. Experimental investigations in nonlinear acoustics for damage characterisation of composite materials. *Ultrasonics*, ??, 2006.
- [79] A. Baltazar, S. I. Rokhlin, and C. Pecorari. On the relationship between ultrasonic and micromechanical properties of contacting rough surfaces. *J. Mech. Phys. Solids*, 50:1397–1416, 2002.

- [80] J.-Y. Kim, A. Baltazar, and S. I. Rokhlin. Ultrasonic assesment of rough surface contact between solids from elastoplastic loading-unloading hysteresis cycle. *J. Mech. Phys. Solids*, 52:1911–1934, 2004.
- [81] M. Fink, D. Cassereau, A. Derode, C. Prada, P. Roux, M. Tanter, J.L. Thomas, and F. Wu. Time-reversed acoustics. *Rep. Prog. Phys.*, 63:1933–1995, 2000.
- [82] B. Y. Zel’dovich, N.F. Pilipetsky, and V.V. Shkunov. *Principles of Phase Conjugation*. Springer, Berlin, 1985.
- [83] D.M. Pepper. *Laser Handbook*, chapter Nonlinear optical phase conjugation, pages 333–485. North Holland, Amsterdam, 1988.
- [84] D.V. Vlasov, E.A. Zabolotskaja, and Y.A. Kravtsov. Acoustic pahse conjugation in water containing bubbles. *Sov. Phys. Acoust.*, 29:69–70, 1983.
- [85] E.A. Zabolotskaja. Phase conjugation of sound beams in connection with four-phonon interaction in a liquid containing gas bubbles. *Sov. Phys. Acoust.*, 30:462–463, 1984.
- [86] T. Sato, H. Kataoka, T. Nakayama, and Y. Yamakoshi. Ultrasonic phase conjugator using micro particle suspended cell and its application. In *Acoustical Imaging*, pages 361–370. Plenum, New York, 1989.
- [87] F.V. Bunkin, D.V. Vlasov, E.A. Zabolotskaja, and Y.A. Kravtsov. Phase conjugation of sound beams in four-phonon interactions withe temperature waves. *Sov. Phys. Acoust.*, 28:440–441, 1983.
- [88] D. Cassereau and M. Fink. Time-reversal of ultrasonic fields-part iii: Theory of the closed time-reversal cavity. *IEEE Trans. Ultrason. Ferroelec. Freq. Contr.*, 39(5):579–592, september 1992.
- [89] R.P. Porter and A. J. Devaney. Holography and the inverse source problem. *J. Opt. Soc. Amer.*, 72:327–330, 1982.
- [90] J. de Rosny and M. Fink. Overcoming the diffraction limit in wave physics using a time-reversal mirror and a novel acoustic sink. *Phys. Rev. Lett.*, 89(12):124301–1/4, 2002.
- [91] M. Fink. Time reversal of ultrasonic fields-part i: Basic principles. *IEEE Trans. Ultrason. Ferroelec. Freq. Contr.*, 39(5):555–566, september 1992.
- [92] M. Fink, C. Prada, F. Wu, and D. Cassereau. Self focusing with time reversal mirror in inhomogeneous media. In *Proc. IEEE Ultrason. Symp. 1989*, pages 681–686, Montreal, PQ, Canada, 1989. IEEE.
- [93] F. Wu, J. L. Thomas, and M. Fink. Time reversal of ultrasonic fields-part ii: Experiemntal results. *IEEE Trans. Ultrason. Ferroelec. Freq. Contr.*, 39(5):567–578, 1992.
- [94] A. Papoulis. *Signal Analysis*. McGraw-Hill, New York, 1984.
- [95] M. Fink and C. Prada. Acoustic time-reversal mirrors. *Inverse Problems*, 17:R1–R38, 2001.
- [96] C. Prada, M. Fink, and F. Wu. The iterative time reversal mirror: a solution to self-focusing in the pulse-echo mode. *J. Acoust. Soc. Amer.*, 90(2):1119–1129, 1991.
- [97] C. Prada, J.L. Thomas, and M. Fink. The iterative time reversal process: analysis of convergence. *J. Acoust. Soc. Amer.*, 97(1):62–71, 1995.

- [98] G. Montaldo, M. Tanter, and M. Fink. Revisiting iterative time reversal: real time detection of multiple targets. *J. Acoust. Soc. Amer.*, 512(2):776–784, 2004.
- [99] M. Fink, G. Montaldo, and M. Tanter. Time reversal acoustics in biomedical engineering. *Annual Review of Biomedical Engineering*, 5:465–497, 2003.
- [100] A. Derode, P. Roux, and M. Fink. Robust acoustic time reversal with high order multiple scattering. *Phys. Rev. Lett.*, 75:4206–4209, 1995.
- [101] A. Ishimura. *Propagation and scattering in random media*, volume 1 and 2. Academic Press, New York, 1978.
- [102] P. Roux, B. Roman, and M. Fink. Time-reversal in an ultrasonic waveguide. *Appl. Phys. Lett.*, 70(14):1811–1813, 1997.
- [103] D.R. Jackson and D. R. Dowling. Phase conjugation in underwater acoustics. *J. Acoust. Soc. America*, 89(1):171–181, 1991.
- [104] W.A. Kupperman, W.S. Hodgkiss, H. Song, T. Akal, C. Ferla, and D. Jackson. Phase conjugation in the ocean: experimental demonstration of an acoustical time reversal mirror. *J. Acoust. Soc. America*, 103:25–40, 1998.
- [105] W. Hodgkiss, H. Song, W. Kupperman, T. Akal, C. Ferla, and D. Jackson. A long range and variable phase conjugation experiment in shallow water. *J. Acoust. Soc. America*, 105:1597–1604, 1999.
- [106] H. Song, W. Kupperman, W. Hodgkiss, T. Akal, and C. Ferla. Iterative time reversal in the ocean. *J. Acoust. Soc. America*, 105:3176–3184, 1999.
- [107] L. Bunimovitch. On the ergodic properties of nowhere dispersing billiards. *Commun. Math. Phys.*, 65:295–312, 1979.
- [108] C. Draeger and M. Fink. One-channel time reversal of elastic waves in a chaotic 2d-silicon cavity. *Phys. Rev. Lett.*, 79(3):407–410, 1997.
- [109] C. Draeger and M. Fink. One-channel time-reversal in chaotic cavities: experimental results. *J. Acoust. Soc. America*, 105(2):618–625, 1999.
- [110] C. Draeger and M. Fink. One-channel time-reversal in chaotic cavities: theoretical limits. *J. Acoust. Soc. America*, 105(2):611–617, 1999.
- [111] J-L Thomas and M. Fink. Ultrasonic beam focusing through tissue inhomogeneities with a time reversal mirror: application to transskull therapy. *IEEE Trans. Ultrason. Ferroelec. Freq. Contr.*, 43:1122–1129, 1996.
- [112] M. Tanter, J-L. Thomas, and M. Fink. Focusing and steering through absorbing and aberrating layers: application to ultrasonic propagation through the skull. *J. Acoust. Soc. America*, 103:2403–2410, 1998.
- [113] K.B. Cunningham, M.F. Hamilton, A. P. Brysev, and L. M. Krutyansky. Time-reversed sound beams of finite amplitude. *J. Acoust. Soc. Amer.*, 109(6):2668–2674, 2001.
- [114] M.F. Hamilton and D.T. Blackstock, editors. *Nonlinear Acoustics*. Academic Press, Chestnut Hill, MA, USA, 1998.

- [115] M. Tanter, J-L. Thomas, F. Coulouvrat, and M. Fink. Time reversal invariance of nonlinear acoustic wave propagation in weakly viscous media. In *Proceedings of the IEEE Ultrasonics Symposium, 1999*, pages 1419–1422. IEEE, 1999.
- [116] A.P. Brysev, F.V. Bunkin, M.F. Hamilton, L.m. Krutyanskii, K.B. Cunningham, V.L. Preobrazhenskii, Y.V. Pyl'nov, and A.d. Stakhovskii. Nonlinear propagation of a quasi-plane conjugate ultrasonic beam. *Acoust.Phys.*, 44:641–650, 1998.
- [117] P. Roux, A. Derode, and A. Peyre. Acoustical imaging through a multiple scattering medium using a time-reversal mirror. *J. Acoust. Soc. Amer.*, 107(2):L7–L12, 2000.
- [118] G. Montaldo, D. Palacio, M. Tanter, and M. Fink. Time reversal kaleidoscope: a smart transducer for three-dimensional ultrasonic imaging. *Appl.Phys.Lett.*, 84(19):3879–3881, 2004.
- [119] G. Montaldo, D. Palacio, M. Tanter, and M. Fink. Building three-dimensional images using a time-reversal chaotic cavity. *IEEE Trans. Ultrason. Ferroelec. Freq. Contr.*, 52(9):1489–1497, 2000.
- [120] C. Prada, E. Kerbrat, D. Cassereau, and M. Fink. Time reversal techniques in ultrasonic nondestructive testing of scattering media. *Inverse Problems*, 18:1761–1773, 2002.
- [121] C. Prada and M. Fink. Eigenmodes of the time reversal operator: a solution to selective focusing in multiple target media. *Wave Motion*, 20:151–163, 1994.
- [122] C. Prada, S. Manneville, D. Spoliansky, and M. Fink. Decomposition of the time reversal operator: detection and selective focusing on two scatterers. *J. Acoust. Soc. Amer.*, 99:2067–2076, 1996.
- [123] L. Borcea, G. Papanicolaou, C. Tsogka, and J. Berryman. Imaging and time reversal in random media. *Inverse Problems*, 18:1247–1279, 2002.
- [124] M.A. Haider, K.J. Mehta, and J-P Fouque. Time-reversal simulations for detection in randomly layered media. *Waves in Rand. Media*, 14:185–197, 2004.
- [125] C. H. Wang, J. T. Rose, and F-K. Chang. A computerized time-reversal method for structural health monitoring. In *Proc. SPIE*, volume 5046, pages 4858–4869, 2003.
- [126] H.W. Chun, J.T. Rose, and F-K. Chang. A synthetic time-reversal imaging method for structural health monitoring. *Smart. Mater. Struct.*, 13:415–423, 2004.
- [127] T. Leutenegger and J. Dual. Detection of defects in cylindrical structures using time reverse method and a finite-difference approach. *Ultrasonics*, 40:721–725, 2002.
- [128] T.J. Ulrich, P.A. Johnson, and A. Sutin. Imaging nonlinear scatterers applying the time reversal mirror. *J. Acoust. Soc. Amer.*, 119(3):1514–1518, 2006.
- [129] K. Mehta and R. Snieder. Time reversed imaging for perturbed media. *Am. J. Phys.*, 74(3):224–231, 2006.
- [130] A.S. Gliozzi, M. Griffa, and M. Scalerandi. Efficiency of time-reversed acoustics for nonlinear damage detection in solids. *J. Acoust. Soc. Amer.*, 120(5):2506–2517, 2006.
- [131] S.K. Lehman and A.J. Devaney. Transmission mode time-reversal super-resolution imaging. *J. Acoust. Soc. Amer.*, 113(5):2742–2753, 2003.

- [132] F.K. Gruber, E.A. Marengo, and A.J. Devaney. Time-reversal imaging with multiple signal classification considering multiple scattering between the targets. *J. Acoust. Soc. Amer.*, 115(6):3042–3047, 2004.
- [133] P. Blomgren, G. Papanicolau, and H. Zhao. Long distance time reversal and imaging in random media: Numerical simulations (a). *J. Acoust. Soc. Amer.*, 110(5):2633, 2001.
- [134] T.J. Ulrich, R.A. Guyer, and P.A. Johnson. *Phys. Rev. Lett.*, 2005. submitted.
- [135] P.A. Johnson, T.J. Shankland, R.J. O’Connell, and J.N. Albright. Nonlinear generation of elastic waves in crystalline rock. *J. Geophys. Res.*, 92:3597–3602, 1987.
- [136] P.A. Johnson and T.J. Shankland. Nonlinear generation of elastic waves in crystalline rock and sandstone: continuous wave travel time observations. *J. Geophys. Res.*, 94:17729–17734, 1989.
- [137] P.A. Johnson, A. Migliori, and T.J. Shankland. Continuous wave phase detection for probing nonlinear elastic wave interactions in rocks. *J. Acoust. Soc. Amer.*, 89:598–603, 1989.
- [138] E.H. Field, P.A. Johnson, I. Beresnev, and Y. Zeng. Nonlinear ground-motion amplification of sediments during the 1994 northridge earthquake. *Nature*, 390:599–602, 1997.
- [139] J. Gomberg, P.A. Reasenber, P. Bodin, and R.A. Harris. Earthquake triggering by seismic waves following the landers and hector mine earthquakes. *Nature*, 411:462–466, 2001.
- [140] J. Gomberg, P. Bodin, K. Larson, and H. Dragert. Earthquake nucleation by transient deformations caused by the $m = 7.9$ denali, alaska earthquake. *Nature*, 427:621–624, 2004.
- [141] C. Larmat, J-P. Montagner, M. Fink, Y. Capdeville, A. Tourin, and E. Clévéde. Time-reversal imaging of seismic sources and application to the great sumatra earthquake. *Geophys. Res. Lett.*, 33:L19312, 2006.
- [142] D. Komatitsch and J. Tromp. Introduction to the spectral element method for three-dimensional seismic wave propagation. *Geophys. J. Int.*, 139:806–822, 1999.
- [143] D. Komatitsch and J. Tromp. Spectral-element simulations of global seismic wave propagation-i. validation. *Geophys. J. Int.*, 149:390–412, 2002.
- [144] D. Komatitsch and J. Tromp. Spectral-element simulations of global seismic wave propagation-ii. three-dimensional models, oceans, rotation and self-gravitation. *Geophys. J. Int.*, 150:303–318.
- [145] D. Komatitsch, C. Barnes, and J. Tromp. Simulation of anisotropic wave propagation based upon a spectral element method. *Geophysics*, 65(4):1251–1260, 2000.
- [146] D. Komatitsch, J. Ritsema, and J. Tromp. The spectral-element method, beowulf computing and global seismology. *Science*, 298:1737–1742, 2002.
- [147] D. Komatitsch, R. Martin, J. Tromp, M.A. Taylor, and B.A. Wingate. Wave propagation in 2-d elastic media using a spectral element methods with triangles and quadrangles. *J. Comp. Acoust.*, 9(2):703–718, 2001.
- [148] G. Bertotti. Dynamic generalization of the preisach model of hysteresis. *IEEE Trans. Magn.*, 1992.

- [149] S.H. Charap and A. Ktena. Vector Preisach. *J. Appl. Phys.*, 1993.
- [150] I.D. Mayergoyz. Vector Preisach hysteresis models. *J. Appl. Phys.*, 63:2995–3000, 1988.
- [151] K. Helbig. A formalism for the consistent description of non-linear elasticity of anisotropic media. In P.N.J. Rasolofosaon, editor, *Proceedings of the Eighth International Workshop on Seismic Anisotropy*, volume 53 of *Rev. de l'Institut Français du Pétrole*, pages 693–708, 1998.
- [152] K. Helbig and P.N.J. Rasolofosaon. A theoretical paradigm for describing hysteresis and nonlinear elasticity in arbitrary anisotropic rocks. In *Anisotropy 2000: Fractures, converted waves and case studies*. The Society of Exploration Geophysicists.
- [153] J. Dongarra, I. Foster, G. Fox, W. Gropp, K. Kennedy, and A. Whyte, editors. *Sourcebook of parallel computing*. Morgan Kaufmann Publishers, 2003.